

DOCTOR OF PHILOSOPHY

Repair of Nickel-base Superalloy Components using Direct Energy Deposition

Sarkar, Riddhi

Award date:
2023

Awarding institution:
Coventry University
Deakin University

[Link to publication](#)

General rights

Copyright and moral rights for the publications made accessible in the public portal are retained by the authors and/or other copyright owners and it is a condition of accessing publications that users recognise and abide by the legal requirements associated with these rights.

- Users may download and print one copy of this thesis for personal non-commercial research or study
- This thesis cannot be reproduced or quoted extensively from without first obtaining permission from the copyright holder(s)
- You may not further distribute the material or use it for any profit-making activity or commercial gain
- You may freely distribute the URL identifying the publication in the public portal

Take down policy

If you believe that this document breaches copyright please contact us providing details, and we will remove access to the work immediately and investigate your claim.

Repair of Nickel-base Superalloy Components using Direct Energy Deposition

By

Riddhi Sarkar

PhD

June 2022



Repair of Nickel-base Superalloy Components using Direct Energy Deposition

By

Riddhi Sarkar

June 2022



A thesis submitted in partial fulfilment of the University's requirements for the Degree of Doctor of Philosophy. This thesis is a jointly supervised Cotutelle Programme with Coventry University and Deakin University.



DEAKIN UNIVERSITY CANDIDATE DECLARATION

I certify the following about the thesis entitled

Repair of Nickel-base superalloy components using Direct Energy Deposition

submitted for the degree of **Doctor of Philosophy**

- a. I am the creator of all or part of the whole work(s) (including content and layout) and that where reference is made to the work of others, due acknowledgment is given.
- b. The work(s) are not in any way a violation or infringement of any copyright, trademark, patent, or other rights whatsoever of any person.
- c. That if the work(s) have been commissioned, sponsored or supported by any organisation, I have fulfilled all of the obligations required by such contract or agreement.
- d. That any material in the thesis which has been accepted for a degree or diploma by any university or institution is identified in the text.
- e. All research integrity requirements have been complied with.

'I certify that I am the student named below and that the information provided in the form is correct'

Full Name: Riddhi Sarkar

This item has been removed due to 3rd Party Copyright. The unabridged version of the thesis can be found in the Lanchester Library Coventry University
Date: 24/06/2022



**DEAKIN UNIVERSITY
ACCESS TO THESIS - A**

I certify the following about the thesis entitled

Repair of Nickel-base superalloy components using Direct Energy Deposition

submitted for the degree of **Doctor of Philosophy**

This thesis may be made available for consultation, loan and limited copying in accordance with the Copyright Act 1968.

'I certify that I am the student named below and that the information provided in the form is correct'

This item has been removed due to 3rd Party Copyright. The unabridged version of the thesis can be found in the Lanchester Library, Coventry University.

This item has been removed due to 3rd Party Copyright. The unabridged version of the thesis can be found in the Lanchester Library, Coventry University.

CUDU Candidate's Declaration Form



Certificate of Ethical Approval

Applicant: Riddhi Sarkar
Project Title: Repair of superalloy components using Laser Engineered Net Shaping (LENS)

This is to certify that the above named applicant has completed the Coventry University Ethical Approval process and their project has been confirmed and approved as Low Risk

Date of approval: 07 Dec 2020
Project Reference Number: P115813

Acknowledgment

I would like to thank many people for their support and contribution during my PhD and made this thesis possible. Firstly, I feel blessed that I got the opportunity to work in a jointly supervised cotutelle program offered by Deakin University-Coventry University. I express my gratitude to all my supervisors, of A/Prof Daniel Fabijanic (IFM), A/Prof Tim Hildith (SOE) at Deakin University, Australia, and Prof. Michael Fitzpatrick, Dr David Parfitt, and Prof. Bo Chen at Coventry University, UK, for their consistent scientific and moral support, encouragement, and motivation throughout the PhD project. I especially thank them for their innovative and unique ideas and directions and for many discussions in solving different issues during the project.

My sincere gratitude to Dr Andrew Sullivan and Dr Adam Taylor for electron microscopy training and for assisting in microstructural characterization. I am also thankful to all technical staff, Mr John Vella, Mr Rob Pow, Mr Mohan Shetty, Mr Alex Orokity, and Mr Rob Lovett, for their assistance in performing my experiments. I would also like to thank Deakin University for the financial support through the DUPR scholarship and for providing all the required equipment, materials, and facilities for my studies. Special thanks to the IFM HDR support, Deakin University and Doctoral College, Coventry University, for supporting all admin and paperwork throughout my candidature.

During these three and half years, I came across many people, and a few of them made my stay memorable in some or other ways. I want to thank my friends Roshan, Suman, Hridip, Nishan, Swastika, Surupa, Srikant, Acchut, Amrito, and Vamshi for their support during my PhD. I especially thank Dr Murugesan Annasamy, post-doc at IFM, for his immense support and advice throughout these years. At this point, I also remember my previous teacher Prof. Saradindukumar Ray from Jadavpur University, Kolkata, India, for his invaluable teaching and encouragement.

I have lived an amazing journey that started two decades earlier, from schooling in a small town in India to pursuing a PhD in Australia. This journey would not have been possible without adequate support, encouragement, and motivation from my family members, especially my parents and in-laws. So, I take this opportunity to thank and express my gratitude to them. Last but not the least, I would like to thank my wife, Moumita Mondal, for her unconditional love, patience, and sacrifice during my PhD. Without her support, it would not have been possible for me to pursue this endeavour.

Abstract

In the present study, repair of Inconel 718 (IN718) components was conducted using direct energy deposition (DED) technology. The deformation behaviour of Inconel 718 (IN718) components repaired using DED was examined using 4 – point bend tests and high cycle fatigue (HCF) tests. Investigations were performed on the entire repaired part- including the substrate and the deposit zone. A gradient microstructure was observed in the repaired IN718- the substrate exhibiting uniformly distributed equiaxed grains with grain size $\sim 90 \mu\text{m}$ and high fraction of annealing twins; however, the deposit zone microstructure differed significantly from the wrought substrate consisting of a mix of columnar and equiaxed dendrite with average grain size $\sim 28 \mu\text{m}$. Due to the sharp difference in grain size and morphology in the substrate and the deposit zone, the DED-repaired IN718 components are referred to as “repaired composites” in the thesis. Micro-hardness results highlighted the need for heat treatment as it can remove the heat-affected zone and hardness dip, creating a uniform hardness profile across the joint. The mechanical tests and microstructural investigation were performed in the as-deposited and under two different heat-treated conditions: direct aged (DA), where the repaired composites were aged at 720°C for 8 hours and 620°C for 8 hours, and solution-treated and aged (STA) where the repaired composites were solution treated at 980°C followed by ageing. These heat treatments were chosen to enable solid-state phase transformation in the repaired composites while preventing coarsening of the substrate grains.

The 4-point bend tests were performed on the repaired composites with two groove angles, and the strain evolution in the repaired components was compared using digital image correlation. In all the repaired composites, strain concentration was observed in the deposit zone – substrate interface due to NbC liquation resulting in Nb-rich film formation on the substrate grain boundaries and an effect of groove angle was observed. The repaired composites with a low/shallow groove angle exhibited higher deformability compared to the ones with a higher/steep groove angle.

Corresponding room temperature high cycle fatigue (HCF) properties of DED repaired IN718 joints are studied using hour-glass HCF samples were machined which were half substrate and half deposit with the substrate to deposit zone interface at the narrowest section of the hour-glass specimens. Although the monolithic DED deposit had a similar tensile strength to the wrought substrate, the DED repaired joint exhibited an overall decreased HCF performance, regardless of the heat treatment conditions.

When the fatigue stress was low (below 50% of the yield stress), the STA condition had a better HCF performance than the DA, however, the opposite trend appeared for the high stress (over 70% of the yield stress), resulting in a cross-over point on the stress-life S-N plot. Based on the S-N curve results, a series of interrupted fatigue tests were performed at selected maximum stresses to study the progress of fatigue cracks in terms of the initiation and growth at the corresponding stress levels. Using single-specimen tests, the progression of fatigue cracks on the surfaces of the specimens was studied using scanning electron microscopy (SEM). Interrupted fatigue tests, combined with microscopy and fractography, revealed that the fatigue failure occurred in the substrate for the DED joint in the DA condition, whilst in the deposit zone for the STA condition due to the distribution and fracture of the Laves and δ phases. Grain boundary cracking in the substrate near the substrate-to-deposit interface can occur in both heat-treated conditions due to the Nb-rich liquid films.

Additionally, this study investigated the effect of TiB_2 particles on inducing columnar to equiaxed transformation (CET) in the as-deposit IN718, deposited using two sets of energy densities: high energy and low energy density. The addition of TiB_2 to IN718 resulted in significant grain refinement in the as-built microstructure. In the high-energy deposit, grains of size $>300\mu\text{m}$ occupied $\sim 22\%$ of the total grain area and $\sim 10\%$ in the low-energy deposits, which were reduced to $\sim 5\%$ upon TiB_2 addition. Moreover, a preferential $\{100\}$ texture observed along the building direction in the as-deposit IN718 became weak and random in the IN718/ TiB_2 deposits. The resulting IN718/ TiB_2 microstructure was found to be sensitive to the wt% of TiB_2 particle content. TiB_2 content >1.5 wt% was optimal for inducing grain refinement. The Laves phase often observed in the as-deposit IN718, is greatly reduced upon TiB_2 addition and replaced by needle-shaped phases rich in Cr, Mo, and B. The TiB_2 particles and the needle-shaped secondary phases formed a high fraction of heterogenous nucleation sites, causing grain refinement. Moreover, the strength properties exhibited a significant increase due to TiB_2 addition. IN718/ TiB_2 exhibit significantly high hardness and strength properties from uniaxial tensile tests. The tensile strength increased from 570 MPa in IN718 to 988 MPa in IN718/ TiB_2 tested parallel to the building direction. When tested perpendicular to the build direction, increased yield strength of 840 MPa was observed in IN718/ TiB_2 compared to 475 MPa in IN718 deposits. The conventional strengthening mechanisms were presented to explain the effect of TiB_2 on the refined microstructure. The major contributing strengthening

mechanisms included grain refinement, Orowan strengthening and increased GND density due to TiB_2 addition.

Table of Contents

Acknowledgment	i
Abstract	iii
Table of Contents	vi
List of Figures	xi
List of Tables	xxi
1. Introduction	1
1.1 Background and aim of the project	1
1.2 Thesis Structure.....	3
2. Literature review	6
2.1.1 Introduction.....	6
2.1.2 Classification of Metal AM technologies	6
2.1.3 Powder Bed Deposition and Powder Blown Direct Energy Deposition (DED): comparison.....	6
2.2 Laser Engineered Net Shaping (LENS)	8
2.2.1 Process Parameters	8
2.2.1.1 Laser Power.....	9
2.2.1.2 Scan speed.....	9
2.2.1.3 Powder feed rate.....	9
2.2.1.4 Shielding and carrier gas flow rate	9
2.2.1.5 Laser spot diameter and percentage overlap	10
2.2.2 Energy density in AM process.....	10
2.3 Direct Energy Deposition (DED) as a repair technique	11
2.3.1 Effect of DED process parameter on repair.....	12
2.3.2 Effect of groove geometry on repairs	13
2.4 Ni-base superalloys	16
2.4.1 Strengthening Mechanisms.....	16
2.4.1.1 Precipitation Strengthening.....	16
2.4.1.2 Solid Solution Strengthening	17
2.4.1.3 Other Specialty Alloys	17

2.4.2 Inconel 718 (IN718).....	18
2.4.2.1 AM manufactured IN 718: microstructure and texture	19
2.4.2.2 Role of geometry	22
2.4.2.3 Role of Scan strategy.....	23
2.4.3 Heat treatment and mechanical properties of IN718	25
2.4.3.1 Standard heat treatment adopted for Laser AM fabricated IN718	25
2.4.3.2 Tensile properties and anisotropy in Laser AM fabricated IN718	28
2.4.3.3 Fatigue in Laser AM fabricated IN718	33
2.4.4 Grain refinement of IN718.....	39
2.4.4.1 Columnar to equiaxed transformation (CET).....	39
2.4.4.2 Grain refinement of IN718 using inoculants	41
2.4.4.3 Grain refinement in AM products using inoculants	42
2.5 Summary, gaps and research questions	47
3. Experimental Methods.....	51
3.1 Material and Methods	51
3.2 Direct Energy Deposition (Optomec LENS MR-7)	52
3.3 Heat treatment.....	53
3.4 Method of inoculant identification using Edge-to-Edge Model (E2EM)	54
3.4.1 Identification of matching direction.....	54
3.4.2 Identification of matching planes.....	54
3.5 IN718/Inoculant powder preparation using ball milling	55
3.6 Microstructural characterisation techniques	56
3.6.1 Metallographic preparation	56
3.6.2 Microstructure analysis	56
3.6.2.1 SEM – imaging.....	56
3.6.2.2 SEM – Electron Backscattered Diffraction (EBSD) analysis	57
3.6.2.3 X-ray Diffraction	58
3.7 Mechanical testing methods	59

3.7.1 Hardness testing.....	59
3.7.2 4-point bend test with Digital Image Correlation (DIC) for strain analysis	59
3.7.3 Tension testing.....	61
3.7.4 Fatigue testing.....	62
3.7.5 Interrupted fatigue tests	63
4. Deformation Behaviour of Inconel 718 Repaired using Direct Energy	
Deposition process.....	65
4.1 Introduction	65
4.2 Experimental methods.....	66
4.2.1 Groove repair using LENS	66
4.2.2 4-point bend test	69
4.3 Results	71
4.3.1 Effect of deposition parameters on the microstructure of DED IN718	71
4.3.1.1 Porosity	71
4.3.1.2 Microstructure of as-built deposits	73
4.3.1.3 Analysis of minor phases	80
4.3.1.4 Hardness.....	84
4.3.2 Microstructure and mechanical properties of repair deposits.....	87
4.3.2.1 Microstructure and Hardness	87
4.3.2.2 Mechanical properties: 4 – point bend test results	98
4.4 Discussion	110
4.4.1 Repairability (weldability) of IN718	110
4.4.2 Effect of groove angle on mechanical properties	112
4.5 Conclusion.....	114
5. Mechanism of Damage in DED Repaired IN718 Composites under Cyclic	
Loading	117
5.1 Introduction	117
5.2 Experimental Method.....	118

5.2.1 Fabrication of repaired coupons for fatigue testing	118
5.2.2 Mechanical testing	120
5.2.3 Scanning Electron Microscopy	121
5.3 Results.....	122
5.3.1 Repaired Microstructure	122
5.3.2 Tensile tests	127
5.3.3 Fatigue tests.....	128
5.3.4 Interrupted Fatigue tests.....	130
5.3.5 Final failure in uninterrupted test specimens	140
5.4 Discussion.....	144
5.4.1 Rationalisation of room temperature fatigue performance with the microstructure of the repaired composite under the heat-treated condition.....	144
5.4.2 Comparison to wrought material and published additive manufactured IN718	146
5.5 Conclusion	149
6. Effect of TiB₂ addition on microstructure and mechanical properties in Inconel 718 processed via Direct Energy Deposition	151
6.1 Introduction.....	151
6.2 Experimental details	152
6.2.1 Powder preparation and DED deposition process.....	152
6.2.2 Fabrication of tensile test pieces and tensile testing details.....	154
6.2.3 Microstructure characterisation.....	155
6.3 Results.....	156
6.3.1 IN718/TiB ₂ microstructure	156
6.3.1.1 Grain size and texture analysis	156
6.3.1.2 Identification of the secondary phases	169
6.3.2 Mechanical properties	174
6.3.2.1 Hardness	174
6.3.2.2 Tensile test result.....	175

6.4 Discussion	180
6.4.1 TiB ₂ as the inoculant for DED IN718	180
7.1.1 Selecting TiB ₂ as an inoculant for grain refinement in AM IN718	181
7.1.2 Mechanical properties and anisotropy	184
7.1.3 Strengthening in IN718/TiB ₂	186
6.5 Conclusion.....	191
7. Conclusions and Suggestions for Future Work	194
14.1 Summary and conclusions.....	194
14.2 Suggestions for further work	196
14.2.1 Repair AM substrate	196
14.2.2 Investigation of repair weldability of IN718 after multiple repair cycles.	197
14.2.3 Investigation of fatigue damage mechanism at elevated temperature ...	197
14.2.4 Modification of energy density equation to include powder input flow rate	197
14.2.5 Explore the parameter combination and other inoculants for columnar to equiaxed transition (CET).....	198
Appendix 1	199
Appendix 2	200
Appendix 3	203
References	210

List of Figures

Figure 2.1: Classification of metal AM technologies.....	7
Figure 2.2: Schematic showing (a) powder bed deposition process, (b) direct energy deposition process [23].....	7
Figure 2.3: Schematic of a layer built by LENS, showing the track width, track height and the overlap.	10
Figure 2.4: Scan parts used by Zhang[81] to repair a cylindrical section (a) Helix; (b) circle-line-circle; (c) line-arc-line.	13
Figure 2.5: Repair geometries used by Pinkerton et al. [78].	14
Figure 2.6: V-shape geometries with flat bottom used by Zhang et al. [70].	14
Figure 2.7: Repair geometries used by Liu et al. [6].....	15
Figure 2.8: Illustration of a laser-repaired zone in the tensile specimen [80].	15
Figure 2.9: Typical microstructure of IN718 manufactured using DED technique: (a),(b),(c) microstructure variation with varying process parameters [11]; and (d) IPF maps superimposed on the optical micrograph [54].	20
Figure 2.10: Columnar grain structure leading to {001} texture along build direction in as-deposit IN718 [108].	20
Figure 2.11: (a) Laves phase and (b) carbides in DED fabricated Inconel [11].	21
Figure 2.12: A graded IN718 sample manufactured using AM [97].	22
Figure 2.13: Increasing interest in AM IN718 through years [12].	22
Figure 2.14: Different scanning strategies used DED: (a) Alternate (b) Bidirectional; (c) Unidirectional; (d) Spiral.	23
Figure 2.15: Effect of change in scanning strategy in grain orientation and grain structure (a) IN 718 by unidirectional laser scanning, and (b) IN 718 by bidirectional laser scanning [10].	24
Figure 2.16: Different scanning strategies and resulting microstructure in SLM IN718 [110].	25
Figure 2.17: Microstructure after heat treatment at different conditions: (a), (b) Direct aged; (c), (d) Solution treatment at 980 ⁰ C and ageing; (e), (f) Solution treatment at 1080 ⁰ C; (g), (h) Solution treatment at 1080 ⁰ C and ageing [112].	27
Figure 2.18: (a) Cellular structures of IN718 after solution treatment at 980 ⁰ C; the dislocations along the (b) cellular walls and (c) along γ'' precipitate [90].	28
Figure 2.19: Typical tensile properties of IN718 under different heat treatment conditions [93].	29

Figure 2.20: Stress-strain curves of the samples at different orientations and energy density (a–c) and (d) the schematic maps of the loading direction and build direction for the tested samples; (e) Taylor factor maps for the corresponding samples[119]. 32

Figure 2.21: Taylor factor maps and Mechanical properties of EBM deposit IN718 tested in different orientations (a),(d) Parallel to build direction; (b), (e) Perpendicular to build direction [115]. 33

Figure 2.22: High cycle fatigue data for IN718: (a) at room temperature and (b) 500 °C[129]..... 35

Figure 2.23: High-cycle fatigue properties of AM IN718 and wrought IN718 tested at 650°C and R =0.1 [121]. 35

Figure 2.24: S-N curve of the IN 718 samples fabricated with LENS technique tested at R = 0.1[131] 36

Figure 2.25: S-N curve for GTA/TIG and EB weldments in two post-weld heat-treated conditions: (a) DA and (b) STA[136]. 38

Figure 2.26: S-N curves of reference and TIG welded specimens of IN 718 tested at R = 0.1 [138]. 38

Figure 2.27: The effect of G and R on the solidification microstructure morphology [140]. 39

Figure 2.28: Relation between degree of undercooling and growth velocity [23]. ... 40

Figure 2.29 Effect of prior nucleation sites in EBM IN718 process (a)high number, (b) low number of pre-existing nuclei [107]. 41

Figure 2.30: As-built IN718+inoculants along the transverse direction [152]. 43

Figure 2.31: Grain refinement due to inoculant addition: (a) 316L/TiB₂[154]; (b) Al-12Si/TiB₂ [158]. 44

Figure 2.32: Defects in prints with inoculant addition due to insufficient energy densities: (a) 316L/TiB₂; (b) IN718/TiC. 45

Figure 3.1: (a) SEM image of the GA Inconel 718 Powders (b) powder size distribution. 52

Figure 3.2: (a) SEM micrograph showing substrate microstructure; (b) EBSD map showing high angle (black) and low angle (green) grain boundaries and $\Sigma 3$ twin boundaries (red), (c) XRD patterns and (d) the relative frequency of the misorientation distribution of the as-received IN718 plates. 52

Figure 3.3: Heat treatment schedule for repairs (a) Direct ageing (DA); (b) Solution treatment and ageing (STA). 53

Figure 3.4: Ball Mill setup.	56
Figure 3.5: Grain reconstruction from EBSD data (a) grain size calculation using equivalent circle diameter; (b) aspect ratio calculation.	58
Figure 3.6: Schematic of the 4-point bend tests specimen geometry.	59
Figure 3.7: 4-point bend test setup on the INSTRON with DIC.	60
Figure 3.8: (a) Geometry of the repaired-bend test specimens; (b) Strain evolution at P_{max} on the top surface during 4-point bend tests with varying span ratio: (c) 80:30; (d) 60:30.	61
Figure 3.9: Schematic of the tensile test specimens (<i>all dimensions are in mm</i>).	62
Figure 3.10: Hourglass geometry fatigue test specimen design (all dimensions are in mm).	63
Figure 4.1: SEM image of the GA Inconel Powders.	66
Figure 4.2 (a) As-built specimens on the substrate; (b) Schematic of the scanning pattern used for printing and the section under investigation (z is the building direction).	67
Figure 4.3: Schematic sketches showing the cross-sectional view of Grooves with varying sidewall angles (a) 60°, (b) 30° and the two different scanning patterns used for repairing the grooves (c) alternate pattern and (d) spiral pattern.	68
Figure 4.4: Schematic representation of the investigation plane.	69
Figure 4.5: Schematic of the grooves prepared for 4-point bend tests (a) groove angle 30°; (b) groove angle 60°; (c) illustration showing the setup for 4-point bend test on the repaired components (60° groove angle), arrows indicate loading direction.	70
Figure 4.6: (a) Representative cross-section of the as-build sample (C1) for porosity measurement; (b) SEM micrograph of spherical porosities observed in the deposits.	71
Figure 4.7: (a) variation of porosities with linear energy density; (b) size distribution of the porosities in the deposits.	73
Figure 4.8: IPF map of the as-build samples showing the grain structure: (a) C1, (b) C2; (c) C3, (d) C4; (e) C5. The (100) pole figures are shown below each EBSD map. The legends for the multiple of uniform density (MUD) values for the pole figures are kept constant for comparison. The parameter combination for the corresponding deposits is shown in Table 4.1.	74
Figure 4.9: Grain size distribution in the as-built samples.	75
Figure 4.10: Relative frequency of the aspect ratio distribution in the as-built sample, displaying the significant variation in grain aspect ratio within the depositions.	76

Figure 4.11: A representative figure showing the aspect ratio of an elongated grain (marked in pink) in the deposit C1..... 77

Figure 4.12: The effect of G and R on the solidification morphology and size [140]. 78

Figure 4.13: Primary dendritic arm spacing (PDAS) measured in the as-deposit samples: (a) variation of PDAS with linear energy density; (b) variation along the built direction for individual deposits. 79

Figure 4.14: Variation of cooling rate of all the as-deposit samples with position along build direction. 80

Figure 4.15: (a) Representative ASB SEM micrograph showing Laves network (b) high magnification micrograph showing the intermetallic precipitates analysed using EDS. 81

Figure 4.16: Representative EDS area scan maps that depict Nb, Ti and Mo micro-segregation in the as-deposited microstructure. 82

Figure 4.17: Representative SEM micrograph showing EDS point scans and their corresponding chemical compositions of the various precipitates..... 83

Figure 4.18: Area percentage of Laves phase/carbides in the as-built samples..... 84

Figure 4.19: (a) Representative micrograph showing the typical as-built Inconel 718 microstructure; (b) high magnification image of the marked area; (c) determination of Laves phases by converting to a binary image and applying a contrast threshold. 84

Figure 4.20: (a) – (e) Hardness map of the vertical sections of all the as-build samples of C1, C2, C3, C4, and C5, respectively; the building direction of the deposits and the colour scale bar for the contour maps are indicated. 86

Figure 4.21: Microstructure of base material (a) BSE -SEM micrograph showing columnar grains with blocky NbC carbides; (b) EBSD map showing high angle (black) and low angle (green) grain boundaries and $\Sigma 3$ twin boundaries (red); (c), (d) EDS line analysis for identification of NbC and TiC. 88

Figure 4.22: (a) EBSD map showing the microstructure of the repaired composite, (1)- the deposit zone and (2)- substrate, and (b) the misorientation distribution in 1 and 2. 89

Figure 4.23: Microstructure of the repaired composites in as-deposited condition: (a) 60° groove angle; Alternate Pattern; (b) 60° groove angle; Spiral Pattern; (c) 30° groove angle; Alternate Pattern; (d) 30° groove angle; Spiral Pattern..... 90

Figure 4.24: EBSD maps of the repaired composites in different as-deposited conditions: (a) 60° groove angle; Alternate Pattern; (b) 60° groove angle; Spiral

Pattern; (c) 30° groove angle; Alternate Pattern; (d) 30° groove angle; Spiral Pattern. The corresponding {100} pole figures of the deposit zone are shown in (a') – (d').	.91
Figure 4.25: Grain size distribution and average grain size in the deposit zone of the repaired composites in as-deposit condition.	92
Figure 4.26: EBSD maps for 60° grooves: (a) Alternate pattern, (b) Spiral pattern; and (c), (d) their respective {100} pole figures for deposit zone only; arrows indicate the dendritic growth direction.	93
Figure 4.27: Schematic of the heat flux directions and dendritic growth.	94
Figure 4.28: EBSD maps with grain boundaries superimposed on the repaired composite after heat treatments: (a) As-deposited; (b) Direct aged; (c) Solution treated and aged; (d), (e), (f) are high magnification BSE-SEM micrographs showing the distribution of the phases in the deposit zone in (a), (b) and (c) respectively.	95
Figure 4.29: EDS point analysis on the deposit zone of a repaired sample under STA condition.	96
Figure 4.30: Effect of groove angle and post deposit heat treatment for the repaired composites: (a) variation of hardness from the deposit zone to substrate across the repaired interface; and (b) average grain size in the deposit zone and substrate.	98
Figure 4.31: Load – displacement curves for the 4-point bend tested samples.	99
Figure 4.32: 4-point bend test results: (a) Maximum load, P_{max} (b) Actuator displacement at P_{max} .	100
Figure 4.33: Strain distribution on the top surface at P_{max} of the 4-Point bend specimen substrate (a) Strain map; (b) value of strain in the region between the loading pins (pure bend region).	101
Figure 4.34: Strain distribution maps on the top surface at P_{max} of the 4-point bend specimens in As-deposited condition (a) Groove angle 30°; (b) Groove angle 60°; (c) value of strain in the pure bend region.	102
Figure 4.35: Strain distribution on the top surface at P_{max} of the 4-point bend specimens in DA condition (a) Groove angle 30°; (b) Groove angle 60°; (c) value of strain in the pure bend region.	103
Figure 4.36: Strain distribution on the top surface at P_{max} of the 4-point bend specimens in STA condition (a) Groove angle 30°; (b) Groove angle 60°; (c) value of strain in the pure bend region.	104
Figure 4.37: Microstructure in the interface of the repaired component after various heat-treated conditions: (a) As-deposit; (b) Direct aged (DA); (c) Solution Treatment	

and aged (STA).....	106
Figure 4.38: (a) SEM micrograph of repaired samples near the deposit zone-substrate interface in STA condition; (b) high magnification micrograph showing several EDS point scans and their respective chemical compositions.....	107
Figure 4.39: The longitudinal section of one fractured sample 60° groove angle; STA condition: (a) Deposit side; (b) Substrate side.	108
Figure 4.40: The longitudinal section of one fractured sample 60° groove angle; DA condition: (a) Deposit side; (b) Substrate side.	109
Figure 4.41: Fracture morphologies of the failed bend tested repaired IN718 component after (a) STA; (b) DA condition.	109
Figure 4.42: Interface at 80% P_{max} 60° groove angle, DA condition. The top of the micrograph is close to the top surface of the bend specimen.....	111
Figure 4.43: EDS map scans showing crack initiation at Nb rich grain boundaries near the interface.....	111
Figure 4.44: (a) Bending moment and shear stress diagram for 4-point bend test; (b) Schematics showing shear stress in the repaired component under loading.....	112
Figure 4.45: Maximum strain at P_{max} from DIC observation.	113
Figure 4.46: Evolution of strain ($\Delta\varepsilon$) on the top surface till P_{max} in the repaired component in various heat treated conditions: (a) Direct aged; (b) Solution Treatment and aged; (c) representative figure showing the strategy adopted to measure strain at points corresponding to deposit, interface, and substrate.	114
Figure 5.1: SEM image of the feedstock Inconel Powders.....	119
Figure 5.2: Schematic of (a) DED repaired blocks, (b) hourglass fatigue samples- the region under SEM investigation is marked; (c) samples for tensile testing.....	120
Figure 5.3: EBSD maps showing the grain morphology and distribution in the repaired specimens at (a) Direct Aged (DA); (b) Solution Treated and Aged (STA) condition; (c) Misorientation distribution in the repaired composites in the deposit zone and substrate; {100} pole figure of the deposit zone microstructure in (d) DA and (e) STA condition.....	123
Figure 5.4: Hardness variation in the repaired composite from deposit zone to substrate across the deposit zone-substrate interface in as-deposit and post-HT conditions.	124
Figure 5.5: SEM image showing the microstructure (a) near the deposit zone-Substrate interface at DA condition; (b) high magnification micrographs showing the phases in the substrate, and (c) deposit zone. The EDS test positions and the results	

are shown; and (d) the corresponding EDS map showing Nb, Mo, and Ti segregation.	125
Figure 5.6: SEM image showing the microstructure (a) near the deposit zone- Substrate interface at STA condition; (b) high magnification micrographs showing the phases in deposit zone, and (c) Substrate. The EDS test positions and the results are shown; and (d) the corresponding EDS map showing Nb, Mo, and Ti segregation.	126
Figure 5.7: Engineering stress-strain response in tension measured using tensile specimen as per Figure 5.2(c).....	128
Figure 5.8: S-N curve showing raw data points and a power-law fit for the substrate and repaired composite conditions.	129
Figure 5.9: Fatigue microcracks initiating at various preferential sources on the sample surface (a) Substrate grain boundary near the repair interface (b) Broken metal carbides; (c) Transgranular cracks (d) Broken Laves phases/ δ phases.....	131
Figure 5.10: (a) Total crack length and (b) number density of fatigue cracks growing on different sources on the specimen surface at various stages of fatigue life at σ_{max} = 70pct of YS in DA condition.	133
Figure 5.11: Representative figures showing the development of crack in DA specimen at 70% of YS in various stages of fatigue life: (a) 40 % N_f ; (b) 60 % N_f ; (c) 80 % N_f ; (d) 90 % N_f	133
Figure 5.12: (a) Total crack length and (b) number density of fatigue cracks growing on different sources on the specimen surface at various stages of fatigue life at σ_{max} = 70pct of YS in STA condition.....	134
Figure 5.13: Representative figures showing the development of crack in STA specimen at 70% of YS in various stages of fatigue life: (a) 20 % N_f ; (b) 40 % N_f ; (c) 60 % N_f	135
Figure 5.14: (a) Total crack length and (b) number density of fatigue cracks growing on different sources on the specimen surface at various stages of fatigue life at σ_{max} = 45pct of YS in DA condition.	137
Figure 5.15: Representative figures showing the development of crack in DA specimen at 45% of YS in various stages of fatigue life: (a) 10 % N_f ; (b) 40 % N_f ; (c) 70 % N_f ; (d) 90% N_f	138
Figure 5.16: Total crack length of fatigue cracks growing on different sources on the specimen surface at various stages of fatigue life at σ_{max} = 45pct of YS in STA	

condition..... 139

Figure 5.17: Representative figures showing the development of crack in STA specimen at 45% of YS in various stages of fatigue life: (a) 20 % N_f ; (b) 70 % N_f 139

Figure 5.18: The surface of the uninterrupted test samples showing the region of final fracture, tested at 70 % of YS in (a) DA: failure in the substrate and (b) STA condition: failure in the deposit zone. 140

Figure 5.19: The surface of the uninterrupted test samples showing the region of final fracture, tested at 50 % of YS in (a) DA: failure in the substrate and (b) STA condition: failure in the deposit zone. 140

Figure 5.20: Appearances of the fracture surface of DA-repaired specimen tested at 70% of YS: (a) crack initiation sites, (b) facets and (c) cracks on the fractured surface, (d) striation marks on the fracture surface..... 142

Figure 5.21: Appearances of the fracture surface of DA-repaired specimen tested at 50% of YS: (a) crack initiation sites, (b) facets and (c) cracks on the fractured surface, (d) striation marks..... 142

Figure 5.22: Appearances of fracture surface of STA-repaired specimen tested at 70% of YS: (a) crack initiation sites, (b) defects and (c) unmelted powder particles on the fractured surface, (d) striation marks on the fracture surface. 143

Figure 5.23: Appearances of fracture surface of STA-repaired specimen tested at 50% of YS: (a) crack initiation sites, (b) defects and (c) unmelted powder particles on the fractured surface, (d) striation marks on the fracture surface. 144

Figure 5.24: Comparison of S-N curve with existing data for IN718. For comparison, data from wrought, weld and AM IN718 were tested at room temperature, and $R = 0.1$ is used. (TIG: Tungsten Inert Gas welding, LPBF: Laser Powder Bed Fusion; EBM: Electron Beam Melting; DED: Direct Energy Deposition). 148

Figure 6.1: IN718 powders mixed with 1.5 wt% TiB_2 powders: (a), (b), (c) are TiB_2 powders with size of $< 1 \mu m$, $< 10 \mu m$ and $< 40 \mu m$, respectively; The corresponding TiB_2 decorated feedstock powders with TiB_2 particle size: (d) $< 1 \mu m$ (e) $< 10 \mu m$ (f) $< 40 \mu m$ 153

Figure 6.2: Schematics showing (a) build process; and (b) the observation plane for EBSD analysis..... 154

Figure 6.3: Schematic diagrams showing the specimen extraction locations with respect to the DED deposit sample blocks; dimensions of tensile specimen are noted. 155

Figure 6.4: (a) EBSD IPF map for as-deposit IN718; (b) The grain size distribution as relative fraction of grain count and area fraction are compared; (d) the {100}, {111}, and {110} pole figures for as-deposit IN718.....	157
Figure 6.5: As-deposit IN718 microstructure showing (a) grain orientation, and (b) {100} pole figures of high energy deposit; (c) grain orientation, (d) pole figures of low energy deposit; (e) grain size distribution and (f) legends showing the IPF colour and building direction.....	158
Figure 6.6: The EBSD maps and the respective {100} pole figures of high energy density deposits in the following conditions: (a) and (e) as-deposit IN718; IN718/TiB ₂ deposited with : (b) and (f) 0.5 wt%; (c) and (g) 1.5 wt%; (d) and (h) 2.5 wt% TiB ₂ ; (i) grain size distribution in IN718 and IN718/TiB ₂ deposits.	160
Figure 6.7: The EBSD maps and the respective {100} pole figures of low energy density deposits in the following conditions: (a) and (e) as-deposit IN718; IN718/TiB ₂ deposited with : (b) and (f) 0.5 wt%; (c) and (g) 1.5 wt%; (d) and (h) 2.5 wt% TiB ₂ ; (i) grain size distribution in IN718 and IN718/TiB ₂ deposits.	161
Figure 6.8: Low energy deposits having interlayer defects. Unmelted particles are observed within the interlayer defects.	162
Figure 6.9: EDS of unmelted particles shows presence of TiB ₂	163
Figure 6.10: Effect of powder flow rate on the densification of IN718/TiB ₂ deposits: (a) 12g/min; (b) 8 g/min; (c) 7g/min; (d) 6g/min.	165
Figure 6.11: EBSD IPF maps showing effect of powder flow rate on the grain size of low energy deposits: (a) 12g/min; (b) 8g/min; (c) 7g/min; (d) 6g/min; the grain size distribution is shown.	166
Figure 6.12: IPF EBSD maps and grain size distribution maps for high energy deposits: (a), (b) EBSD map; (c), (d) grain size map of as-deposit IN718 IN718/TiB ₂ with 1.5wt%, <10μm TiB ₂ ; and (e) grain size distribution.....	168
Figure 6.13: IPF EBSD maps and grain size distribution maps for low energy deposits: (a), (b) EBSD map; (c), (d) grain size map of as-deposit IN718 IN718/TiB ₂ with 1.5wt%, <10μm TiB ₂ ; and (e) grain size distribution.....	169
Figure 6.14: SEM images showing typical microstructures of IN718 with and without inoculants: (a), (c) As-deposit IN718; (b), (d) IN718/TiB ₂ ; (a), (b) are high energy deposits and (c), (d) are low energy deposits respectively.	170
Figure 6.15: High Magnification SEM micrographs of IN718/TiB ₂ showing the needle-shaped phases and spherical phases in IN718/TiB ₂ (a) High Energy deposits, (b) low energy deposits; (c) the area fraction of these round and needle-shaped	

phases; (d) aspect ratio frequency distribution of the needle-shaped phases in high and low energy deposits. 171

Figure 6.16: EDS elemental map for IN718/TiB₂ deposits with high energy density. 172

Figure 6.17: EDS elemental map for IN718/TiB₂ deposits with low energy density. 173

Figure 6.18: EDS line scan of IN718/TiB₂ low energy deposit showing (a) segregation of Cr, Mo, and Nb at the needle-shaped phases and (b) Ti segregation at the round phase. 173

Figure 6.19: XRD patterns for as-deposit IN718 and IN718/TiB₂. 174

Figure 6.20: Hardness of as-deposit IN718 and IN718/TiB₂ (HE- high energy deposit; LE- low energy deposit). 175

Figure 6.21: (a) Engineering stress- engineering strain curves for high energy density deposits IN718 and IN718/TiB₂ tested in vertical (V) and horizontal (H) direction; (b) quantified yield stress, tensile stress, and percentage elongation to fracture for each condition. 176

Figure 6.22: Position of atoms in the lattice and corresponding closed-packed direction indicated in (a) IN718 matrix; (b) TiB₂ [235]; Atom configurations on (c) (1011) and (c) (1120) planes of TiB₂ [147]. 183

Figure 6.23: Taylor factor maps for as-deposit IN718 for High Energy deposits (a) Vertical specimen; and (b) horizontal specimen Taylor factor maps for IN718/TiB₂ for High Energy deposits: (a) Vertical specimen; and (b) horizontal specimen, Taylor factor colouring legend and average Taylor factor is indicated. 185

Figure 6.24: EBSD maps for high energy density deposits showing (a), (d) Band contrast maps, (b), (e) IPF maps, (c), (f) local area misorientation maps for As-deposit IN718 and IN718/TiB₂ respectively, (g) compares the distribution of the local misorientation for IN718 and IN718/TiB₂. 189

List of Tables

Table 2.1: Important process parameters for a DED deposition	8
Table 2.2: Typical composition of IN718	18
Table 2.3: Purpose of the common elements in IN718	18
Table 2.4: The standard heat treatment procedures of IN718 (industrial standard) [94, 103].....	26
Table 2.5 Mechanical properties of IN718.....	30
Table 2.6: Various reinforcement particles/ refiners used in different alloy systems manufactured using AM route.....	45
Table 4.1: LENS deposition parameters.....	67
Table 4.2: Designations of the specimens and the details of the corresponding post-deposit heat treatment conditions.	68
Table 4.3: Summary of porosity measurements.	72
Table 5.1: DED repair parameters.....	119
Table 5.2: Tensile properties of IN718 in different post-heat-treated conditions (Figure 5.2(c)).	128
Table 5.3: Parameters of fit for the HCF tests.....	129
Table 6.1: Printing parameters	154
Table 6.2: Percentage of total grain area occupied by small grains (<20 μm) and large grains (>300 μm) in as-deposit IN718 and IN718/TiB ₂ deposits.....	161
Table 6.3: Low energy density deposition parameters.....	164
Table 6.4: Tensile properties of high energy and low energy density deposits IN718 and IN718/TiB ₂ tested in the vertical and horizontal direction.....	177
Table 6.5: Tensile properties of as-deposit IN718 in different post-heat-treated conditions. All samples are manufactured using high energy density and tested in vertical specimen orientation.....	177
Table 6.6: Atomic mismatch between IN718 and TiB ₂	182
Table 6.7: Measured Schmid factors and Taylor factors of the specimens for the {111} < 110 > slip system.....	184

CHAPTER 1

Introduction

1.1 Background and aim of the project

Ni-based superalloys exhibit an excellent combination of mechanical properties, corrosion and oxidation resistance. Ni has relatively high melting temperature and do not exhibit any solid state phase transformation from room temperature till melting temperatures. Additionally, the close-packed FCC lattice enables operation at elevated temperatures and withstands high thermal stresses caused by rapid temperature changes and large temperature gradients compared to equivalent BCC systems. Ni-based superalloys are often strengthened by precipitates (γ' , γ'') that increases their creep resistance and enables engineering applications above 600°C. As a result, they have found widespread application in fabricating aviation and aerospace components that would operate in extremely harsh conditions. In fact, they constitute 40% - 50% of the total weight of aircraft engines and are mainly used in combustors and turbines [1].

Inconel 718 (IN718) is a nickel-base superalloy with high-temperature strength, excellent oxidation and hot corrosion resistance, and good weldability. IN718 has found wide applications in gas turbine engines. The high replacement costs associated with the raw materials and initial manufacturing process justify the demand for developing effective repair technology that would provide lifecycle cost reduction of superalloy components [1,2]. The conventional repair methods, including welding and brazing, present certain disadvantages limiting their usage. The high heat input associated with welding processes results in several defects such as weld cracks, micro-fissures, high residual stress, distortion and other heat-related problems in the repaired component [2]. HAZ liquation cracking, typical to IN718 superalloy, occurs due to the formation of Nb-rich liquid films at grain boundaries of the base material during the weld cycle and the subsequent inability of this film to accommodate thermal contraction stresses during weld cooling [3,4]. Another form of cracking often encountered in gas turbine engines is fatigue cracking since they are subjected to cyclic loading [5]. The brazing process is generally limited to small defects ~250 μm joints, and the strength of the brazing (repaired) joints are usually weak as they can achieve a maximum of 50% of the strength of the base metal [6,7].

Laser additive manufacturing (AM) techniques are comparatively recent techniques that offer several advantages over conventional repair techniques. Compared to conventional welding processes, direct energy deposition (DED) additive manufacturing processes, such as laser engineered net shaping (LENS), provide an attractive alternative for repairs of these superalloy components. The AM techniques introduce a much smaller melt-pool due to highly concentrated energy transfer to the workpiece, enabling finer control over the process parameters. Moreover, DED processes can directly produce metallic parts from powder, enabling the repair of components with complex geometries.

In spite of the several advantages of using AM methods as repair techniques, there are some challenges associated with AM processing that limits its usage. Firstly, achieving an identical microstructure to the base material is generally difficult. The thermal cycling and high cooling rates during DED processing would affect the microstructure formation upon cooling [8,9]. As a result, the metallurgical features and mechanical properties of the deposit/repared zone may differ from the substrate/base material. A DED IN718 microstructure is generally characterised by columnar grains growing in the opposite direction of the heat flow. Elongated grains with a favoured $\{001\} \parallel$ build direction (BD) texture is often reported [10,11]. The elongated grains often result in an anisotropic mechanical property in the DED deposit. The high cooling rates result in the formation of non-equilibrium phases such as Laves phase in the inter-dendritic region and inhibit the formation of strengthening γ'' , γ' precipitates. Therefore, post-deposit heat treatments are generally employed to achieve the desired strength, however, the precipitation of the strengthening γ'' , γ' precipitates are often localised near the Laves phases, that result in inconsistent mechanical properties. The mechanical properties from uniaxial tensile and fatigue tests of wrought IN718 vary in DED deposited IN718 [12–14]. Moreover, the current literature lacks in-depth investigation of microstructure and mechanical properties of the repair-zone – substrate interface, which is critical especially when adopting AM process as a repair technique.

In the present study, as a first step, the effect of various process parameters – laser power and scan speed, on the DED IN718 microstructures is explored. The best parameter combination that could produce a dense microstructure with a mixed equiaxed – columnar microstructure was used for subsequent repairs and grain refinement study. Two post-deposit/repared heat treatments: direct aged (DA) and

solution treated at 980°C and Aged (STA), are employed in the current study. The heat treatments ensured desired strength increase in the deposit/repared zone while preventing coarsening of the microstructure (both in the substrate and deposit zone). The mechanical performance of the repaired grooves is studied using 4-point bend tests under as-deposited and post-heat-treated conditions. The strain evaluation during deformation under bending conditions is studied using digital image correlation (DIC). The fatigue performance of repaired IN718 components in post-heat-treated conditions is explored and compared to the wrought substrate. The mechanism of the fatigue damage, focusing on the deposit zone – substrate joint, in the repaired IN718 parts are studied in detail using interrupted tests coupled with scanning electron microscopy. Finally, a novel method of using inoculant was adopted to transform the elongated DED microstructure into the fine equiaxed microstructure. A suitable grain refiner/inoculant particle is identified using crystallographic model and introduced during the DED process to induce heterogeneous nucleation sites. The subsequent effect of inoculant addition on the resulting microstructure, texture and mechanical properties is studied.

1.2 Thesis Structure

The research work in the current thesis is structured into seven chapters: literature review, experimental methods, followed by three results chapters, conclusions, and future work.

Chapter 2 presents a literature survey, which reviews the background and fundamentals of metal additive manufacturing, with the various classification in metal additive manufacturing especially focussing on the direct energy deposition (DED) process. An overview of laser additive manufacturing as a repair process is presented. The strengthening mechanism and the microstructure, texture and phases formed during laser additive manufacturing of IN718 are reviewed. Moreover, the post-deposit heat treatments adopted and their effect on microstructure, tensile and fatigue properties are reviewed. The literature review also includes the various strategies for refining the grain structure and methods to promote a columnar to equiaxed transition in DED IN718. Finally, a summary of the existing knowledge and research questions addressed in the current study is provided.

Chapter 3 outlines the material, general experimental procedures, and methods used in the current research. The processing of the material(s) under investigation is

performed using laser engineered net shaping (LENS), a DED-type AM process. The modification of feedstock IN718 powders by decorating with inoculant particles using a ball milling technique is described. The chapter also includes the characterisation techniques adopted to investigate the microstructure, texture, and mechanical response of the material under various conditions. The microscopic characterisation techniques include optical microscopy, scanning electron microscopy including electron backscattered diffraction, energy dispersive spectroscopy, and X-ray diffraction. The study of mechanical properties includes hardness measurement, 4-point bend, tensile, and fatigue tests.

Chapter 4 initially explores the relationship between deposition parameters and key microstructural characteristics, such as degree and size distribution of porosity, γ grain size and aspect ratio, the distribution and morphology of Laves phase, and then further relates these microstructures to mechanical properties (in the form of hardness tests) of DED IN718 bulk deposits. The parameter combination producing the most favourable combination of microstructure and properties was applied for repair studies on wrought Inconel 718 plates. These plates were produced to have "defects" machined into the surface having various designed groove wall angles, and repair using DED was conducted using various contrasting scanning patterns. Subsequently, a study was conducted to understand the effects of post-heat treatment (direct aged (DA) and solution treated at 980°C and aged (STA) condition) on the microstructure and properties of the repair deposit and surrounding substrate. The deformation behaviour and failure mechanisms of the resulting repaired composite were investigated using 4-point bend testing coupled with digital image correlation (DIC) and cross-sectional microscopy.

Chapter 5 seeks to understand the room temperature failure mechanism in DED repaired IN718 under cyclic loading under direct aged (DA) and solution treated at 980°C and aged (STA) condition. The prevailing mechanism of the initiation and growth of fatigue cracks arising from phases present near the repaired joint (Lave phase, Carbides, liquified NbC along grain boundaries, and δ phase (for STA)) has been studied. The progression of fatigue cracks (on the surfaces) at various levels of applied stress and with an increasing number of loading cycles is studied by intermittently stopping the test at multiple stages of fatigue life between 10 – 90 % of the average cycles to failure (N_f) for each of the chosen stress amplitude (max stress) and characterised using SEM.

Chapter 6 explores the possibility of using inoculants to modify the DED microstructure to achieve a columnar-to-equiaxed transition. With reference to the crystallographic models, TiB_2 is identified as an efficient grain refiner, and the effect of TiB_2 addition to IN718 during DED deposition to aid the transformation of the columnar-to-equiaxed microstructure is investigated. Moreover, the effect of addition of TiB_2 on the tensile properties of IN718/ TiB_2 is elaborated.

CHAPTER 2

Literature review

2.1.1 Introduction

Additive manufacturing (AM) is a technique that can be used to construct complex 3-dimensional components by depositing molten material one layer at a time. The heat source used to melt the material is generally a laser, an electric arc, or an electron beam. The beam moves in a predefined path and a layer-by-layer deposition takes place [15,16]. However, there are some limitations of the AM processes, such as (a) post-machining is generally required to achieve the desired surface finish; and (b) defects such as porosities and insufficient fusion between layers may result in poor mechanical properties. Moreover, the high cost associated with certain metal powders and limited availability of pre-alloyed powders limits the usage of AM techniques to a wide range of metal/alloy systems.

2.1.2 Classification of Metal AM technologies

The classification of the various AM processes is depicted in Figure 2.1. The additive manufacturing (AM) techniques can be broadly classified on the mechanism of feeding the feedstock material in the system: direct energy deposition (DED) – where blown powders are melted using a heat source, and powder bed fusion (PBF) – where a bed of metal powder is melted to form each layer. The various processes are further categorised based on feedstock material: powder or wire; and the heat source: laser, arc or electron beam; and. Despite these differences, all these processes share a common approach, i.e. starting with a 3-D model of the part/component to be manufactured, followed by a layer-by-layer build.

2.1.3 Powder Bed Deposition and Powder Blown Direct Energy Deposition (DED): comparison

In powder bed fusion-based additive manufacturing processes like selective laser melting (SLM) and electron beam melting (EBM), metal powders are first spread in thin layers with pre-defined layer thickness. Depending upon the geometry of the part to be built, the laser beam selectively interacts with the powder bed in the x-y-plane depicted schematically in Figure 2.2 (a), melting the metal powders along the scanning path. After a layer is deposited, the build plate is lowered, and another powder layer is

applied. The process of melting the newly deposited powder layer is repeated until the complete section is built [15–21].

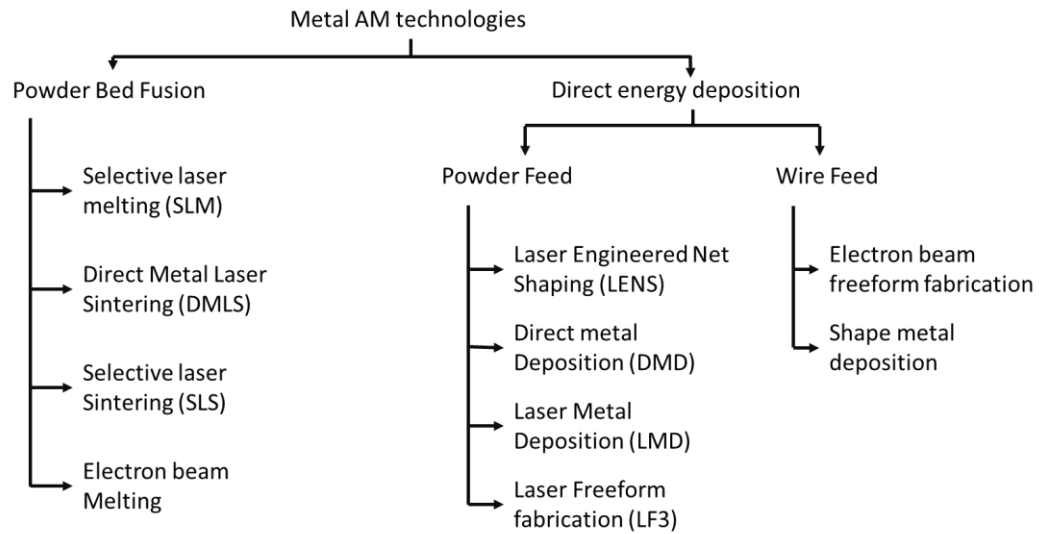


Figure 2.1: Classification of metal AM technologies [22].

In laser direct energy deposition (DED) techniques, the laser beam melts the surface of the substrate, creating a melt pool, and the metal powders are applied simultaneously. Various proprietary names have been adopted for the DED technique, as shown in Figure 2.1. A shielding gas is used to protect the melt pool and deliver the powders from the nozzle to the melt pool. The components are built layer-by-layer via a user-defined path (Figure 2.2 (b)). Once a layer is deposited, the laser, along with the powder delivery system, moves up by an increment equivalent to one-layer thickness and the process is repeated till completion [22–24]. However, better precision and surface finish can be achieved in powder-based techniques due to its finer melt pool and smaller layer thickness compared [24].

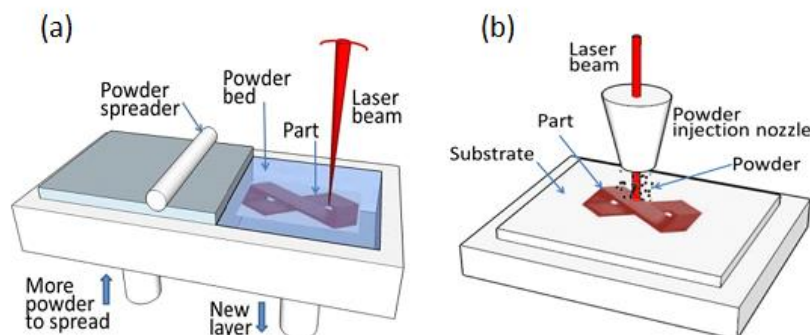


Figure 2.2: Schematic showing (a) powder bed deposition process, (b) direct energy deposition process [22].

2.2 Laser Engineered Net Shaping (LENS)

Laser engineered net shaping (LENS®), developed at Sandia National Laboratory in the late 1990s, is a powder-blown DED additive manufacturing technique. A LENS machine generally includes multiple nozzles that ensure a better powder delivery compared to other DED techniques. As a result, LENS has grown to be the most widely used DED additive manufacturing technique in industries and for research purposes. Some of the major advantages of LENS over other conventional manufacturing and repair processes are as follows:

- (a) Ability to build complex shapes, including hollow thin-walled sections.
- (b) In terms of using LENS as a repair technique, the small size of the melt pool ensures better control over the process and results in minimizing distortion. The Heat Affected Zone (HAZ) is relatively small compared to other conventional techniques.
- (c) Faster manufacturing that shortens the overall production time.

Some common materials that have been investigated for powder-blown DED AM processes include: titanium alloys [25–30], steels [31–33], nickel-base alloys [6,8,11,23,34–43], cobalt-base alloys [44,45] and high entropy alloys [46–50].

2.2.1 Process Parameters

There are several process parameters that are of importance in DED manufacturing. In the following Table 2.1, some of the parameters and their description are listed.

Table 2.1: Important process parameters for a DED deposition

Parameter	Unit	Description
Power	<i>W</i>	The power of the laser beam that fuses the powder with the substrate
Scan speed	<i>mm/s</i>	The traverse travel speed of the laser head
Powder feeding rate	<i>g/min</i>	The amount of powder that is fed into the melt pool
Shielding and carrier gas flow rate	<i>l/min</i>	The flow rate of the shielding and carrier gas
Laser spot diameter	<i>mm</i>	The diameter of the laser beam

2.2.1.1 Laser Power

Laser power is one of the most important parameters in any laser additive manufacturing process. As the laser power increases, the temperature in the melt pool increases. Low laser power can lead to insufficient fusion resulting in weaker metallurgical bonds between the layers[51]. On the contrary, high laser power, results in higher melt pool temperature, the heat sink effect of the substrate is reduced, that results in lower cooling rates. The resultant microstructure is generally characterised by coarse columnar grains with preferred orientation [11,52]. Prashanth et al. [51] observed higher densification and hence improved tensile properties when the laser power of SLM fabricated Al-12Si alloy by performing deposits was increased from 40W to 240W.

2.2.1.2 Scan speed

Along with laser power, the other most important parameter in a DED process is the scanning speed. Similarly, Erica et al. [53], in DED manufactured IN718, reported a finer microstructure with increasing scan speed. Average grain area with scan speed 2mm/s was $\sim 1800 \mu\text{m}^2$ compared to $\sim 900 \mu\text{m}^2$ when the scan speed was 5mm/s. However, the effect of scan speed on the densification of the deposits and the mechanical properties were not explored.

2.2.1.3 Powder feed rate

This is the amount of powder that is fed into the melt pool. Therefore, a high feeding rate means more powder being fed in the melt pool, which would lead to increased layer height during the deposition process. Additionally, the powder feed rate affects the surface roughness of the build component. A high feeding rate results in higher roughness and defects due to incomplete remelting [54].

2.2.1.4 Shielding and carrier gas flow rate

At the elevated working temperatures in AM, there is a high chance of formation of metal oxides or nitrides, which are undesirable. The shielding gas provides a protective atmosphere for the melt pool from oxidation. The shield gas can produce some porosities that can be avoided by modification of the process parameters. The carrier gas carries the powder from the feeder to the nozzle to the melt pool. Argon is the most used shielding and carrier gas used in DED techniques. The shield gas also prevents the powder particles from spattering and damaging the laser optics [55].

2.2.1.5 Laser spot diameter and percentage overlap

Laser spot size is a very important process parameter as it directly affects the size and shape of the melt pool. A high-powered laser beam is generally coupled with a wider laser spot size to maintain the desired deposition rate. Additionally, spot size influences the surface finish and formation of potential flaws [22]. The overlap percentage between two consecutive tracks is also crucial in DED processes to produce a near defect-free, dense deposit. For DED techniques, the hatch distance and layer thickness must be carefully determined, for an overlap percentage, to avoid any undesirable overbuild and underbuild of the components. Also, it has been reported that higher residual stresses form in the overlapping regions [56]. Figure 3 shows the schematic of a layer built by laser metal deposition. If the hatch spacing is too far apart, it may result in undesirable underbuilds, and if too close, overbuilds occurs.

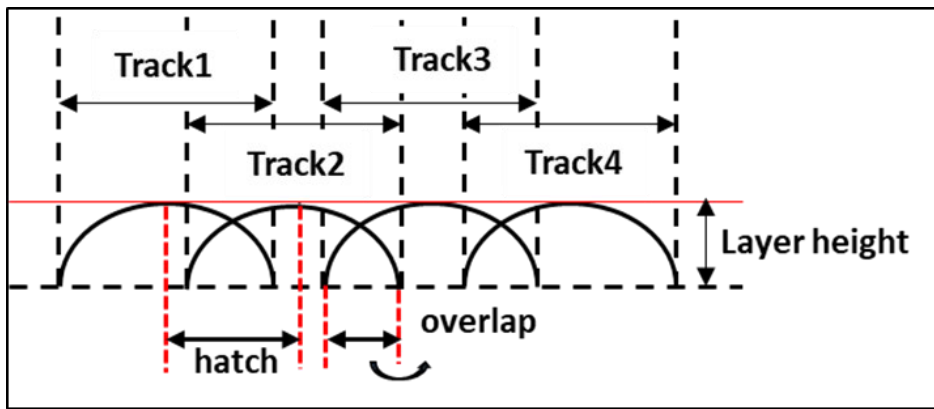


Figure 2.3: Schematic of a layer built by laser DED process, showing the track width, track height and the overlap.

2.2.2 Energy density in AM process

An appropriate combination of process parameters is essential to manufacture a component using additive manufacturing techniques. This is required to manufacture a dense structure with minimum defects and desirable properties. The energy density is a measure of heat input during the AM process by correlating the important process parameters. It is a measure of the average energy provided per unit volume per unit time, as shown in Equation 2.1 [51,57–59],

$$E_{VED} = \frac{P}{vht} \quad [2.1]$$

Where volumetric energy density E (J/m^3), laser power P (J/s), scanning speed v (m/s), hatch spacing h (m), layer thickness t (m).

The above may be simplified into the form of describing linear energy density [53,57]:

$$E_{LED} = \frac{P}{v} \quad [2.2]$$

For AM deposits, the energy density is generally used as a metric to compare manufactured deposits. However, the equations do not consider other important factors such as the percentage of overlap or powder flowrate. Investigations regarding the applicability of the Equation [2.1] were studied by Bertoli et al. [59] on SS316L, and Prashanth et al. [51] on Al-12Si alloys fabricated via SLM. Keeping the layer thickness and hatch spacing constant, Prashanth et al. [51] studied a series of deposits manufactured with the same volumetric energy density but a different combination of power and scan speed. It was observed that the Al-12Si SLM samples obtained at a constant energy density but with varying laser power and scan speed combinations had different densification levels. Therefore, it can be concluded that the combination of various process parameters, laser power and scan speed play a significant role, and it is of utmost importance to understand the effect of each property individually and how these parameters interact among themselves to co-relate the process parameters and the properties of the deposit.

2.3 Direct Energy Deposition (DED) as a repair technique

The conventional repair processes of superalloy components mostly include welding and brazing. These techniques have certain imitations or drawbacks that make them unsuitable for repairs. The heat-affected zone (HAZ) micro fissures or HAZ liquation cracking is often observed in the welded components [60–62]. Electron Beam (EB) welding needs a vacuum environment which is expensive and difficult to apply to larger parts. The ones which are relatively easy to use, such as the Tungsten Inert Gas (TIG) welding, generate a lot of heat that results in high residual stresses, distortion and heat-related effects in the base metal [60,63]. Brazing is often used for repairing superalloy components, such as turbine blades; however, it is limited to repairing very small defects (~250 μm). The wide gap brazing technique was proposed to overcome this problem; however, the strength of the brazing (repaired) joints are found to be weak, and they can achieve a maximum of 50% of the strength of the base metal [6,7]. The transient liquid phase (TLP) bonding combines brazing and solid-state diffusion bonding and is also used for joining Ni-base superalloy parts [64]. However, the high bonding temperature and holding time may cause coarsening of the base material, thus, limiting its usage. In the recent past, the DED techniques have gained significant popularity as a manufacturing process. Apart from building complex structures,

various DED processes have found widespread application in surface modification, such as cladding and repair [6,35,65–78]. Note that DED techniques can directly rebuild a worn-out or damaged part; unlike conventional repair techniques, welding and brazing are often used to join components. This technology also allows the material gradient to be designed at a microstructure level because of small, localized fusion in the melt pool. Moreover, due to the flexibility in the deposition technique, a flat initial surface is not essential, allowing new material to be deposited on the damaged part, which is otherwise not possible in other deposition or repair techniques [79].

Cracking or wearing out is very common in metal parts during service. However, repairing a crack is not straightforward because the defects cannot be simply removed by refilling materials on the gap region. To repair these defects, a slot or groove needs to be machined to remove material around cracks to reveal a regular and accessible geometry; thereafter, the necessary volume is then filled [6,70,73,75,78,80]. Some of the studies on the repair of metal parts, such as gas turbine air foils and disks, using AM processes in the literature are discussed as follows.

2.3.1 Effect of DED process parameter on repair

Qi et al. [65] developed the repair of turbine compressor air foils by DED process. Different process parameters were investigated, such as laser power, defocus distance, powder feed rate, laser scan speed, height increment and shielding gas flow rate. A design of experiments was employed to obtain adaptive deposition bead widths for repairing an air foil, and it was concluded that laser power and scan speed were the main parameters controlling the repair process. Lin et al. [74] studied the repair of a steam turbine blade by laser cladding technology. Paydas et al. [77] employed the laser cladding technology to repair a Ti-6Al-4V alloy part and investigated the influence of the building strategy and energy densities on the microstructure and hardness of the specimen. Based on their observations, a thermo-metallurgical scheme was proposed to achieve near uniform properties across the repaired part. Liu et al. [75] investigated the repair process and properties of the TC17 titanium alloy using DED process. Different combinations of laser powers, scanning speeds and powder feeding rates were employed to repair circular grooves (defects). A parameter combination with 1000W laser power and a scan speed of 8 mm/s enabled repair of the component with 99% density. Petrat et al. [35] repaired cylindrical IN718 parts using laser DED. A set of parameters with a spiral scanning pattern starting point changed after every layer was adopted for the repair. They could not observe any significant differences while

using low or high-power sources; however, the study lacked detail on microstructure or texture changes due to varying parameters. Zhang et al. [81] used various scanning patterns to deposit multi-layer cobalt-based alloy on tool steel. A helix, circle-line-circle, and line-arc-line scanning pattern were used for the coating purpose (Figure 2.4). They observed that the helical tool path to be most efficient in terms of deposit time, however, in terms of efficient usage of the powders during the coating/deposition process, the circle-line-circle, and line-arc-line scanning pattern were found to be better. Therefore, the process parameters and the scanning patterns used for DED repairs seems to have a significant effect on the properties of the repaired part.

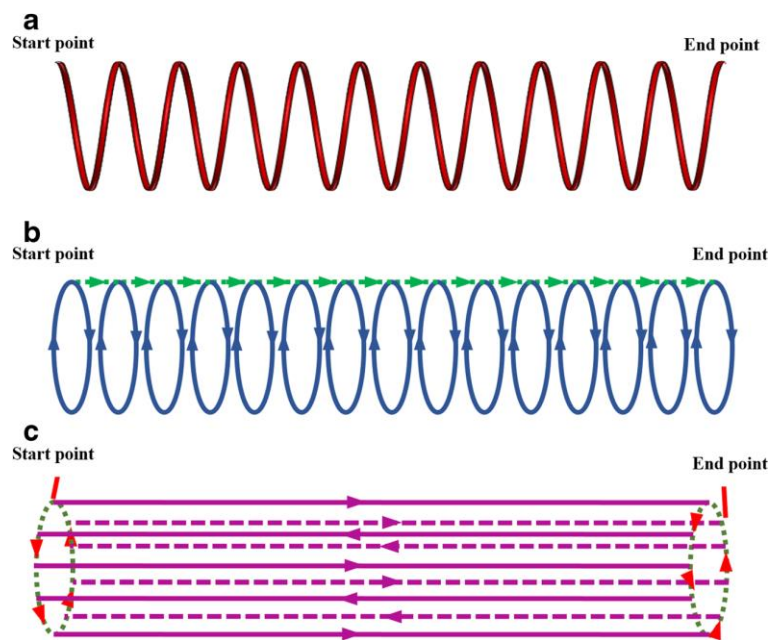


Figure 2.4: Scan parts used by Zhang[81] to repair a cylindrical section (a) Helix; (b) circle-line-circle; (c) line-arc-line.

2.3.2 Effect of groove geometry on repairs

The shape of the repaired component is influenced by the inclination angle of the slot machined for the deposition process [6,70]. The effect of various groove geometries on the repair of tool steel H13 was investigated by Pinkerton et al.[78]. Two different slot geometries (V-shaped 60° and rectangular 90°), as depicted in Figure 2.5, were repaired using DED process. It was observed that the rectangular (90°) shaped defects had the presence of pores due to insufficient fusion since the laser was not able to melt the materials in the vertical zone.

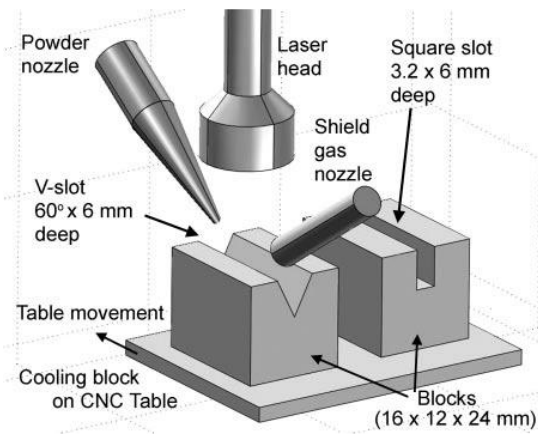


Figure 2.5: Repair geometries used by Pinkerton et al. [78].

In a similar study, Zhang et al. [70] deposited Co-Ni-Cr-W alloy Wallex 50 on H13 tool steel V-shaped grooves (Figure 9) with different sidewall angles: 45°, 75°, and 90° to study the influence of the angle of inclination on the properties of repaired parts. An alternating scanning raster (90° rotation after each layer) was selected for the repair; similar to Pinkerton et al. [78], they also observed poor repair for the 90° sidewall grooves. It was observed that the deposited material was unable to bond well with the substrate, causing lack of fusion and resulting in porosities.

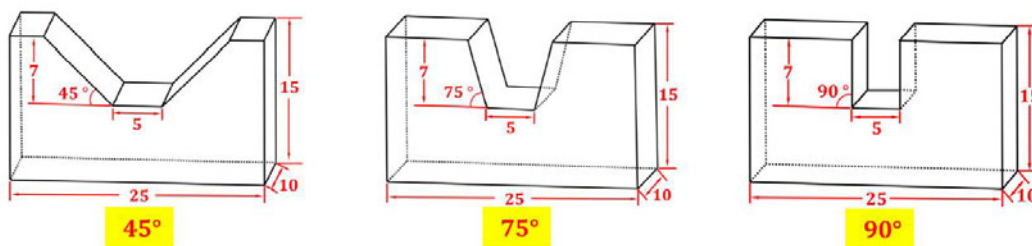


Figure 2.6: V-shape geometries with flat bottom used by Zhang et al. [70].

Liu et al. [6] repaired IN718 and Waspaloy alloys using DED technique. Several defect geometries, including rectangular and circular geometries and through holes, were repaired using varied processing parameters, as shown in Figure 2.7. Different scanning patterns such as alternating, spiral and concentric were adopted for the repairs. The effect of process parameters and geometries repaired using DED was investigated. It was observed that IN718 was repaired with minimum defects and distortion over a wide processing window. However, the effect of varying groove angles and scanning patterns on the resulting microstructure and mechanical properties of the repaired IN718 was not explored.

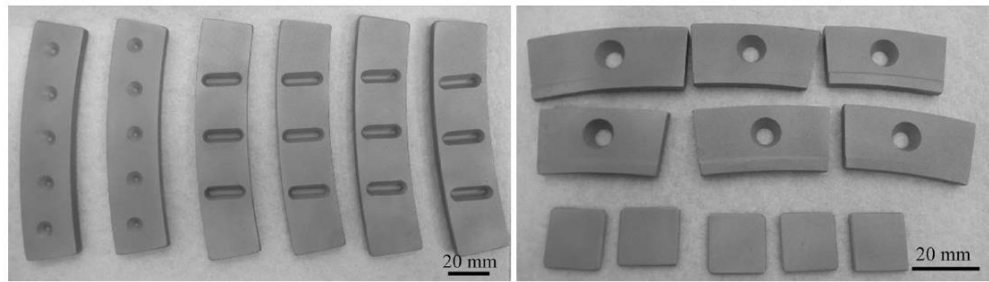


Figure 2.7: Repair geometries used by Liu et al. [6]

Zhang et al. [74] performed repair of IN718 components with pre-made trapezoid groove (Figure 2.8) using laser additive manufacturing technique, and the microstructure and tensile properties of the repaired section are investigated. The properties of repaired IN718 alloy post hot corrosion was also investigated. It was observed that after exposure to hot corrosion test for 50 hours, tensile strength improved from 736.6 MPa to 1022.9 MPa; however, the elongation reduced significantly from 12.5 % to 1.7 %. The strength and elongation were further reduced to 955.8 MPa and 1.2%, respectively, when the hot corrosion testing time was increased to 150 hours. However, the study was limited to single groove wall angle, and the effect of post deposit heat treatment on the properties of the repaired component was not explored.

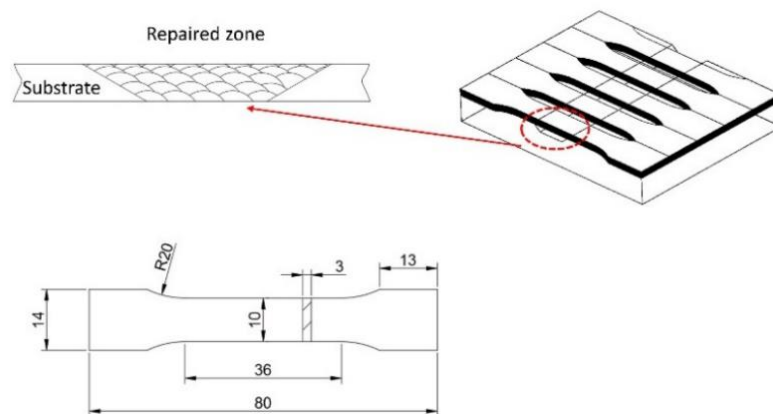


Figure 2.8: Illustration of a laser-repaired zone in the tensile specimen [80].

The literature review indicates that the process parameters, scanning patterns and geometry of the repaired section are of prime importance when using AM processes to repair metallic components. For a defect-free repair process, the first step includes the determination of a combination of process parameters that enables highly dense deposits with minimum defects and porosities. A smaller tilt angle (Figure 2.6) provides better contact between the defective area and substrate, although it results in

higher material loss. If the sidewall is too steep, the laser has difficulty melting materials on the sidewall, where this situation can be observed [70,73,78]. Therefore, the as-deposited material cannot be fused well with the substrate and defects were observed due to insufficient metallurgical bonding between the substrate and deposit. Studies on the effect of the sidewall inclination on the microstructure and mechanical properties of the sections repaired via DED processes are limited in literature and need detailed investigation. Moreover, the final microstructure in the deposit is generally different from the base material. In some alloy systems, such as superalloy IN718, undesirable non-equilibrium phases are formed at the cost of strengthening phases, which are reviewed in detail in the following sections. This can affect the mechanical properties of the repair adversely [22].

2.4 Ni-base superalloys

Superalloys can be categorised into three main groups, nickel (Ni)-based, cobalt (Co) - based and nickel-iron (Ni-Fe)-based superalloys [82]. Superalloys have unique capabilities of maintaining a high yield strength, tensile strength, creep resistance, corrosion resistance and fatigue resistance at elevated temperatures, where most other metal alloys are rendered unstable. This makes superalloys well suited in the aero, nuclear and petrochemical industries. Ni-base superalloys are highly utilized in aeronautic industries. More than 50% of a jet engine's weight consists of Ni-base superalloys [83].

2.4.1 Strengthening Mechanisms

Superalloys, in general, are strengthened by solid solution strengthening, precipitation strengthening and dispersion strengthening [83,84]. The role of various strengthening mechanism in Ni-Base superalloys especially in IN718 are discussed as below.

2.4.1.1 Precipitation Strengthening

Precipitation hardening is the primary strengthening mechanism in Ni-base superalloys, such as IN718. The precipitation of the Nb rich or (Al, Ti) rich ordered phases γ'' and γ' , respectively, impart strengthening in the superalloy. The elements Niobium (Nb), Titanium (Ti), and Aluminium (Al) have limited solubility in the γ matrix. Fine precipitates are formed during ageing treatment following solution treatment. The ordered precipitates result in a coherency strain in the matrix that resists the dislocation movement through the matrix. Moreover, additional work is required to create an Antiphase Boundary due to dislocations passing through precipitates

having an ordered lattice [85]. A dislocation moving through the matrix may cut through the precipitate or get pinned at the precipitate. A pinned dislocation at a precipitate may either climb over it, which becomes favourable at high temperatures, or bow around it. The volume and size of the precipitation control the degree of strengthening. When the precipitates grow larger than a particular size (corresponding to peak hardness), the precipitates become “too large”, and for a finite volume fraction of phase, the precipitates become sufficiently sparse that it becomes easier for the dislocation to bow around rather than shear the precipitate [84].

2.4.1.2 Solid Solution Strengthening

Solid solution strengthening occurs due to differences in the atomic radii of solutes present in the solution, which cause an elastic strain field in the crystal lattice and restricts the mobility of dislocations. The melting point, diffusivity, and extent of atomic mismatch of the solute atoms dictate the strengthening effect they can generate. Solid solution strengthening is also generally associated with lower stacking fault energy, thus making cross-slip difficult. This would prevent dynamic recovery [85]. In the Ni-Fe alloy, commonly known as INVAR, the primary strengthening mechanism is solid solution strengthening [2]. In IN718, elements such as Molybdenum (Mo), Aluminium (Al), and Chromium (Cr) provide good solid solution strengthening; however, at higher temperatures, their effect is significantly lowered [84].

2.4.1.3 Other Specialty Alloys

Other alloys, such as MA6000 and MA754, are oxide dispersion strengthened alloys and exhibit good high temperature creep strength [86]. There are some similarities in the strengthening mechanism of dispersion strengthening and precipitation strengthening, albeit some major differences. The strengthening particles are generally oxides that are added during manufacturing rather than forming in-situ. These oxides are incoherent with the matrix; therefore, their distribution and size dictate the efficiency of strengthening. However, the oxides have a high melting point, making them chemically stable in the metal matrix, thus helping retain their strengthening effect better than any other strengthening mechanisms at very high temperatures (up to 1300°C) [84].

2.4.2 Inconel 718 (IN718)

IN718 is a Nickel-Iron base superalloy exhibiting excellent mechanical properties and corrosion resistance in the medium to high-temperature class. The typical composition of IN718 is depicted in Table 2 [84]:

Table 2.2: Typical composition of IN718

IN718	Wt %
Ni	53
Cr	18.6
Mo	3.1
Nb	5
Al	0.4
Ti	0.9
Fe	18.5
Mn	0.2
Si	0.3
C	0.04

IN718 has found widespread application, especially in gas turbines and aerospace engines because of its excellent mechanical properties- especially strength, creep resistance, and oxidation resistance at elevated temperatures (~650 °C) [83]. The addition of several elements aids in the formation of the properties. The purpose of the most common elements in IN718 are listed below in Table 3 [87]:

Table 2.3: Purpose of the common elements in IN718

Element	Purpose
Nb	Forms γ'' , δ ($\text{Ni}_3\text{Nb} - \text{BCT DO}_{22}$) precipitation; Promotes formation of Carbides and Laves phase
Al	Promotes formation of γ' (Cubic (Ll_2) - $\text{Ni}_3(\text{Al}, \text{Ti})$) precipitates.
C	Promotes metal carbide formation.
Cr	Improves the hot corrosion and oxidation resistance; helps with carbide formations; Solid solution strengthening element;
Ti	Promotes formation of γ' ; TiC/TiN precipitation.
Mo	Solid solution strengthening element
Ni	Forms the FCC matrix

IN718 consists of an FCC γ -matrix, strengthened by embedded γ' and γ'' precipitates in the heat-treated and aged condition. Al and Ti are the main elements that form the γ' (Cubic (L1₂) - Ni₃(Al, Ti)) precipitate, whereas Nb forms the γ'' (BCT (DO₂₂) - Ni₃Nb) precipitate. These elements have limited solubility in the FCC Ni matrix; therefore, the precipitates are formed during an ageing treatment after cooling from the solution treatment temperature. Metal carbides (MC) and δ phase are also often found in a typical IN718 microstructure. The γ'' precipitate is a metastable phase, an ordered precipitate (DO₂₂) with a Body Centered Tetragonal (BCT) structure that acts as the main strengthening phase. The FCC γ' phase, which is often the main strengthening phase for other Ni-base superalloys like CMSX-4 or Nimonics, does not contribute significantly to the strengthening in IN718. The coherency strain between the matrix phase and the precipitates hinders the movement of dislocations and thus causes strengthening. Additionally, the movement of a dislocation (shearing) through ordered precipitates results in anti-phase boundary resisting dislocation movement between ordered strengthening phases. The morphology of the γ' precipitates are generally cuboidal or spherical, while the γ'' precipitates generally have a lenticular, disc-shaped morphology with thickness in the range of 9-20 nm [88,89]. The metastable γ'' starts to transform into a stable δ phase (Ni₃Nb) with an orthorhombic structure ($a \neq b \neq c$; $\alpha \neq 90^\circ$) if exposed to long ageing times or temperatures higher than 650°C peaking around 900°C [90]. Since γ'' and δ have the same composition, the growth of the δ phase occurs to the detriment of the γ'' phase. The δ phase is incoherent with the matrix and thus, does not contribute to the strengthening of the alloy. As a result, IN718 is used in conditions where the service temperatures generally do not exceed 650°C. However, the δ phase has a beneficial effect on ductility and toughness [84,91,92]. The fine acicular δ precipitates form at the grain boundaries and thereby restrict grain boundary sliding, restricting undesirable grain growth, which improves toughness and creep resistance [93,94].

2.4.2.1 AM manufactured IN 718: microstructure and texture

The microstructure and properties of IN718 fabricated by DED type of AM technique have been investigated in detail [8,11,20,23,35,36,40,68,88,94–105]. Figure 2.9 shows the typical microstructure of DED fabricated IN718.

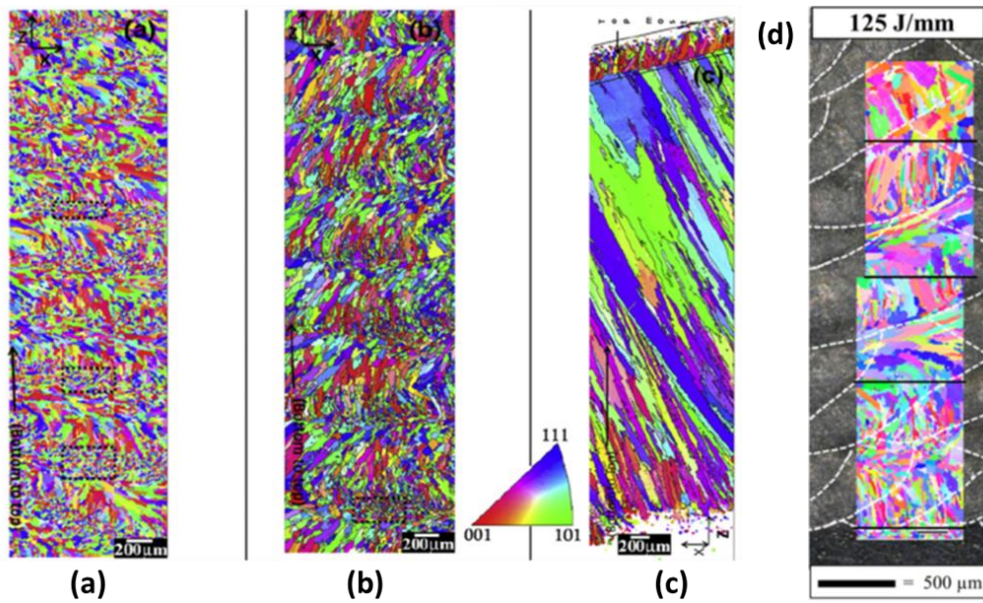


Figure 2.9: Typical microstructure of IN718 manufactured using DED technique: (a),(b),(c) microstructure variation with varying process parameters [11]; and (d) IPF maps superimposed on the optical micrograph [53].

A typical DED-produced IN718 microstructure is characterized by columnar dendrites growing epitaxially from the substrate. The substrate acts as the main heat sink. Heat flow occurs through the previously deposited layers. The heat flux is towards the substrate, and the dendrites grow opposite to the substrate [10,106]. As a result, a $\{001\}$ texture is often reported in AM IN718, the $\{001\}$ direction being a preferred growth direction in the FCC matrix γ (Figure 2.10)[10,11,95,107]. The effect of such columnar microstructure and preferential texture on the mechanical properties of the as-deposited parts are discussed in Section 2.4.3.2.

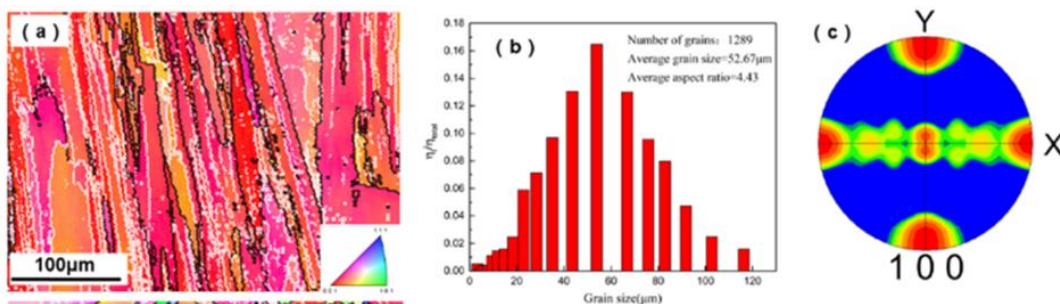


Figure 2.10: Columnar grain structure leading to $\{001\}$ texture along build direction in as-deposit IN718 [108].

The high cooling rates associated with AM techniques result in non-equilibrium solidification conditions and the formation of brittle Nb-enriched Laves phases $((\text{Ni,Cr,Fe})_2(\text{Nb,Mo,Ti}))$ along the inter-dendritic regions [94,109]. Figure 2.11 (a) shows the typical distribution of Laves phases in a laser deposited (DED) IN718. It

has been reported that 10% – 12% Nb is required for the formation of Laves phases; the δ phase requires 6% – 8% Nb, the γ'' and γ' phase can form at 4% Nb [62]. The Laves phase formation depletes the availability of Nb for the strengthening precipitates (γ'' and γ') to form, therefore, deteriorating the strength properties of the IN718 deposit. Additionally, Laves phases were found to have a profound effect on the γ'' precipitates and less on the γ' precipitates. Laves phase leads to inhomogeneous distribution and coarsening of the γ'' precipitates [107].

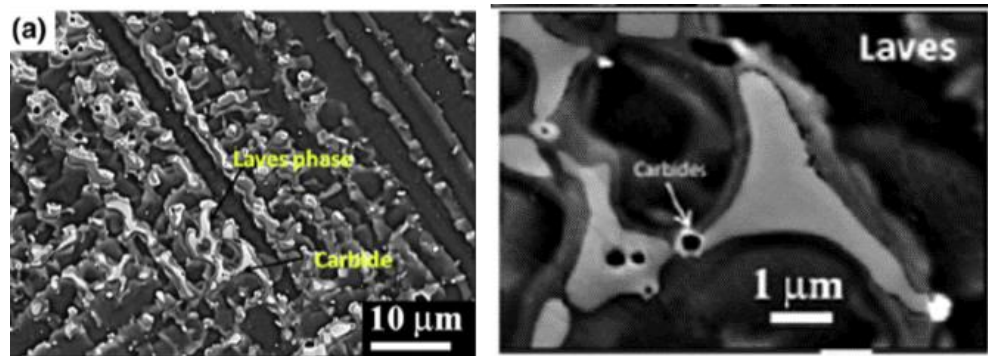


Figure 2.11: (a) Laves phase and (b) carbides in DED fabricated Inconel [11].

Several attempts were made to tailor the microstructure and distribution of Laves phases in AM IN718. Xiao et al. [102] used a laser with a quasi-continuous wave and were able to achieve higher cooling rates during fabrication, thereby significantly reducing the size of dendrite arm spacing (DAS). This resulted in significantly less segregation of Nb and hence, less Laves phase in the deposit. Liu et al. [41] reported that the DAS increases as the thermal gradient decreases in regions further from the substrate. Also, DAS increases with an increase in pool temperature, which is seen when laser power increases. Parimi et al. [11] showed that the texture in a DED builds was significantly influenced by the laser power applied. They found that with increasing laser power to 910W from 310W, keeping all other parameters constant, a significant change in microstructure was observed: from a mix of coarse and fine microstructure with weak or random texture to a coarse columnar microstructure with strong texture. Stevens et al. [53] found that with decreased laser scanning speed, microstructures would become coarser. Furthermore, Additive manufacturing techniques provide high process control, enabling manufacturing parts with graded microstructure. Popovich et al. [97] varied the power and scan speed during the deposition process and were able to design functional gradients within the components with tailored properties, as shown in Figure 2.12. In principle, the microstructure of AM deposit IN718 depends on the temperature gradient (G) and the solidification rate (R), which depend directly on the parameter selection in the laser DED process.

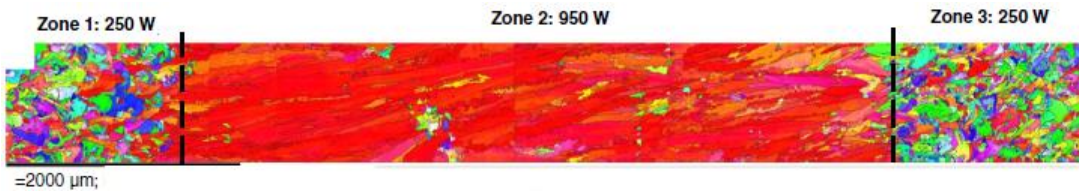


Figure 2.12: A graded IN718 sample manufactured using AM [97].

IN718 is one of the alloy systems extensively studied in the AM community. As shown in Figure 2.13, the interest in AM IN718 is increasing over the last decade. The attractive process control and degrees of freedom in manufacturing parts make AM a very attractive option for manufacturing IN718; however, the existence of defects such as porosity and bonding defects further restrict wider industrial usage. Moreover, the widespread use of AM is restricted due to the complexity of the produced microstructure – such as formation of Nb-rich Laves phase, that are found to deteriorate the mechanical properties by providing crack initiation sites. During the post heat treatments, the strengthening precipitates form around the vicinity of the Laves phase which result in their non-uniform distribution. This often leads to difficulty in reproducibility and predictability of the mechanical properties. Furthermore, the geometry of the part being built, and the scanning strategy adopted during AM process also significantly impact the microstructure and properties of the built, as discussed in the following sections.

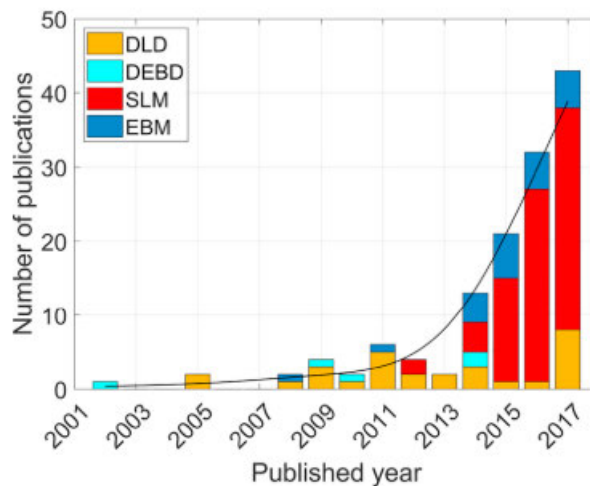


Figure 2.13: Increasing interest in AM IN718 through years [12].

2.4.2.2 Role of geometry

The effect of shape and size of the manufactured component or the repair part on Laser DED deposit/repairs of IN718 is scarce in the open literature. Liu et al. [6] used circular and rectangular geometries (Figure 2.7) to repair turbine parts. As discussed in Section 2.2, better finishing was achieved using a groove with a greater side angle; however,

the effect of the resultant repair geometries on the microstructure of the deposits was not reported. Also, the role of different geometries on the microstructure of the heat-affected zone and the substrate was not studied. Babu et al. [107] reported a study conducted on EBM deposit of IN718. A change in geometry of the build from $16 \times 16 \text{ mm}^2$ to $20 \times 20 \text{ mm}^2$ resulted in a significant change in G/R values that resulted in a subsequent change in the microstructure of the as-deposited IN718.

2.4.2.3 Role of Scan strategy

The scan strategy or the scan pattern has an important role in the DED processes. Different scanning patterns for a set of laser power and scan speed parameters can result in different properties and microstructure [11]. Schematic for various scanning patterns often used in DED techniques are shown in Figure 2.15.

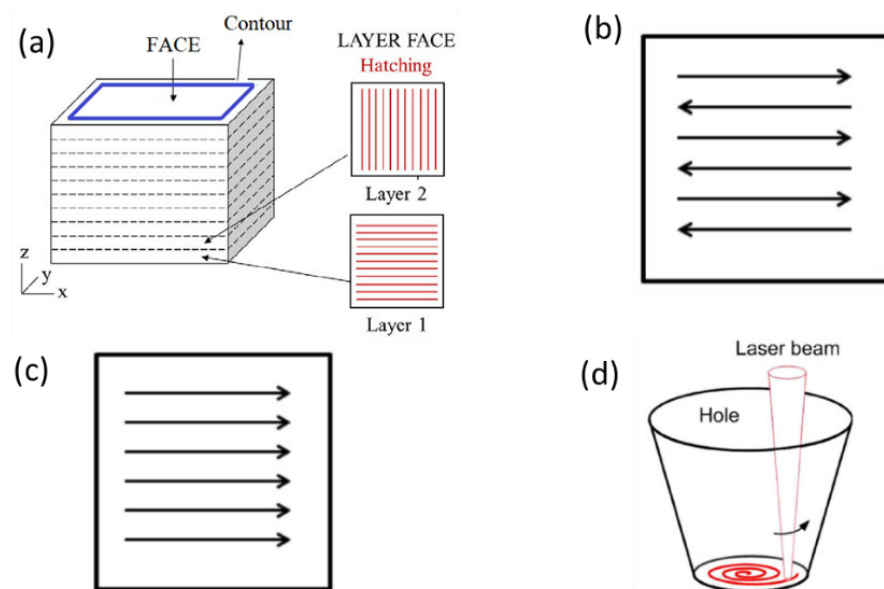


Figure 2.14: Different scanning strategies used in DED: (a) Alternate [53] (b) Bidirectional [110]; (c) Unidirectional [110]; (d) Spiral [6].

Unidirectional [11] and Bidirectional (Figure 2.14 (b)) [6,53] scan strategies are often adopted in DED IN718; however, the unidirectional and bidirectional are generally used for single wall deposit. A bi-directional pattern with a 90° rotation between the layers results in an alternate pattern, which is also often adopted in DED processes [15, 22]. Variations in microstructure and properties are reported in AM IN718 deposits. Parimi et al. [11] used both unidirectional and bi-directional scan strategies for laser DED IN718. For the same set of process parameters, a change in the orientation angle of the as-deposited microstructure with respect to the building direction was observed for the different scanning strategies (Figure 2.9(a), (b)). Variation of grain size and

orientations is reported by Dinda et al. [10] by changing scanning strategies as shown in Figure 2.15(a) – Figure 2.15(f). The grain orientation changed from a constant 60° tilt along the build direction while using a unidirectional pattern to a zig-zag type orientation upon changing to a bidirectional scanning pattern. The texture in the build parts also changed from a fibre texture to a cube-type texture. However, a preferred {001} texture still prevails with either scanning pattern (Figure 2.15 (c), (d)).

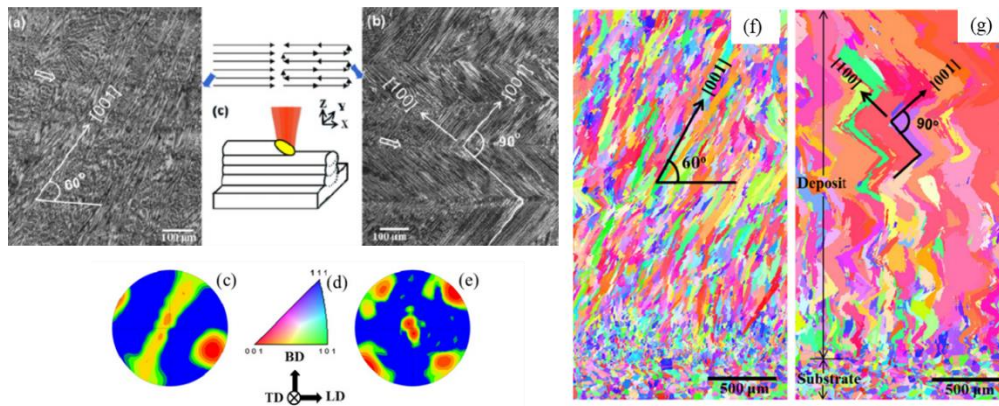


Figure 2.15: Effect of change in scanning strategy in grain orientation and grain structure (a) IN 718 by unidirectional laser scanning, and (b) IN 718 by bidirectional laser scanning [10].

Scanning patterns influence the resulting microstructure for AM processes, as shown in Figure 17. Furthermore, an appropriate selection of scan strategy and pattern is found to decrease distortion, and residual stresses in the fabricated component [14,16], especially an island pattern or chessboard pattern often used in SLM and EBM techniques has been reported to decrease the residual stress developed [16]. In SLM IN718, S. Hibino et al. [111] used a bidirectional laser scanning with the scanning lines moved to a predefined degree after each layer, as shown in Figure 2.16 (a-c). A significant change in the grain orientation can be seen due to altering the scanning pattern, and a change in mechanical properties was also reported.

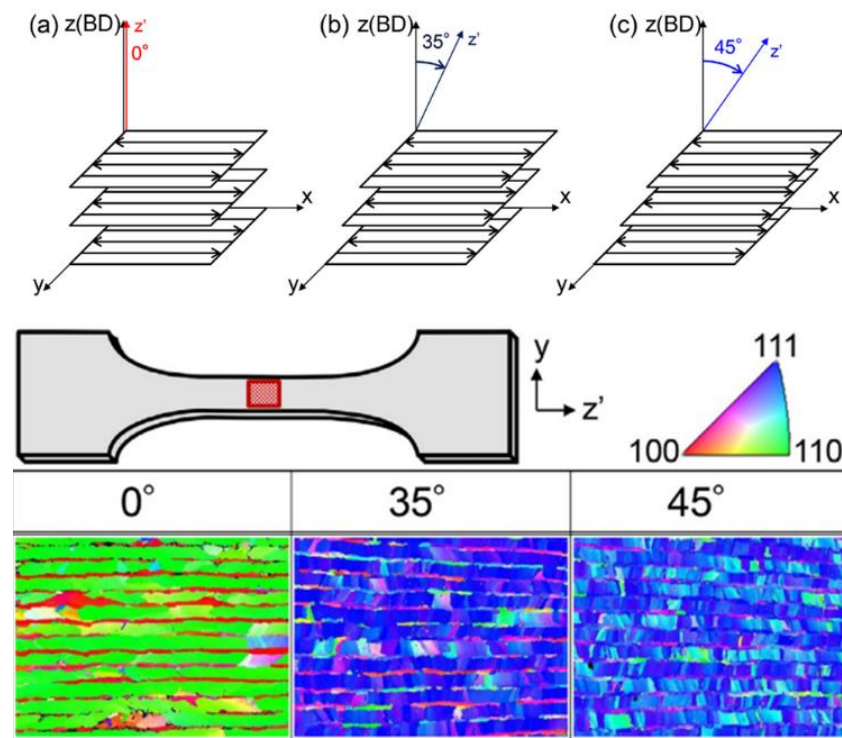


Figure 2.16: Different scanning strategies and resulting microstructure in SLM IN718 [111].

For IN718 repairs, a spiral pattern and alternate pattern were used by Liu et al. [6] to repair turbine components using DED (LENS); however, the effect of the scanning pattern on the resulting microstructure was not discussed. The effect of the scanning patterns on the distribution of Laves phase and δ phase, its effect on the mechanical properties requires further investigation.

2.4.3 Heat treatment and mechanical properties of IN718

2.4.3.1 Standard heat treatment adopted for Laser AM fabricated IN718

The standard heat treatment commonly used for cast and wrought IN718 consists of three main steps, which are as follows [14,93,104]:

- Homogenization: 1100°C/ 1-2 hrs hold followed by air cooling.
- Solution treatment: 950°C – 980°C/ >1 hr followed by air cooling or faster.
- Ageing: 720°C 8 hrs; furnace cooling 620°C 10 hr followed by air cooling or faster.

The industrial standard for wrought and cast IN718 is listed in Table 2.4 below. Generally, a direct ageing HT or a combination of heat treatment procedures are adopted.

Table 2.4: The standard heat treatment procedures of IN718 (industrial standard) [94, 103]

Sl no.	HT Procedure	Conditions	AMS-5383D (cast IN718)	AMS-5662M (Wrought IN718)
1	Homogenization treatment	1080°C, 1.5h/air cooling or faster	✓	
2	Solution treatment	980°C, 1h, air cooling or faster	✓	✓
3	Ageing treatment	720°C, 8h/furnace cooling at 55°C/h; 620°C, 8h/air cooling	✓	✓

Several combinations, including direct ageing; solution treatment and ageing; homogenisation and ageing, have been studied for heat treatment of additive manufactured IN718 [44, 90, 94, 103]. The as-built AM components have low strength because of the absence of strengthening phases γ' and γ'' . Thus, post-deposit heat treatment is often employed to strengthen the deposit. The microstructure of AM IN718 deposited using SLM is shown in Figure 2.17. The columnar nature of the microstructure is still evident after direct ageing. It has been observed that the temperature used in direct ageing is not sufficient to dissolve Laves phases. Laves phases were still observed after direct ageing, but the strength after ageing increased several folds due to precipitation of the strengthening precipitates [7, 90, 94]. It was found that post solution treatment at 980°C, the Laves phases were partly dissolved and released Nb for the formation of strengthening precipitates. However, some δ phase precipitates are observed at the cost of γ'' precipitates. At temperatures over 1080°C, all Laves phase and δ phase are dissolved and the γ' and γ'' precipitates form [14,93,103,112]. During homogenisation treatment, slow heating and soaking enables the formation of γ'' precipitates at the cost of Laves phases. Therefore, the soaking time and temperature is also an important criteria during heat treatment [14]. Although these studies claimed to achieve recrystallized equiaxed microstructure after heat treatment, the microstructures are highly heterogeneous.

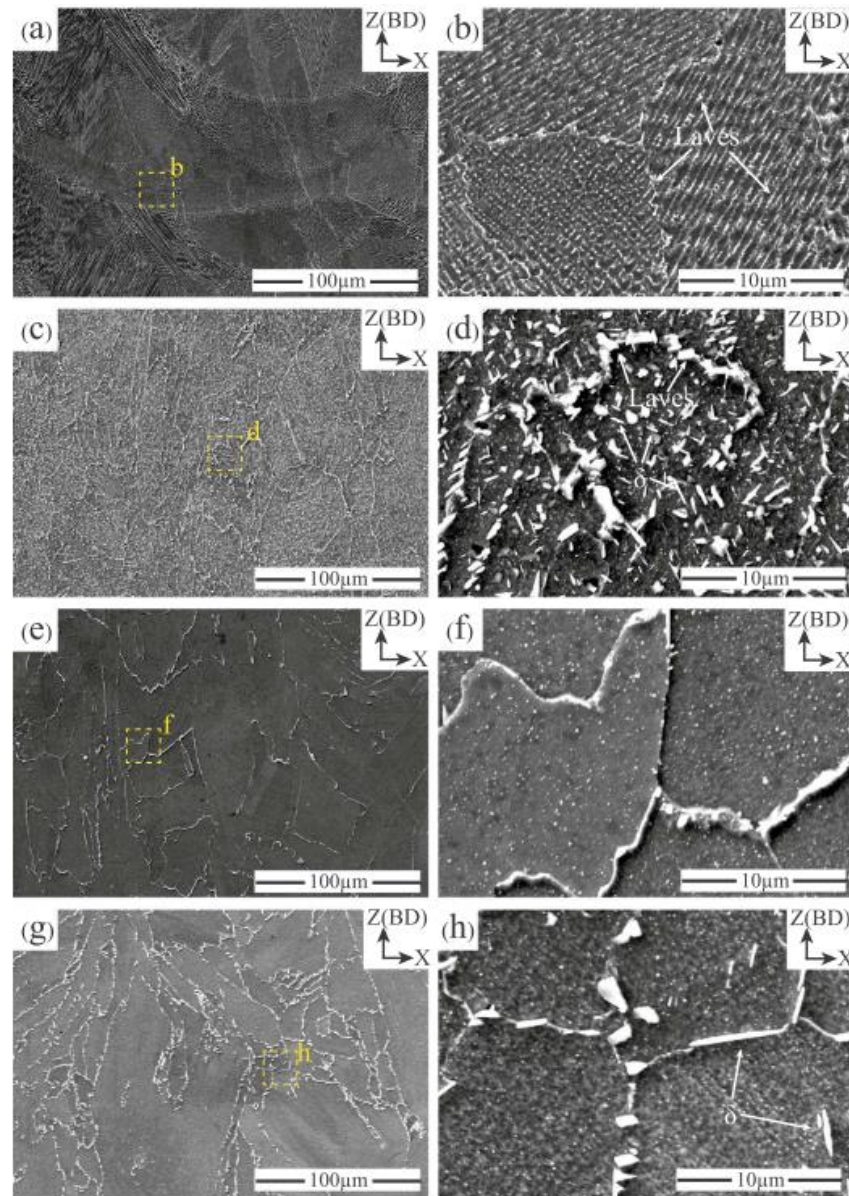


Figure 2.17: Microstructure after heat treatment at different conditions: (a), (b) Direct aged; (c), (d) Solution treatment at 980°C and ageing; (e), (f) Solution treatment at 1080°C ; (g), (h) Solution treatment at 1080°C and ageing [113].

Recrystallization for AM manufactured IN718 has been reported after holding at a temperature above 1100°C [114]. The residual thermal stress results in accumulation of localised strain energy during the AM process that acts as the driving force for the recrystallization process, unlike the traditional wrought IN718 superalloy, where the stored energy due to deformation acts as the driving force for dynamic recrystallization. Recrystallization was also found to be a function of holding time. However, the distribution of the grains was very uneven. Some columnar grains underwent recrystallization while others did not, depending on the distribution of the thermal residual stresses [56,114]. Zhu et al. [104] observed that recrystallization starts

in the regions with higher residual stress. The AM manufactured part with the highest residual stress had the finest microstructure, thus confirming that the localised strain energy accumulated due to residual stress is the driving force for recrystallization. However, Chlebus et al. [14] argued that heating the alloy to the homogenisation temperature ($\sim 1100^{\circ}\text{C}$) would result in some degree of stress relief. Furthermore, they claimed that the heat treatment (solution treatment and ageing) resulted in grain boundary migration induced by the reduction of the grain boundary area, discontinuous dissolution of columnar arrayed phases and solute diffusion along the boundaries. Moreover, twinning occurred and was considered to be an important factor in the microstructure refinement [14,56,114].

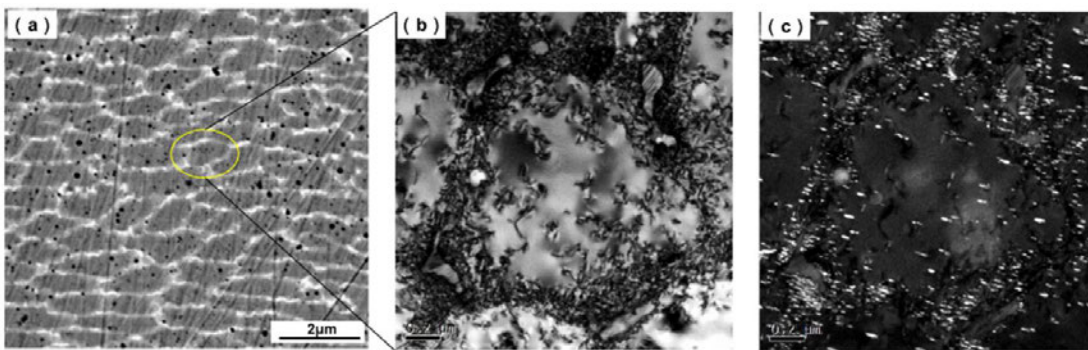


Figure 2.18: (a) Cellular structures of IN718 after solution treatment at 980°C ; the dislocations along the (b) cellular walls and (c) along γ'' precipitate [90].

2.4.3.2 Tensile properties and anisotropy in Laser AM fabricated IN718

The majority of the studies on the mechanical properties of AM manufactured components involve tensile tests and hardness measurements. Tensile tests to measure yield strength (YS), ultimate tensile strength (UTS) and elongation are the most used tests to compare Inconel components fabricated or heat-treated under different conditions. AM mechanical properties are often compared to traditionally processed materials [18,23,88,93,96,100]. Additive manufactured IN718 without any post-treatments exhibit better ductility properties than post-heat treatment as depicted in Table 2.5 and Figure 2.19.

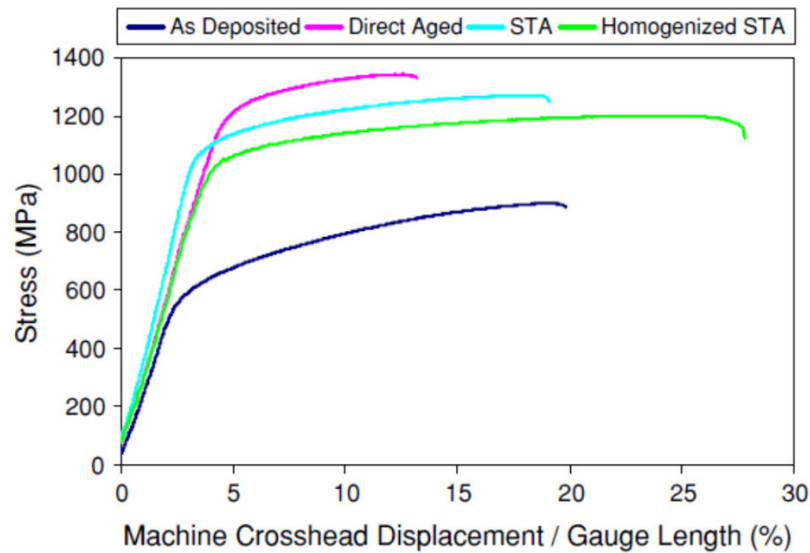


Figure 2.19: Typical tensile properties of IN718 under different heat treatment conditions [93].

The strengthening precipitates form during post-heat treatment that pins the dislocation movement; thus, strength increases at the cost of ductility. It was demonstrated by Mang Ni et al. [90] using TEM investigation how the hardening phases pin the dislocations, resulting in high dislocation density (Figure 2.18). A summary of tensile properties for IN718 fabricated using different laser additive manufacturing routes are listed in Table 2.5. The directional microstructure in the components manufactured by laser AM techniques results in anisotropy. In general, the specimens with a loading axis perpendicular to the build direction (i.e. x-y direction) typically exhibit higher strength properties and inferior ductility as compared to those which had their loading axis in the build direction (i.e. z direction) [14,89]. Post-heat treatment was successful in decreasing the anisotropy in mechanical properties. However, anisotropy was still observed after heat treatment, especially in the ductility property [89]. The various heat treatment processes resulted in varying microstructures, especially in terms of the distribution of the precipitates and grain sizes. This resulted in the differences in the mechanical properties post heat treatment. Ni et al. [89] and Zhang et al. [103] studied various heat treatment strategies for laser AM deposited IN718 to find an optimum heat treatment condition. A homogenisation treatment followed by solution treatment and double ageing was found to produce near- recrystallised microstructure (to some extent) with mechanical properties comparable to wrought IN718. However, the same heat treatment procedure may not be suitable for repairs, as homogenisation treatment at 1100⁰C for 1 hour may result

in massive grain growth in the substrate. Therefore, for developing/recommending a heat treatment process after DED deposit, care should be taken to avoid unnecessary grain growth in the base material, which may lead to undesirable performance. The post-deposit heat treatment should be able to produce desired strength properties in the deposit without any significant changes to the base material.

Table 2.5 Mechanical properties of IN718

Sl No	Conditions	AM Tech	Tensile strength (MPa)		Yield Strength (MPa)		Elongation (%)	
			∥ BD	⊥ BD	∥ BD	⊥ BD	∥ BD	⊥ BD
			(z)	(x-y)	(z)	(x-y)	(z)	(x-y)
1 [88]	HIP + annealed	DED	1140	1120	850	890	28	28
2 [23]	As-D	DED	1000		650		38	
	HSA		1436		1257		13	
3 [14]	As-D	SLM	904 ± 22	991 ± 62	572 ± 44	643 ± 63	19 ± 4	13 ± 6
	STA		1320 ± 6	1377 ± 66	1074 ± 42	1159 ± 32	19 ± 2	8 ± 6
4 [93]	As-D	SLM	904		552		16.2	
	DA		1333		1084		8.4	
	STA		1221		1007		16.0	
	HSA		1994		949		19.9	
5 [104]	STA	DED	687 – 718		313 – 340		54 – 61	
	HSA		1278 – 1342		1061 – 1129		19 – 16	
6 [89]	As-D	SLM	1110	1167	711	858	24.5	21.5
	DA		1398	1457	1181	1211	13.5	10.4
	STA		1471	1505	1235	1276	14.1	13.3
	HSA		1381	1402	1164	1181	18.2	18.1
7 [102]	As-D	SLM	1126		849		22.8	

	STA		1371		1084		10.1	
	HSA		1371		1046		12.3	
8 [115]	STA	SLM	1400	1440	1180	1186	20.4	18.5
	As-D		1110	1000	910	760	31.5	40.0
9 [116]	DA	EBM	1260	1190	1105	1010	22.5	32
	STA		1175	1205	1095	860	20.5	37.5
 BD: Parallel to build direction; ⊥ BD: perpendicular to build direction								
As-D: As-Deposit; DA: Direct Aged; STA: Solution Treated and aged; HSA: Homogenised Solution treated and Aged.								

A difference in the tensile properties is often observed when the loading direction is parallel to the build direction and perpendicular to the build direction [12,13,117–119]. The difference in the mechanical properties is often attributed to the morphology and texture of the grains in the as-deposit component [13,14,108,111,120]. Taylor factor analysis is often employed to describe the difference in mechanical properties. A high value of the Taylor factor would suggest that more stress is required to initiate slip, leading to higher yield stress values. AM IN718 deposits tested in different orientations have a higher average Taylor Factor on the cross-section parallel to the build direction [113,120]. Thus, the relatively high value of the Taylor factor for the grains on the cross-section of the horizontally built sample is responsible for the high strength. Liu et al. [120] tested SLM IN718 deposits manufactured with varying energy densities and tested in orientation at 0°, 90°, and 45° to the build direction. The Taylor factor maps shown in Figure 2.20 (e) for deposits with the same energy densities, but different orientations show higher values of the Taylor factor for samples tested at 90° and 45° to the build direction. Higher mechanical strength was also seen in the corresponding specimen. Most results reported in the literature follow this trend; however, Deng et al. [116] observed lower strength for samples oriented perpendicular to the build direction when they tested EBM IN718 under tension, although higher values for Taylor factor are still observed for samples tested in perpendicular direction. A possible reason for such anomaly was attributed to the directional alignment of micro-pores and columnar grains in the as-manufactured condition as shown in Figure

2.21 (d), (e). The difference in the elongation is generally attributed to different cracking mechanisms due to varying grain morphologies.

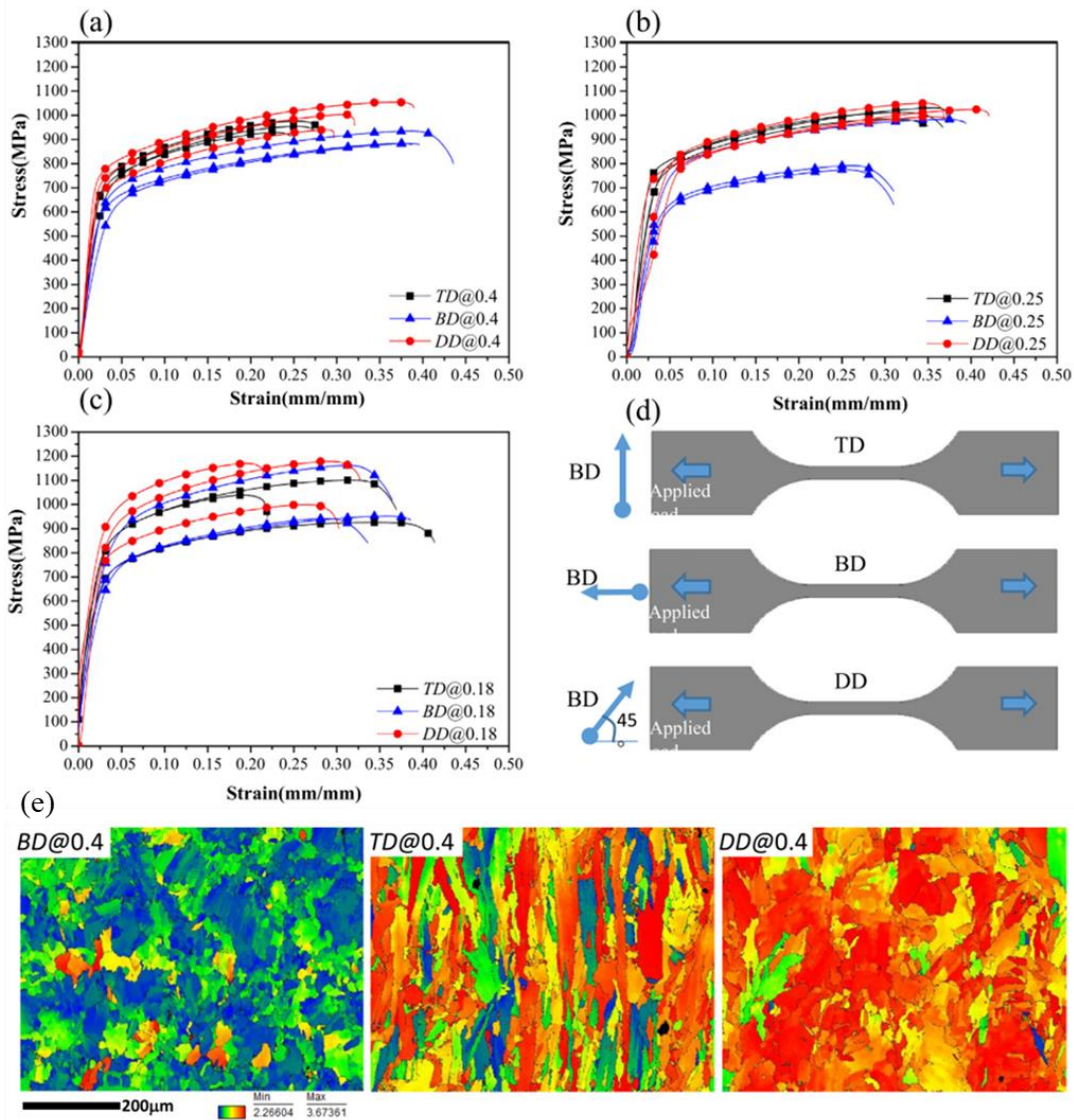


Figure 2.20: Stress-strain curves of the samples at different orientations and energy density (a–c) and (d) the schematic maps of the loading direction and build direction for the tested samples; (e) Taylor factor maps for the corresponding samples[120].

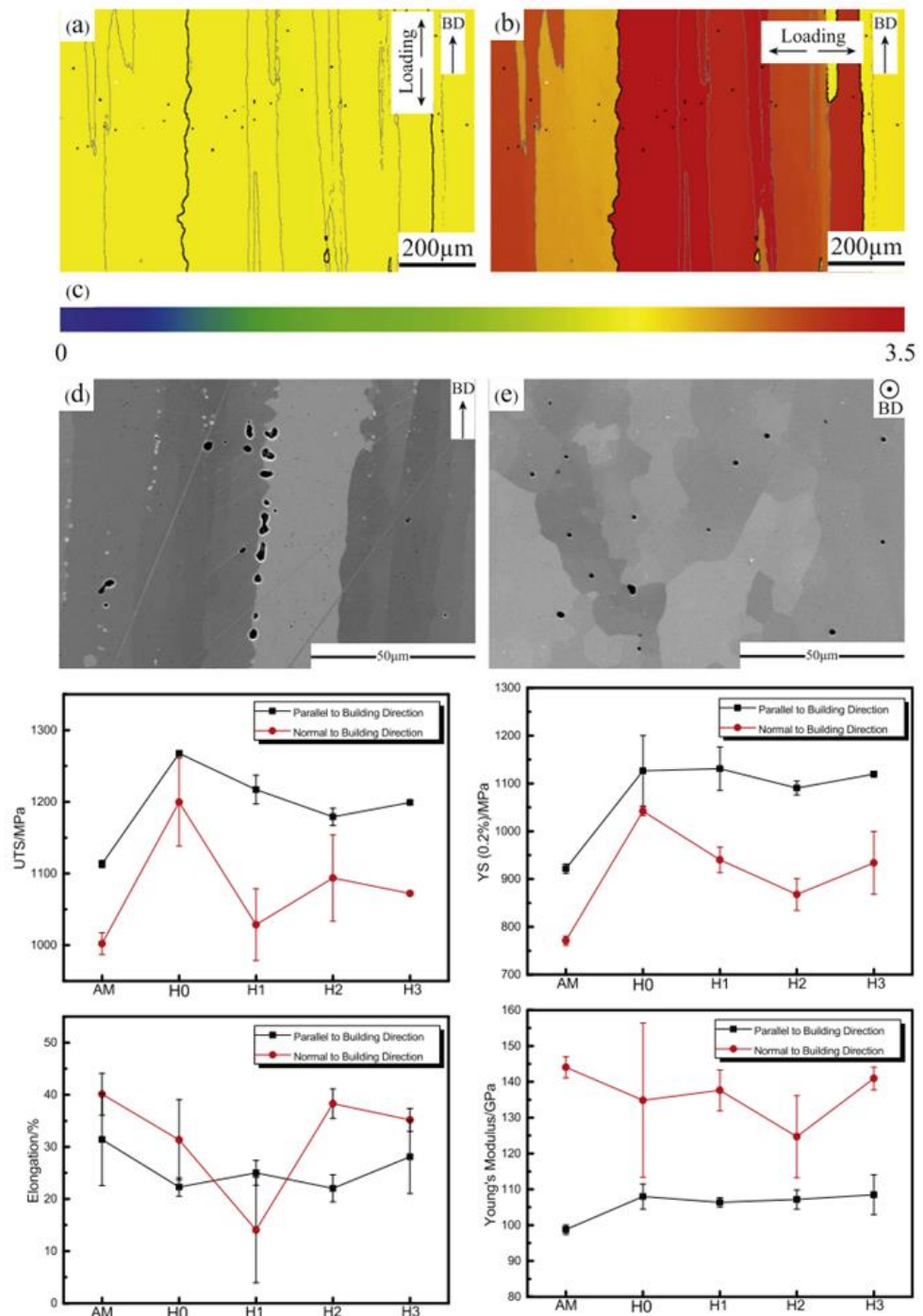


Figure 2.21: Taylor factor maps and Mechanical properties of EBM deposit IN718 tested in different orientations (a),(d) Parallel to build direction; (b), (e) Perpendicular to build direction [116].

2.4.3.3 Fatigue in Laser AM fabricated IN718

Cyclic loading may prompt either elastic or elasto-plastic responses in a material. At low loads, the material behaviour is elastic, and the material will survive a large number of cycles. Failure under this condition is generally categorised as high cycle fatigue (HCF). But at loads near or above the yield stress, the material deforms

plastically, and failure occurs at a substantially lower number of cycles. In this case, the corresponding failure falls under the category of low cycle fatigue (LCF). Damage leading to failure under cyclic loading is characterised by different approaches, e.g. total-life approach and the defect-tolerant approach. In the total-life approach, material resistance under cyclic loading is quantified by characterising total fatigue life in terms of stress or strain amplitudes. The ‘stress-life’ method and the ‘strain-life’ method are the most used methods for fatigue life analysis. The stress-life method relates nominal stresses to local fatigue strengths and does not incorporate the effects of plastic deformation. Therefore, its usage is generally limited to high cycle fatigue regimes. On the other hand, the strain-life approach incorporates plastic deformation in localised regions. As a result, the strain-life approach is more comprehensive, especially for low cycle fatigue life analysis [85,121].

HCF has been established in industrial applications as one of the most common and important failure mechanisms [85,122]. Generally, the crack initiation step dominates the fatigue behaviour in the high cycle regime. On the contrary, low cycle fatigue life is dominated by the crack propagation step [123]. Therefore, a material having higher strength properties would have better high cycle fatigue life. However, a higher strength can typically result in a microstructure being more susceptible to a propagating crack. The highly complex thermal history during laser additive manufacturing leads to significant variation of microscopic details, including grain sizes, distribution of secondary phases etc., that would affect the fatigue performance of the material. Also, the other factors affecting fatigue life are (a) specimen geometry, (b) surface roughness [124], (c) direction of testing with respect to the build direction [125], and (d) residual stresses [126,127]. In contrast to the wrought materials, where the slip-bands and microstructural elements such as the grain boundaries result in crack initiation during cyclic loading, the voids/porosities that occur during laser AM can act as the major crack initiation sites resulting in low fatigue life in AM components, especially for HCF [24,128,129].

Gribbin et al. [130] investigated the effect of SLM-deposited microstructure on the fatigue performance (HCF) of IN718 in various sample orientations. An orientation dependence of fatigue (and tensile) properties was observed. The reason for such orientation dependence was attributed to inherent defects during the deposition process and distribution of the phases. Johnson et al. [131] also observed that fatigue cracks (trans-granular) initiated from the hard phases/particles or the pores at or near the

surface of the component. Amsterdam et al. [132] investigated the high cycle fatigue properties of LENS manufactured IN718. It was observed that the fatigue performance of the IN718 was similar to wrought material, even with the presence of pores within the LBD material. However, samples with larger defects performed much worse (Figure 2.24). Balachandramurthi et al.[133] observed improvement in fatigue life was due to the reduction of porosities that occurred during the deposition process. HIPing was adopted to reduce the porosities. It was also reported that post deposit HT, such as direct aging and solution treatment and aging, improved the fatigue life of IN718 coupons manufactured via SLM and EBM. Similarly, Popovich et al.[134] observed that post deposit solution treatment and aging on laser AM IN718 significantly improved the high-temperature fatigue life. The dissolution of brittle Laves phases and formation of δ phase precipitates, which provided restrictions to grain boundary sliding, post HT improved fatigue life.

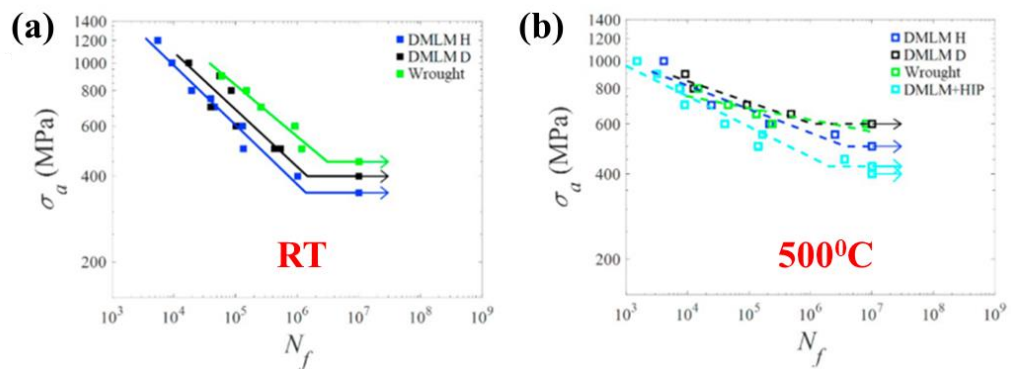


Figure 2.22: High cycle fatigue data for IN718: (a) at room temperature and (b) 500 °C [130].

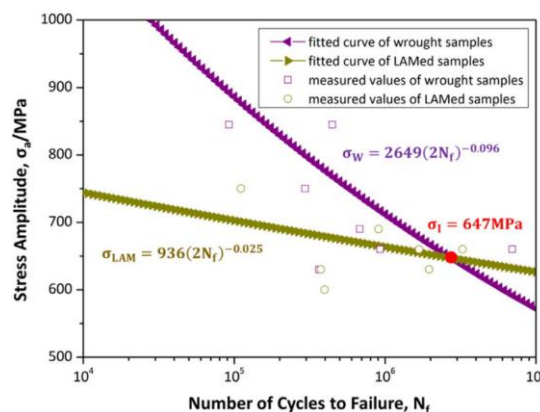


Figure 2.23: High-cycle fatigue properties of AM IN718 and wrought IN718 tested at 650°C and $R = 0.1$ [122].

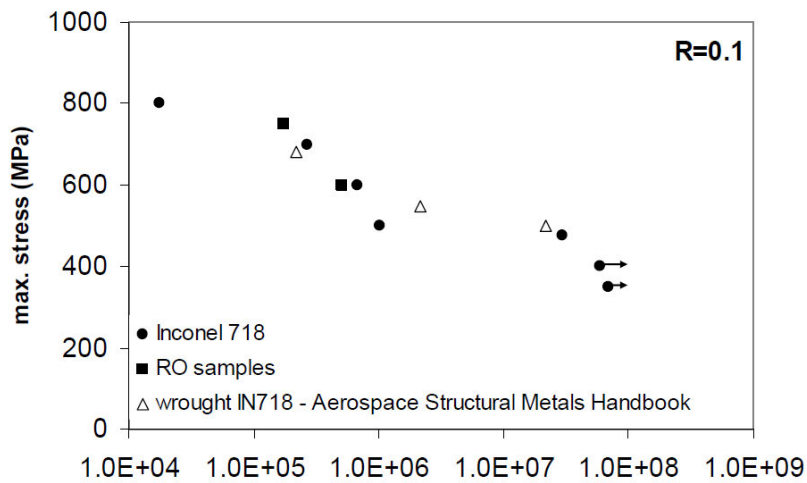


Figure 2.24: S-N curve of the IN 718 samples fabricated with LENS technique tested at $R = 0.1$ [132]

Ardi et al. [127] studied the fatigue performance of laser deposited IN718 in solution treated (at 980°C) and aged condition. They adopted the HIP technique post-deposit to reduce the porosities in the deposit, and the effect of shot peening on the laser deposited IN718 was also investigated. Although porosities were considerably reduced by HIP treatment, but this did not translate to improvements in fatigue performance. This was attributed to the presence of inclusions and yield strength reduction resulting from γ'' solutionisation. Moreover, shot peening induced high compressive residual stresses, but the fatigue performance deteriorated post-shot peening. On the contrary, Karimbaev et al. [124] observed beneficial effects of ultrasonic nanocrystal surface modification (UNSM) treatment at room and high temperatures (RT and HT) on the mechanical properties and fatigue performance of AM IN718. The improvement in fatigue properties was attributed to the introduction of a high compressive residual stress (CRS) and the generation of a nanostructured surface layer. UNSM treatment shifted the crack initiation site into the subsurface from the surface in untreated samples. Shang Sui et al. [122] investigated the high cycle fatigue performance of Laser AM IN718 in a direct aged condition and compared them with the wrought counterparts. Fatigue tests at high temperatures (650°C) revealed that the wrought samples exhibited better fatigue resistance at higher stress amplitudes than the AM IN718 counterparts, which was owed to the presence of the δ phase in wrought samples. However, at lower stress amplitudes, improved fatigue life was observed that was attributed to the Laves phases hindering the crack propagation. It was argued that the Laves phase fragmented at higher stress levels, and microvoids were created in the

Laves-matrix interface, leading to crack initiation and poor fatigue life. Kawagoishi et al. [135] studied fatigue properties of IN718 at room temperature and elevated temperatures. Although uniaxial tension tests exhibited lower strength values at elevated temperatures, greater fatigue strength was observed at low-stress regimes at elevated temperatures than at room temperature. It was found that the oxide film on the material surface resisted crack growth, especially at low stresses, which outweighed the material softening due to thermally activated slip, and as a result, the fatigue life of the material was improved. Similarly, Gribbin et al. [130] observed longer fatigue lives for IN718 tested at 500°C for lower stress amplitudes than the materials at room temperature.

2.4.3.3.1 Fatigue properties of repaired/welded IN718

Ono[136] investigated the effect of microstructural features on the tensile and high cycle fatigue properties of electron beam welded IN718. It was found that high-cycle fatigue cracks predominantly initiated from coarse Nb-enriched carbides and faceted structures that mainly corresponded to the carbides at cryogenic temperatures. At room temperatures, the high-cycle fatigue strength of the welded joint was slightly lower than that of the base metal, similar to their corresponding tensile properties. The cracks occurred in the HAZ region, and no inclusions, such as niobium-enriched MC-type carbides, Laves phases or δ phases, were observed at the fatigue crack initiation site at room temperature. However, the possibility of cracks initiating from Nb-rich grain boundaries, which occurs due to liquation of the NbC present in the base material, was not explored. Sivaprasad [137] studied the HCF performance of IN718 TIG and EB weldments. In a direct aged condition (DA), both TIG and EB weldments exhibited similar fatigue at high-stress levels. However, at lower stress levels, the EB weldment exhibited superior fatigue life compared with the TIG weldment in either DA or STA conditions (Figure 2.25). Failure predominantly happened in the weld zone, and transgranular fatigue crack growth with an irregular crack path was observed. The carbide particles deflected the crack path to a small extent, and failure occurred predominantly through the Laves phase in DA conditions and in the regions around δ and Laves in the STA weldment samples. Subsequently a magnetic arc oscillation and current pulsing technique was adopted by Sivaprasad and Raman [138] to vary the quantity of Laves phase formed during the welding process. The effect of post-weld heat treatment on the fatigue life of the weldments was explored. It was observed that larger amounts of Laves phase resulted in the reduction of life. Moreover, In the

solution treated and aged condition, the δ -needles affected the fatigue life more adversely compared to the Laves phase. It was observed that STA heat treatment had better fatigue performance at low-stress levels; however, at higher stress levels, the DA seemed to perform better than the STA counterparts. Alexopoulos et al. [139] tested TIG-welded IN718 specimens. Compared to the wrought IN718, a higher decrease in fatigue performance was observed at the higher stress regimes compared to lower stress regimes, as shown in Figure 2.26. However, the possible metallurgical reasons responsible for such behaviour were not explored.

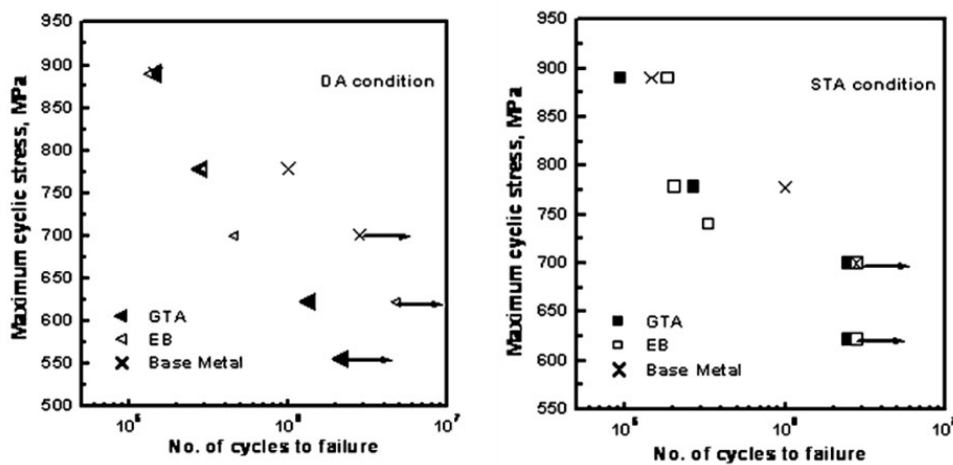


Figure 2.25: S-N curve for GTA/TIG and EB weldments in two post-weld heat-treated conditions: (a) DA and (b) STA[137].

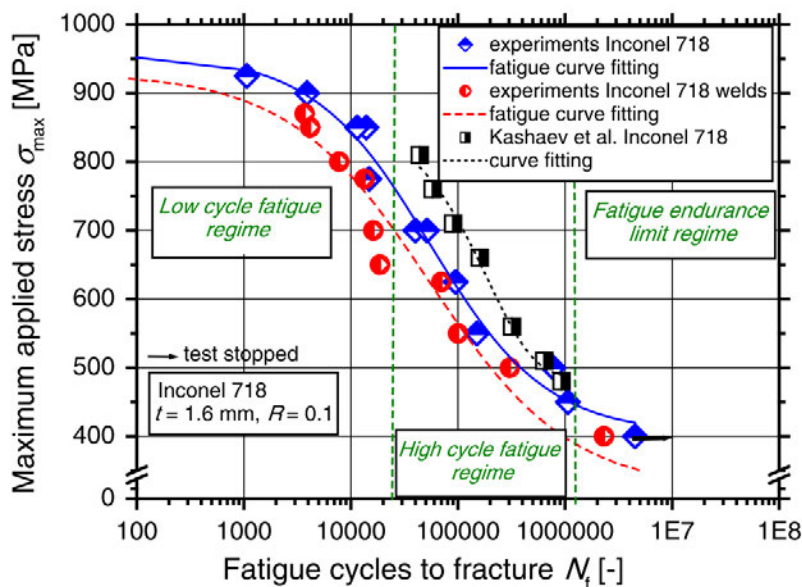


Figure 2.26: S-N curves of reference and TIG welded specimens of IN 718 tested at $R = 0.1$ [139].

2.4.4 Grain refinement of IN718

2.4.4.1 Columnar to equiaxed transformation (CET)

Solidification under varying conditions leads to the following grain morphology: (a) fully columnar, (b) mixed columnar and equiaxed, and (c) full equiaxed. Different morphologies are attributed to the thermal gradient (G) (K/m) and the solidification rate (R) (m/s) during solidification. Process parameters including laser power (P), travel speed (v), substrate temperature, and beam diameter affect the G and R values, resulting in a variation in the grain morphology of the laser deposited sample. Process maps were developed by Gäumann et al. [140] to predict the transition from equiaxed to columnar microstructure based on Hunt's model for columnar and equiaxed growth of dendrites where a lower G/R ratio would result in an equiaxed structure. During the directional solidification in AM, the substrate and the previously deposited layers act as the heat sink for the melt pool. This results in heat flux in the direction opposite to the growth direction. The rate of advance of the isotherms would direct the velocity at which the solid–liquid interface grows. Figure 2.27 shows the solidification microstructure schematic using a combination of G and R . The ratio of G/R dictates the morphology of the resulting microstructure. The product $G \cdot R$ is the cooling rate. As depicted in the schematic in Figure 2.27, a higher cooling rate would result in a finer microstructure and a lower cooling rate results in a coarse solidification microstructure.

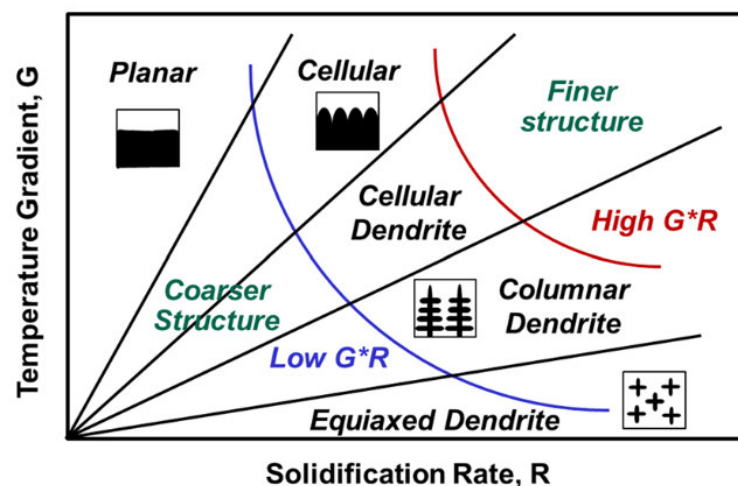


Figure 2.27: The effect of G and R on the solidification microstructure morphology [141].

Another important parameter when discussing the solidification structure is the degree of undercooling (ΔT). The relation between undercooling and dendrite growth

velocity for IN718 is shown in Figure 2.28. A higher undercooling (ΔT) results in a high growth velocity of the solid-liquid interface, thereby increasing R . Thus, higher (ΔT) would result in higher cooling rates ($G \cdot R$) and finer resulting microstructure. However, during laser based additive manufacturing of IN718, the magnitude of the G is often too high to form a full-equiaxed grain structure without any external aid [142,143].

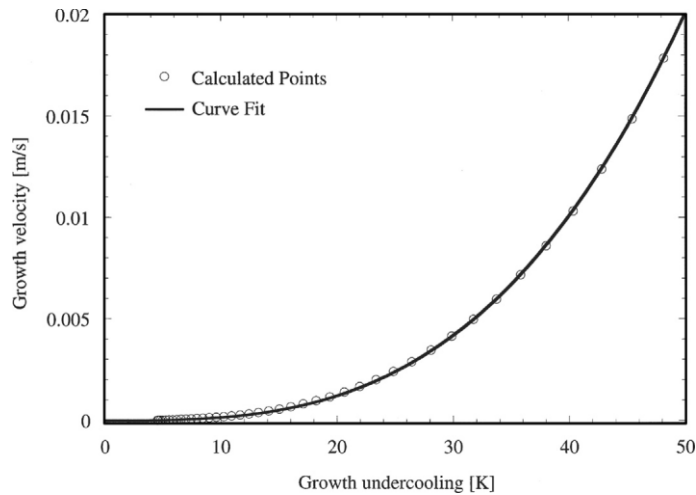


Figure 2.28: Relation between degree of undercooling and growth velocity [22].

As shown previously in Section 2.4.3, the columnar nature of the AM microstructure leads to anisotropy in the manufactured part. An equiaxed microstructure is expected to reduce the anisotropy in the mechanical properties of the fabricated component. In order to produce an equiaxed microstructure, the process parameters would need to be adjusted to find a suitable combination of the thermal gradient (G) and solidification velocity (R) to provide sufficient undercooling for equiaxed grain formation. However, this requires extensive manipulation of parameters. Moreover, the laser AM processes are associated with high thermal gradient, making it very difficult to manipulate the process parameters to achieve a homogenous and equiaxed microstructure. Theoretically, for IN718, columnar to equiaxed transformation is possible by controlling the process parameters. However, in reality, the window to achieve CET while maintaining a high density built is very narrow and generally very difficult to achieve [144]. Based on theoretical models, the effect of pre-existing nuclei on the G/R maps was shown by SS Babu et al. [107] for IN718 parts manufactured via EBM process. It was observed that a greater number of pre-nucleation sites favoured equiaxed grain formation. A high number of nucleation sites can be achieved by: (a) mechanically agitating the melt pool during solidification;

or (b) chemically adding nucleation-promoting inoculants.[145]. Inoculation is considered as a successful melt treatment approach to effectively achieve grain refinement. This refers to adding grain refiners or/and a small number of solute elements to promote heterogeneous nucleation and restrict the grain growth.

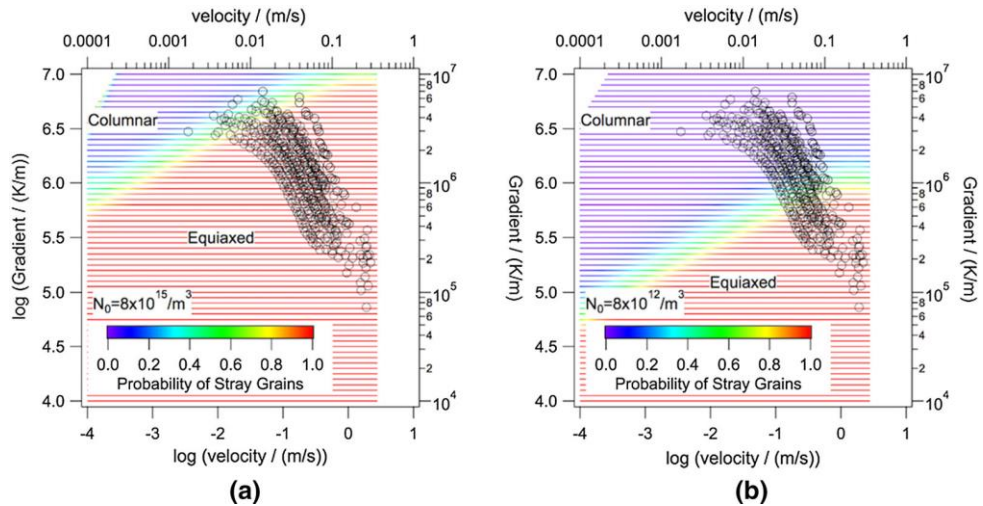


Figure 2.29 Effect of prior nucleation sites in EBM IN718 process (a)high number, (b) low number of pre-existing nuclei [107].

2.4.4.2 Grain refinement of IN718 using inoculants

The method of refinement of grain structure by the addition of inoculants that aids nucleation and hinders grain growth is very effective. According to Murthy et al. [146], a good inoculant should be (a) a stable substance for heterogonous nucleation, i.e. ability to initiate freezing at minimum undercooling; (b) be stable in the melt pool; (c) finely dispersed in the pool; (d) have a similar density to the melt. Metal oxides and Boron has been used as refiners in some superalloys [147]. The former resulted in introducing inclusions that deteriorated the mechanical properties by creating void nucleation sites. On the other hand, Boron was able to refine the grain structure and improve fatigue properties; however, a decrease in primary melting temperature hindered the manufacturing process [148].

2.4.4.2.2 Models used for evaluating the potency of inoculants based on crystallographic matching

The interfacial surface energy and the strain energy play an important role during phase transformation (solid-solid) [149]. Generally, the parent and product phase try to minimise the interfacial energy by forming a coherent or partially coherent interface. This, in turn, increases the lattice energy between these two phases when there is a mismatch (disregistry) between the lattice spacing of these phases. Therefore, the

atoms in both the parent and product phase tend to match, thereby reducing the strain energy as much as possible. The crystallographic models: the “plane-on-plane” matching model [150,151] as well as the “edge-to-edge” matching model [148,152,153] consider that the interfacial energy between the inoculant/substrate and the nucleating solid is critical to the potency of a substrate. To achieve low interfacial energy, the two solids must be coherent or partially coherent, which leads to a certain orientation relationship (OR) between these two phases. In a coherent or partially coherent interface, strain energy is present if there is no exact matching between the substrate and the solid. To minimize this strain energy, it requires maximum atom matching on the interface.

The Edge-to-Edge Matching Model (E2EM)

The edge-to-edge matching model is based on the matching of rows of atoms across the interface of the parent phase and the nucleating phase. It can predict the Orientation Relation (ORs) and, therefore, can be directly applied to new and existing alloy systems for grain refinement. The E2EM has been applied successfully to various Al and Mg systems by Zhang et al. [149,153] and Wang et al. [148] on superalloys and subsequently is validated by experimental data suggesting significant grain size reduction. This model is governed by minimization of the strain energy of the interface (fully or partially coherent) and considers both the morphology and the ORs between the parent and nucleating/ product phase. The necessary conditions for minimization of the interfacial energy are the matching of rows of atoms in the two phases and the additional requirement that these matching or coincident atom rows consist of directions in the two crystals that are close-packed or nearly close-packed. The probability of achieving atom row matching in consecutive atom rows across an interface is maximized if planes that contain the atom rows in the two phases and have the same (or very similar) inter- planar spacing are arranged to meet edge-to-edge in the interfaces.

2.4.4.3 Grain refinement in AM products using inoculants

Various grain refinement methods of IN718 using chemical methods (inoculants) have been mostly limited to cast and wrought products. Ho et al. [154] studied microstructure evolution in SLM fabricated IN718 by WC-W₂C eutectic powders were used as inoculants. The motivation was to enhance the hardness and wear properties. However, the size of the inoculants used was almost similar to that of the IN718 powders (d₅₀ ~ 50 μm). These inoculants can act as inclusions, promoting

crack formation. Grain refinement was not observed in the IN718 matrix. The resulting mechanical properties after inoculant addition was not reported.

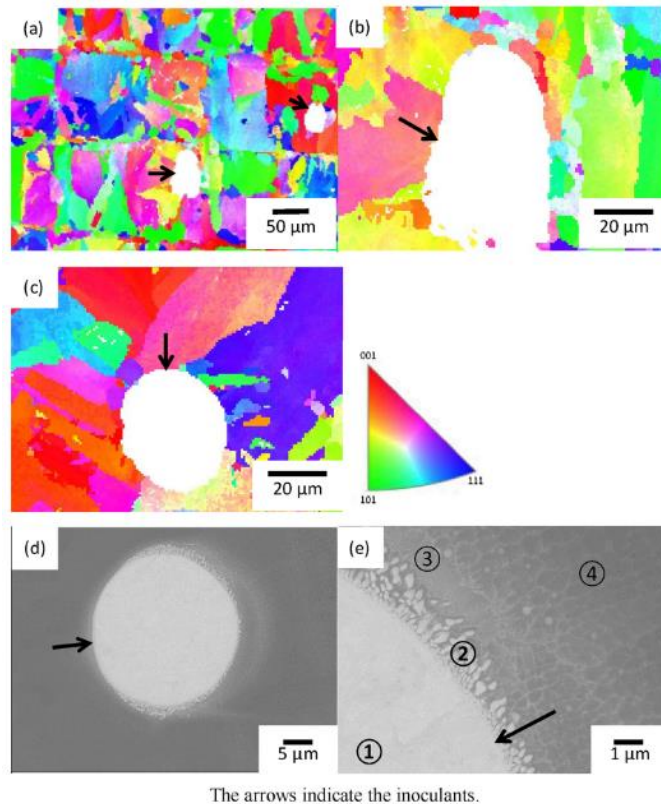


Figure 2.30: As-built IN718+inoculants along the transverse direction [154].

Martin et al. [155] used nanoparticles to create nucleation sites in SLM-produced high-strength Aluminium alloys. Nano-sized inoculants were electrostatically assembled on the alloy powders, and a fine fully equiaxed microstructure with significantly high strength properties was achieved. Nanocomposites using AM manufacturing processes are abundant in the literature. Most used alloy systems for such nanocomposites are Steels [156–158], Aluminium [159,160], Titanium [161], and Ni-based superalloys [162–167]. The general motivation for using inoculant has been tailoring the machinal properties, and in some studies, microstructure modification was achieved. AlMangour et al. processed SLM-produced TiB_2 / 316L stainless steel composites [156–158]; They found a significant change in the microstructure morphology after the addition of $\geq 5\text{vol}\%$ of TiB_2 ; the columnar grains were broken down to very fine equiaxed grains. Xi et al. [160] used TiB_2 to induce grain refinement (columnar to equiaxed transformation) in SLM-produced Al-12Si alloy. A 2wt% TiB_2 addition could refine the columnar as-deposited microstructure to fine equiaxed

isotropic microstructure. Also, TiB_2 addition had beneficial effects on the strength properties of the composite.

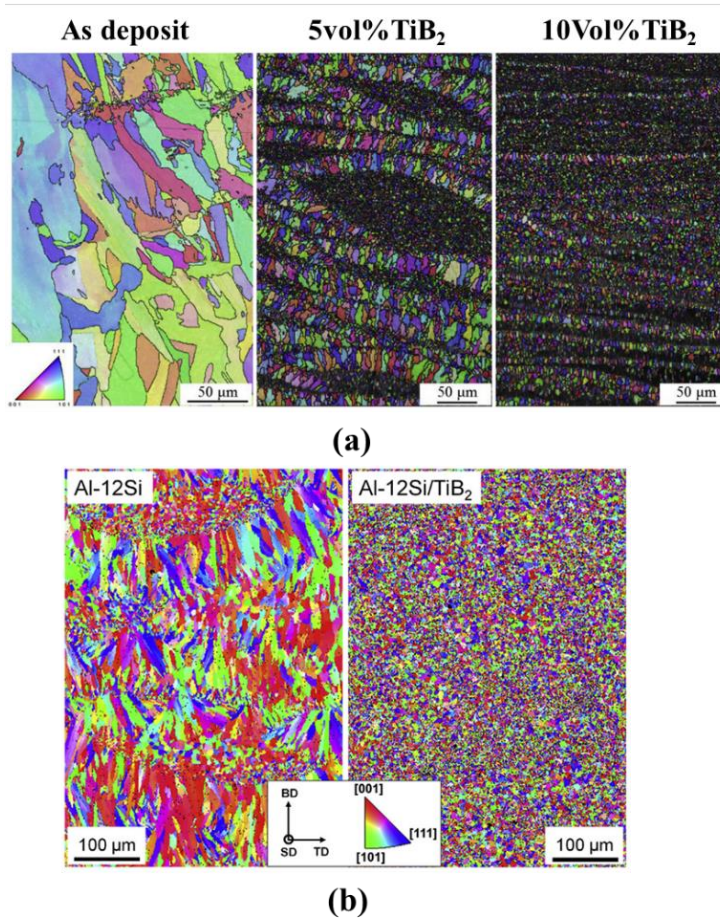


Figure 2.31: Grain refinement due to inoculant addition: (a) 316L/TiB₂[156]; (b) Al-12Si/TiB₂ [160].

TiC was used by Jia et al. [162] and Gu et al. [165] to improve strength and wear performances in SLM fabricated IN718. The addition of inoculant generally improves the strength properties in the resulting composites, in some cases at the cost of ductility properties[168]. Densification problems generally arise with inoculant usage if the processing parameters, i.e. energy density, are insufficient. A low energy density would result in interlayer defects [157,165], and too high an energy density might dissolve the inoculants completely and not yield desired results.

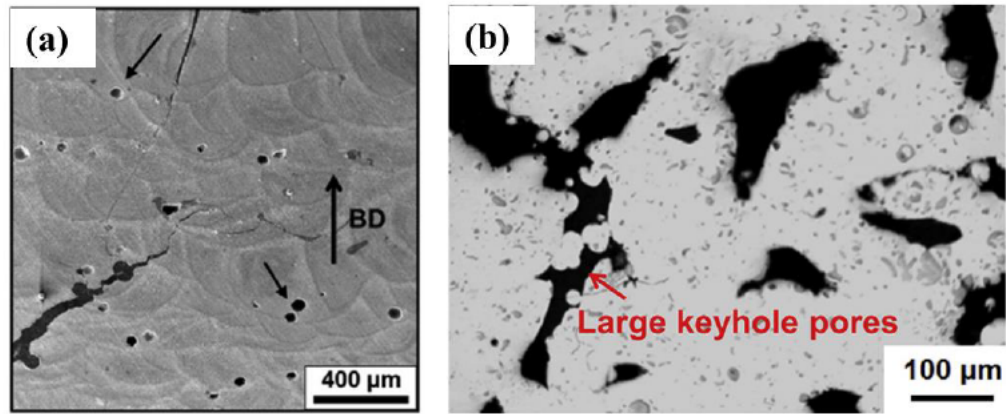


Figure 2.32: Defects in prints with inoculant addition due to insufficient energy densities: (a) 316L/TiB₂; (b) IN718/TiC.

The selection of these inoculants/ secondary particles in the aforementioned studies was generally random and aimed at increasing the strength of the resulting composites. However, the selected reinforcing secondary particles/inoculant can act as effective grain refiners if there is a crystallographic agreement between the inoculant and the matrix phase. An even distribution of inoculants is needed to create nucleation sites uniformly throughout the deposit. The addition of inoculants is aimed at processing fully dense deposits and transforming the columnar microstructures often associated with DED processes into an equiaxed microstructure and achieving isotropic properties. Ho et al. [169] used CoAl₂O₄ inoculants to refine the as-deposit microstructure in SLM produced IN718. They observed that the CoAl₂O₄ particles formed a dispersion of Al-rich nano-oxide particles in the matrix, resulting in the formation of equiaxed grains with improved creep properties. The degree of crystallographic texture and anisotropy was reduced, albeit the degree of grain refinement was limited. A summary of the literature review that uses various reinforcement or refiners in standard alloy systems using additive technologies is shown in Table 2.6.

Table 2.6: Various reinforcement particles/ refiners used in different alloy systems manufactured using AM route

Sl no	AM Route	Base Alloy	Reinforcement/ inoculant	Powder preparation	Remarks
1[154]	SLM	IN718	WC	Rolling ball mill without ball	Grain refinement did not occur; W rich zones around the inoculants

					were observed post-heat treatment;
2[165]	SLM	IN718	TiC	Ball mill 5:1 ball: powder; 4 hr; 200RPM	Grain refinement was not reported, and wear and hardness improved
3[169]	SLM	IN718	CoAl ₂ O ₄	Roller mill operated at 130 rpm for 1 h	Dispersion of Al-rich nano-oxide particles leads to grain refinement, degree of refinement not significant; improvement in creep rupture life noted.
4[167]	SLM	IN625	TiB ₂	Ball mill 5:1 ball: powder; 12 hr; 250RPM	No grain refinement was noted, and improvement in tensile properties, hardness, and surface wear resistance was noted.
5[168]	SLM	HEA	TiN	Ball mill 6:1 ball: powder; 1.5 hr; 150RPM	Very low ductility; high strength, and grain refinement occurred
6[161]	SLM	Ti	TiC	Ball mill 5:1 ball: powder; 4 hr; 200RPM	insufficient densification and disappearance of nanostructured TiC reinforcement at a high TiC content above 17.5 wt.% decreased the hardness and wear performance
7[156–158,161]	SLM	SS316L	TiB ₂	Ball mill 5:1 ball: powder; 4 hr; 200RPM	TiB ₂ is a highly potent refiner; a significant increase in strength and wear resistance
8[170]	SLM	SS316L	Al ₂ O ₃	Roller mixer for about 4 h	Significant strength increases at the cost of ductility
9[144]	SLM	Al-Mg(-Sc)-Zr	Al ₃ Sc	In-situ precipitation	Grain refinement occurred, and homogenous equiaxed microstructures
10[155]	SLM	Al alloy 6000, 7000 series	Zr Nanoparticle	Powders are electrostatically assembled	Nanoparticle compositions selected using a matching crystallographic lattice;

					fine equiaxed microstructure
11[171]	WAA M	Ti-6Al- 4V	ZrN, TiN	Inoculant premixed with a polyurethane adhesive before being applied as a thin coating to the top of each deposited layer	TiN is a better refiner than ZrN due to better crystallographic matching and better survivability in the melt

Various grain refinement methods of IN718 using chemical methods (inoculants) have been limited to cast and wrought products. For AM, the existing literature shows that the secondary reinforcement particles or inoculants used in AM IN718 are successful in strengthening and improving the wear properties of the composites formed. However, grain size refinement is generally not noted. Additionally, the rationale for the selection of a particular reinforcing particle is not discussed. For DED processes, the use of refiners is virtually absent. An even distribution of inoculants is needed to create nucleation sites uniformly throughout the deposit. The addition of inoculants is aimed at achieving a homogenised equiaxed microstructure with isotropic mechanical properties, although its usage for laser additive manufacturing is very limited in the literature. Identification of suitable inoculants and mixing of inoculants with the feedstock powder to be fed in for the DED process offers the biggest challenge for using inoculants in DED processes. However, using inoculants offers an attractive solution to transform the columnar microstructures to isotropic equiaxed microstructure and deserves further investigation.

2.5 Summary, gaps and research questions

Laser additive manufacturing has emerged as a subject of considerable attention in the past decades. IN718 has been studied quite extensively for building components using various AM techniques. Additive manufacturing (AM) processes have also found usage as repairing techniques for restoring both geometrical and mechanical properties of the damaged components. AM techniques as repair techniques provide many advantages over traditional techniques such as welding or brazing, as discussed in previous section 2.2. Laser AM techniques, especially powder blown techniques such as DED, possess immense potential for application as a repair technique. However, the

use of DED techniques as repair techniques is mostly limited to surface repairs/modifications and coating, as reported in the literature.

To use laser AM technologies for repair purposes, a set of process parameters that allows a dense deposit with minimum defects is essential. Studies on bulk AM deposit IN718 indicate that several process parameters such as power, scan speed and scanning pattern affect the microstructure and the mechanical properties of the deposit. The combination of the process parameters is often expressed as energy density which is the measure of the heat input during an AM deposition process. However, using energy density as a design parameter can be questioned as multiple process parameter combinations can yield the same energy density. Therefore, understanding the process parameters becomes an essential prerequisite for using AM techniques for repair. The limited reports for large repairs lack in-depth metallurgical characterisation, including microstructure evolution, Laves phase distribution and the dendritic arm spacing in the repaired part due to different groove angles and scanning patterns. Moreover, along with the weld zone, the heat-affected zone (HAZ) in a repair is of utmost significance as failures have been reported to occur from the HAZ and weld zone welds. However, for repairs using AM techniques, microstructural characterisation and mechanical properties investigations of the entire repaired composite – including the deposit zone, the substrate and the deposit – substrate interface are limited in the literature.

High-cycle fatigue (HCF) has been established as one of the most common and important failure mechanisms in industrial applications. Fatigue studies on wrought and bulk AM Inconel 718 are well explored in the literature. Fatigue properties for AM IN718 components are found to be unpredictable due to heterogeneous microstructure and non-uniform distribution of the secondary phases such as Laves phase and δ phase. The fatigue properties of repaired IN718 are mostly restricted to welding, and fatigue properties of IN718 components repaired by AM techniques are virtually absent in the literature. Therefore, it would be necessary to study the fatigue properties of IN718 repaired using AM techniques, co-relating the fatigue properties to the repaired microstructure and comprehensively understanding the failure mechanism. An AM repaired component would possess a non-uniform microstructure with several phases such as the Laves phase, metal carbides (MC) in the deposit and coarse equiaxial grain boundaries with NbC liquified along the coarse substrate GB. The effect of these phases on crack initiation and propagation during cyclic loading, especially near the repaired joints, requires further exploration.

The high thermal gradient associated with the laser AM processes makes achieving a homogenous and equiaxed microstructure difficult. A typical laser-based AM microstructure is characterised by columnar dendrites that grow epitaxially opposite to the heat flow direction, often resulting in a microstructure with a preferred {100} texture along the build direction. Moreover, the high cooling rates often restrict the formation of strengthening precipitates and favour the formation of non-equilibrium phases that may adversely affect the properties of the repaired/built part. Post deposition heat treatments are often employed to dissolve the high Nb-content Laves phases, thus allowing the strengthening precipitates to form. However, a homogenous and equiaxed structure is still difficult to achieve. The G/R maps provide a theoretical solution to control the microstructure in a Laser AM technique, although the operating window to achieve homogenous equiaxed microstructure might be too narrow. The directional nature of the microstructure and texture results in anisotropy in the mechanical properties. Inoculant addition offers an attractive solution for refining the as-deposit microstructure and columnar to equiaxed transformation. There are several different grain refiners or reinforcing particles used in additive processes, as summarized in Table 2.6. For IN718-based composites manufactured by DED techniques, improvements in mechanical properties such as hardness, strength and wear performances are often noted; however, grain refinement is limited, making it an important research area that deserves detailed investigation.

These observations led to the following research questions to be addressed in this project. Also, the underlying objectives involved in each of these research questions are discussed.

1. What is the effect of repair geometry and post deposit heat treatment on the deformation behaviour of IN718 superalloy components repaired with direct energy deposition?

- Study the effect of linear energy density (process parameters) on the microstructure of the deposit to find a suitable set of parameters for repair in terms of the degree of densification, grain size, aspect ratio, distribution of Laves phase, and mechanical properties (in the form of hardness tests).
- Study the effect of varying deposition path and repair geometry (various groove angles and sizes) on the properties of the repaired part focussing on microstructure and hardness of the as-deposit section, HAZ and substrate.

- Study the deformation behaviour of the repaired component tested under 4-point bend test.
- 2. What is the effect of post-deposit heat treatments on the high cycle fatigue properties of Laser DED, the repaired component?**
- Investigate the HCF properties in DED repaired IN718 at room temperature under the following heat-treated conditions:
 - Direct aged (DA)
 - Solution treated at 980°C and aged (STA).
 - Study the micro-mechanism of fatigue failure in the repaired components using interrupted tests and correlate the cyclic deformation mechanism and repaired microstructure.
- 3. What is the effect of inoculant additions in grain refinement, texture evolution, and mechanical properties of IN718 manufactured using the laser DED technique?**
- Investigate crystallographic models to select inoculants to be introduced with IN718.
 - Study the effect of energy densities and inoculant loading on the resulting microstructure and texture.
 - Study the mechanical properties of the resulting composite in the form of hardness and tensile tests.

CHAPTER 3**Experimental Methods**

This chapter outlines the experimental procedures used in the current work. A detailed description of the materials, general manufacturing process, heat-treatment, various mechanical testing procedures, phase evaluation and microstructural evaluation techniques are provided. In addition, the microstructure and texture characterisation methods, such as optical microscopy, scanning electron microscopy (SEM), including electron backscattered diffraction (EBSD), and X-ray diffraction (XRD), are described.

3.1 Material and Methods

Wrought Inconel 718 plates with 21 mm thickness were used as substrates for the depositions. The thickness of the substrates was kept constant for all the depositions. For all the DED processing, Plasma Atomised (PA) Inconel powders were acquired from AP&C pvt. Limited (GE additive). The powders used for the deposits had a size range varying from 45 μm – 140 μm . Figure 3.1 (a) shows the SEM image of the spherical feedstock IN718 powders. The plasma atomised powders are spherical without any significant defects or porosities. The size distribution of the feedstock IN718 is shown in Figure 3.1 (b). The cumulative distribution shows that $d_{50} \sim 80 \mu\text{m}$ and $d_{90} \sim 105 \mu\text{m}$, i.e., 50% of the powders are smaller than 80 μm , and 90% are smaller than 105 μm . Similar powder distribution is typical for powder blown type DED additive manufacturing processes [2,9,10] and powder bed based additive processes such as electron beam melting (EBM) [11]. Other powder bed based additive processes such as SLM used finer powders in the range $\sim 10 \mu\text{m}$ – 50 μm [12,13]. Figure 3.2 (a) and Figure 3.2 (b) display an SEM micrograph and EBSD map showing the substrate microstructure. The wrought substrate was received in an annealed and aged condition with an average hardness of $H_v 410 \pm 20$. The wrought substrate exhibited a high fraction ($\sim 42\%$) of $\Sigma 3$ twin boundaries, as shown in Figure 3.2 (d). Figure 3.2 (c) shows the corresponding XRD pattern of the substrate material. The XRD pattern reveals peaks corresponding to the typical γ FCC matrix. It is known that the XRD peaks of the γ'' precipitate and γ matrix overlap in (200) and (220) planes [13,34,172]; however, the γ'' , γ' precipitates are expected in the matrix of the wrought substrate as a result of precipitation during the ageing heat-treatment.

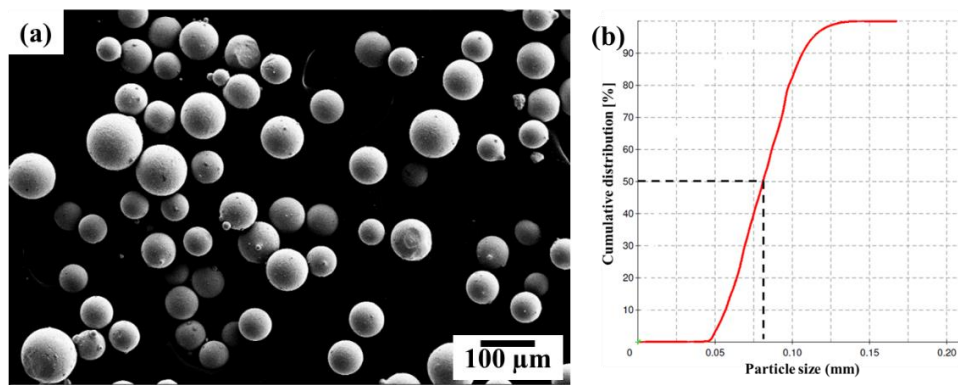


Figure 3.1: (a) SEM image of the GA Inconel 718 Powders (b) powder size distribution.

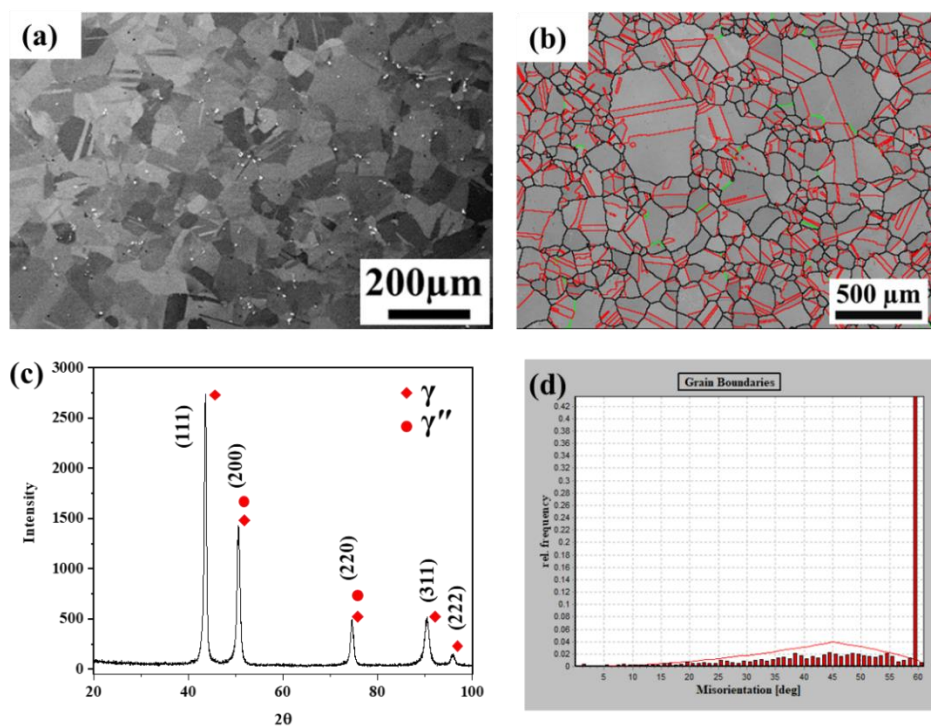


Figure 3.2: (a) SEM micrograph showing substrate microstructure; (b) EBSD map showing high angle (black) and low angle (green) grain boundaries and $\Sigma 3$ twin boundaries (red), (c) XRD patterns and (d) the relative frequency of the misorientation distribution of the as-received IN718 plates.

3.2 Direct Energy Deposition (Optomec LENS MR-7)

LENS or laser Engineered net shaping is one of the most used additive manufacturing processes. The Optomec LENS MR-7 apparatus utilised in this work has an enclosed fabrication chamber with 4 powder feeders. It is equipped with a 1kW IPG fibre laser with a coaxial powder delivery system. Argon was used as a shielding gas and carrier gas for all the deposits with a flow rate of 15 l/min and 6 l/min,

respectively. The oxygen level was kept below 3 ppm for all the deposits. The present study is concerned with bulk deposits and large section repairs. Hence, all the deposits had multiple tracks and layers. Laser power P (W) and scanning speed v ($\text{mm}\cdot\text{s}^{-1}$) were the main process parameters that were varied. The parameters used for the deposits are detailed in the subsequent chapters Chapter 4 – Chapter 6. Six layered deposits for each parameter set were performed initially to determine the hatch distance and layer thickness for the corresponding combination of laser power and scan speed. After every deposit, the substrate was allowed to cool down for 10-15 minutes prior to the next deposit.

3.3 Heat treatment

All heat treatments were performed in a muffle furnace under an Argon atmosphere capable of reaching a maximum temperature of 1600°C . For the DED repaired plates, two post-deposit heat treatments were performed:

- (1) Direct ageing (DA): Heating to 720°C and holding for 8 hrs, subsequently furnace cooling at $55^{\circ}\text{C}/\text{hr}$ to 620°C and holding for 8 hrs, followed by air cooling to ambient.
- (2) Solution treatment and ageing (STA): Solution treatment was performed at 980°C for 1 hr, followed by water quenching. The solution treatment was followed by ageing treatment, and the ageing treatment was identical to the DA treatment.

The corresponding heat treatment schedules for DA and STA are depicted in Figure 3.3 (a) and Figure 3.3 (b), respectively.

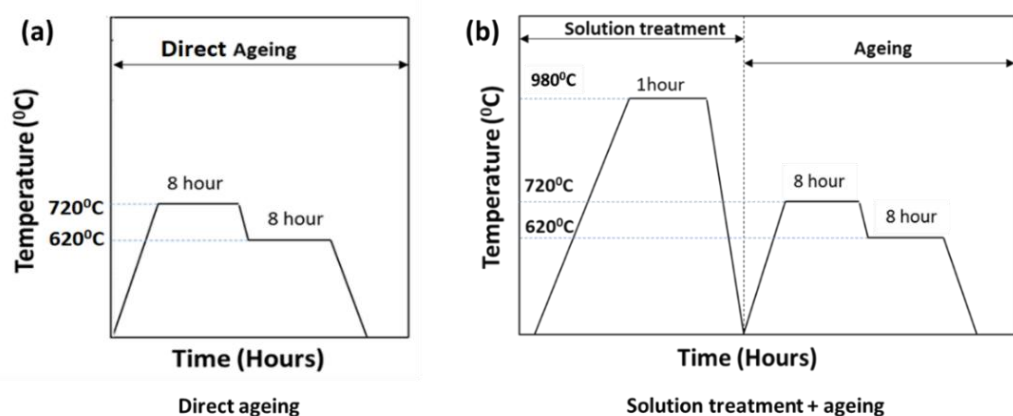


Figure 3.3: Heat treatment schedule for repairs (a) Direct ageing (DA); (b) Solution treatment and ageing (STA).

Previous work on selective laser melted (SLM) IN718 showed that solution treatment at 1100°C caused significant grain growth, despite a complete dissolution of Laves

phase [14]. Thus, the solution treatment temperature in the present work was chosen to be 980 °C. In addition, both the STA and DA heat treatment parameters conform with those adopted for the cast and wrought IN718 [14,93,104].

3.4 Method of inoculant identification using Edge-to-Edge Model (E2EM)

3.4.1 Identification of matching direction

If it is assumed that phase-A is the matrix and phase-B is the nucleating phase, based on the E2E model assumptions, the prediction of the orientation relation (OR) between the phases A and B from the model can be ascertained.

With knowledge of the crystal structure of the phases A and B (e.g., by using XRD), the atom positions in both the phases are identified. Unlike the “plane-to-plane” model, where the lattice positions are considered, the E2EM considers the atom positions in A and B phases. The atomic density (linear) identifies the closed-packed directions in which the misfit calculations are performed. Thereafter, the interatomic misfit is calculated between the phases A and B using the following equation 3.1:

$$\% \Delta_a = \left(\frac{\rho_A - \rho_B}{\rho_A} * 100 \right) \quad [3.1]$$

Where, $\% \Delta_a$ is the atomic mismatch percentage; ρ_A is the interatomic distance in a closed-packed direction on phase A; ρ_B is the interatomic distance in a closed-packed direction in phase B. Zhang et al. [149] identified a interatomic mismatch value of less than 10% is necessary for an OR to exist between the phases A and B.

3.4.2 Identification of matching planes

To identify the matching planes, first, the closed-packed or nearly closed-packed planes in phases A and B are identified. These planes must contain the matching directions as identified in the previous step. These planes are termed as the matching planes. According to X-ray diffraction theory, the closed-packed plane normally corresponds to the plane with the highest structure factor [149]. Hence, this analysis stage involves calculating the structure factors of each plane of the phases. The planes with the highest diffraction intensity are the closed-packed or nearly closed-packed planes. The second step is to examine the d-values mismatch between the matching planes using the following equation 3.2,

$$\% \Delta_P = \left(\frac{d_A - d_B}{d_A} * 100 \right) \quad [3.2]$$

Where, $\% \Delta_p$ is the interplanar mismatch percentage; d_A is the interplanar distance in a closed-packed direction on phase A; d_B is the interplanar distance in a closed-packed direction on phase B. According to the model, the matching planes between phases A and B should have similar d-values. It has been observed that the probability of forming an OR is highly likely when the d-value mismatch along the matching direction is less than 10%. The lower the mismatch higher is the probability. It is important to note that the matching planes must contain matching directions. The matching direction, together with the matching plane pair, defines an approximate OR.

In the existing literature, CrFeNb has been identified as an efficient inoculant for a refining grain size of cast IN718 [148,173,174]. From crystallographic models, it has been identified that CrFeNb has three distinct matching crystal planes with low degree of disregistry with the matrix lattice. However, the low melting point of CrFeNb makes it unsuitable for DED-type AM processes, where temperatures $>3000^\circ\text{C}$ can be reached. Therefore, ceramic compounds with high melting temperatures were considered for grain refinement. Using the E2E model, TiB_2 was chosen as an effective inoculant to induce heterogeneous nucleating sites for grain columnar to equiaxed transition in the microstructure. The details of the calculation based on the E2E model for TiB_2 are reported in detail in Chapter 6. Other ceramic materials considered for calculation using E2E model include TiC , ZrC and WC . The corresponding mismatch calculations are reported in Appendix 2.

3.5 IN718/Inoculant powder preparation using ball milling

Low energy ball milling was utilised to mix inoculant powder with the feedstock IN718 powders. A custom “vertical ball mill”, as shown in Figure 3.4, was used for the mixing process. Low energy ball milling was applied as it was necessary to ensure that the inoculant powders were decorated on the feedstock powders without compromising the sphericity of the feedstock powder. Vertical ball milling was performed using 25 mm hardened steel balls for 6 hours at a fixed RPM of 200. To avoid oxidation of the powders, the ball mill jars were filled with Argon gas prior to the ball mill process. After ball milling, the powders were dried in a vacuum oven at 150°C for 1.5 hours.

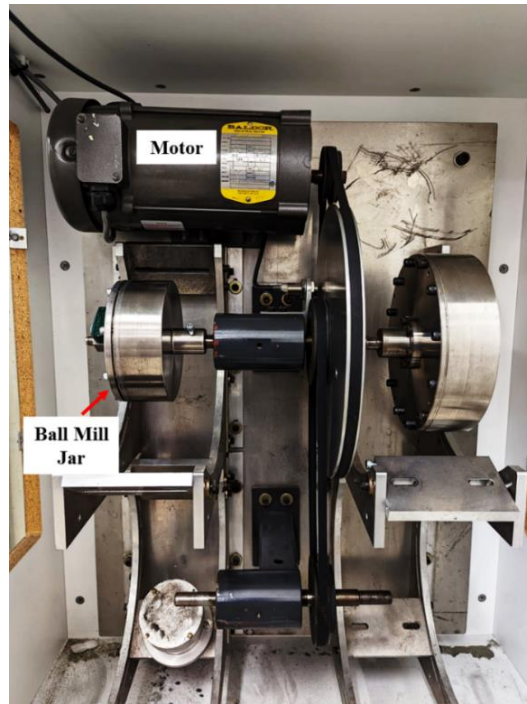


Figure 3.4: Ball Mill setup.

3.6 Microstructural characterisation techniques

Standard metallographic sample preparation was performed on the DED manufactured/repaired IN718 samples before analysing through X-Ray Diffraction (XRD), Scanning Electron Microscopy (SEM) and Electron Backscatter Diffraction (EBSD).

3.6.1 Metallographic preparation

Small specimens were machined from the additive manufactured components (cubes), and the repaired composites in as-deposit, and post-heat treated conditions using Struers Accutom-100 cutting machine. The cut samples were mounted using conductive poly-fast powders and polished using standard polishing and grinding methods; grinding using SiC abrasive paper from 80 to 1200 grit, followed by polishing with dispersions of 9, 6, 3 and 1 μm diamond suspension, and a final OPS polish prior to imaging. Samples were ultrasonically cleaned with ethanol for 5 min after each polishing stage.

3.6.2 Microstructure analysis

3.6.2.1 SEM – imaging

A Field Emission Scanning Electron Microscope (FESEM) SUPRA 55-VP (Zeiss) was used for microstructural analysis characterisation of the DED IN718 and powder

samples. The powders samples were characterised using the Secondary Electron (SE2) imaging. For the bulk samples, SEM is performed using a 60 μm aperture and an operating voltage of 20kV in high current mode. An angular selective backscattered (SEM-AsB) detection system, which enables the collection of low-angle backscattered electrons coming from different scattering processes, was used for the bulk samples. The Supra V55 was equipped with an Oxford X-Max 20 SDD Energy Dispersive X-ray (EDX) detector from Oxford Instruments, which was used for local qualitative and quantitative chemical analysis of the phases present in the samples. Elemental Mapping was performed for qualitative analysis, and the composition of selected regions of the microstructure was quantified using point analysis.

3.6.2.2 SEM – Electron Backscattered Diffraction (EBSD) analysis

EBSD analysis was carried out on a Zeiss LEO 1530 or SUPRA 55-VP SEM operated at 20 kV in the high current mode using a working distance ranging from 12 to 16 mm. The samples were tilted 70° with respect to the electron beam. Both the microscopes were equipped with an EBSD detector that collects and analyse the diffraction patterns. In an automated EBSD system, typical Kikuchi bands of the electron backscatter diffraction pattern (EBSP) are captured and then viewed with a fluorescent phosphor screen and a sensitive charge-coupled device (CCD) camera, respectively.

The EBSD acquisition software (Aztec 5.0) was used to control the data acquisition, solve the diffraction patterns, and store the data. Aztec Crystal and Channel 5 HKL software were used to analyse, manipulate, and display the data. The step size for the EBSD maps was selected based on the size of the features under investigation and the type of maps. The advantage of EBSD is that there is no ambiguity about the grain boundaries since they are measured in terms of crystallographic data. A step size of 2.5 μm – 5 μm was used to study grain size and texture analysis, also detailed in the subsequent Chapters 4 – Chapter 6. For grain size and texture analysis, the noise in the EBSD data was reduced by using the standard noise reduction filter in HKL and Aztec software, which allows the removal of zero solutions (EBSPs that could not be indexed) and isolated points that have been incorrectly indexed and appear as wild spikes. Following the removal of wild spikes and zero solutions, a ‘Kuwahara filter’ with a smoothing angle of 5° and size of 3 × 3 is used to reduce the noise further. For grain boundary analysis, the High Angle Grain Boundaries (HAGB) were identified with misorientation > 10° and Low Angle Grain Boundaries (LAGB) > 2° misorientation. The $\sum 3$ <110> Twin boundaries were

identified with misorientation of $60^{\circ} \pm 5^{\circ}$. During grain reconstruction, the $60^{\circ} \langle 111 \rangle$ twin boundary was ignored in the calculation, as the twin boundaries are not real grain boundaries. Moreover, the grains with an area of fewer than 10 pixels were not used for the analysis according to ISO standard. The HKL software used circle equivalent diameter from the EBSD data to generate the grain size measurements, as shown in Figure 3.5 (a). Subsequently, the aspect ratio was calculated from the ratio of the major and minor axis of the fitted ellipse Figure 3.5 (b).

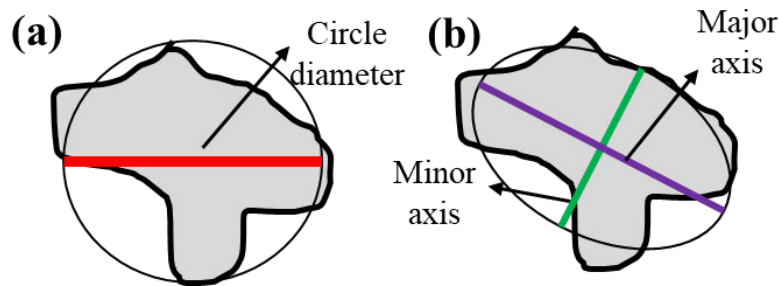


Figure 3.5: Grain reconstruction from EBSD data (a) grain size calculation using equivalent circle diameter; (b) aspect ratio calculation.

3.6.2.3 X-ray Diffraction

In order to determine the phases present in the samples, X-ray diffraction (XRD) studies were performed. d_{hkl} was calculated from the Bragg's equation at each 2θ peak position of the sample. For cubic crystal structure, the inter-planer spacing (d) is related to lattice parameter (a) as,

$$d_{hkl} = a / \sqrt{h^2 + k^2 + l^2} \quad [3.3]$$

$$n\lambda = 2d \sin\theta \quad [3.4]$$

For all the phases, the lattice parameter was calculated from the respective interplanar spacing and hkl values. An X'Pert Pro MRD XL X-ray spectrometer from PANalytical was used for this purpose. The XRD tests were conducted using a monochromatic radiation Cu K α ($\lambda = 1.54\text{\AA}$), applied at a voltage of 40kV and a 30 mA current. The diffraction angle 2θ varied from 20 to 100° . The resultant pattern peaks were analysed with X'Pert High Score Plus software with ICDD (The International Centre for Diffraction Data) – PDF (Powder Diffraction File) database files.

3.7 Mechanical testing methods

3.7.1 Hardness testing

As a simple means to determine mechanical properties, a microhardness tester was used to quantify the hardness of the as-deposited and heat-treated IN718. The microhardness measurements were performed with a Struers Microhardness testing machine equipped with a Vicker's indenter with 500 gf load and a dwell time of 15 sec. 8 – 10 indents were performed on the deposits to determine the average hardness of a sample. Hardness maps were performed in build-direction cross-sections with a spacing of 1 mm between indents. To understand the spatial variation in hardness, indentations were performed with a spacing of 200 μm in the repaired composites: within the deposits, at the interface between the deposited material and the substrate.

3.7.2 4-point bend test with Digital Image Correlation (DIC) for strain analysis

4-point bend tests were conducted on an INSTRON 8802 servo-hydraulic machine with constant crosshead speed (displacement controlled) corresponding to a constant nominal strain rate of 10^{-4}s^{-1} . The loading direction was such that the repaired surface was on the top surface that was under tension during the bend test, as shown in Figure 3.6, where h and W represents the height and width of the specimens tested. L is the distance between the support pins, and the distance between the loading pins is denoted by l . Bluehill software within the Instron Wave Console was used to control the tests. The specimens were tested to fracture or until the limits of bending allowable on the testing rig.

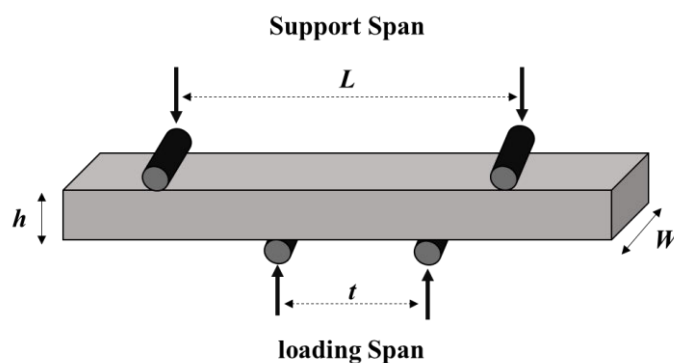


Figure 3.6: Schematic of the 4-point bend tests specimen geometry.

The strain evolution during the bend tests were measured using GOM Aramis Digital Image Correlation (DIC) equipment, as shown in Figure 3.7, A GOM Aramis 5 M

(GOM mbH, Braunschweig, Germany) with two cameras equipped with a Titanar lens (focal length of 50 mm) was used to carry out three-dimensional (3D) strain measurements at a resolution of 2448×2050 pixels and a frame rate of 1 fps. The camera lens was calibrated with a measurement area size of $100 \text{ mm} \times 50 \text{ mm}$. The top surface of the sample was painted with a black-and-white speckled pattern, and the strain evolution between the support rollers (80 mm) was monitored. The built-in ARAMIS software was used to analyse the measured images. The GOM uses a dual high-speed camera setup to allow 3-dimensional strain measurements on the specimen. The experimental setup is shown in Figure 3.7.

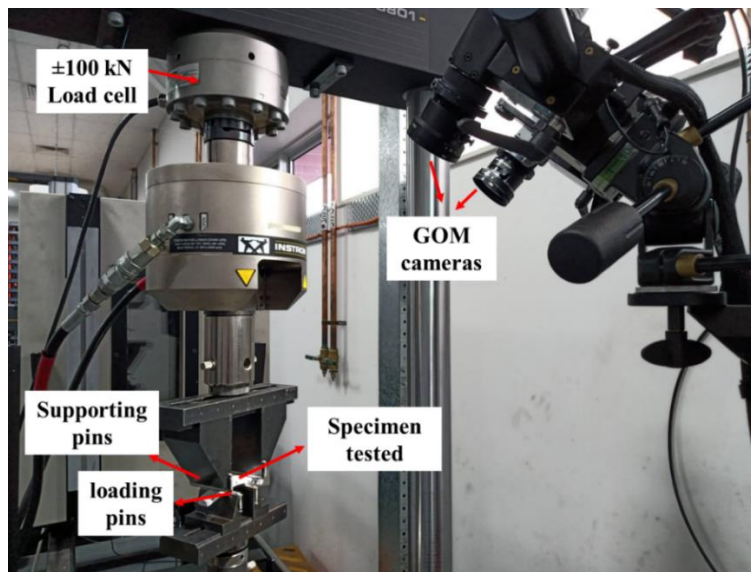


Figure 3.7: 4-point bend test setup on the INSTRON with DIC.

In a 4-point bend test, the region between the loading pins is considered to be under pure bend and, therefore, should have a uniform stress distribution. In the present study, the dimensions h and W were fixed due to the dimensions of the substrate plates and the geometry of the repaired grooves. Moreover, the repaired samples had grooves of 20 mm in length, and to ensure that the entire repaired component, including the substrate and the repaired region, was tested together, t was fixed at 30 mm. A schematic is shown in Figure 3.8 (a). From numerical modelling, it has been shown for Aluminium alloys that a $t/h=1.2-1.5$ and $L/t=4-5$ results in uniform stress distribution in the sample between the loading span [175]. Using the DIC method, the strain distribution across the surface (tensile) of the bend samples was monitored by testing the substrate material with identical external dimensions, varying L while keeping t constant. The results are shown in Figure 3.8 ((b) – (d)). When the span ratio (L/t) was 2:1 (60:30), the strain values were not uniform, with high strain over the

loading pins. With increasing the span ratio to 2.67:1 (80:30), it was observed that the strain across the pure bend region was uniform. Tests at a higher span ratio were not performed because the maximum length of the repaired composites was ~ 100 mm; when L was > 80 mm, the support pins could not clamp the testing specimen on the testing rig properly the specimens slipped off the testing rig. Therefore, all the bend tests were performed with a span ratio of 80:30.

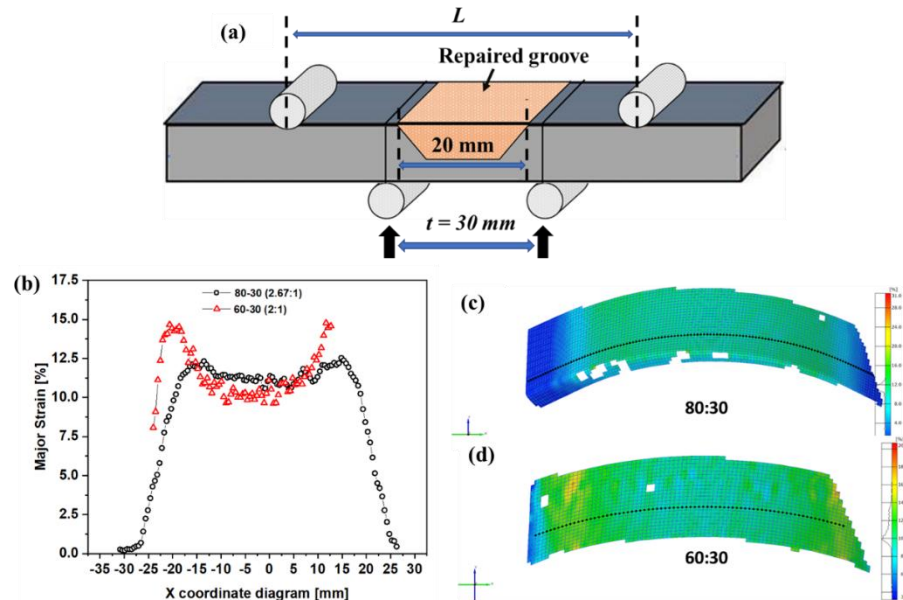


Figure 3.8: (a) Geometry of the repaired-bend test specimens; (b) Strain evolution at P_{max} on the top surface during 4-point bend tests with varying span ratio: (c) 80:30; (d) 60:30.

3.7.3 Tension testing

Tension tests were conducted at ambient temperatures on the wrought IN718, and DED deposited IN718 in as-deposited and post-heat treated conditions. Flat sub-size tensile specimens were machined according to ASTM standards (ASTM E8), as shown in Figure 3.9. The uniaxial tension tests were carried out on Instron 8802 servo-hydraulic machine with a load cell capacity of ± 100 kN. All the tensile tests were performed until fracture at constant crosshead speed (displacement controlled), corresponding to constant nominal strain rates of 10^{-4} s^{-1} . A non-contact video extensometer was used to measure the displacement (strain) during the tension test. Bluehill software in Instron Wave Console was used to control the tests. The digitally stored data sets were analysed to determine various mechanical properties.

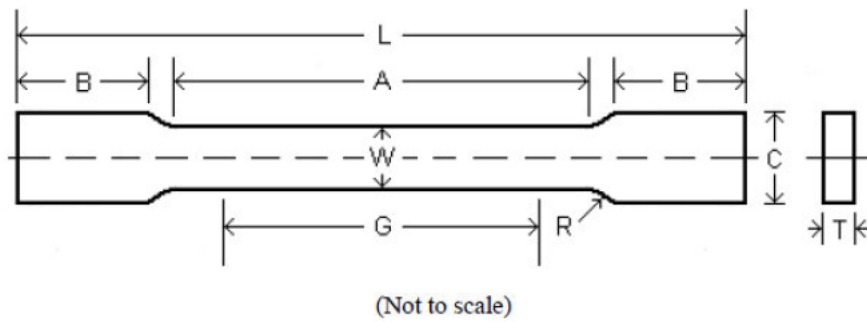


Figure 3.9: Schematic of the tensile test specimens (*all dimensions are in mm*).

G— Gage length: 12.5 ± 0.1 mm

W— Width: 3.0 ± 0.1 mm

T— Thickness of material: 1.5 mm (approx)

R— Radius of fillet: 3 mm

A— Parallel length: 16 mm

B— Length of grip section: 10 mm

C— Width of grip section: 5 mm

L— Total length: 80 mm

3.7.4 Fatigue testing

Fatigue tests were performed at ambient temperature using an Instron E10000 with an electrically operated crosshead and a ± 10 kN load cell. Fatigue tests were conducted under load control mode with a sinusoidal waveform load cycling at $R = 0.1$ and a frequency of 50 Hz. A tension–tension test at $R = 0.1$ ensured that there was no bending or buckling of the specimen during specimen fixing and testing. As shown in Figure 3.12, hourglass samples were machined using electro-discharge machining (EDM) from the repaired composite for HCF testing according to ASTM E466-15 standard [176]. The HCF samples were 50% wrought substrate and 50% laser DED deposit with the repair interface in the narrowest part of the samples; the details are reported in Chapter 5. Testing was performed on repaired IN718 specimens and the wrought substrate under the following conditions:

- (a) Wrought substrate in STA condition.
- (b) Repaired specimen in -Direct aged (DA) condition.
- (c) Repaired specimen in -Solution treated and aged (STA) condition.

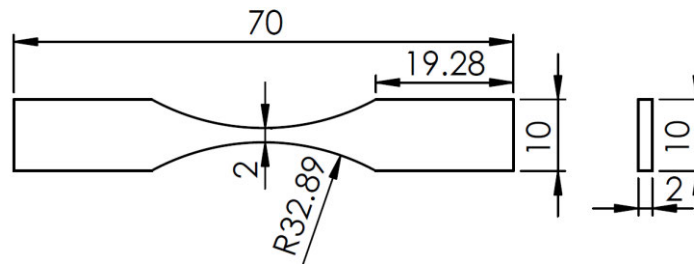


Figure 3.10: Hourglass geometry fatigue test specimen design (all dimensions are in mm).

For generating the stress-life (S-N) curve, cyclic loading was performed between 35-90% of the wrought IN718 yield strength (YS). To reduce the effect of surface roughness on the fatigue properties of the tested specimens, the specimen surfaces were progressively ground and polished using the standard metallographic technique to a final 1 μm diamond suspension finish. The S-N curve was constructed by plotting the maximum applied stress against the corresponding number of cycles to failure (N_f).

3.7.5 Interrupted fatigue tests

For these experiments, the sample surface was polished and etched for SEM investigation prior to testing, as any polishing or grinding operation post-testing would alter the surface conditions under investigation. A single specimen test was designed to eliminate specimen – to – specimen error, which can be significant in HCF tests. The generated S-N curves were utilised to study the initiation and growth of fatigue cracks using single-specimen interrupted tests conducted at various stages of fatigue life. These experiments consisted of 3 steps:

- (i) the specimen was mounted on the testing machine and loaded at predefined stress levels,
- (ii) after a certain percentage of average N_f the actuator movement was arrested to allow load relaxation, the specimen was then ultrasonically cleaned, and the surface was inspected under SEM;
- (iii) the specimen was remounted in the testing machine for the subsequent cycles. Extreme care was taken to ensure that the loading axis remained symmetrical in every cycle. The loading was interrupted at various stages of fatigue life between 10 – 90 pct of the average N_f .

CHAPTER 4**Deformation Behaviour of Inconel 718 Repaired using Direct Energy****Deposition process****4.1 Introduction**

Metal parts during their service life are often prone to wear and damage. Additive manufacturing (AM) techniques have emerged as an attractive alternative for the fabrication and repair of Ni-base superalloy components [177]. Laser AM techniques such as Direct Energy Deposition (DED) have recently gained popularity as a manufacturing process since they can build complex structures. In DED processing, a laser beam melts the surface of the substrate to create a melt pool while metal powders are simultaneously supplied to the melt pool zone. The components are built layer-by-layer via a user-defined toolpath. Various DED processes have also found widespread application in claddings for surface modification and component repairs [6,178–180].

The microstructures and properties of Inconel 718 (IN718) fabricated by DED differ significantly relative to its wrought counterpart. Wrought IN718 consists of equiaxed grains with metal carbides (MC) and δ phases located at the grain boundaries. In contrast, a typical DED synthesized Inconel 718 microstructure is characterized by fine columnar dendrites growing epitaxially from the substrate [107]. The microstructure can be controlled by varying process parameters such as power [11] and scan speed [53]. The laser scanning strategy controls the direction of heat flux and the morphology and texture of the resulting component [10]. Moreover, the high cooling rates associated with AM techniques are generally excessive for the formation of strengthening precipitates, resulting in non-equilibrium solidification conditions and the formation of brittle Nb-enriched Laves phases $((\text{Ni,Cr,Fe})_2(\text{Nb,Mo,Ti}))$ located at the inter-dendritic regions [40,93]. Laves phases are found to be detrimental to the mechanical properties of components manufactured by laser AM processing [8]. In order to recover strength, AM manufactured IN718 components are generally post-heat-treated [14].

The literature review indicates that the process parameters, scanning patterns and geometry of the repaired section are important when using AM processes to repair metallic components. The deformation behaviour of IN718 repairs done using Laser AM techniques was studied by Sui et al. [8] and Guévenoux et al. [9] using tensile tests. Repaired composites exhibit a non-uniform microstructure across the substrate, deposit, and interface, and failures are found to occur in the deposit section. The

presence of Laves phase in the deposit was found to be the determining factor that causes failure in the deposit.

The current study initially explores the relationship between deposition parameters and key characteristics of DED Inconel 718 bulk deposits. These key characteristics are the degree and size distribution of porosity γ grain size and aspect ratio, the distribution and morphology of Laves phase, and mechanical properties (in the form of hardness tests). The best parameter combination was applied for repair studies on wrought Inconel 718 plates with various designed groove wall angles and various contrasting scanning patterns. Subsequently, a study was conducted to understand the effects of post-heat treatment (direct ageing and solution treatment at 980°C followed by ageing) on the microstructure and properties of the repair deposit and surrounding substrate. The deformation behaviour and failure mechanisms of the resulting repaired composite were investigated using 4-point bend testing coupled with digital image correlation (DIC) and cross-sectional microscopy.

4.2 Experimental methods

4.2.1 Groove repair using LENS

Wrought IN718 plates with ~20 mm thickness were used as substrates for the repairs. Plasma Atomised (PA) Inconel powders were obtained from AP&C pvt. Limited (GE additive) with a size range varying from 45 μm – 105 μm , as shown in Figure 4.1. An Optomec LENS MR-7 apparatus equipped with a 1kW IPG fibre laser with a coaxial powder delivery system was used.

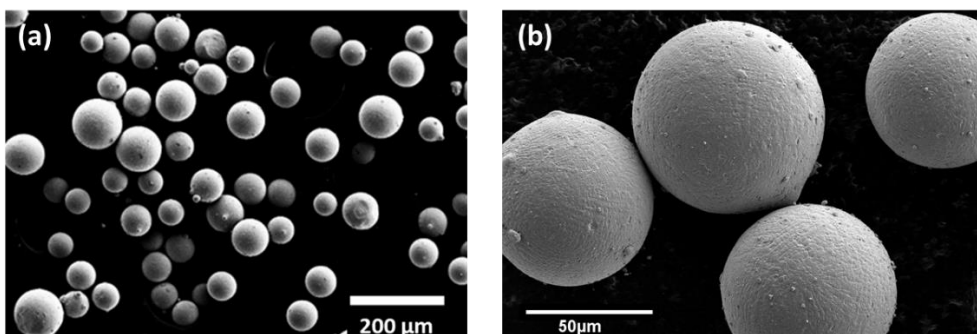


Figure 4.1: SEM image of the GA Inconel Powders.

The process parameters for the repairs were determined by performing several depositions with varying laser power between 350 W and 825 W and scan speed between 6.35 mm/s and 14.8 mm/s. Cubes of dimensions 12 × 12 × 10 (length × width × height) mm³ were deposited with an alternating pattern with 90° rotation after each

layer, as shown in Figure 4.2. Hence, all the deposits had multiple tracks and layers. Process parameters of laser power P (W) and scanning speed v ($\text{mm}\cdot\text{s}^{-1}$) were varied in the deposits. Table 4.1 shows the deposition parameters adopted to fabricate IN718 cubes. Argon was used as the shielding gas and carrier gas for all the deposits with a flow rate of 15 l/min and 6 l/min, respectively. The powder flow rate of 12 g/min and oxygen level below 3 ppm was maintained in all the deposits. These bulk deposits were extensively characterised, as detailed below, and the results were used to guide the deposition parameters to be used in the repair deposit trials.

Table 4.1: LENS deposition parameters

Sample identity	Power (W)	Scan speed (mm/s)	Hatch spacing (h) (mm)	layer thickness(t) (mm)	linear Energy Density (J/mm)
C1	500	14.8	0.67	0.25	33.75
C2		10.6	0.75	0.30	47.24
C3		6.3	0.95	0.48	78.74
C4	350	10.6	0.60	0.28	33.08
C5	825		0.75	0.30	77.98

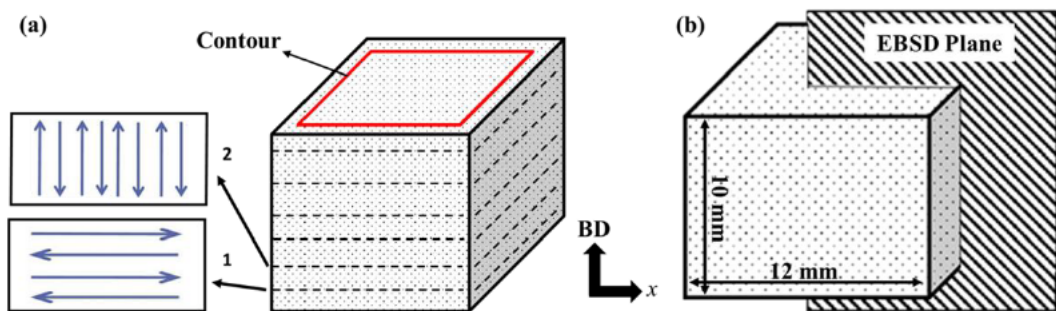


Figure 4.2 (a) As-built specimens on the substrate;(b) Schematic of the scanning pattern used for printing and the section under investigation (z is the building direction).

During the repair process, the groove angle affects the properties of the repair. To study the effect of groove angle on the properties of the repair, circular grooves (5 mm depth and 20 mm diameter) were machined on a 20 mm IN718 plate to obtain two different groove angles, 30° or 60° , as shown in Figure 4.3 (a) and Figure 4.3 (b). To determine the effect of scanning patterns on the repair process, each groove angle was repaired/filled using two different scanning patterns, alternate and spiral. The

schematic for the adaptive tool paths for the scanning patterns are shown in Figure 4.3 (c) and (d).

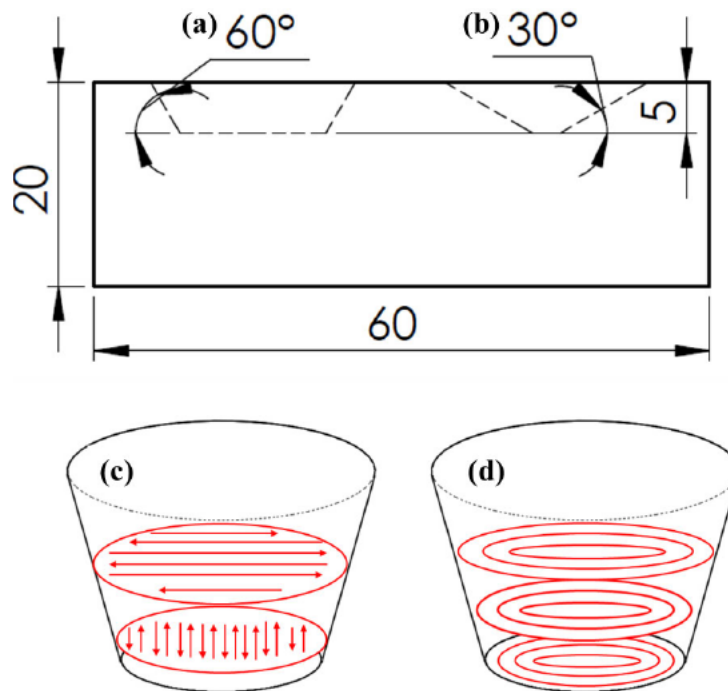


Figure 4.3: Schematic sketches showing the cross-sectional view of Grooves with varying sidewall angles (a) 60°, (b) 30° and the two different scanning patterns used for repairing the grooves (c) alternate pattern and (d) spiral pattern.

Subsequently, these repaired grooves were subjected to two post-repair heat treatments (i) Direct ageing (DA) and (ii) Solution treatment and ageing (STA). The corresponding post-deposit heat treatment conditions are listed in Table 4.2.

Table 4.2: Designations of the specimens and the details of the corresponding post-deposit heat treatment conditions.

Designation	Solution Treatment	Ageing treatment
As-deposit	None	None
Direct aged (DA)	None	720°C/8 h/FC at 55 °C/h to 620 °C + 620 °C/8 h/AC
Solution Treatment and aged (STA)	980 °C for 1 h/WQ	

WC: Water Quenching; FC: Furnace Cooling; AC: Air Cooling

Cross-sectional specimens were machined from the repaired components for metallographic investigation. Figure 4.4 represents a schematic of the cut-section and the plane on which post-repair investigations were performed. The as-deposited

samples were ground and polished to $1\mu\text{m}$ and finally with an OPS solution. A Field Emission Scanning Electron Microscope (Supra 55-VP) equipped with EDS and EBSD detectors was used for the characterisation of the as-built and heat-treated samples. The EDS detector was used for local qualitative and quantitative chemical analysis. EBSD analysis was performed on the repaired samples with a step size of $5\mu\text{m}$. Hardness testing was conducted on repaired samples polished along the vertical cross-section ($10\text{ mm} \times 12\text{ mm}$) using a Vicker's indenter with 500gf load and a dwell time of 15 sec.

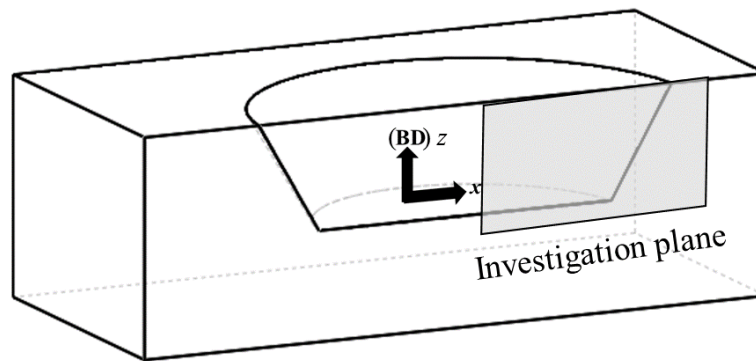


Figure 4.4: Schematic representation of the investigation plane.

4.2.2 4-point bend test

The mechanical properties of the repaired component were determined using 4-point bend tests. The 4-point bend test was adopted to evaluate the mechanical properties of weld joints in Stainless steel by Alam et al. [181] and pipeline steels by Al-Abtah et al. [182]. The motivation for using the 4-point bend test was to test the specimens under a more complex state of stress compared to uniaxial tests. Moreover, a 4-point bending test provides the opportunity to test the entire repaired composite, including the deposit and surrounding substrate, which would otherwise require significantly bigger size specimens that would be difficult to prepare and test. Moreover, a bending test provides the opportunity to test Grooves of 5 mm depth and 20 mm width: either a 30° or 60° groove angle was machined across 50 mm wrought IN718 plates and subsequently repaired using LENS with the alternating scanning pattern. A schematic of the machined grooves with 30° or 60° groove angles is shown in Figure 4.5 (a) and Figure 4.5 (b) respectively. Following the groove repairs, the repaired plate sections were subjected to post-deposition heat treatment: (a) direct aged (DA); and (b) solution treatment and aged (STA) as described earlier in Table 4.2.

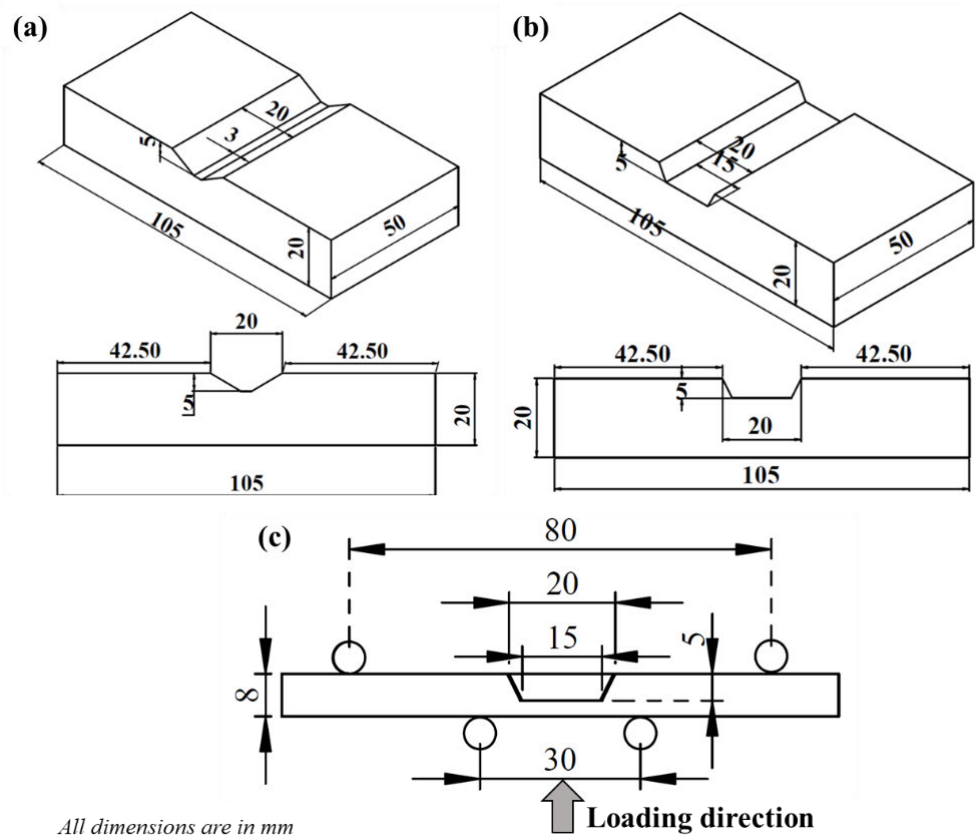


Figure 4.5: Schematic of the grooves prepared for 4-point bend tests (a) groove angle 30°; (b) groove angle 60°; (c) illustration showing the setup for 4-point bend test on the repaired components (60° groove angle), arrows indicate loading direction.

A 4-point bending test tool was installed in a ± 100 kN INSTRON 8801 universal testing machine and combined with a GOM Aramis Digital Image Correlation (DIC) system to record strain at the outer surface during deformation. A schematic of the test setup is shown in Figure 4.5 (c). The actuator travel speed was 4.8 mm/min, corresponding to a nominal strain rate of $\sim 10^{-3} \text{ s}^{-1}$. For every condition, at least two samples were tested. The machining of the 4-point bend samples was performed in as-deposit condition, i.e., before performing the post deposit heat treatments and due to the geometrical constraints, only limited samples could be machined. As a result, 2 tests were heat treated and tested in every condition and a third test was performed only if the error in the first 2 tests was significantly high. A GOM Aramis 5 M (GOM mbH, Braunschweig, Germany) with two cameras equipped with a Titanar lens (focal length of 50 mm) was used to carry out three-dimensional (3D) strain measurements at a resolution of 2448×2050 pixels and a frame rate of 1 fps. The camera lens was calibrated with a $100 \text{ mm} \times 50 \text{ mm}$ measurement area. The top surface of the sample was painted with a black-and-white speckled pattern, and the strain evolution between

the support rollers (80 mm) was monitored. The built-in ARAMIS software was used to analyse the measured images. A 30 mm loading span ensured that the base material, deposit-substrate interface, and deposit co-exist in the pure bend region.

4.3 Results

4.3.1 Effect of deposition parameters on the microstructure of DED IN718

As mentioned above, this broad parameter study was designed to understand process-structure relationships in IN718 cube deposits above the substrate surface in order to guide desirable parameter sets to carry forward to below-surface repair processes.

4.3.1.1 Porosity

Porosity measurements were performed for all the deposited samples using light optical microscopy on a full cross-section z-x plane of the cube deposits. A representative image of the entire cross-section for the as-deposited sample C1 is shown in Figure 4.6 (a). Spherical pores were observed in all the builds, which were distributed throughout the build, as shown in Figure 4.6 (b). During DED fabrication or AM processes in general, the inert gas entrapped in the hollow particles could not escape easily from the molten pool due to the high cooling rate, which results in the formation of spherical-shape gas porosities randomly distributed in the deposit [36,183]. As the tool path during every build was kept constant and the same powders were used during the deposit, the difference in area % and distribution of the porosities can be attributed to the deposition process parameters.

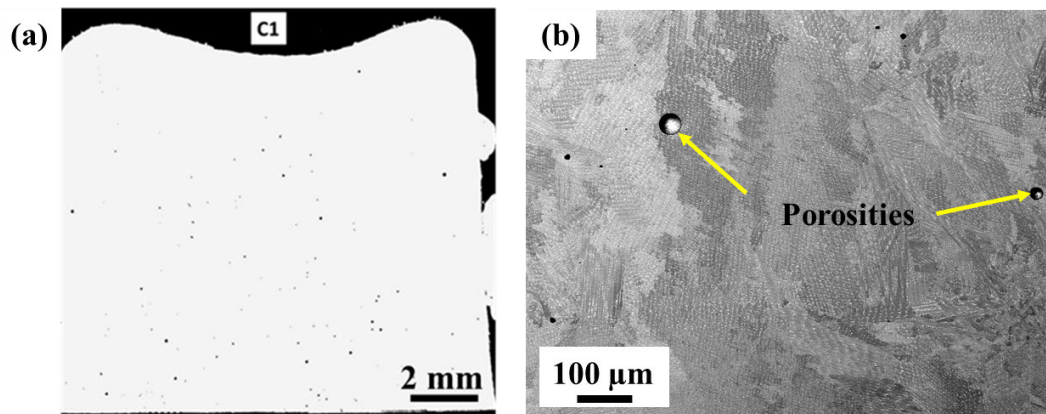


Figure 4.6: (a) Representative cross-section of the as-build sample (C1) for porosity measurement; (b) SEM micrograph of spherical porosities observed in the deposits.

Figure 4.7 (a) shows the variation of porosities with linear energy density. The percentage of porosities in the deposits is found to decrease with increasing energy

density. A similar observation was made by Qi et al. [93] on DED (LENS) deposit IN718 where the densification increases with linear energy density. The cumulative size distribution of the porosities in all the as-deposited samples is shown in Figure 4.7 (b). The size distribution plot indicates that in all the as-deposited samples, the majority of the porosities (~80% of the total porosities) are under 30 μm . The low energy deposits C1 and C4 exhibited higher porosity count. The summary of the porosity measurements is reported in Table 4.3. The detected pores generally have a size of a few micrometres with the mean pore radius <20 μm in all the deposits. Among all the deposits, the biggest porosity observed is ~80 μm . The deposits were found to be generally dense, with the number of porosities varying between 0.04% and 0.13%. The area percentage is low compared to the literature and is not expected to affect the mechanical properties significantly. Qi et al. [93] observed a mean porosity of 0.03 % in IN718 manufactured using the DED process using plasma-rotating electrode process (PREP) powders. In other studies on AM fabricated IN718, Tillmann et al. [184] reported a porosity of ~0.13 % measured optically on SLM manufactured IN718. Smith et. Al. [185] reported slightly higher porosity ~0.18% when direct metal laser sintering (DMLS) was adopted for manufacturing IN718.

Table 4.3: Summary of porosity measurements.

Specimen	Maximum	Minimum	Mean	Standard	Area %
	Radius	Radius	Radius	Deviation	
	(μm)	(μm)	(μm)	(μm)	
C1	53.54	7.52	16.45	9.62	0.11
C2	35.69	6.36	13.63	7.96	0.07
C3	43.71	7.14	14.95	9.12	0.04
C4	50.48	5.84	12.40	8.38	0.13
C5	81.78	7.24	18.66	14.26	0.05

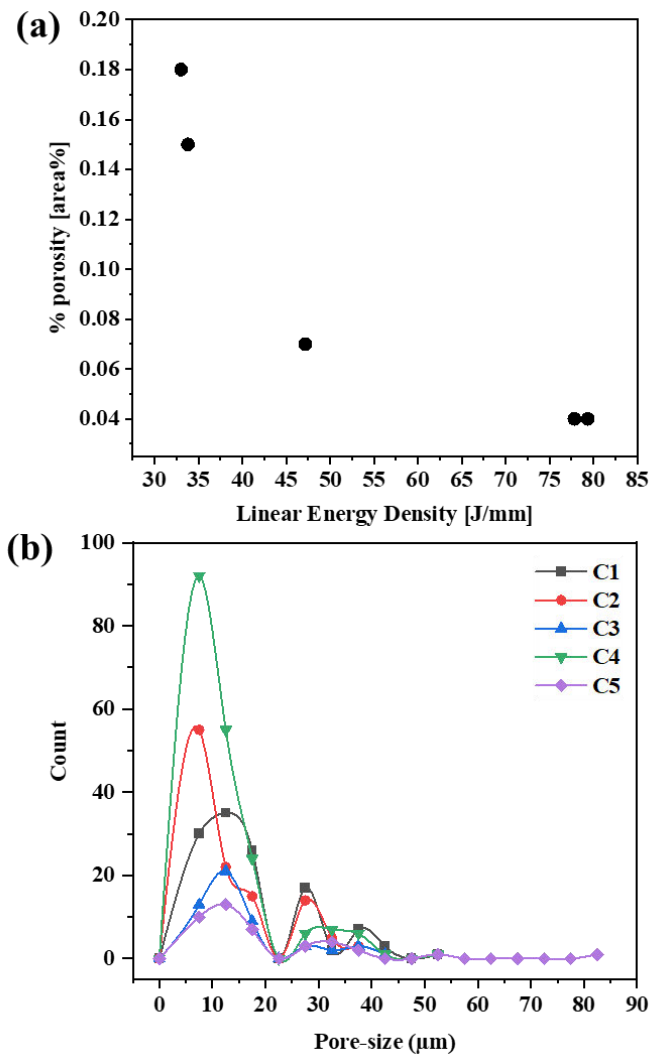


Figure 4.7: (a) variation of porosities with linear energy density; (b) size distribution of the porosities in the deposits.

4.3.1.2 Microstructure of as-built deposits

The microstructures of the as-built samples were examined on the vertical section along the build direction (x - z plane). The EBSD IPF maps and the corresponding $\{100\}$ pole figures along the build direction (BD) for each deposit are shown in Figure 4.8 (a – e). The deposits C3 (Figure 4.8 (c)) and C4 (Figure 4.8 (d)) exhibit a mix of equiaxed and columnar microstructure, whereas the C1 (Figure 4.8 (a)) and C5 (Figure 4.8 (e)) displayed predominantly columnar microstructure. The primary grain structure correlates well to prior studies on DED processed IN718 [34,53,93]. It can be noted that specimens with similar energy densities (C1, C4 and C3, C5) but different process parameters have significantly different grain morphology. A change of as-deposit microstructure from a mix of columnar and equiaxed to a columnar microstructure was reported by Parimi et al. [11] in DED deposit IN718 upon changing

the processing parameters. The change in morphology of the microstructure was attributed to the thermal history experienced by the deposits as a function of the process parameters used in the deposition process.

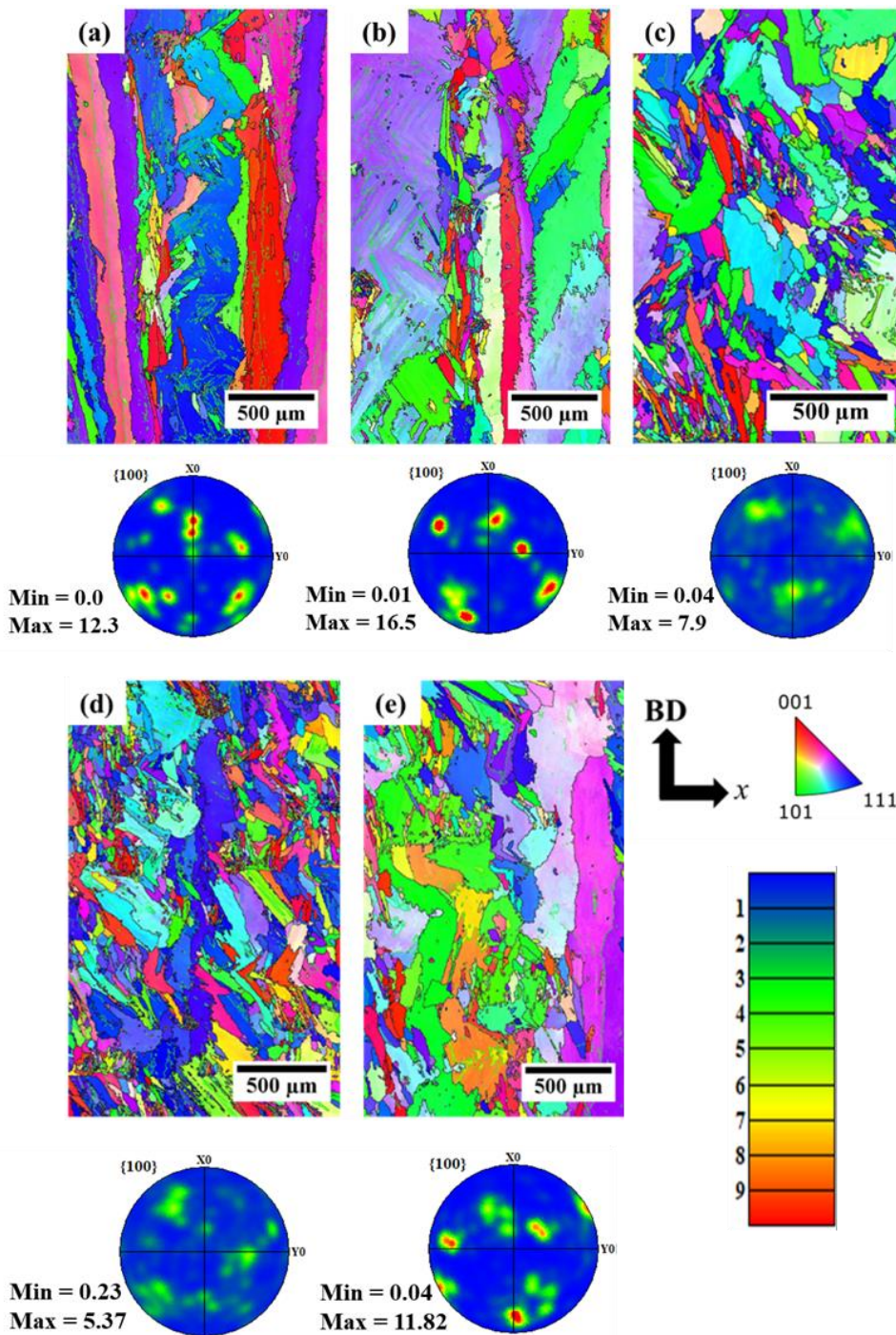


Figure 4.8: IPF map of the as-build samples showing the grain structure: (a) C1, (b) C2; (c) C3, (d) C4; (e) C5. The (100) pole figures are shown below each EBSD map.

The legends for the multiple of uniform density (MUD) values for the pole figures are kept constant for comparison. The parameter combination for the corresponding deposits is shown in Table 4.1.

The relative frequency of the grain size and the aspect ratio is shown in Figure 4.9. The grain size measurement in the complex as-deposit microstructure was done using the EBSD data. HKL Channel 5 software is used for grain reconstruction, grain size and aspect ratio measurement. The circle equivalent diameter from the EBSD data is used to generate the grain size measurements. During grain reconstruction, the $\Sigma 3$ twin boundaries identified as $60^\circ \pm 5^\circ <111>$ are ignored in grain size measurements; also, the grains with grain area less than 10pixel were not used for the analysis. Grain sizes varied from as low as $<10 \mu\text{m}$ to greater than $100 \mu\text{m}$. This demonstrates the heterogeneous nature of the grain size distribution in the as-deposited samples. Although the deposits C3 and C4 exhibit finer microstructure relative to the coarse-columnar microstructure in C1, C2, and C5, the grain size distribution does not exhibit any significant difference. For the deposits with coarse-columnar microstructure (C1, C2, C5), the relative frequency of grains $>100\mu\text{m}$ was high. To study the grain distribution in further detail, the grain aspect ratio distribution was quantified for each deposit using the EBSD data. For the grain size analysis and $\{100\}$ pole figures shown in Figure 4.8 the analysis was performed on at least 500 grains for the coarse columnar deposits (C1, C2, C5) and for the finer deposits (C3 and C4) at least 2000 grains were included for the analysis.

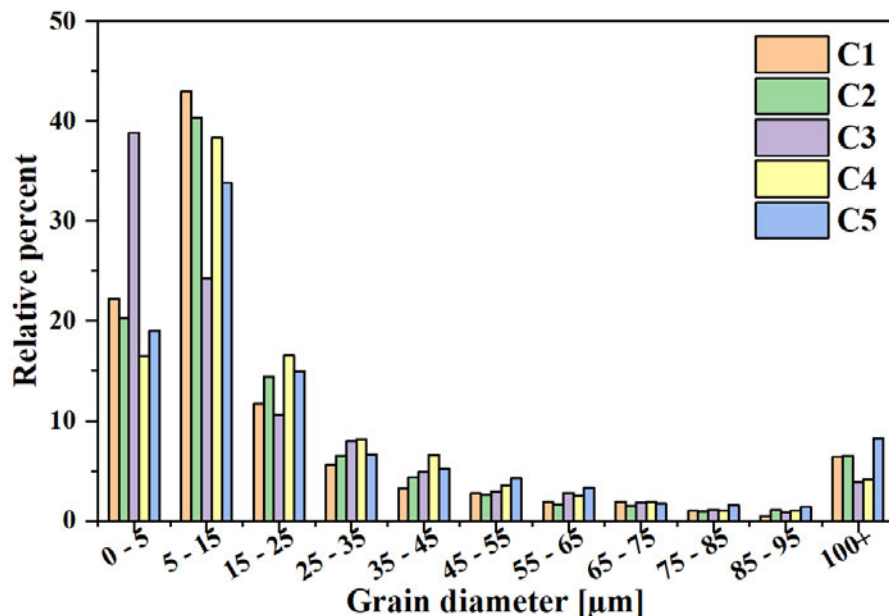


Figure 4.9: Grain size distribution in the as-built samples.

Figure 4.10 depicts the aspect ratio distribution of the individual deposits. The HKL Channel 5 software uses the major and minor axis of the fitted ellipse of every grain detected to calculate the aspect ratio. The aspect ratio is defined as the ratio of the long

to short axes measured. Therefore, an aspect ratio ~ 1 indicates a fully equiaxed microstructure, and a higher aspect ratio indicates a columnar microstructure. A representative figure showing the aspect ratio of an elongated grain in deposit C1 is represented in Figure 4.11. The selected grain exhibits a high aspect ratio of 14.3 and a grain size of 1.4mm. The as-deposited samples exhibited a wide range of distribution of the aspect ratio from 1.0 - 1.5 to over 6. In all the as-deposited samples, the large grains ($>300\mu\text{m}$) had the highest aspect ratio; therefore, their frequency was low. Therefore, in this present study, the wide distribution of grain size and aspect ratio is of more relevance than the respective average values, as the average values do not represent the dominant columnar nature of the microstructure. The columnar microstructure in the deposits C1, C2 and C5 results in a strong $\{100\}$ texture along the build direction in the resulting microstructure, as represented by the pole figures in Figure 4.8. The $\{100\}||\text{BD}$ is the preferential growth direction in FCC metals and is often found in AM IN718[10,11].

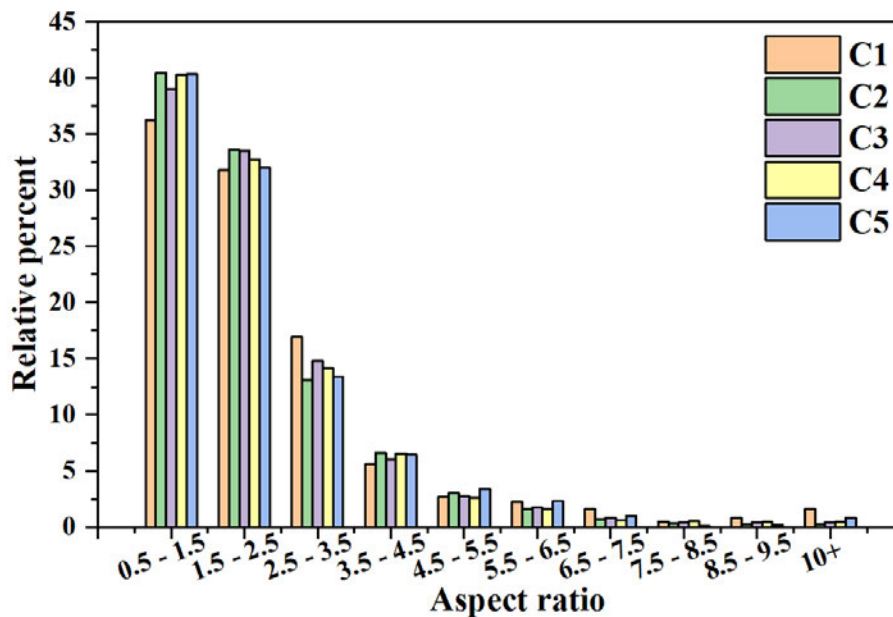


Figure 4.10: Relative frequency of the aspect ratio distribution in the as-built sample, displaying the significant variation in grain aspect ratio within the depositions.

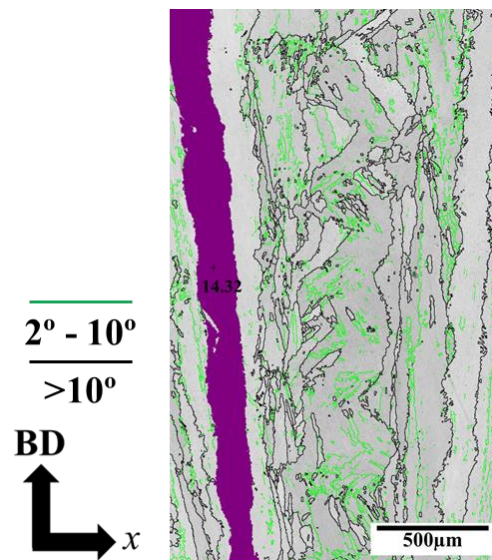


Figure 4.11: A representative figure showing the aspect ratio of an elongated grain (marked in pink) in the deposit C1.

During the solidification process in alloy systems, the redistribution of constituent elements leads to concentration gradients ahead of the solid-liquid interface, leading to constitutional supercooling. Critical parameters such as temperature gradient (G), solidification rate (R), undercooling (ΔT), and alloy constitution determine the resulting microstructure. The microscopic shape of the solid-liquid interface can be planar, cellular dendritic, columnar dendritic, or equiaxed dendritic, depending on the solidification conditions [141]. This would result in 3 types of grain morphology: (1) fully columnar, (2) columnar plus equiaxed and (3) fully equiaxed. Based on nucleation and dendritic growth models, columnar to equiaxed transition (CET) models and microstructure selection maps were developed by Gäumann et al. [186]. However, the variation of the values of G and R inside the melt pool makes precise measurement of G and R values extremely challenging during the deposition process [187]. Therefore, numerical simulation, including heat transfer and fluid convection, is often adopted to estimate the G and R values during an AM process. Nie et al. [187] and Lee et al. [141] used numerical modelling to determine the values of G and R DED IN718 to develop an understanding of controlling the as-deposited microstructure. The effect of G and R on the solidification morphology in AM IN718 is shown in Figure 4.12. A low G/R and a high cooling rate ($G \cdot R$) assist in CET. However, the thermal gradients associated with laser additive manufacturing processes usually reach $10^3 - 10^7$ K/m, which is generally too high to achieve fully equiaxed microstructures [188].

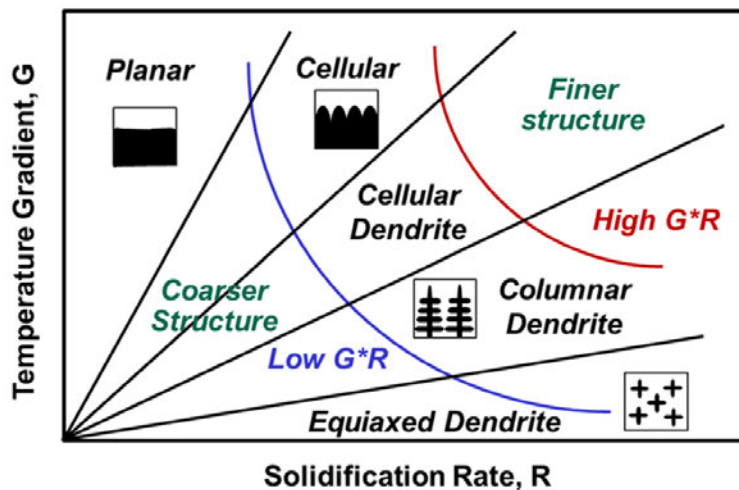


Figure 4.12: The effect of G and R on the solidification morphology and size [141].

During the directional solidification in AM, the substrate and the previously deposited layers act as the heat sink for the melt pool. This results in heat flux in the direction opposite to the build direction. Depending upon the thermal conditions, solidification of the microstructure can occur by epitaxial growth or nucleation. During the directional solidification in AM, the substrate and the previously deposited layers act as the heat sink for the melt pool. This results in heat flux in the direction opposite to the growth direction. The previous layer acts as the substrate for every layer built in the AM process. Considering the case of C3 and C5, where the linear energy densities are similar, the higher power and faster scan speed in C5 results in higher heat accumulation. Therefore, following the completion of layer 'n' deposition and just before starting layer 'n + 1', the temperature at the starting point of layer (n + 1) would be higher in C5 than in C3. This thermal condition favoured the growth of the dendritic structure rather than nucleation (Figure 4.8(e)). The heat input for C5 was high enough for the grains to grow epitaxially from the previous layer. On the contrary, the thermal conditions in C3 favour nucleation in the remelting regions (Figure 4.8(c)). This results in equiaxed grains forming in the regions where the layer changes during the deposition process. Similarly, for C1 and C4 (having similar energy density), the higher heat accumulation in C1 results in columnar growth.

The solidification microstructure can be related to the G and R values from the Dendritic Arm Spacing. The primary dendritic arm spacing (PDAS) was measured using the SEM micrographs. For every deposit, the dendritic arm spacing was measured at various locations on the vertical cross-section, corresponding to the bottom, middle and top regions along the build direction. The average PDAS is

measured in the as-deposit cubes along the build direction at the bottom, middle and top locations. The relationship with the linear energy density is shown in Figure 4.13 (a). The average PDAS was found to vary over $3\ \mu\text{m}$ – $5.25\ \mu\text{m}$ and is found to increase with increasing energy density. The values of PDAS measured agree well with the values of PDAS quantification reported in the literature using the DED technique for the additive manufacture of IN718 [11,68,141]. Figure 4.13 (b) depicts that the DAS spacing increases as the deposit moves away from the substrate, which agrees with existing work in the literature on DED manufactured IN718 [95].

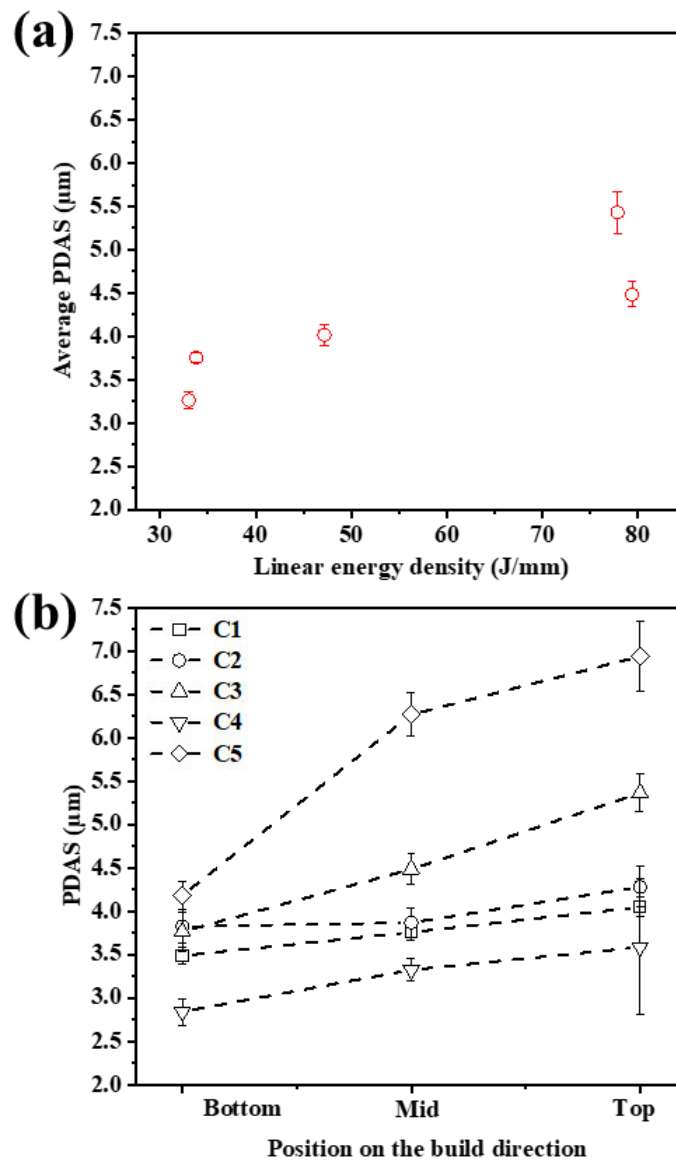


Figure 4.13: Primary dendritic arm spacing (PDAS) measured in the as-deposit samples: (a) variation of PDAS with linear energy density; (b) variation along the build direction for individual deposits.

For AM IN718 cladding processed via laser DED method, the cooling rate can be related to the primary dendritic arm spacing (PDAS) as follows:

$$\lambda = 80 \dot{\epsilon}^{-0.33} \quad [4.1]$$

Where λ is the primary dendritic arm spacing in μm ; $\dot{\epsilon}$ is the cooling rate in K/s or $^{\circ}\text{C/s}$. The cooling rates for each deposit in the bottom, middle and bottom of the deposits are calculated using Equation [4-1] as shown in Figure 4.14. The cooling rates in the deposits are observed to vary from 10^3 K/s to 10^4 K/s. The cooling rates decreased in the top layers for all the samples. The builds that experienced higher energy density also resulted in lower cooling rates. It was reported by Sui et al. [68] that the cooling rates in DED processes typically vary in the range between 10^3 K/s - 10^5 K/s, which agrees well with the cooling rates calculated in the present investigation.

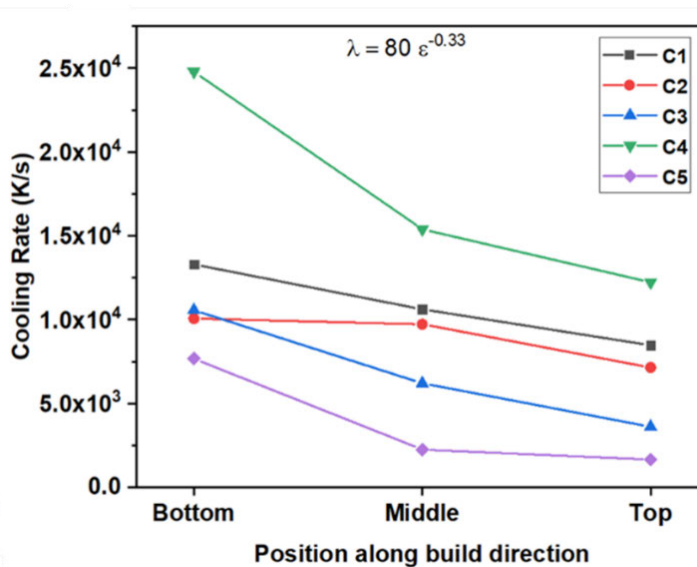


Figure 4.14: Variation of cooling rate of all the as-deposit samples with position along build direction.

4.3.1.3 Analysis of minor phases

Figure 4.15 (a) shows a typical microstructure of the as-built Inconel 718 samples. In general, all the builds exhibited a dendritic γ phase microstructure (dark phase), with bright contrast (white phases) segregated in the inter-dendritic regions as shown in backscattered SEM micrographs in Figure 4.15 (b).

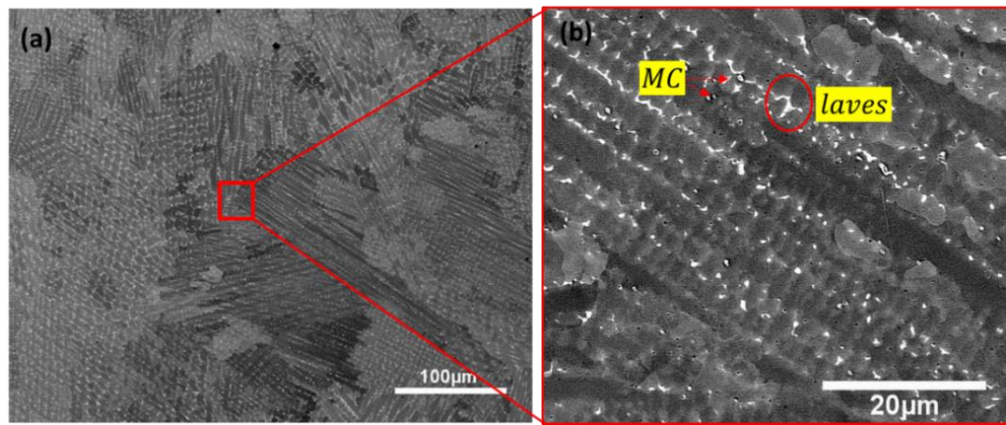


Figure 4.15: (a) Representative ASB SEM micrograph showing Laves network (b) high magnification micrograph showing the intermetallic precipitates analysed using EDS.

It can be inferred from the EDS map shown in Figure 4.16 that these secondary interdendritic phases are enriched with Nb, Mo, and Ti, while the matrix of the dendritic core area was enriched with Nb, Fe, and Cr. The chemical composition of the phases is evaluated using point EDS analysis, shown in Figure 4.17. It was shown that these bright contrast phases are mostly Laves phases. As shown in Figure 4.16 and Figure 4.17, a few spherical precipitates with high concentrations in Ti and Nb were also observed in the as-deposited microstructure, which are metal carbides (NbC, TiC). Such Metal carbide precipitates are often found in DED manufactured IN718 [11,93]. It is well established in the literature that Laves phase is formed due to Nb, Mo segregation that is a result of rapid solidification, and requires more than 10 wt% Nb to form, as shown by Qi et al. [93] and Zhai et al. [95] for IN718 manufactured using DED techniques. During solidification in IN718, $L \rightarrow (\gamma + \text{NbC})$ and $L \rightarrow (\gamma + \text{Laves})$ eutectic-type reactions are found to occur; however, the general solidification sequence that is widely accepted is $L \rightarrow L + \gamma \rightarrow L + \text{NbC}/\gamma \rightarrow L + \gamma \rightarrow \text{Laves}/\gamma$ [189,190]. The segregation of solutes during solidification is a time-dependent phenomenon and depends on the heat input and the cooling rate [191]. During solidification, elements such as Nb, Mo, and C have a high tendency to segregate, especially Nb with the lowest value of partition coefficient, $k < 0.5$: they are segregated to the last remaining liquid in the inter-dendritic region [191]. Laves phases are formed due to inter-dendritic Nb and Mo segregation with a typical composition of $(\text{Ni, Fe, Cr})_2(\text{Mo, Nb, Ti})$. Laves phase is detrimental to tensile ductility properties in IN718 welds [192] and DED (and other AM processes) fabricated IN718 [22,93] as it aids crack initiation and propagation. Due to high cooling rates in laser DED processed

IN718, the precipitation of the strengthening phases (γ' , γ'') is suppressed. Moreover, the formation of Laves phases depletes the available Nb for formation of the strengthening precipitates.

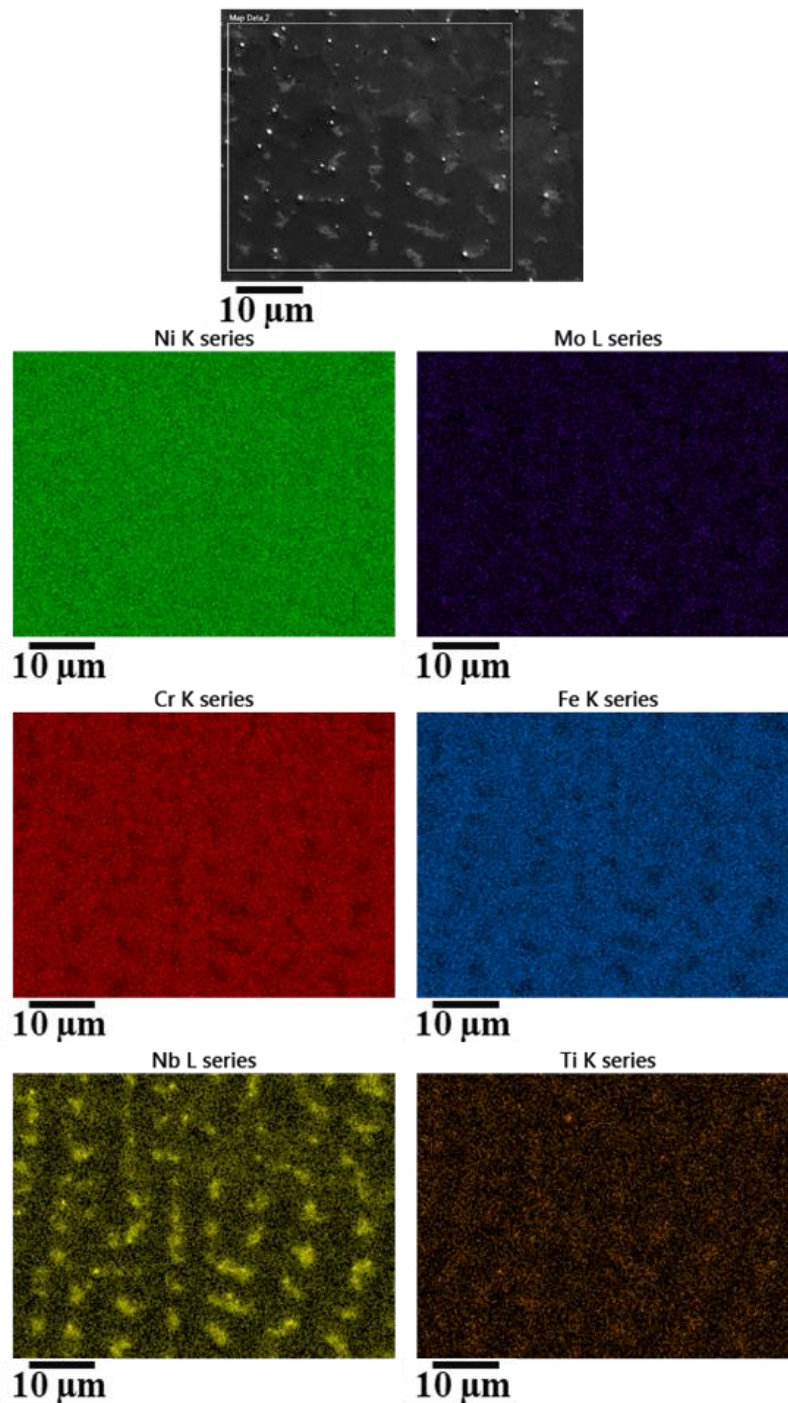


Figure 4.16: Representative EDS area scan maps that depict Nb, Ti and Mo micro-segregation in the as-deposited microstructure.

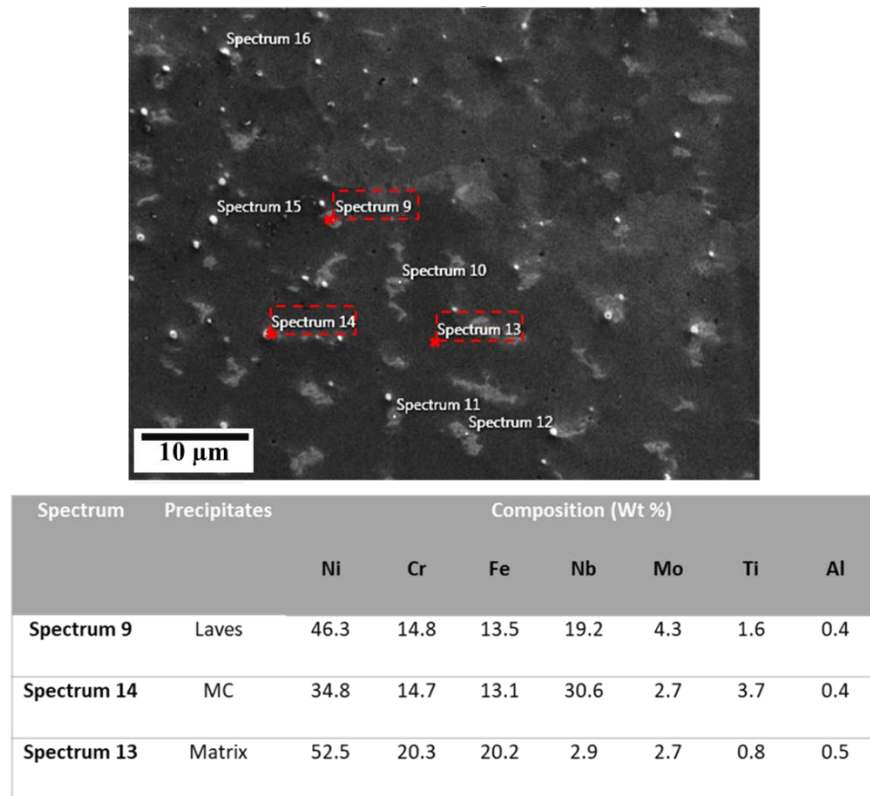


Figure 4.17: Representative SEM micrograph showing EDS point scans and their corresponding chemical compositions of the various precipitates.

The area percentage of Laves phase/carbides in the as-built samples at various heights along the deposit is shown in Figure 4.18. For every deposition condition, a minimum of 12 microstructures were analysed. The backscattered SEM images shown in Figure 4.19 (a) – (c) depict the procedure of evaluating the area fraction/percentage of Laves phase formed during the deposition. The backscattered SEM images were converted into binary images, and the Laves phase was identified by adjusting the contrast threshold (Figure 4.19 (c)) and measured using ImageJ software. The average area percentage of Laves phases does not change significantly with varying process parameters; the average area fraction (percentage) varied from a minimum of 1.9% to a maximum of 2.2%. However, the percentage of Laves phases is found to increase along with the height of the deposit. The increased segregation along the build direction can be attributed to the increase in DAS, as shown in Figure 4.13(b). A similar trend in Laves phase distribution along the build direction of additively manufactured Inconel 718 was reported by Ma et al. [193] and Segerstark et al. [194].

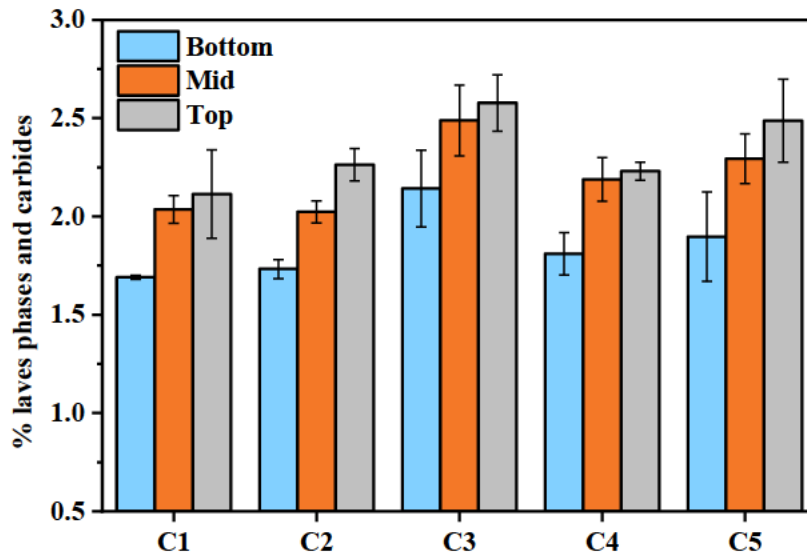


Figure 4.18: Area percentage of Laves phase/carbides in the as-built samples.

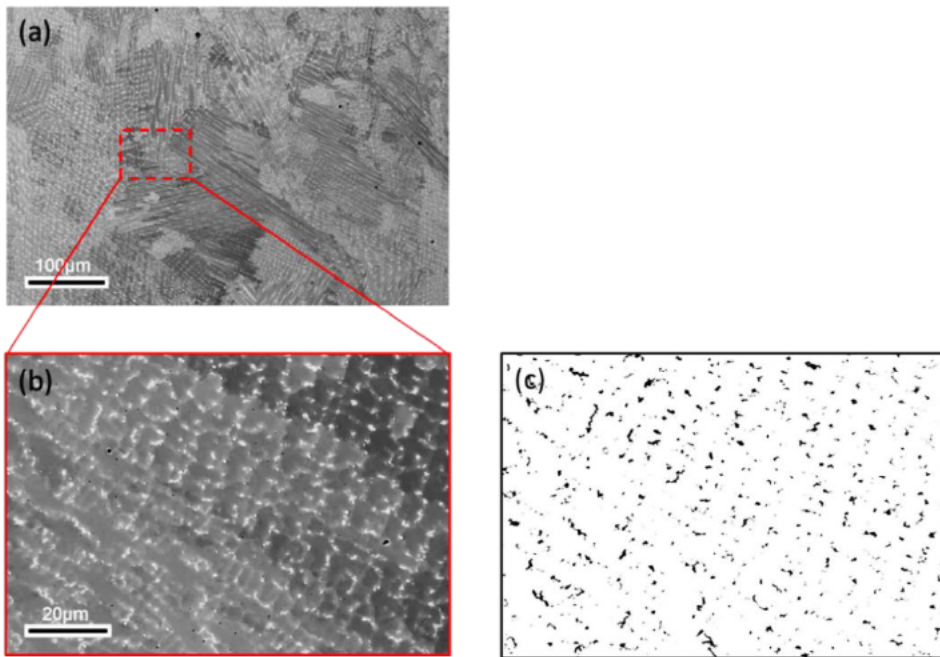


Figure 4.19: (a) Representative micrograph showing the typical as-built Inconel 718 microstructure; (b) high magnification image of the marked area; (c) determination of Laves phases by converting to a binary image and applying a contrast threshold.

4.3.1.4 Hardness

The mechanical properties of the as-deposited samples were characterised using a microhardness test. Hardness measurements were done on the polished as-deposited samples along the build direction on the x - z plane (Figure 4.4). The hardness measurement was done with a Vicker's indenter with 500gf load and a dwell time of

15 sec. Hardness measurements were done across the entire section with 1 mm between the indents. Figure 4.22 (a – e) shows the hardness maps for the as-deposit samples. The average hardness of the samples C1, C2, C3, C4, and C5 were 251 ± 3 HV; 248 ± 2 HV; 244 ± 2 HV; 255 ± 3 HV; and 252 ± 3 HV, respectively. The average hardness value did not exhibit significant variation with the varying process parameters. Similar hardness values are reported for laser AM Inconel 718 [53,194]. However, this hardness value is much lower than the industrial requirement of 350HV [195]. The lower hardness value is attributed to the absence of the strengthening phases γ'/γ'' in the as-built samples. The γ'/γ'' precipitates are unable to form due to the high cooling rates during the DED processing. The hardness maps depict that the hardness in the contour region for all depositions, as shown in Figure 4.2 (a – e), is consistently less than in the inner regions. A similar hardness profile was shown by Stevens et al. [53] in IN718 manufactured using DED process. The lower hardness in the contour region was attributed to the repeated remelting of the contour regions with respect to the inner hatching region, which results in increased Laves phases in the contour compared to the inner hatching region.

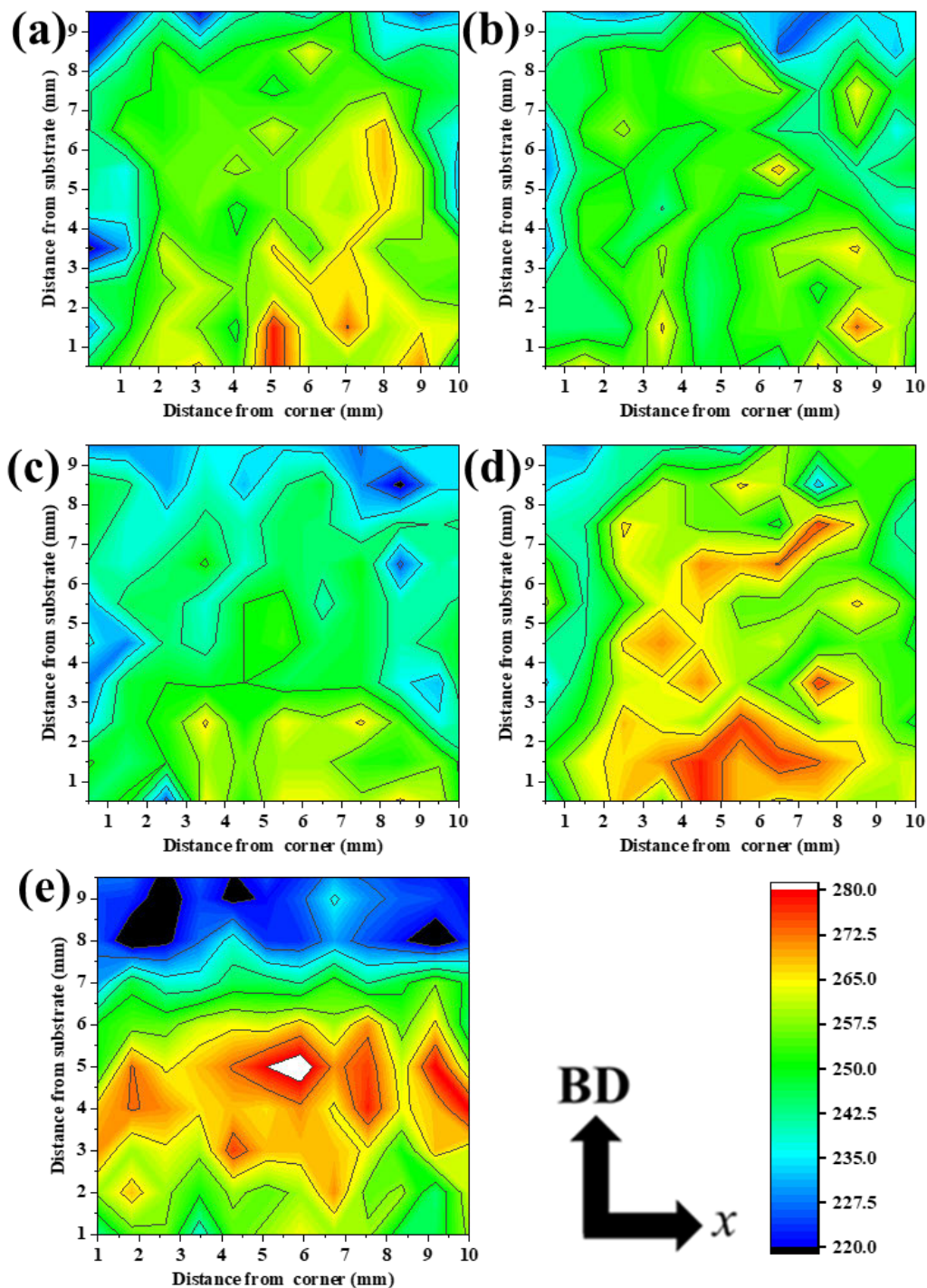


Figure 4.20: (a) – (e) Hardness map of the vertical sections of all the as-build samples of C1, C2, C3, C4, and C5, respectively; the building direction of the deposits and the colour scale bar for the contour maps are indicated.

The above study was used to select a parameter set to apply in the subsequent groove repair study. In deciding which deposition parameters to carry forward, the morphology of the microstructure and porosities in the deposits were considered important. A columnar morphology of the grain structure is expected to introduce

anisotropy in the mechanical properties; therefore, the builds with highly columnar microstructure - C1, C2, and C5 were not considered for the subsequent repairs. The two sets of parameters: 'C4' low energy input; and 'C3', high energy input, exhibited a mix of columnar and equiaxed microstructure and are considered 'best' for repairs. However, the porosities are higher in C4 due to low energy input. This is not desirable, especially for repairs where a good metallurgical bond between the substrate and deposit is expected. Therefore, process parameters corresponding to "C3" have been used for the subsequent repairs.

4.3.2 Microstructure and mechanical properties of repair deposits

4.3.2.1 Microstructure and Hardness

Figure 4.21 (a) shows the BSE SEM photomicrograph of the base material (substrate), An EBSD map showing the wrought microstructure is shown in Figure 4.21 (b). The substrate exhibits a high-volume fraction ~ 0.50 of $\Sigma 3$ twin boundaries calculated from the EBSD map. The as-received plates were in annealed and aged condition and exhibited an average hardness of $H_v 425 \pm 20$. The alloy exhibit coarse equiaxed grains with an average grain size of $\sim 94 \pm 4 \mu\text{m}$, measured using circle equivalent diameter from EBSD data. Dispersed blocky-shaped MC (NbC) particles and twins were present in the microstructure. Figure 4.21 (c) and Figure 4.21 (d) shows the EDS line scan analysis confirming the presence of (Nb, Ti) C in the wrought substrate material. It can be seen that the NbC appears as a bright blocky phase and TiC as a dark round-shaped phase, as shown in Figure 4.21 (d).

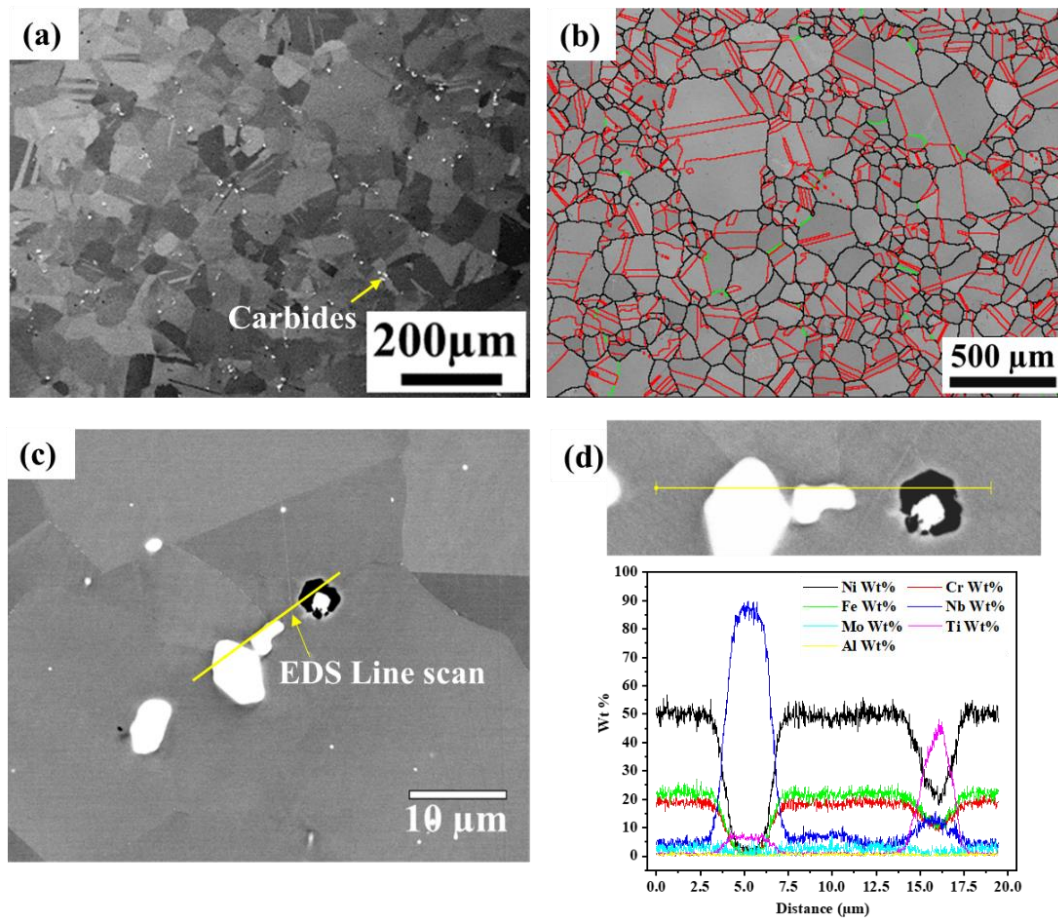


Figure 4.21: Microstructure of base material (a) BSE -SEM micrograph showing columnar grains with blocky NbC carbides; (b) EBSD map showing high angle (black) and low angle (green) grain boundaries and $\Sigma 3$ twin boundaries (red); (c), (d) EDS line analysis for identification of NbC and TiC.

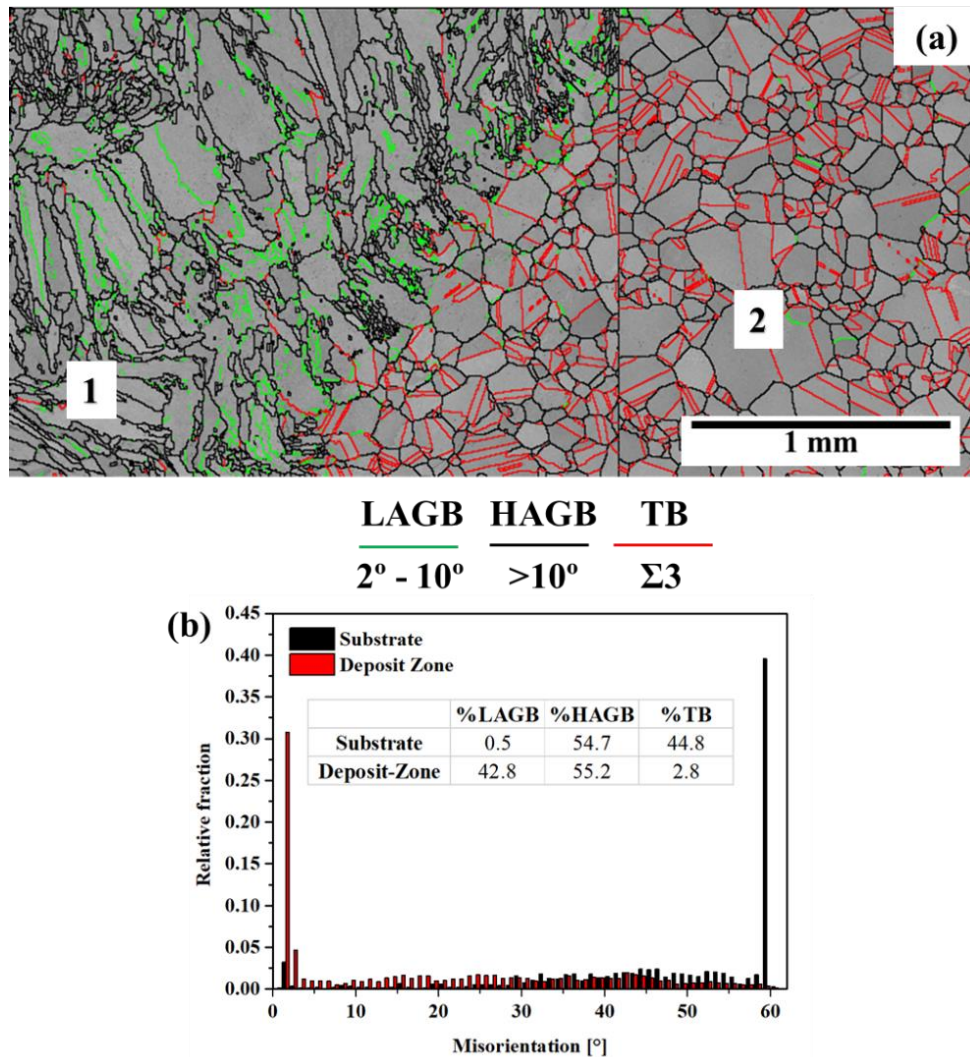


Figure 4.22: (a) EBSD map showing the microstructure of the repaired composite, (1)- the deposit zone and (2)- substrate, and (b) the misorientation distribution in 1 and 2.

The EBSD map showing a representative as-deposit microstructure of the repaired component is shown in Figure 4.22 (a). The repaired component can be classified as (a) deposit – zone (DZ)- indicated as 1 and (b) substrate- indicated as 2 in Figure 4.22 (a); and (c) the deposit-substrate interface. The distribution of the misorientation in the deposit zone and substrate is shown in Figure 4.22 (b). The microstructure in the deposit zone is distinctly different to that of the substrate in terms of grain shape, and distribution. The EBSD measurements further indicate that deposit zone contains a large fraction of low-angle grain boundaries (LAGBs, 2°-10°, ~ 43% of the total GBs) and very low <3 % of $\Sigma 3$ twin boundaries (TB), whereas the substrate consisted of a high fraction of $\Sigma 3$ TB ~45% of the total GBs. The deposit zone microstructure matches well with the as-deposited cubes printed with the same parameter combination

(Section 4.3.1.2). These low-angle grain boundaries are often associated with laser additive IN718 components and are generally a consequence of the very high cooling rates associated with laser AM processes, and are abundantly reported in the literature for AM IN718 [93,188,196,197]. It was shown by Yi et al. [188] that for DED manufactured Ni-base superalloy, high dislocation density is formed along the cells formed during the manufacturing process. These large population of dislocations arrange themselves to accommodate for the lattice curvature and leads to the formation of LAGBs.

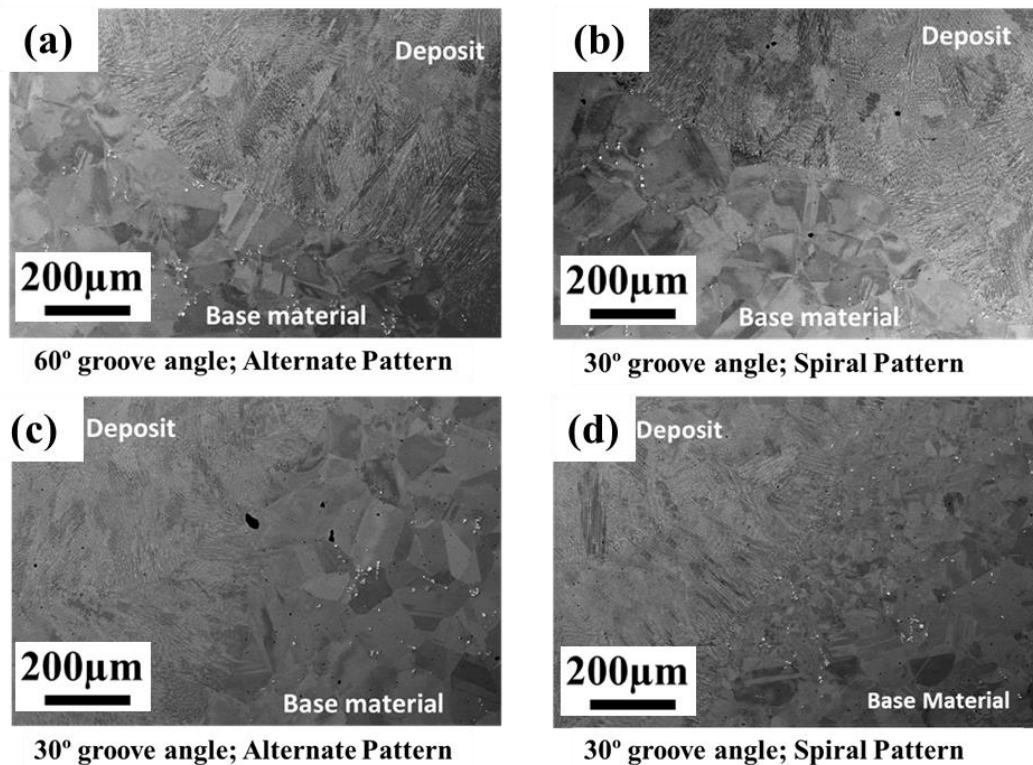


Figure 4.23: Microstructure of the repaired composites in as-deposited condition: (a) 60° groove angle; Alternate Pattern; (b) 60° groove angle; Spiral Pattern; (c) 30° groove angle; Alternate Pattern; (d) 30° groove angle; Spiral Pattern.

Low magnification SEM micrographs showing the microstructure of the repaired composites with different groove angles and scanning patterns adopted during the deposition process are shown in Figure 4.23 (a – d). For all repair angles and scan patterns, the repaired regions (deposit and interface) were free from defects such as porosities, cracks and lack of fusion defects.

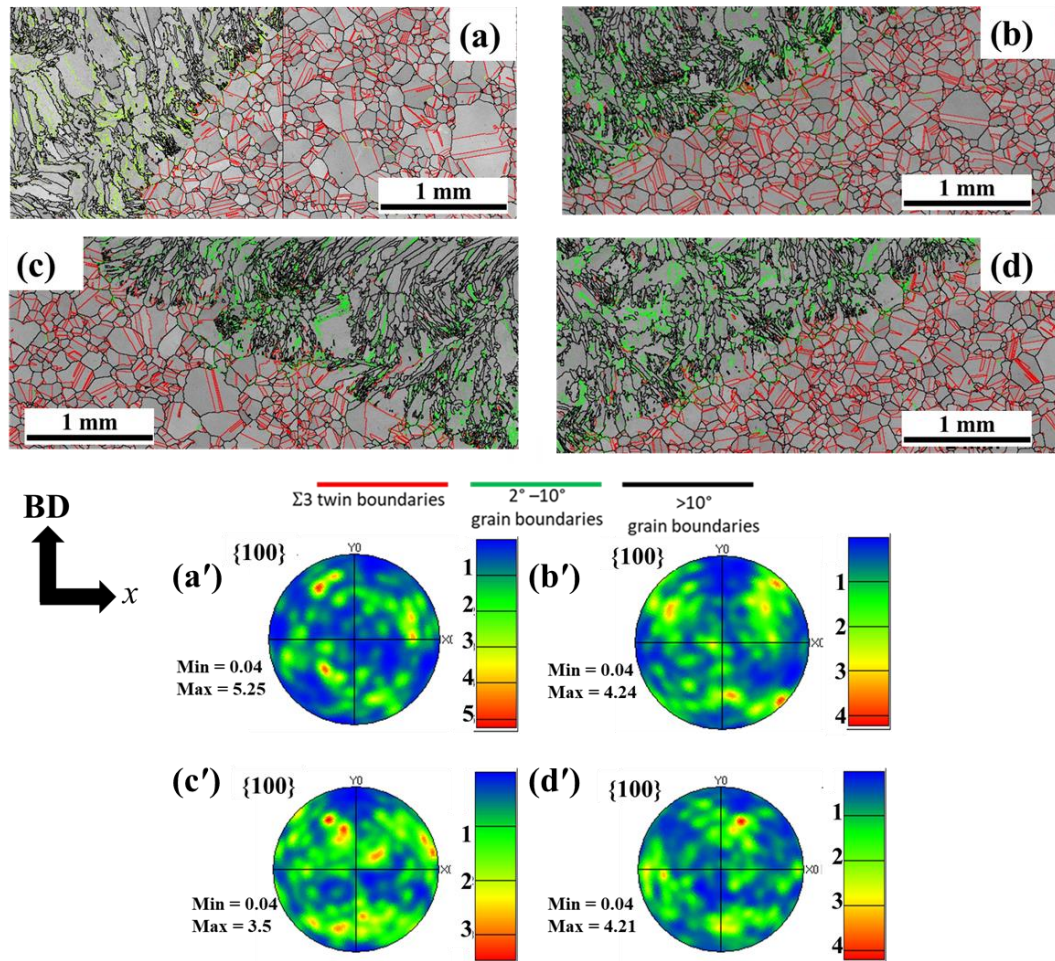


Figure 4.24: EBSD maps of the repaired composites in different as-deposited conditions: (a) 60° groove angle; Alternate Pattern; (b) 60° groove angle; Spiral Pattern; (c) 30° groove angle; Alternate Pattern; (d) 30° groove angle; Spiral Pattern. The corresponding $\{100\}$ pole figures of the deposit zone are shown in (a') – (d').

The EBSD maps of the repaired composites are indicated in Figure 4.24 (a) – (d). The corresponding $\{001\}$ \parallel BD pole figures of the deposit zone are shown in Figure 4.24 (a' – d'). The $\{001\}$ \parallel BD texture component for all the repaired composites in as-deposited conditions exhibits weak and random texture measured over ~ 900 grains in every case. The repaired zone microstructure contained a mix of columnar and equiaxed grains growing along the deposition direction from the machined groove walls. Figure 4.25 shows the effect of groove angle and scanning pattern on distribution and average grain size in the deposit zone of the repaired composites in as-deposit conditions. The grain size analysis was based on >1000 grains; hence, the texture interpretation has the required statistical importance. The different groove angle or scanning pattern does not appear to significantly affect the grain size in the deposit zone. In all the conditions, an average grain size of $\sim 35 \mu\text{m}$ is observed in the

deposit zone measured from the EBSD data using the circle equivalent method. However, some difference in the orientation of the grains is observed with varying scanning patterns discussed as follows. A ‘zig-zag’ type dendritic morphology is observed in the alternate pattern shown in Figure 4.26 (a)), whereas, in the spiral scanning pattern shown in Figure 4.26 (b), the grains are preferably oriented perpendicular to the groove walls. A zig-zag type dendritic morphology occurs due to the primary dendritic growth changing by 90° with changing layers. During solidification of FCC metals and alloys, secondary dendrites grow perpendicular to the primary dendrites as the $\{100\}$ planes are perpendicular to each other. A 90° change happens when there is no nucleation occurring at the layer interface, and primary dendrites grow epitaxially from the secondary dendrites of the previous layer, as reported by Dinda et al. [10] and Parimi et al. [11] for DED-processed IN718. Additionally, some new grains would form at the solid–liquid interface where the $\{100\}$ crystallographic orientation parallel to the heat flow direction is not met. However, only the grains that meet the preferred crystallographic orientation grows, restricting the growth of the other grains. When there was nucleation at the layer boundaries, a change of the primary dendrite by $\sim 60^\circ$ was observed [10,11].

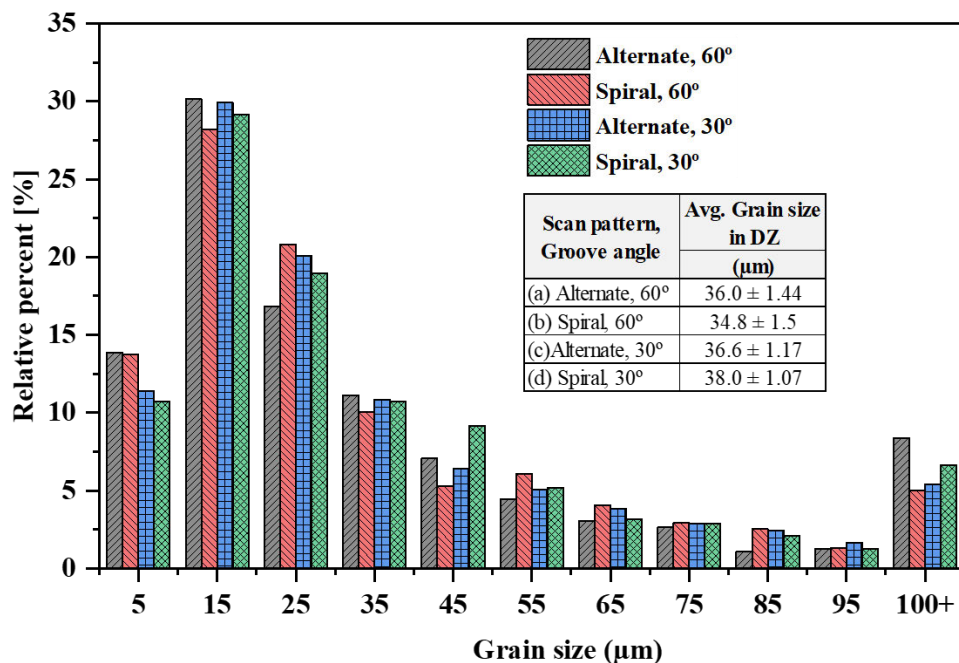


Figure 4.25: Grain size distribution and average grain size in the deposit zone of the repaired composites in as-deposit condition.

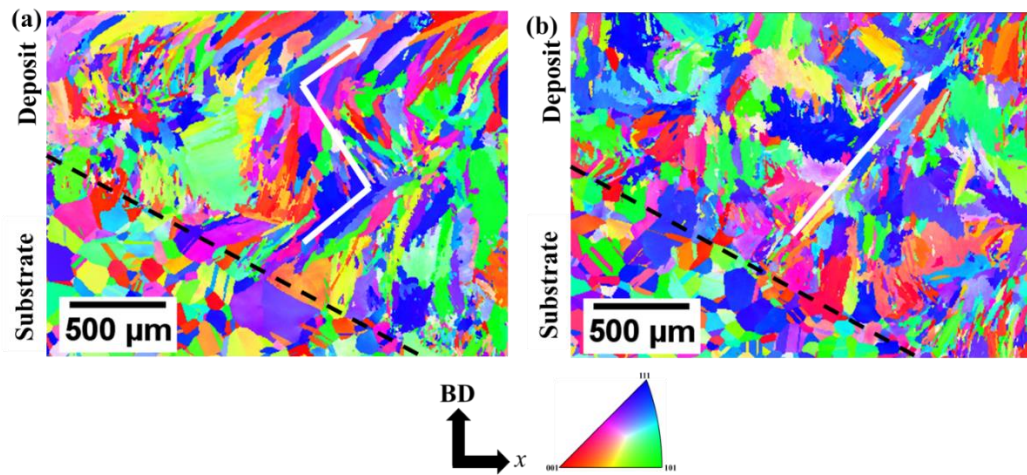


Figure 4.26: EBSD maps for 60° grooves: (a) Alternate pattern, (b) Spiral pattern; and (c), (d) their respective $\{100\}$ pole figures for deposit zone only; arrows indicate the dendritic growth direction.

It is to be noted that the studies by Dinda et al. [10] and Parimi et al. [11] considered single wall builds on substrate, and the heat dissipation through the substrate (and previously deposited layers) was unidirectional. The dendrite orientation is influenced by the direction of the resultant heat fluxes due to the moving heat source (laser head) and the substrate, which is the heat sink. However, during groove repairs, the heat dissipation is more complex as the heat flow occurs through the groove walls and groove-base. Therefore, the local heat flow is not necessarily unidirectional, as in the studies mentioned above. The effective heat flux can be attributed to the position of the laser head in the groove. When the laser head is closer to the groove walls, the dendrites grow perpendicular to the groove walls and gradually become perpendicular to the groove base as the heat source moves away from the sidewalls. Moreover, as the dendrites tend to grow perpendicular to the previous layers of dendrites, this results in a randomly oriented grain morphology. Figure 4.27 shows an illustration of the heat flux directions and dendritic growth. Vector q_x represents the heat flux due to the laser source; the substrate act as the heat sink; however, due to the groove geometry, the heat is dissipated along the groove walls and the groove base. Vector q_{zs} represents the heat flux due to groove sidewalls, and q_{zb} = heat flux due to substrate groove base. q_r is the resultant heat flux direction. When the laser head moves from point A to B (right to the left), the heat flux due to the heat source will be in the opposite direction (left to right). When the laser head is at point A and point C (close to the sidewalls), the resultant heat flux is not necessarily parallel to the building direction, the resultant heat flux will be at an angle to the building direction, and therefore, the dendritic growth

observed is perpendicular to the groove walls. At point B (in the centre of the groove), the heat fluxes due to the groove walls would be equal and opposite and cancel each other; thus, the resultant heat flux will be perpendicular to the groove base. Thus, at every point in the repaired section, there is competition among the dendrites at different angles for growth. This results in a random dendritic growth, and the effect of the scanning pattern is not realised as observed in the literature [10,11].

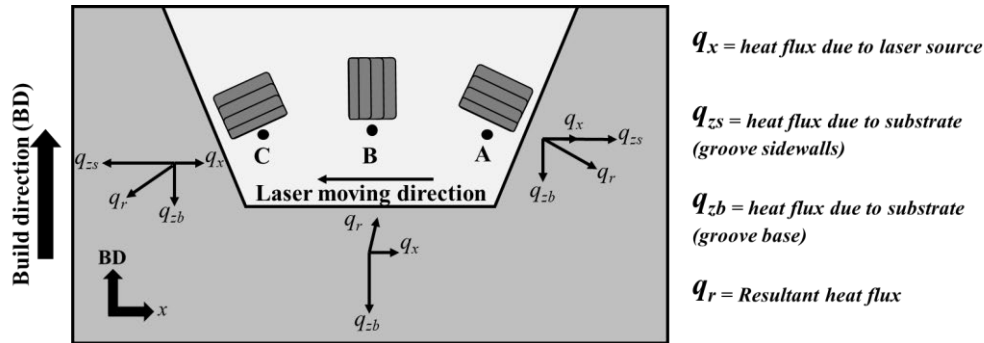


Figure 4.27: Schematic of the heat flux directions and dendritic growth.

The effect of post-deposit heat treatment on the microstructure of the repaired composites is shown in Figure 4.28 (a – f). The morphology of the grains in both the substrate and the deposit zone seems to be unaffected by the post-deposit heat treatment. The as-deposited microstructure exhibited Laves phases in the interdendritic regions, as shown in Figure 4.28 (d). The distribution of Laves phases in the as-deposit microstructure matches well with the cubes printed with the same parameter combination as discussed earlier in Section 4.3.1.3. The direct aged (DA) heat treatment did not alter the size of the dendrites and the morphology of the interdendritic Laves phase, as shown in Figure 4.28 (b) and (e). The solution-treated and aged (STA) microstructure in Figure 4.28 (f) shows the presence of δ phase along with the Laves phase at the interdendritic regions. The δ phase can be easily identified by its needle-like morphology. Needle-shaped δ phase is abundantly reported in AM IN718 literature that forms upon solution treatment between 950°C – 980°C (See for, e.g. [40,198]). Figure 4.29 shows the EDS point analysis showing the presence of needle-shaped delta phase and Laves phase in the deposit zone post-STA heat treatment. The δ phase contains comparatively less Nb (8 – 10 wt %) compared to the Laves phase which contains >10 wt % Nb as reported by Qi et al [93] for DED fabricated IN718. A 980°C solution treatment is unable to dissolve the Laves phase completely, and it is observed in Figure 4.29 that δ phase precipitation occurs

exclusively around Laves particles. The high concentration of Nb in the Laves phase facilitates the formation of the δ phase in these regions[14].

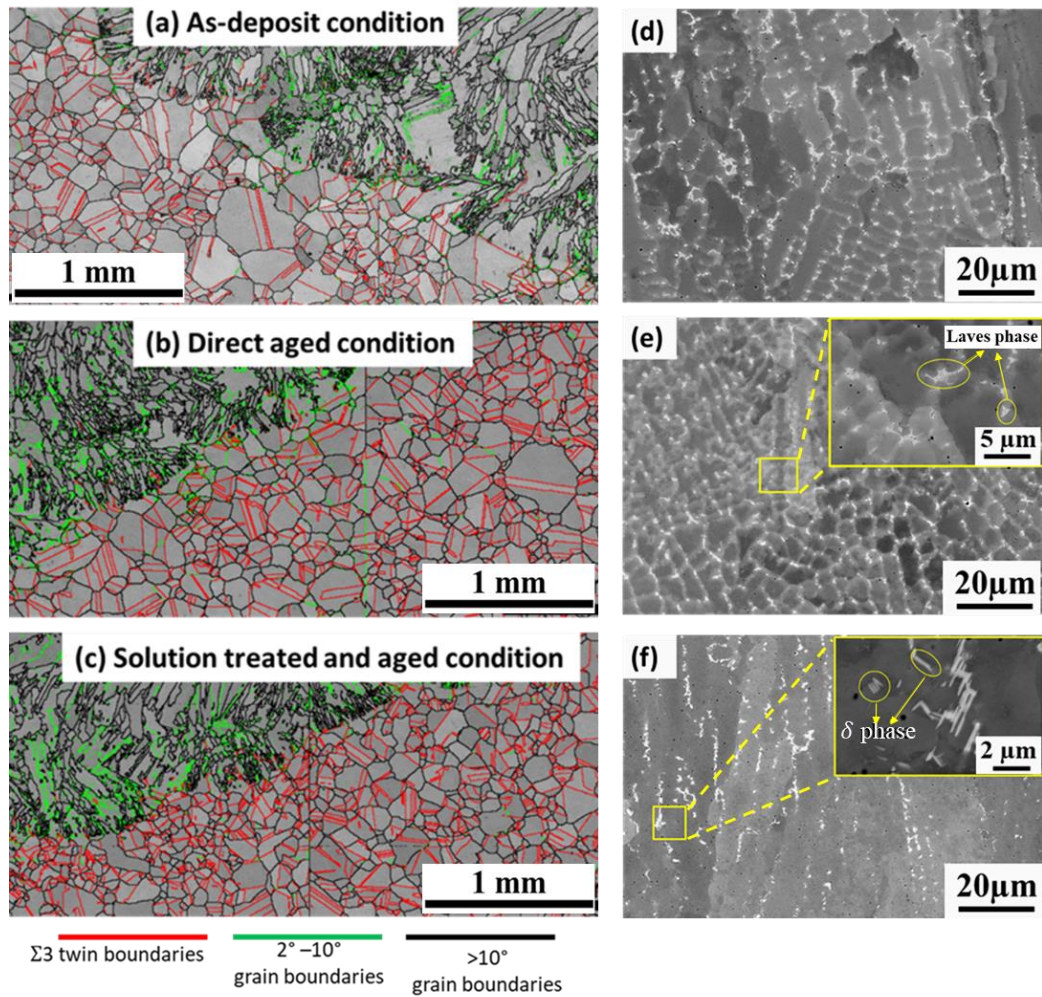
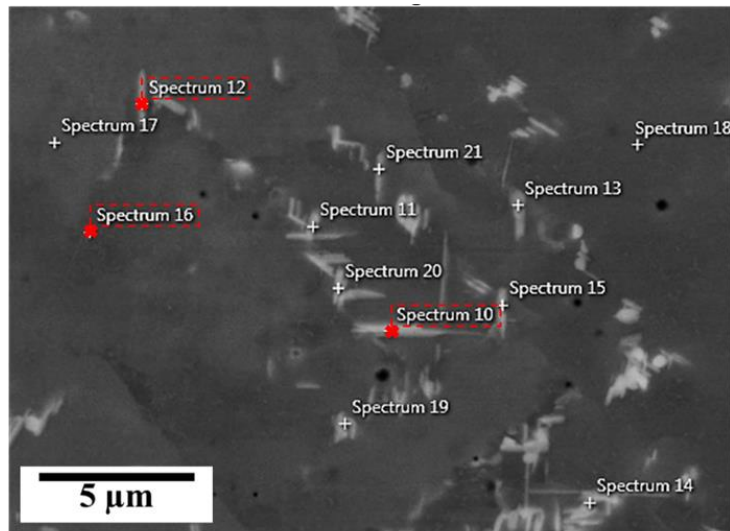


Figure 4.28: EBSD maps with grain boundaries superimposed on the repaired composite after heat treatments: (a) As-deposited; (b) Direct aged; (c) Solution treated and aged; (d), (e), (f) are high magnification BSE-SEM micrographs showing the distribution of the phases in the deposit zone in (a), (b) and (c) respectively.



Element	Composition (Wt%)		
	Spectrum10	Spectrum12	Spectrum16
Ni	57.2	53.8	51.6
Cr	10.9	16.3	20.1
Fe	11	16.1	19.7
Nb	16.8	9.6	4.3
Mo	2.1	2.5	3.0
Ti	1.8	1.2	0.9
Al	0.3	0.4	0.5
Phase	Laves	δ - phase	Matrix

Figure 4.29: EDS point analysis on the deposit zone of a repaired sample under STA condition.

The grain size in the deposit zone and substrate is shown in Figure 4.30 (a). Average grain size of $\sim 35 \mu\text{m}$ is observed in the deposit zone and $\sim 100 \mu\text{m}$ in the substrate, measured from the EBSD data using the equivalent circle method. It is observed that the groove angle or post-deposit heat treatment did not change the grain size in the deposit zone or substrate. The hardness profile across the repair interface in as-deposited and post-HT conditions is shown in Figure 4.30 (a). In the as-deposited conditions, the hardness in the deposit zone is low compared to the substrate. The low hardness in the deposit zone can be attributed to the absence of strengthening precipitates, γ' , γ'' . There exists a region in the substrate side of the deposit zone – substrate interface where a dip in the hardness values is observed. During the deposition process, the local temperature in the substrate near the deposit zone – substrate interface is high enough to dissolve the strengthening phases pre-existing in the aged substrate. The high cooling rates inherent to DED prohibit the reformation of

the hardening precipitates [199]. This result in the formation of a heat-affected zone (HAZ) in the substrate. A low hardness HAZ is also reported by Zhai et al. [95] and Guévenoux et al. [9] in DED manufactured IN718. Interestingly, the groove angle of the repaired component influenced the resulting HAZ. A 30° groove wall angle had a wider HAZ as measured by hardness testing compared to the 60° groove angle. After the post-heat treatment processes, the hardness of the repair region was uniform, despite the variation of the grain size distribution across the substrate and repaired zone. Thus, it appears that the γ'' , γ' precipitates that form upon ageing heat treatment are the dominating factor that determines the hardness of the repaired composite. The results agree well with the ones reported by Zhai et al. [95] in DED IN718, where the hardness values become uniform post heat treatment. Also, it has been reported in wrought IN718, in aged conditions, that the hardness was independent of the grain size. The rapid cooling rates during DED processing do not allow sufficient time for the formation of the strengthening precipitates; therefore, for the repair of IN718 using AM, post-deposit heat treatments are critical in improving the mechanical properties of IN718. Moreover, the solution treatment was restricted to 980°C to avoid grain size coarsening, although 980°C is insufficient to dissolve the Laves phase completely. It has been reported by Chlebus et al. [14] in SLM processed IN718 that solution treatment at 1100°C is able to dissolve the Laves phase; however, this temperature it causes significant grain growth. A coarser grain structure, especially in the substrate, is undesirable because it deteriorates the high-temperature mechanical properties [85].

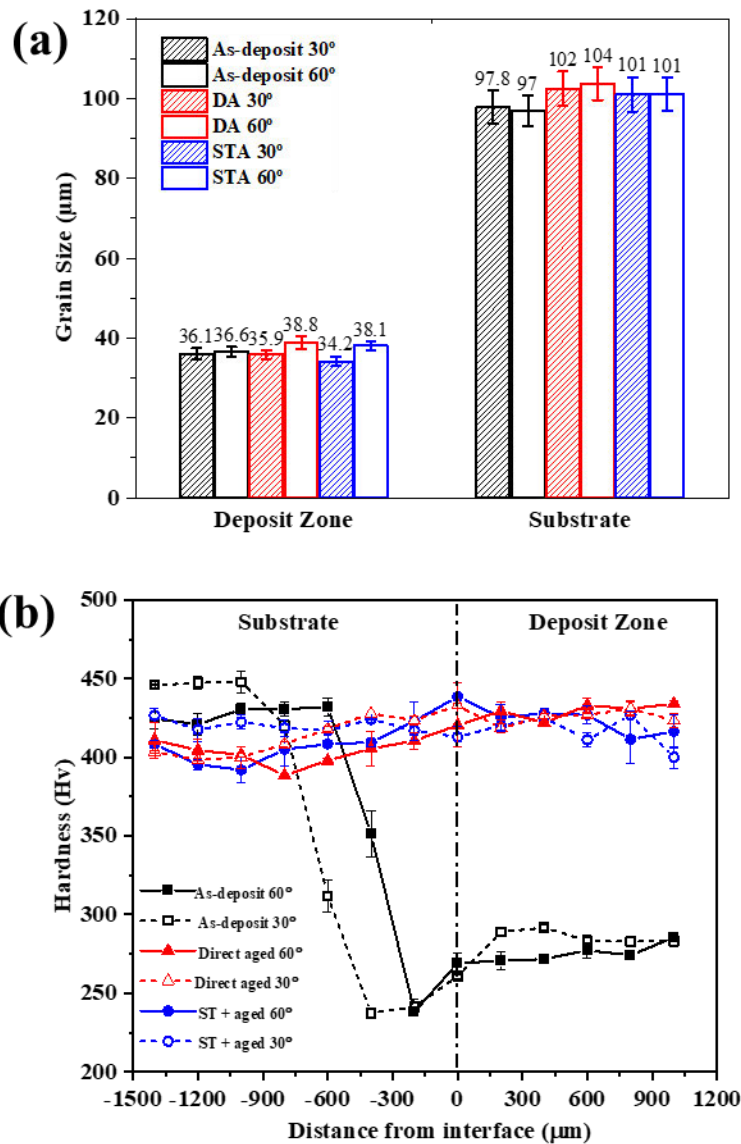


Figure 4.30: Effect of groove angle and post deposit heat treatment for the repaired composites: (a) variation of hardness from the deposit zone to substrate across the repaired interface; and (b) average grain size in the deposit zone and substrate.

4.3.2.2 Mechanical properties: 4 – point bend test results

Figure 4.31 represents the load-displacement curves of the 4-point bend tests of the repaired components. The bend tests were stopped at ~ 15 mm extension for the direct aged (DA) and solution treated and aged (STA) specimens as they started to slip due to the high loads. It was observed that under all conditions, the samples with 30° groove angles did not fail before stopping the bend tests. The average values of the maximum load (P_{max}) for all the specimens tested is shown in Figure 4.32. A significant increase in the values of load ~100% was observed upon post-heat treatment of the repaired composites. It can be inferred that the repaired composites strengthened significantly

upon post HT, as evident from the hardness profile shown in Figure 4.30(a). A similar trend in mechanical properties is often observed in DED manufactured IN718[93,95]. The DA and STA heat treatments did not exhibit significant differences in their peak load; however, a 60° groove angle recorded slightly higher load values compared to a 30° groove angle. As not all the samples were tested to failure, the actuator extension (displacement) at P_{max} is recorded as a measure of ductility. An effect of the groove angle of the repair is observed on the actuator extension at P_{max} as shown in Figure 4.32 (b). The repaired components with 60° groove angle exhibited ~10% lower displacement at corresponding P_{max} points. Therefore, it can be inferred that the 30° groove wall allows higher deformation compared to the 60° groove wall.

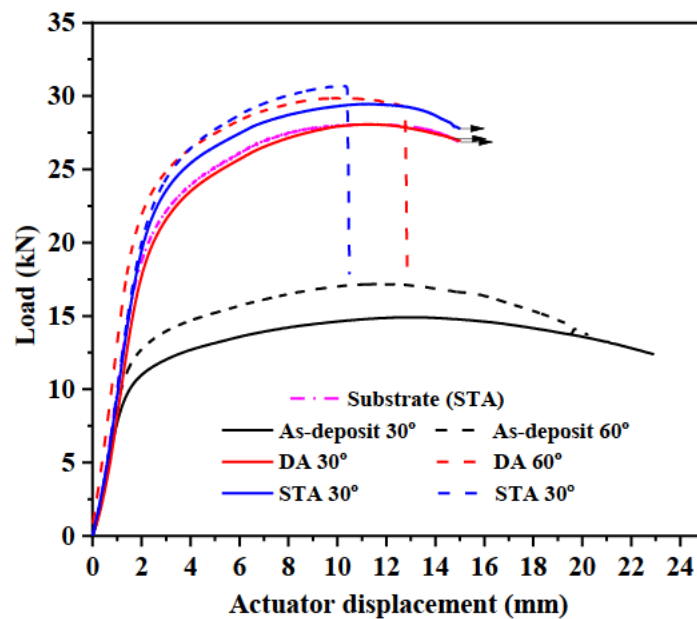


Figure 4.31: Load – displacement curves for the 4-point bend tested samples.

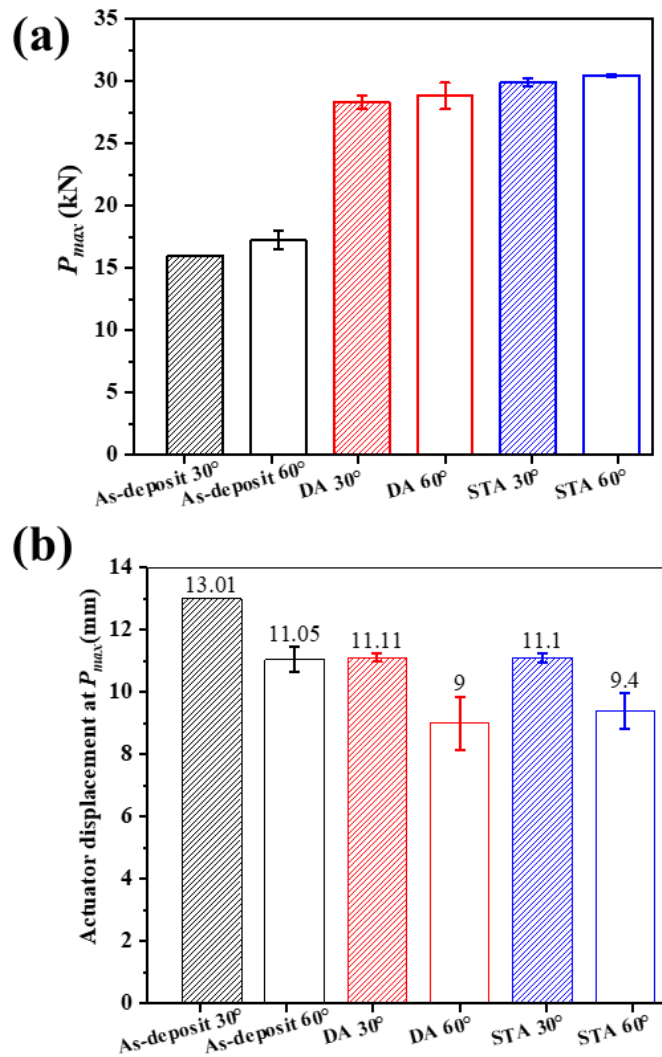


Figure 4.32: 4-point bend test results: (a) Maximum load, P_{max} (b) Actuator displacement at P_{max} .

The strain distribution map on the top surface of the bend specimens at P_{max} is shown for the substrate in Figure 4.33 (a). Figure 4.33 (b) shows the strain values in the span between the loading pins, i.e. the pure bend region. Uniform strain distribution of ~8% is observed across the 30 mm span between the loading pins.

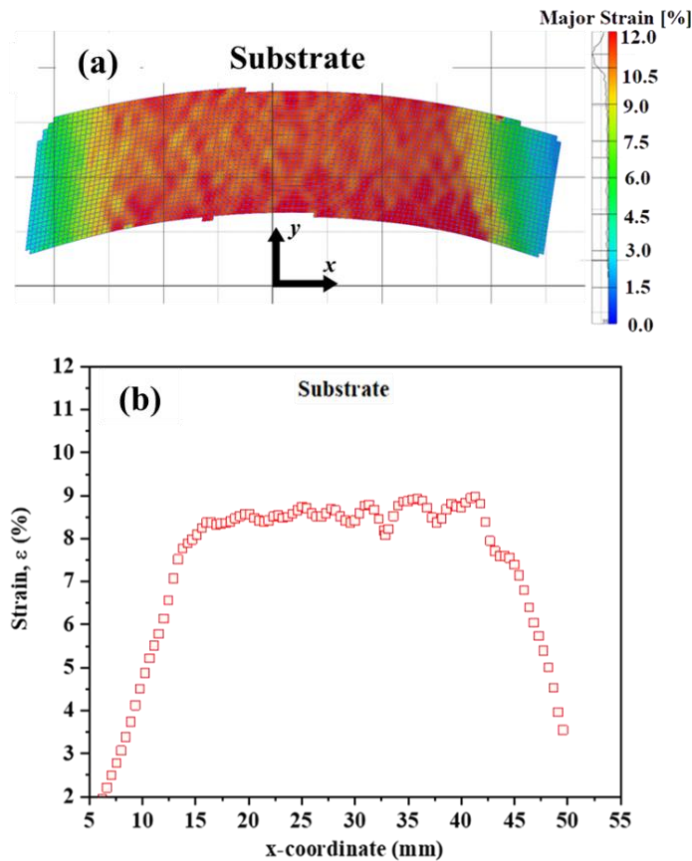


Figure 4.33: Strain distribution on the top surface at P_{max} of the 4-Point bend specimen substrate (a) Strain map; (b) value of strain in the region between the loading pins (pure bend region).

The strain distribution maps and the values of strain measured at P_{max} using DIC across the repaired composite—from substrate to the deposit zone, for the as-deposited, DA and STA specimens at both groove angles are shown in Figure 4.34 (a – c), Figure 4.35 (a – c), and Figure 4.36 (a – c) respectively. It was observed that the strain values were higher for the repairs with a groove angle of 30° in both heat-treated conditions, consistent with the higher extension in the bend test. The effect of groove geometry has been reported in welding studies [200] studied the effect of groove angles on tensile behaviour of Tungsten inert gas (TIG) welded Aluminium alloy; [201] adopted gas metal arc welding (GMAW) to join armour steel plates with V-shaped groove with varying groove angles. Both these studies concluded that, in uniaxial deformation, groove angles with a higher incline of groove angle (corresponding to 30° groove angle in the present study) exhibited higher ductility. Moreover, the strain distribution maps for the repaired composites under all the conditions show strain localisation occurring near the interface between the deposit zone and substrate, which led to subsequent failure at the deposit zone – substrate interface.

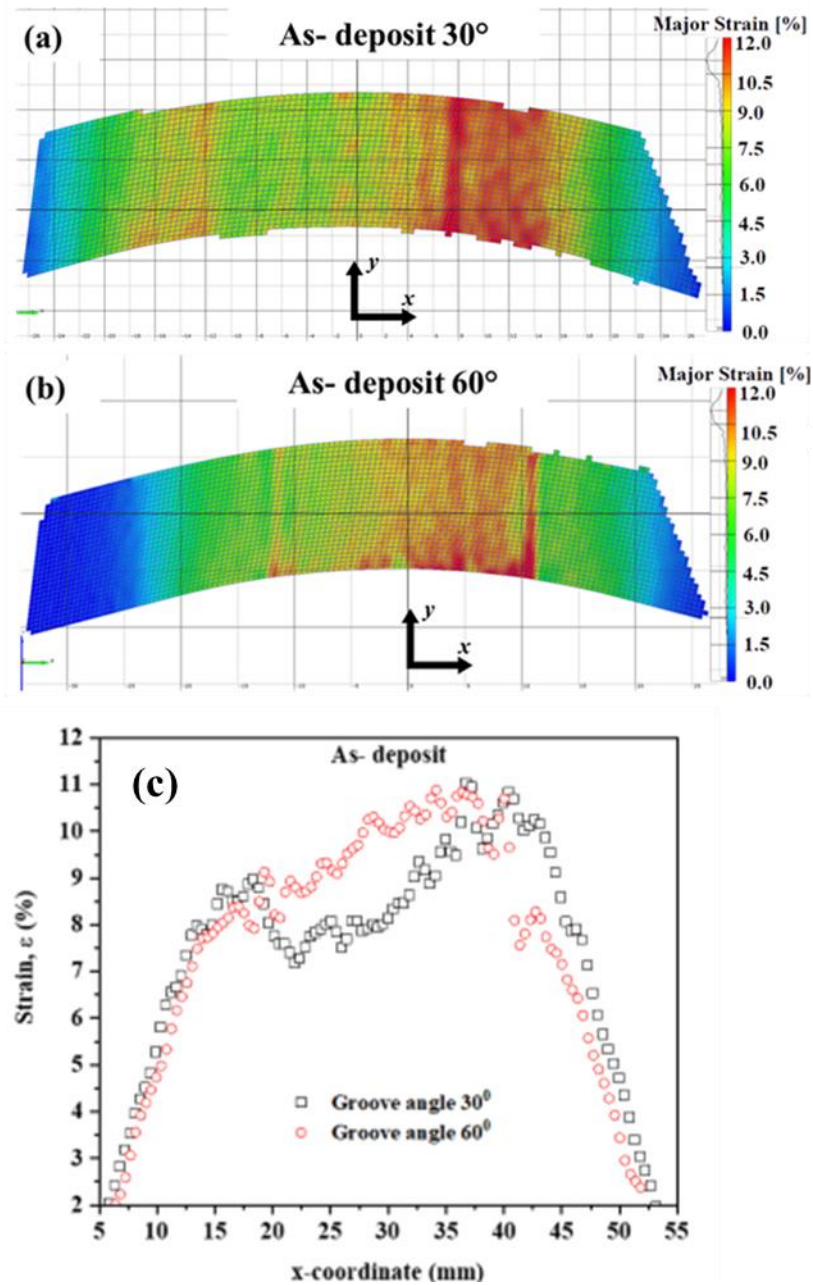


Figure 4.34: Strain distribution maps on the top surface at P_{max} of the 4-point bend specimens in As-deposited condition (a) Groove angle 30°; (b) Groove angle 60°; (c) value of strain in the pure bend region.

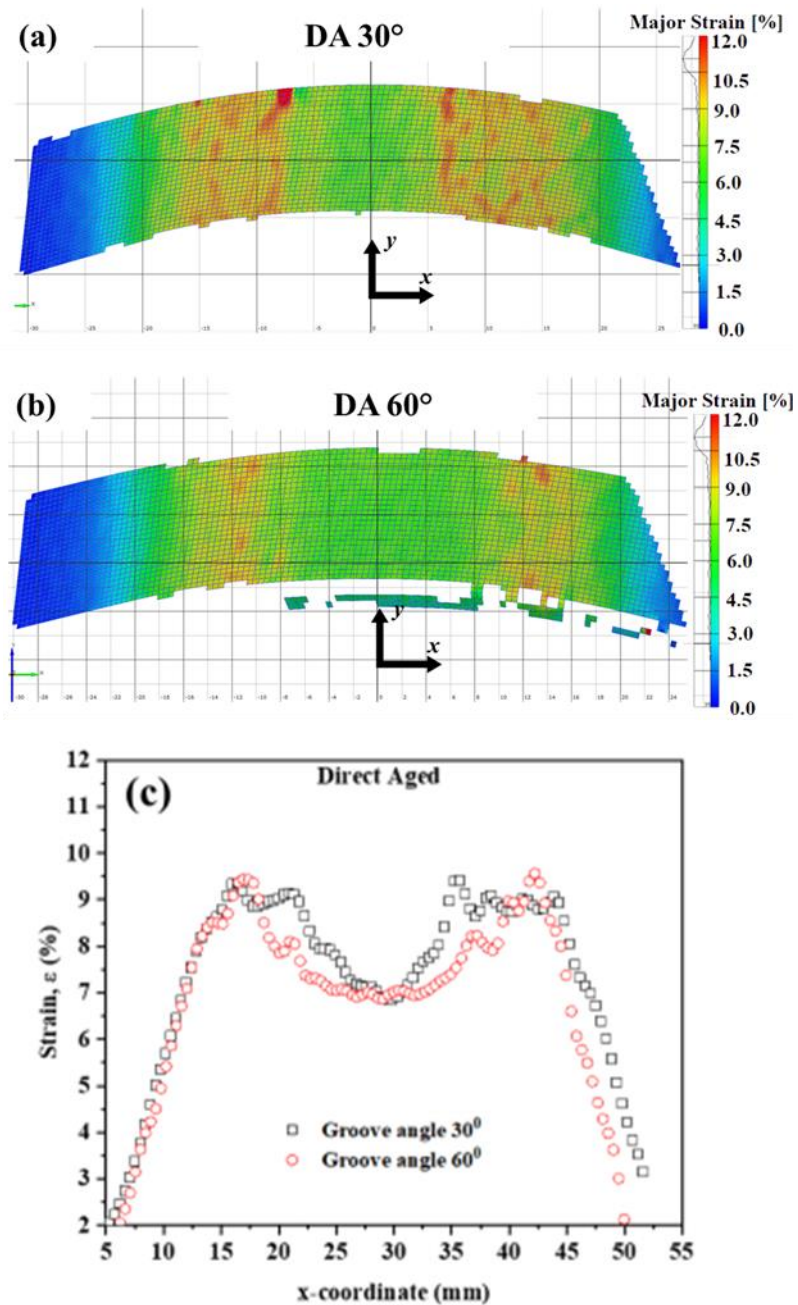


Figure 4.35: Strain distribution on the top surface at P_{max} of the 4-point bend specimens in DA condition (a) Groove angle 30°; (b) Groove angle 60°; (c) value of strain in the pure bend region.

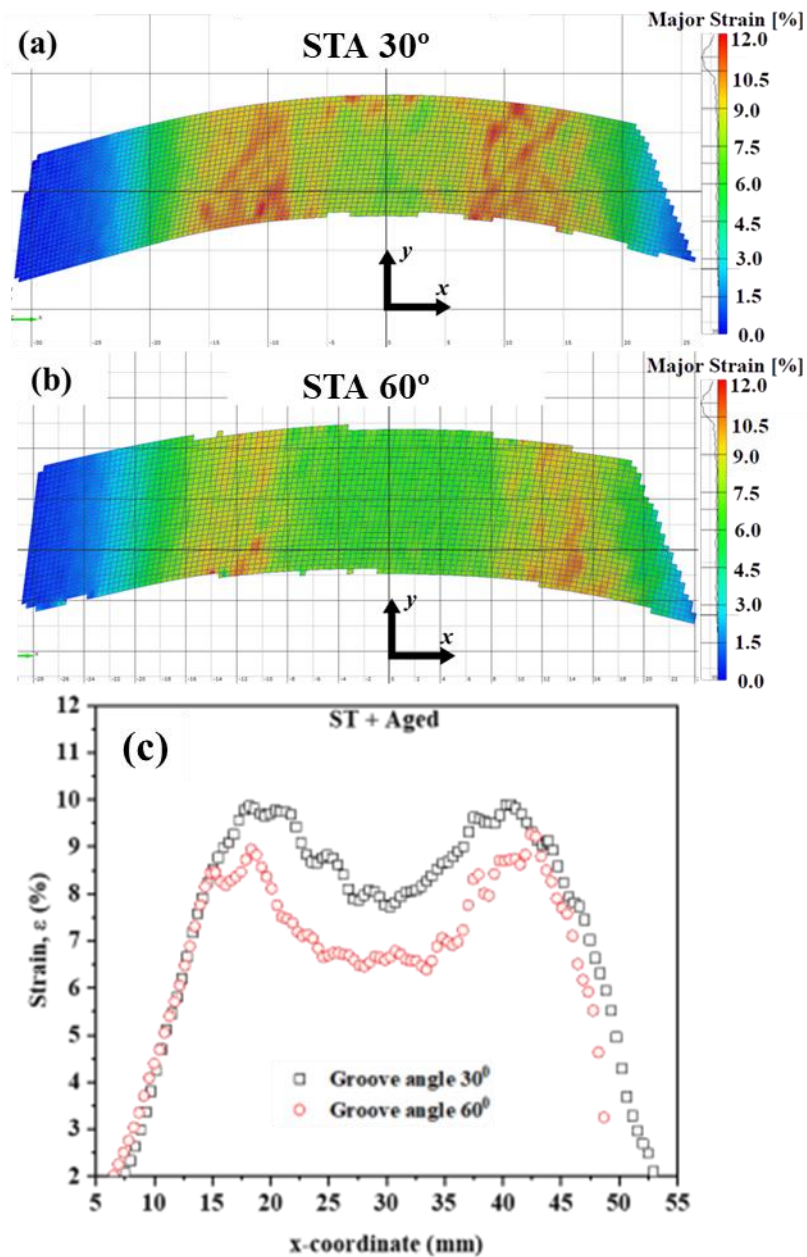


Figure 4.36: Strain distribution on the top surface at P_{max} of the 4-point bend specimens in STA condition (a) Groove angle 30°; (b) Groove angle 60°; (c) value of strain in the pure bend region.

This phenomenon differs from existing literature on IN718 repaired using laser AM techniques where the repaired composites fail in the repaired part. Sui et al. [8] and Guévenoux et al. [9] conducted tensile tests monitored by DIC on “half wrought and half deposit” IN718 with the substrate-deposit interface in the middle of the samples. Both studies revealed that deformation localization occurs in the deposit zone, and the failure mechanism was attributed to the presence of Laves phases in the deposit zone. Moreover, the absence of strengthening precipitates and the presence of columnar grains in the as-deposited condition were attributed to the entire deformation localizing

in the deposit, as observed by Guévenoux et al. [9]. Sui et. al.[68] in an another study found that repaired direct aged samples failed at the interface. The failure at the interface rather than the deposit was attributed to the well-matched mechanical properties of the deposit and the substrate. However, the effect of underlying microstructure in the interface was not explored.

An SEM investigation was conducted to understand the phases present and their distribution near the deposit-substrate interface. Figure 4.37 (a – c) shows the microstructure in the interface of the repaired composite in various heat-treated conditions. In the as-deposited condition shown in Figure 4.37 (a), coarse carbides (NbC) can be seen on the wrought (substrate). Also, some Laves phases are present near the deposit zone-substrate interface. Some wrought grain boundaries near the interface are enriched with Nb. This is expected due to the constitutional liquation of the NbC phases. This phenomenon is often observed during IN718 welding [4,92,202,203]; however, it has not been reported in AM literature. The liquified NbC solidifies in Laves phase composition. Figure 4.38 (a – b) shows the EDS point scans and the chemical compositions of the various phases in the interface region of the repair. A Solution treatment at 980°C is unable to remove these segregations as shown in Figure 4.38 completely (a – b). Laves phases being brittle phases provides easy crack initiation sites, and their presence on the coarse grain boundaries would result in easy crack propagation. Therefore, the presence of Nb-rich phases along the substrate grain boundaries is expected to be highly detrimental to the mechanical properties of the repair.

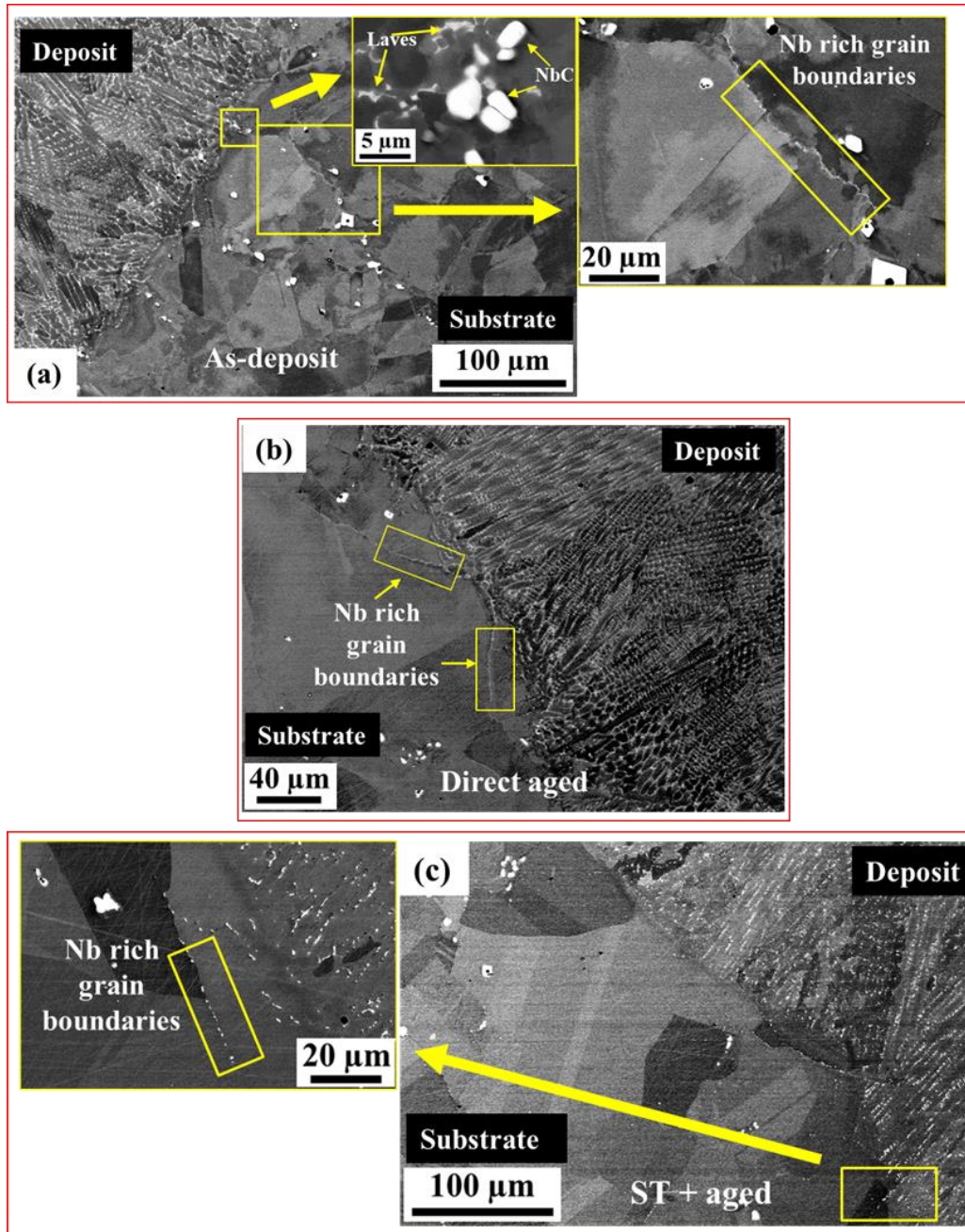
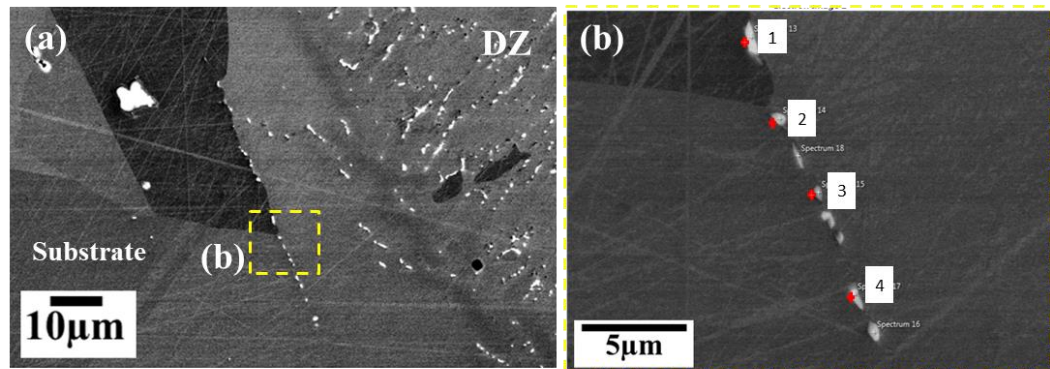


Figure 4.37: Microstructure in the interface of the repaired component after various heat-treated conditions: (a) As-deposit; (b) Direct aged (DA); (c) Solution Treatment and aged (STA).



Spectrum	Element (wt%)							Phase
	Al	Ti	Cr	Fe	Ni	Nb	Mo	
1	0.34	0.59	16.78	19.36	40.29	15.1	7.54	Laves
2	0.41	0.65	17.7	20.49	44.47	10.7	5.53	δ Phase
3	0.47	0.69	18.66	21.5	47.06	7.43	4.19	δ Phase
4	0.54	0.72	18.54	21.29	48.46	6.81	3.64	δ Phase

Figure 4.38: (a) SEM micrograph of repaired samples near the deposit zone-substrate interface in STA condition; (b) high magnification micrograph showing several EDS point scans and their respective chemical compositions.

The longitudinal section of the fracture is shown in Figure 4.39 (a – b) and Figure 4.40 (a – b) in STA and DA conditions, respectively. The investigation is restricted to the repaired composites with 60° grooves as the repaired composites with 30° grooves did not fail during the 4-point bend test. It is observed that the final failure occurred at the deposit zone-substrate interface; therefore, the longitudinal sections on both deposit zone and substrate are examined under SEM. In both the heat-treated conditions, broken Laves phase particles and carbides can be seen in the investigated section in the deposit zone as shown in Figure 4.39 (a) for STA and Figure 4.40 (a) for DA condition. It is clear the final fracture that followed a transgranular path along the groove wall. On the substrate side (Figure 4.39 (b) for STA and Figure 4.40 (b) for DA condition), cracks around large broken carbides particles at the substrate grain boundaries are observed. The failure has initiated from the relatively flat grain boundaries of the coarse grains in the substrate and propagated through the deposit zone-substrate interface. Figure 4.41 (a) and Figure 4.41 (b) show the fracture surface of the samples tested under STA and DA conditions, respectively. Several dimples of varying sizes can be seen that imply regions of ductile failure mode. However, the as-deposited fracture surface Figure 4.41 (b) exhibited some flat and smooth areas where the fracture mode is more cleavage type. Some bright and irregular-shaped particles

are embedded in the fracture dimples, which are mostly Laves phase, δ phase and carbide particles.

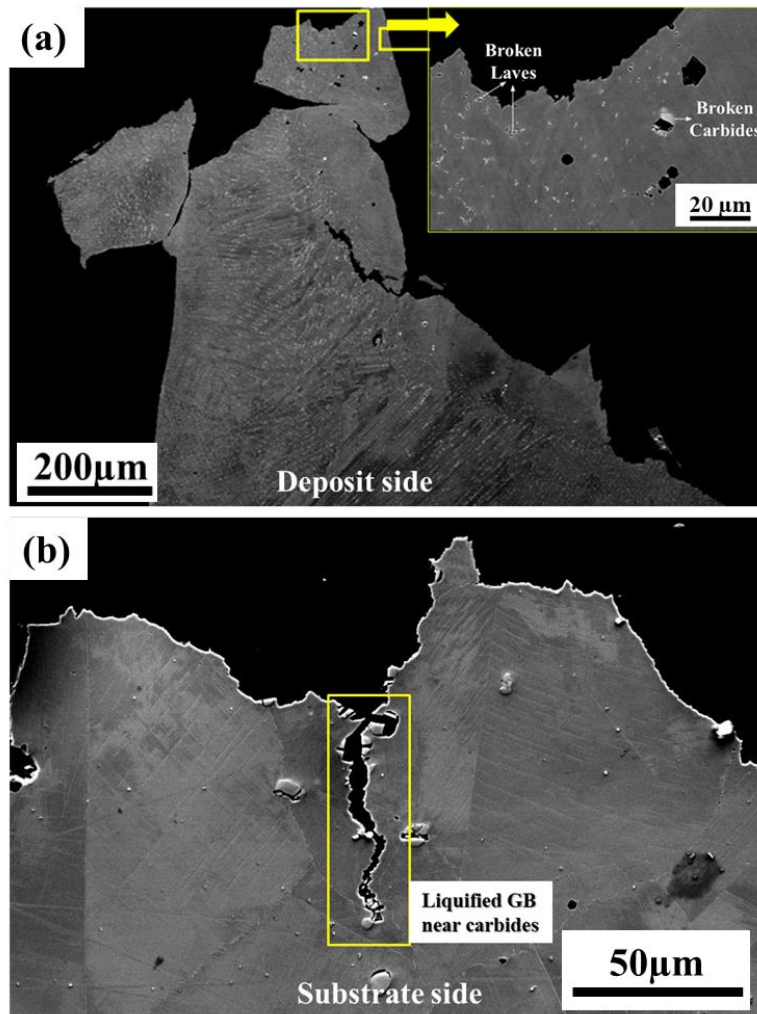


Figure 4.39: The longitudinal section of one fractured sample 60° groove angle; STA condition: (a) Deposit side; (b) Substrate side.

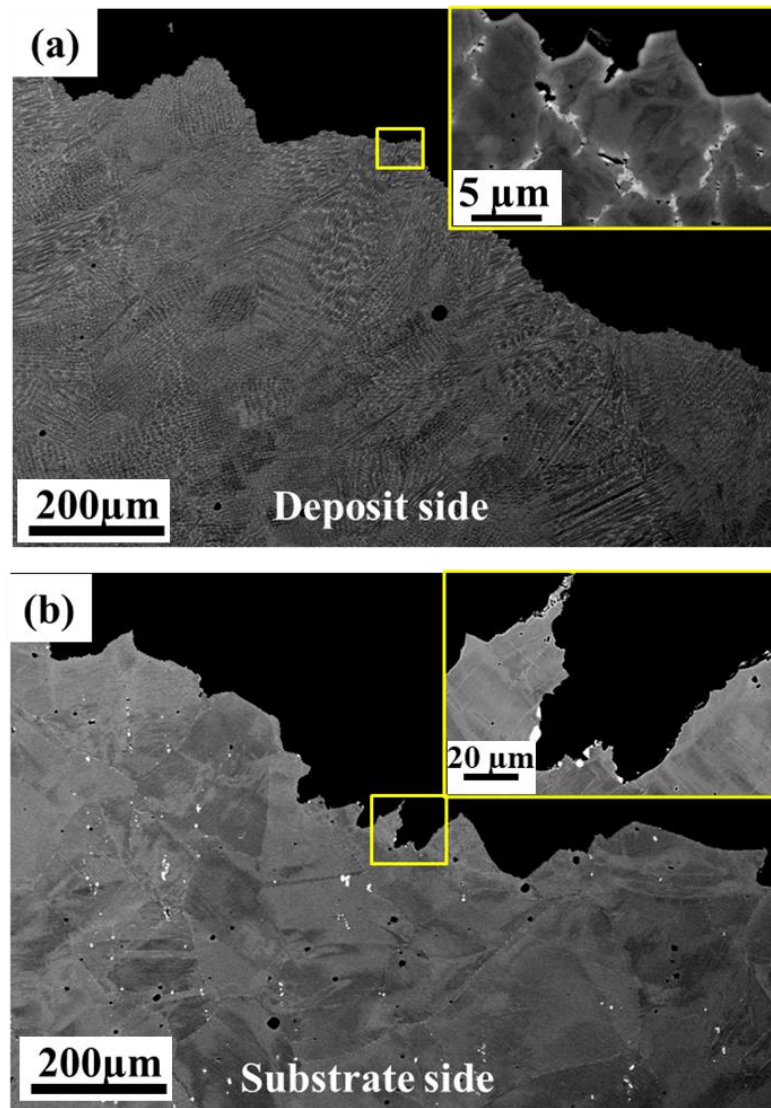


Figure 4.40: The longitudinal section of one fractured sample 60° groove angle; DA condition: (a) Deposit side; (b) Substrate side.

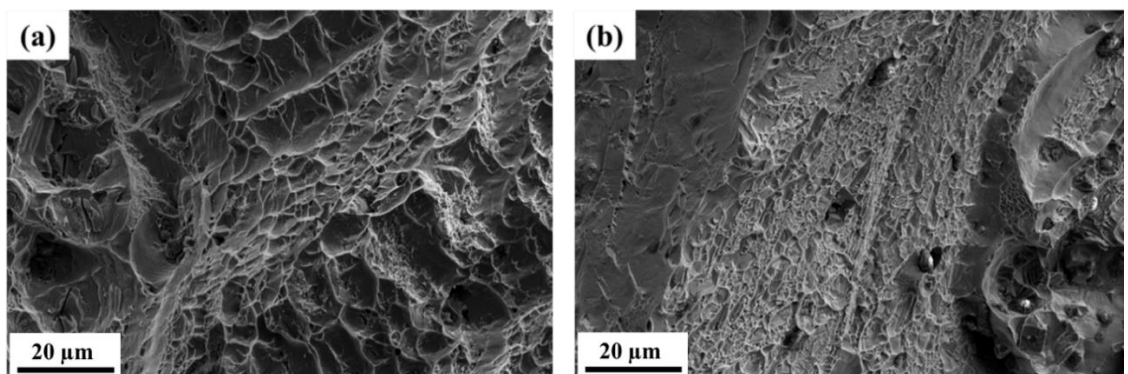


Figure 4.41: Fracture morphologies of the failed bend tested repaired IN718 component after (a) STA; (b) DA condition.

4.4 Discussion

The results from the 4-point bend tests indicate that post-deposit heat treatment restores the strength in the repaired composites. The DIC studies show that the strain localisation in the repaired composite occurs preferentially at the deposit zone-substrate interface. The following section discusses the reason for strain localisation in the repair deposit zone-substrate interface. Moreover, the groove angle also seems to affect the mechanical properties of the repaired composites significantly. The effect of the geometry of the groove on the 4-point test results is also discussed.

4.4.1 Repairability (weldability) of IN718

To understand the failure mechanism in the repaired components, bend tests on direct aged (DA) 60° groove angle specimens were interrupted at 80% of P_{max} . The SEM micrograph for the near interface region of the interrupted specimen (top surface of the specimen) shown in Figure 4.42 exhibits cracks initiating well before reaching instability, i.e. before P_{max} . EDS elemental map of cracks initiated in the HAZ is shown in Figure 4.43. It is observed that the cracks initiate at the substrate grain boundaries rich with Nb or near the Nb carbides (Figure 4.42 (b)). Due to the rapid heating-cooling rate experienced during welding or additive manufacturing processes, the second-phase particles may not be completely dissolved when the eutectic temperature is reached in the HAZ. The metastable liquid may thus nucleate heterogeneously at the interfaces between the remaining second-phase particles and the matrix, followed by rapid melting of the second-phase particles and part of the surrounding matrix [204]. The secondary phases, such as inter-metallics and carbides, suffer local melting at elevated temperatures. In the case of IN718, NbC carbides liquate over a range of temperatures, initiating at a temperature range of 1200°C to 1215°C, below the γ -carbide eutectic $L \rightarrow (\gamma + NbC)$ temperature of 1250°C [205]. Thus, liquid on the HAZ grain boundaries originates due to constitutional liquation of the NbC [92], and the quenched-in liquid formed solidifies to a composition similar to Laves phase. The inability of these liquid films to accommodate the thermal stresses results in crack formation.

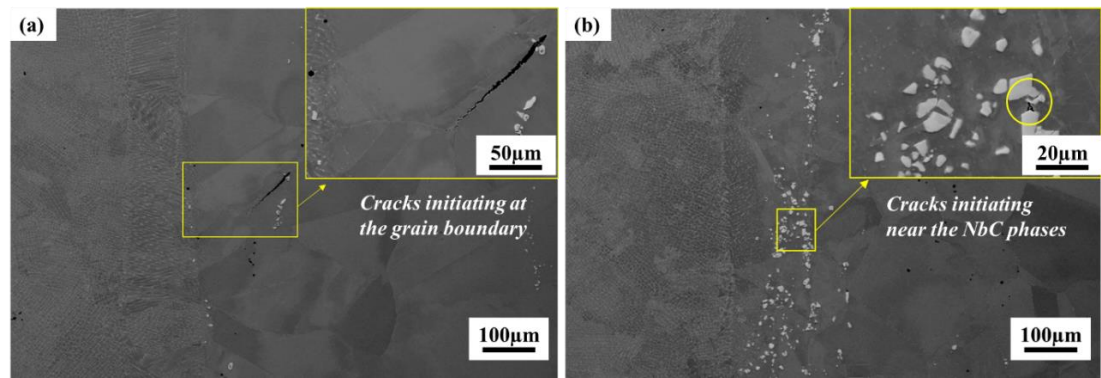


Figure 4.42: Interface at 80% P_{max} 60° groove angle, DA condition. The top of the micrograph is close to the top surface of the bend specimen.

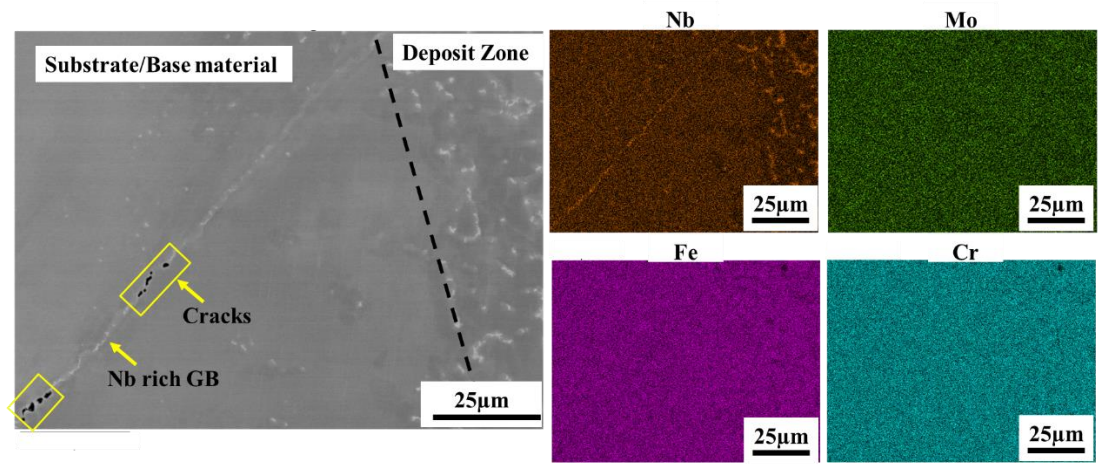


Figure 4.43: EDS map scans showing crack initiation at Nb rich grain boundaries near the interface.

The melting point of the grain boundary is reduced by the segregation of the solute elements of S, P and B, and then the liquid film forms in the grain boundary, thereby further aggravating the tendency of liquation cracking [206] [207,208]. HAZ micro-fissuring is also affected by the substrate/base material grain size. The potency of an intergranular liquid to wet the grain boundaries can be estimated by the following Equation [4]:

$$\gamma_{gb} = 2\gamma_{sl}\cos\theta$$

Where, where θ is the wetting angle, γ_{gb} is the GB energy, and γ_{sl} is the solid-liquid interface energy, respectively. From Eq. (1), the higher GB energy means that the tendency for GB to be wetted and penetrated by the liquid film is higher at a constant γ_{sl} . Moreover, the tensile stresses (σ) required to overcome the solid-liquid interface

energy (surface tension γ_{sl}) on a grain boundary containing liquid film of thickness, h , is given by the Equation below [209]:

$$\sigma = (2\gamma_{sl})/h$$

According to this Equation, a finer intergranular liquid film thickness is expected to enhance the resistance to HAZ cracking by increasing the stress required to cause liquation micro fissuring.

The DED Additive manufacturing processes, due to their advantageous process control compared to traditional repair techniques like welding, result in considerably lower stresses in the HAZ, thereby reducing the chances of micro fissuring in the as-deposit condition. As a result, near-defect-free repairs were observed (Figure 4.23 (a – d)). However, the temperature experienced by the substrate near the interface is high enough to induce liquation of carbides. The constitutional liquefaction of the NbC results in the formation of Nb-rich liquid film on the grain boundaries, which act as sources of crack initiation and growth.

4.4.2 Effect of groove angle on mechanical properties

The standard Bending moment and shear stress diagram for 4-point bend test are shown in Figure 4.44 (a). Ideally, in 4-point bend test, the shear stresses should be zero in the pure bend region (i.e., between the loading pins); therefore, the strain developed in this part should also be constant as reported in the base material/substrate (Figure 4.33(a)).

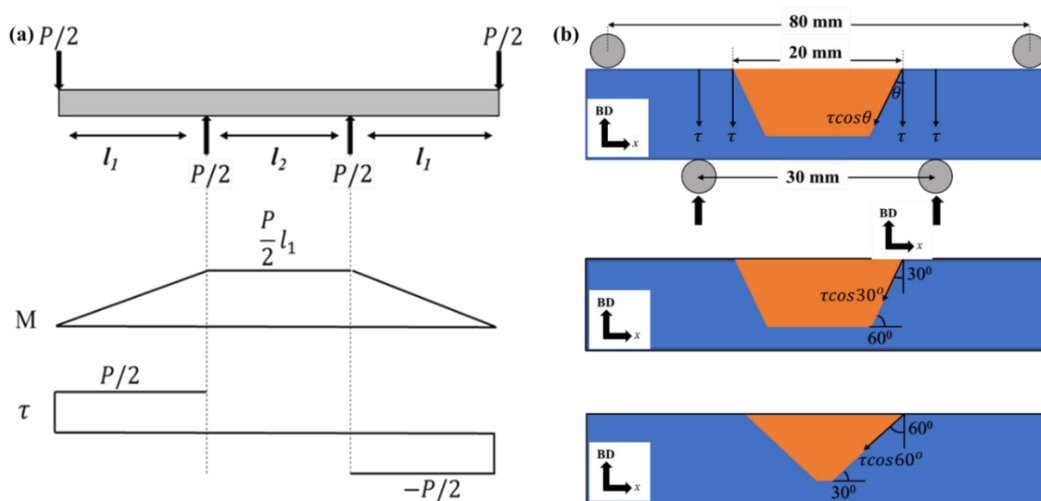


Figure 4.44: (a) Bending moment and shear stress diagram for 4-point bend test; (b) Schematics showing shear stress in the repaired component under loading.

However, due to inhomogeneity in the microstructure of repaired components and cracks developing in the interface, the state of stress would no longer be ideal. As pure bend does not hold, some shear stress is expected to develop. This shear stress would be resolved along the groove sidewall. The component of the resolved shear stress along the groove wall will vary according to the cosine of the angle subtended by the sidewall. The ratio of the resolved shear stress on the groove angle can be calculated as follows:

$$\frac{\sigma_{Groove60^\circ}}{\sigma_{Groove30^\circ}} = \frac{\tau \cos 30^\circ}{\tau \cos 30^\circ} = \sqrt{3}$$

Therefore, stresses on the 60° groove are almost twice as high as in 30°. Thus, the shear stresses in the repaired components would depend on the groove angle and the load experienced by the components during testing. The maximum strain at P_{max} from DIC observation during the 4-point bend test in as-deposit and post-heat-treated conditions is shown in Figure 4.45. It can be seen that the values of ε_{max} are highest in as-deposited components. The absence of strengthening precipitates in as-deposited conditions allows a higher degree of deformability. However, in both the post-heat-treated conditions, an effect of the groove wall angle is apparent. A 30° groove wall angle provides a higher degree of deformability compared to the corresponding 60° counterparts. Therefore, higher resolved shear stresses in the repaired composite with 60° grooves resulted in inferior ductility/deformability and fractured early compared to the repaired composite with a 30° groove angle.

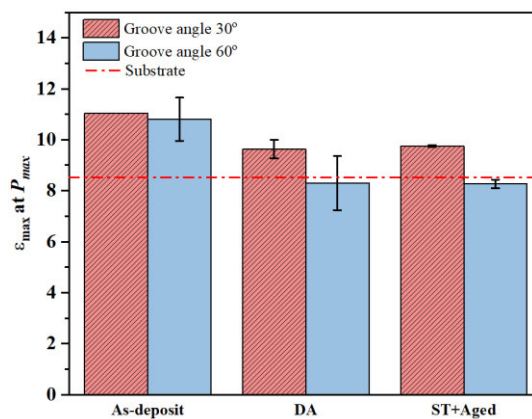


Figure 4.45: Maximum strain at P_{max} from DIC observation.

Figure 4.46 (a – b) demonstrates the evolution of $\Delta\varepsilon$ in direct aged and solution treated and aged conditions, respectively. $\Delta\varepsilon$ is the difference in maximum, and minimum strains in the pure bend region of the sample tested. As observed in Figure 4.34 - Figure

4.36, the maximum strain is generally localised to the interface region, and the repaired zone has the minimum strain; thus, $\Delta\varepsilon$ is the difference between the $\varepsilon_{interface}$ and $\varepsilon_{deposit}$ and the slope $d\varepsilon/dt$ will be a measure of the rate at which the strain localises during loading. Figure 4.46 (c) illustrates the strategy adopted to measure strain at points corresponding to deposit and interface. It can be seen that after initial 20 – 25 seconds, the strains start to localise in the interface, and the strain evolves at a higher rate in the repaired components with a 60° groove angle. The higher rate of strain localisation at a 60° groove angle can be attributed to the component of resolved shear stresses, which is higher for the 60° groove angle, as shown in Figure 4.44 (b).

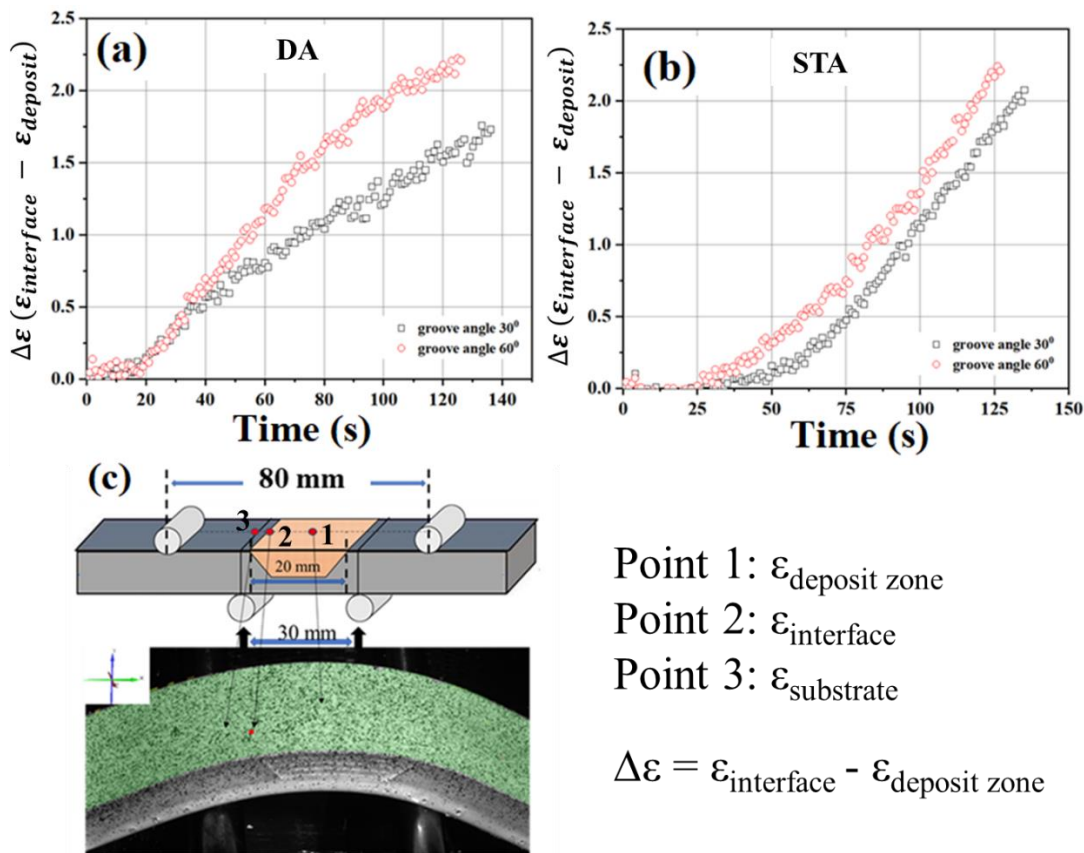


Figure 4.46: Evolution of strain ($\Delta\varepsilon$) on the top surface till P_{max} in the repaired component in various heat treated conditions: (a) Direct aged; (b) Solution Treatment and aged; (c) representative figure showing the strategy adopted to measure strain at points corresponding to deposit, interface, and substrate.

4.5 Conclusion

The study analysed the deposit processed using DED using various process parameters. For groove repairs, a suitable process parameter was selected based on microstructural characterisation and porosity measurements. Groove with varying groove wall angle was machined in the IN718 plates and subsequently repaired using

various scanning patterns. Post-deposit heat treatments were conducted on the repaired composites. The resulting microstructure was investigated, and mechanical properties were studied using 4-point bend tests. The resulting correlation between microstructures and mechanical properties can be summarised as follows:

1. The resultant repaired composite had a non-uniform microstructure: large equiaxed grains $\sim 100\mu\text{m}$ in the substrate and fine mixed columnar and equiaxed grains $\sim 35\mu\text{m}$ in the deposit zone. A high fraction ($\sim 45\%$) of LAGB is observed in the deposit zone, whereas the substrate exhibited $\sim 40\%$ $\Sigma 3$ TB. The varying groove angle had little effect on the microstructure of the deposit zone. The orientation of the grains showed a variation with changing scanning pattern; however, the average grain size and the texture in the deposit zone was not affected.
2. In the as-deposit condition, the hardness and strength in the deposit zone are low due to the absence of γ' , γ'' precipitates, which were not able to form because of the high cooling rates during DED processing. A $\sim 500\mu\text{m}$ wide heat-affected zone (HAZ) was observed in the substrate near the deposit-substrate interface. In post-heat-treated conditions, the corresponding strength values improved, and the hardness becomes constant across the substrate and deposit zone irrespective of the non-uniform microstructure.
3. The mechanical properties of the repaired composites were studied using 4-point bend tests. The maximum load values of the repaired composites in post-heat-treated conditions matched well with the wrought IN718; however, an effect of groove wall inclination was observed during mechanical tests. The repaired composites with a low groove angle exhibited higher deformability compared to the ones with a higher/steep groove angle. It was observed that, in all conditions, the strain localisation occurred at the deposit-substrate interface of repaired composites under a 4-point bend. The repair-substrate interface was the weaker region due to constitutional liquation of the NbC that forms a Nb-rich liquid film on the substrate grain boundary. The inability of these films to withstand the stresses during loading resulted in preferential crack initiation and propagation sites.

CHAPTER 5**Mechanism of Damage in DED Repaired IN718 Composites under Cyclic Loading****5.1 Introduction**

In industrial applications, high cycle fatigue (HCF) has been established as one of the most common and important failure mechanisms [85,122]. In bulk metals, crack initiation dominates the fatigue behaviour in the high cycle regime [123]. Fatigue studies on wrought and AM IN718 are well explored in the literature; however, the variability of AM IN718 fatigue properties relative to wrought IN718 repair can be more unpredictable. The highly complex thermal history during laser additive manufacturing leads to significant variation of bulk microstructural features, including grain sizes, the distribution of secondary phases and voids or pores, that can affect the fatigue performance of the material [130]. In contrast to HCF of wrought materials, where slip-bands and microstructural constituents such as grain boundaries dictate crack initiation during cyclic loading, secondary phases and defects such as voids/porosities can act as the major crack initiation sites in HCF of AM materials resulting in low fatigue life [24,128,129,132]. The literature review (Section 2.4.3) of fatigue properties of laser AM processed IN718 also indicates that the presence of Laves phases adversely affects the fatigue performance relative to the wrought material, especially at load levels close to the yield strength of the material [122,210]. The dissolution of brittle Laves phases and formation of δ phase precipitates during post-deposition heat treatment (HT) can improve fatigue life by restricting grain boundary sliding [211–213].

From an extensive literature review, it can be concluded that the HCF performance of the DED repaired IN718 has received very limited attention and the available literature on the fatigue of IN718 repairs is mostly limited to fusion welding processes. Chapter 4 of this current study has shown that AM repaired composites possess a non-uniform microstructure with several phases, such as the Laves phase, Carbides (MC) in the deposit and coarse equiaxial grain boundaries with NbC liquified along the coarse substrate GB. There have been several studies that found an impact of the microstructural changes or defects created during weld repair of IN718 on fatigue properties, with failures mostly observed in the HAZ [136] or the weld zone [137]. Similar to AM IN718 results, Laves phases or δ phases in weld repair specimens negatively affected the fatigue performance. Additionally, various post-weld heat

treatments generally improved the fatigue life of the repaired composites [138]. However, the possibility of cracks initiating from Nb-rich substrate grain boundaries, which occur due to NbC liquation during AM repair, has not been explored in the literature. The effect of these phases on crack initiation and propagation during cyclic loading, especially near the repaired joints, requires detailed exploration.

This chapter explores the room temperature fatigue performance and failure mechanism in IN718 repaired using DED technique under direct aged (DA) and solution treated at 980°C and aged (STA) condition. The prevailing mechanism of the initiation and growth of fatigue cracks arising from phases present near the repaired joint (Laves phase, Carbides, Liquified NbC along grain boundaries, and δ phase (for STA)) has been studied. The progression of fatigue cracks (on the surfaces) at two cyclic stress levels with increasing cycles was studied under SEM by interrupting the test at various stages of fatigue life between 10 – 90 pct of the average N_f for each stress amplitude (max stress).

5.2 Experimental Method

5.2.1 Fabrication of repaired coupons for fatigue testing

Wrought IN718 plates in annealed and aged condition with dimensions of 50 mm × 20 mm × 40 mm (length × width × height) were used as a substrate for the repairs. Contrary to chapter 4, the repairs in this section were simplified to an AM deposition on wrought plate substrate for the primary purpose of investigating the substrate-deposit interface. Plasma Atomised (PA) IN718 powders were obtained from GE additive with a size range varying from 45 μm – 105 μm , as shown in Figure 4.1. An Optomec LENS MR-7 apparatus was used for the deposition process. The parameters used for the deposition/repair process are shown in Table 4.1. Argon was used as the shielding gas and carrier gas with a flow rate of 15 l/min and 6 l/min, respectively. The powder flow rate of 12 g/min and oxygen level below 3 ppm was used for all the deposits. Figures 5.2 (a) and Figure 5.2 (b) show a schematic for the sample preparation for fatigue tests. Deposits/repairs of similar dimensions to the wrought plate substrates were deposited on the substrate surface. Hourglass samples were machined using electro-discharge machining (EDM) from the repaired composite for HCF testing according to ASTM E466-15 standard [176]. The HCF specimens were 50% wrought substrate and 50% laser DED deposit with the repair interface in the narrowest part of the samples (Figure 5.2 (b)). This hourglass geometry was utilised

to ensure the maximum cyclic stress was localised at a narrow region incorporating the repair interface, as that was the focus of the investigation.

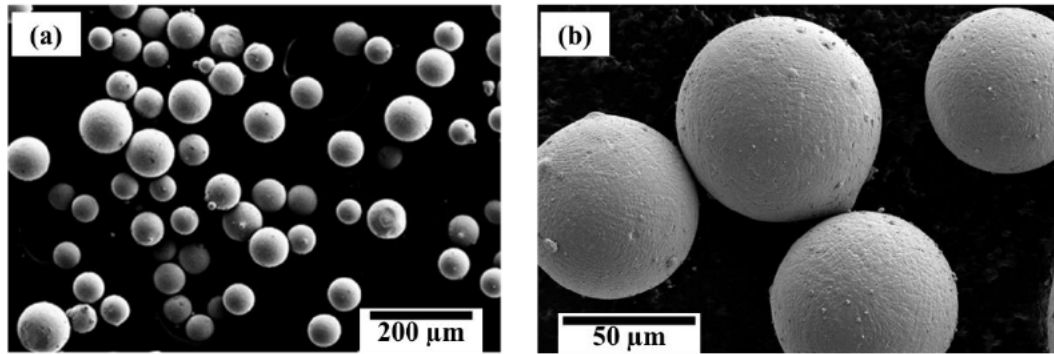


Figure 5.1: SEM image of the feedstock Inconel Powders.

Table 5.1: DED repair parameters.

Power	Scan speed	Hatch spacing (h)	Layer thickness(t)	Linear Energy Density
W	(mm/s)	(mm)	(mm)	(J/mm)
500	6.3	0.95	0.48	78.74

Subsequently, these repaired and machined specimens were subjected to one of two different post-repair heat treatments (i) Direct aging (DA): Heating to 720°C at 10°C/min followed by holding for 8 hours, cooling to 620°C in 2 hours and holding for 8 hours, followed by air cooling; or (ii) Solution treatment and ageing (STA): Solution treatment at 980°C, water quenching followed by double aging. Heat treatment schematics for DA and STA are shown in Figures 3.5 (a) and (b) in Chapter 3.

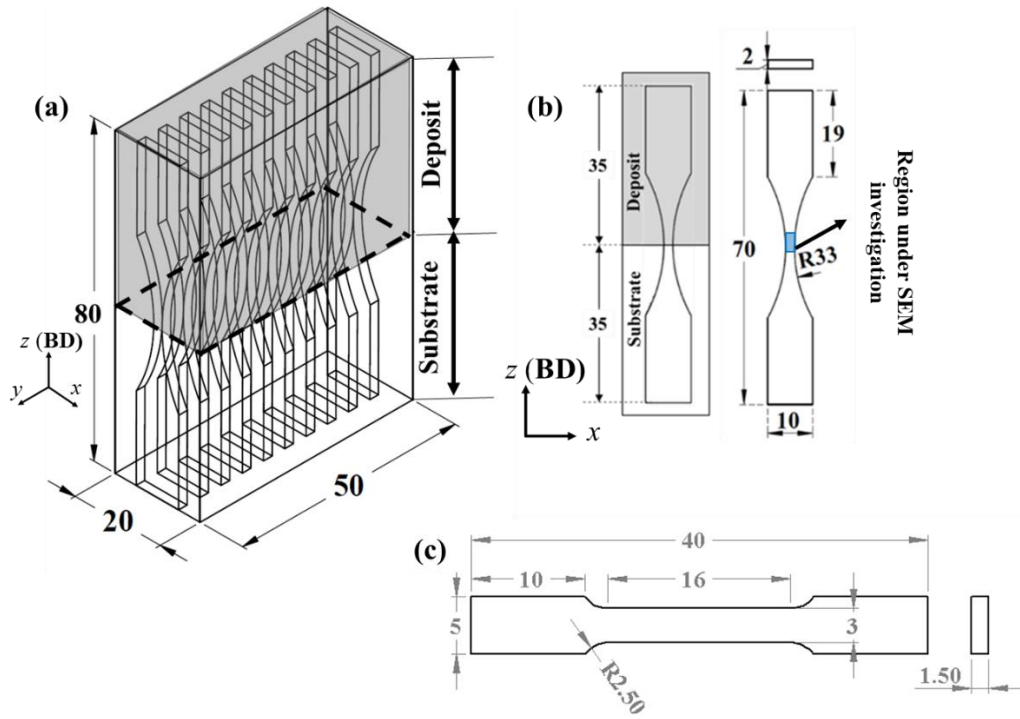


Figure 5.2: Schematic of (a) DED repaired blocks, (b) hourglass fatigue samples- the region under SEM investigation is marked; (c) samples for tensile testing.

5.2.2 Mechanical testing

Tensile tests were conducted on wrought IN718 material heat-treated in the STA condition according to standards [14] and on specimens machined from as-deposited AM IN718 blocks that were subsequently heat treated to either the DA or STA condition. The geometry of these tensile specimens is shown in Figure 5.2 (c). It is important to note that the AM tensile samples were fully laser deposited, unlike the fatigue hourglass samples that were ‘repaired’ samples. These tensile test results were primarily used to calculate the target loads for the subsequent fatigue tests; details are reported in Section 5.3.2. The uniaxial tension tests were carried out at room temperature on a servo-hydraulic INSTRON 8802 tensile-testing machine with a load cell capacity of $\pm 100\text{kN}$ with a constant crosshead speed corresponding to a nominal initial strain rate of 10^{-3} s^{-1} . Bluehill software in Instron Wave Console was used to carry out the tests. The specimens were pulled to fracture. The relevant dimensions were measured on the tested specimens using vernier callipers. For every condition, at least 3 specimens were tested.

The fatigue tests on repaired hourglass specimens were carried out at room temperature, using an Instron E10000 with an electrically operated crosshead and a $\pm 10\text{-kN}$ load cell. Stress (load) – controlled fatigue tests were performed using a

sinusoidal waveform at $R = 0.1$ and a frequency of 50 Hz. A tension – tension fatigue test at $R = 0.1$ ensured that there was no bending or buckling of the specimen during specimen fixing and subsequent testing. For generating the stress-life (S-N) curve, cyclic tests were conducted using a maximum applied stress ranging from 35 to 90 pct of the yield strength (YS) of wrought IN718. The surface was mechanically ground for all samples using emery papers successively from 240 Grit to 4000 Grit. The S-N curve was constructed by plotting the maximum applied stress amplitude against the corresponding number of cycles to failure (N_f). After the S-N curve was generated, the initiation and growth of fatigue cracks were studied using single-specimen interrupted tests. The specimens were further polished for the interrupted tests with diamond suspension from 3 μm to 1 μm and finally with OPS colloidal silica suspension. These interrupted experiments were conducted at several different maximum cyclic stress levels using $R = 0.1$ and consisted of 3 steps: (i) the specimen was cyclically loaded at a target stress level to a predefined pct of average N_f before the actuator movement was arrested to allow load relaxation and specimen removal from the test machine; (ii) the specimen was ultrasonically cleaned before surface inspection under SEM; (iii) the specimen was remounted in the testing machine at the same target stress levels for the next set of cycles until re-examination in the SEM or test end. The loading was interrupted at various stages of fatigue life between 10 – 90 pct of the average N_f . For these experiments, the sample surface was polished and etched for SEM investigation prior to testing. A single specimen interrupted test was preferred for each maximum cyclic stress level to allow the initiation and subsequent propagation of cracks to be followed, minimising the possible impact of specimen-to-specimen variation.

5.2.3 Scanning Electron Microscopy

For microstructural characterisation of the repaired and heat-treated specimens using SEM, samples were sectioned from the middle part of the repaired section across the repaired joint, as shown in Figure 5.2. The samples were mechanically ground successively from 240 Grit to 4000 Grit and polished with diamond suspension from 3 μm to 1 μm and finally with OPS colloidal silica suspension. A Supra VP55 FEG scanning electron microscope (SEM), equipped with an AsB detector, was used for imaging. Energy dispersive X-ray spectroscopy (EDS) was used to ascertain the chemical composition of the phases. An electron backscatter diffraction (EBSD) system from Oxford Instrument was employed to study the texture and grain size.

EBSD was performed with a scanning step size of 2.5 μm and analysed with HKL Channel 5 software.

The primary aim of the interrupted tests was to detect the fatigue cracks and examine the nature of their growth in number and size. Accordingly, the surfaces of the specimens after the interrupted fatigue tests were studied using SEM. For estimating the number density of microcracks, a surface area of approximately $2 \times 2 \text{ mm}^2$ in the centre of the specimen, on either side, as shown in Figure 5.2, was imaged using the SEM at a constant magnification of 250 times. The number density was then calculated as the average number of cracks per unit area (mm^2) recorded at different microstructural locations. The crack measurements were done using ImageJ software. Moreover, the fractured cross-section and surface were also examined under SEM to determine the predominant mode of fatigue failure.

5.3 Results

5.3.1 Repaired Microstructure

Detailed SEM imaging confirmed that the repaired specimens were free from cracks or fusion defects. It has been shown in Fig 4.9(b), Chapter 4 that the parameter combination used for the repairs results in highly dense deposits with porosities $<0.05\%$. Moreover, no other visible defects were observed in the wrought material. The microstructure, misorientations and textures in the repaired composites were studied using EBSD mappings, with the results shown in Figure 5.3 (a - e). The microstructure of the repaired composite can be divided as: (a) the deposit zone; (b) substrate; and (c) the deposit zone – substrate interface. The microstructure in the deposit zone and the substrate were substantially different. In both the heat-treated conditions, the substrate region had equiaxed grains with an average grain size of $\sim 90\mu\text{m}$ and a high fraction ($> 50\%$) of $\Sigma 3 <110>$ of twin boundaries identified with misorientation of $60^\circ \pm 5^\circ$. On the contrary, the repaired zone depicted a heterogenous distribution of columnar and equiaxed grains along the deposition direction with a high fraction of low angle grain boundaries ($2^\circ - 10^\circ$). Since the crystallographic orientations along the building direction (BD) are of interest, inverse pole figure (IPF) maps were constructed along BD from the EBSD data to characterise the grain morphologies and the crystallographic orientations. The average grain size and morphology did not change with post-repair HT. A $\{001\} \parallel$ building direction texture in the laser deposited IN718 is typical and well established in the

Chapter 5 Mechanism of fatigue damage in DED repaired IN718 literature[10,11,111,214]. The $\{100\} \parallel \text{BD}$ pole figures of the deposit zone in DA and STA conditions are shown in Figure 5.3 (d) and Figure 5.3 (e). The $\{100\}$ pole in either heat-treated condition reveals that the crystallographic texture along $\{001\} \parallel$ building direction was weak. Both pole figures were based on >4000 grains; hence, the texture interpretation has the required statistical importance. Moreover, analysing the columnar grains alone in the deposit zone (containing >3000 grains) resulted in the maximum MUD value of 2.98 and 3.08 for the DA and STA conditions, respectively. Therefore, the effect of texture on the fatigue behaviour of these materials is not likely to have a significant impact.

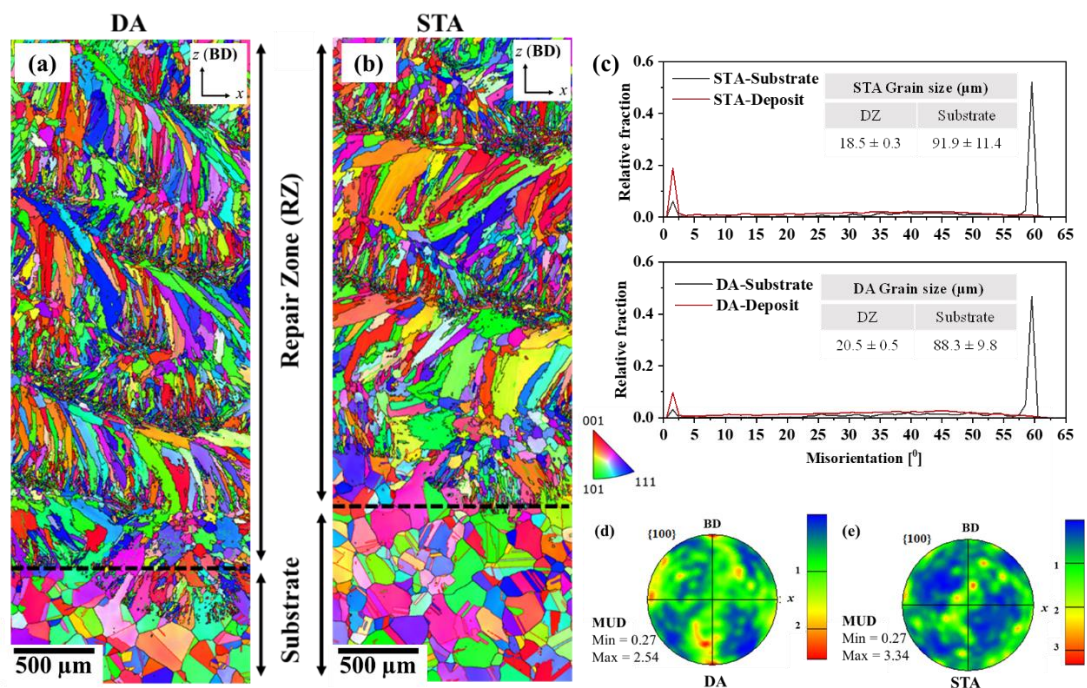


Figure 5.3: EBSD maps showing the grain morphology and distribution in the repaired specimens at (a) Direct Aged (DA); (b) Solution Treated and Aged (STA) condition; (c) Misorientation distribution in the repaired composites in the deposit zone and substrate; $\{100\}$ pole figure of the deposit zone microstructure in (d) DA and (e) STA condition.

The hardness profile of the repaired specimens across the interface is shown in Figure 5.4. In the as-deposited condition, the hardness in the deposit zone was considerably lower ($\sim \text{Hv } 250$) compared to the hardness in the substrate ($\sim \text{Hv } 450$). The parameters used in the repair process result in high cooling rates of 10^3 – 10^5 K/s, as discussed in Chapter 4 (Sec 4.3.1.2). The high cooling rates during DED processing do not allow the formation of the strengthening precipitates γ' and γ'' [95], that results in low

hardness in the deposit zone. A dip in hardness values near the deposit zone-substrate interface towards the substrate is observed, that indicates the presence of a $\sim 500\mu\text{m}$ Heat Affected Zone (HAZ). In this zone, the temperature during repair was high enough for the dissolution of the δ phases in the substrate into the γ matrix (δ solvus temperature is 1269–1288 K) [8,40], resulting in decreased hardness/strength. A similar observation was reported in DED processed IN718 by Zhai et al. [95]. Due to their advantageous process control compared to traditional repair techniques such as welding, Laser AM processes result in considerably lower HAZ stresses, thereby reducing the chances of micro fissuring in the as-deposit condition. As a result, near defect-free repairs were observed. Moreover, Figure 5.4 demonstrates that a uniform hardness was observed across the repaired composite from the substrate to the deposit zone post-heat-treatment due to the formation of the strengthening precipitates γ' and γ'' .

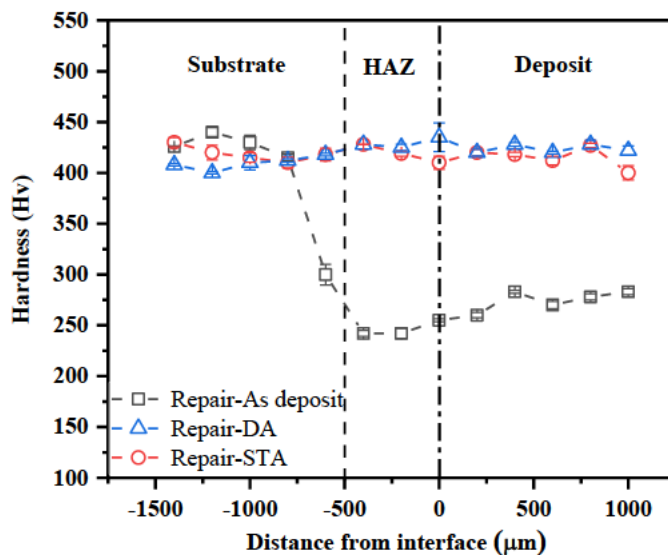


Figure 5.4: Hardness variation in the repaired composite from deposit zone to substrate across the deposit zone-substrate interface in as-deposit and post-HT conditions.

The microstructure of the repaired composite near the deposit zone-substrate interface is shown in Figure 5.5 (a) for DA condition and Figure 5.6 (a) for STA condition. Figure 5.5 (b) and Figure 5.5 (c) show the high magnification micrographs of the deposit zone and substrate, respectively, in DA conditions. The EDS point analysis shows Laves phases present in the microstructure, identified as the bright phase in the microstructure. Laves phases in the deposit zone form in the interdendritic regions due to the segregation of Nb and Mo resulting from non-equilibrium solidification

Chapter 5 Mechanism of fatigue damage in DED repaired IN718 conditions during DED processing [93,199]. Figure 5.5 (d) shows the EDS elemental map of the repaired composite in DA condition. In the substrate, Nb segregation is observed at the grain boundaries near the deposit zone-substrate interface. The EDS point analysis shows that the Nb segregation is >10 wt%, similar to that in the Laves phase. Nb Segregation along the substrate grain boundary occurred due to constitutional liquation of NbC carbides in the substrate. The temperature experienced by the substrate near the interface is high enough to induce liquation of carbides (1200°C - 1250°C). The constitutional liquification of the NbC will result in the formation of Nb-rich liquid film on the grain boundaries with a Laves phase composition [4,207].

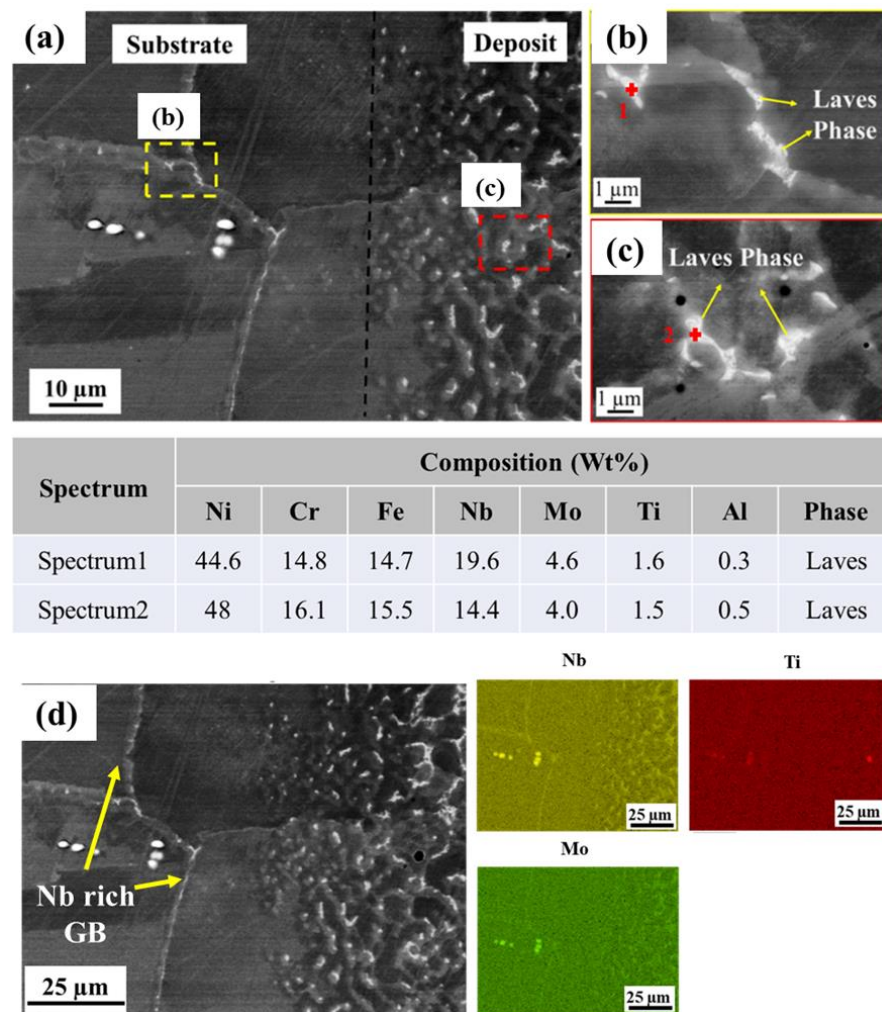


Figure 5.5: SEM image showing the microstructure (a) near the deposit zone-Substrate interface at DA condition; (b) high magnification micrographs showing the phases in the substrate, and (c) deposit zone. The EDS test positions and the results are shown; and (d) the corresponding EDS map showing Nb, Mo, and Ti segregation.

Figure 5.6(b) and Figure 5.6(c) show the high magnification micrographs of the deposit zone and substrate, respectively, in STA conditions. Solution treatment at 980°C resulted in the formation of δ precipitates in the deposit zone, primarily along the dendritic arms (Figure 5.6 (b)); in contrast, δ precipitates are observed along the grain boundaries in the substrate (Figure 5.6 (c)).

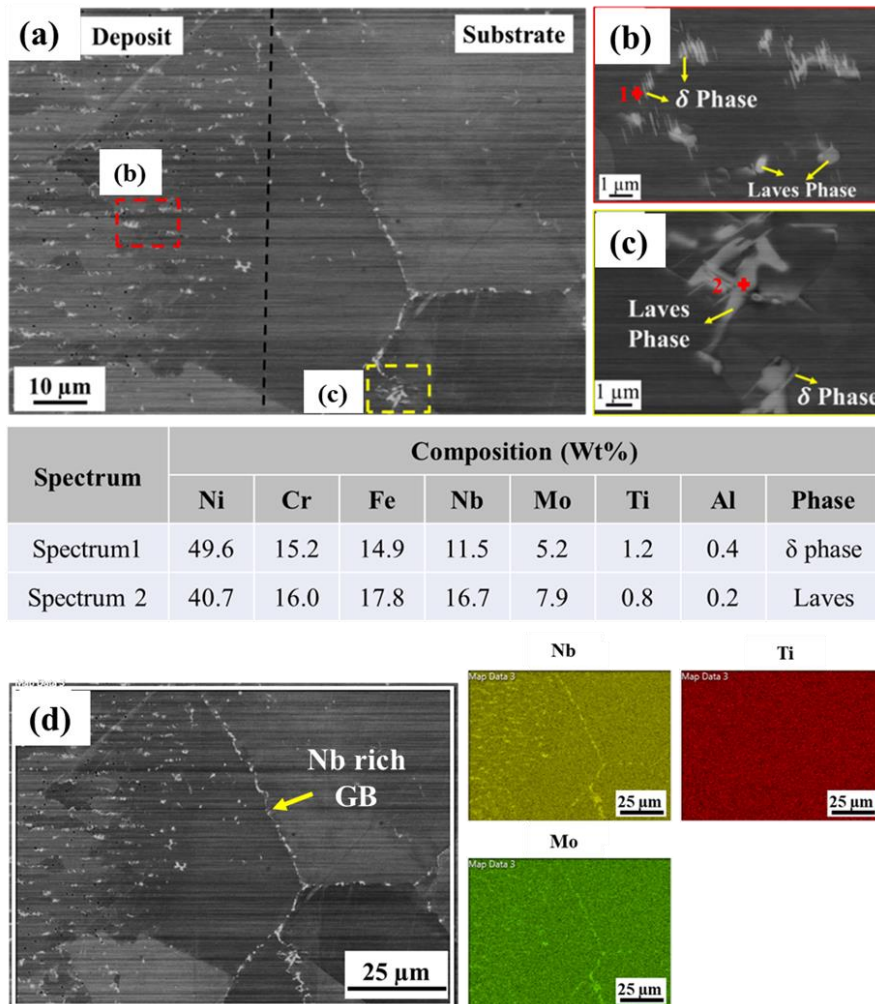


Figure 5.6: SEM image showing the microstructure (a) near the deposit zone-Substrate interface at STA condition; (b) high magnification micrographs showing the phases in deposit zone, and (c) Substrate. The EDS test positions and the results are shown; and (d) the corresponding EDS map showing Nb, Mo, and Ti segregation.

The δ phase can be easily identified by its needle-like structure, and it is observed that δ phase precipitation occurs exclusively around the residual Laves particles. The δ phase is an orthorhombic Ni_3Nb precipitate, which precipitates in the range of 860 °C to 995 °C (See for e.g. [127,215,216]). The high cooling rates during the repair process restrict the formation of the δ phase, and it is believed that the low heating rates during solution treatment at 980°C result in precipitation of the δ phase by dissolving the

Laves phase, as reported by Qi et.al.[93] in DED deposit IN718. Therefore, δ phase precipitation occurs in these regions. The solidification conditions during the repair/deposition process result in heterogenous distribution of δ precipitates in the deposit zone. It is observed that the δ precipitates in the substrate were larger than those in the deposit zone. Moreover, the Nb-rich grain boundary film on the substrate grain boundary that forms during the deposition process still exists post-STA heat treatment, as shown in Figure 5.6 (d).

While the post-repair heat treatment resulted in a significant increase in hardness, the inter-dendritic Laves phase formed during rapid solidification remained post-heat treatment. The hardness was increased due to the formation of γ' and γ'' strengthening precipitates. Therefore, in terms of microstructure, the presence of δ precipitates (in the interdendritic region in the deposit zone and along grain boundaries in the substrate in STA condition) is the primary difference between the two heat treatments.

5.3.2 Tensile tests

Figure 5.7 shows the engineering stress-strain response of the substrate in the solution treated and aged condition, and DED deposited IN718 in DA and STA conditions. For the current study, the yield stress values are of importance as they determined the maximum cyclic stress for each test. The key tensile properties of DED IN718 under different heat-treated conditions are summarised in Table 5.2. The DA samples exhibited the highest strength, followed by the wrought substrate and STA samples. However, the difference in yield stress for samples tested at different heat treatment conditions was <10%. As mentioned earlier, the fatigue hourglass samples were 'repaired' samples, unlike the tensile samples, that are single material bulk deposit samples. Therefore, the different target loads/stress levels used for the different specimen conditions in all fatigue tests were based on a percentage of the wrought substrate yield stress.

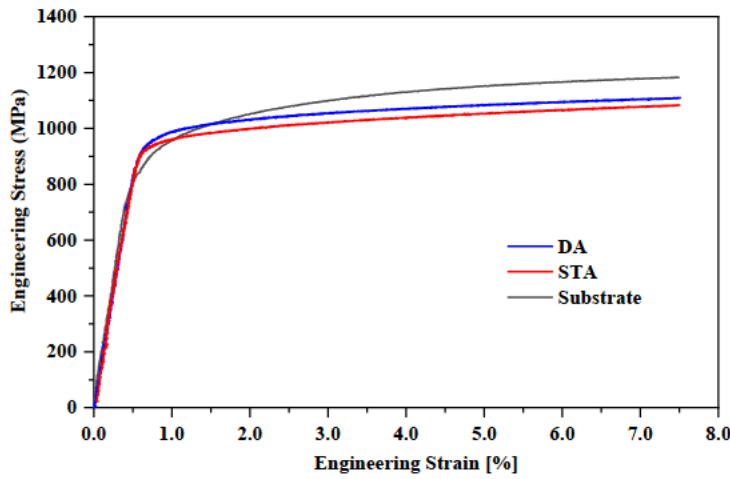


Figure 5.7: Engineering stress-strain response in tension measured using tensile specimen as per Figure 5.2(c).

Table 5.2: Tensile properties of IN718 in different post-heat-treated conditions (Figure 5.2(c)).

Properties IN718 (Vertical Specimen)	HT condition		
	IN718 - DA	IN718 - STA	Wrought
Elastic Modulus [GPa]	194 ± 17	173 ± 10	176 ± 10
$\sigma_{YS(0.2)}$ [MPa]	948 ± 19	959 ± 10	924 ± 12
σ_{UTS} [MPa]	1134 ± 16	1134 ± 18	1226 ± 10
Elongation [%]	8.50 ± 0.2	17.20 ± 3.5	22.4 ± 0.6

5.3.3 Fatigue tests

The S-N curve of the repaired composites is shown in Figure 5.8. Any HCF tests that were still running at 5×10^6 cycles were stopped and considered a run-out. Note that the arrows indicate that the specimen did not fail. A power-law model akin to the well-known Basquin's equation [85] was adopted for fitting the data.

$$\sigma_{max} = aN_f^b$$

where a and b are fitting constants. Basquin's equation only applies to samples that fail; therefore, only specimens that failed prior to 5×10^6 cycles were used for the fit. The dotted lines correspond to the power-law fit representing the fatigue performance of the investigated materials. The coefficients of fit and the corresponding R-Square values are given in Table 5.3.

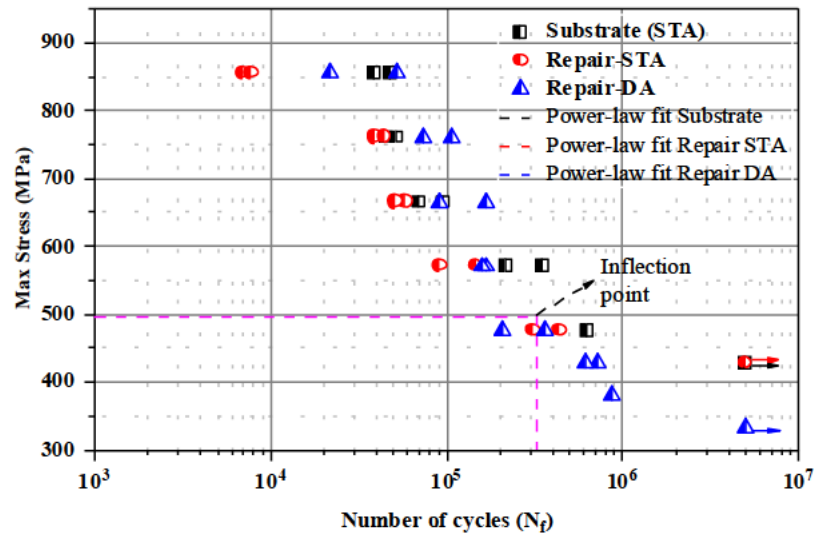


Figure 5.8: S-N curve showing raw data points and a power-law fit for the substrate and repaired composite conditions.

Table 5.3: Parameters of fit for the HCF tests.

	a	b	Adj. R-Square
DA	8415.53	-0.22	0.88
STA	2965.87	-0.14	0.89
Substrate	6641.70	-0.20	0.89

As expected, the general trend is that N_f increases with a decrease in maximum cyclic stress level. The wrought substrate generally outperforms the heat-treated repaired composites. The specimens were repaired with identical deposition parameters, but different post-repair heat-treatment exhibited significant deviations in fatigue performance. The repaired material in STA condition and the wrought material exhibited a similar fatigue limit $\sigma_{max} \sim 430$ MPa; however, the DA condition exhibited a significantly lower fatigue limit. The fatigue limit observed in the DA condition was ~ 100 MPa lower than in the STA condition. This significant difference in fatigue limit was despite the static tensile strength values of the DED samples in both HT conditions being similar. At low maximum cyclic stress levels where failure did occur, the solution treated and aged (STA) specimen also exhibited superior fatigue behaviour to DA. At high load levels corresponding to 90pct to 60pct of yield strength, however, the DA samples performed significantly better than the STA counterparts and matched the performance of wrought IN718. The fatigue plot shows an inflection point, $\sigma_{max} \sim 520$ MPa, where the relative fatigue performance of the two post HT conditions changed. The different heat treatments employed resulted in different phases in the microstructure in both the repaired region and the substrate, as depicted in section

5.3.1. (Figure 5.5 (a – c) and Figure 5.5 (a – c)). The difference in HCF behaviour of the materials can be rationalised in terms of how cracks initiate and propagate in the different microstructures and are discussed in the following section (Section 5.4.1).

5.3.4 Interrupted Fatigue tests

Based on the S-N curve shape, the interrupted tests were performed using two different maximum cyclic stress levels, one above and one below the inflection region shown in Figure 5.8 at 70 % of YS and 45% of YS. Depending upon the heat treatment employed, the applied stress, and the number of loading cycles, there were four main preferential sites for the initiation of microcracks in the repaired composites. Crack initiation and growth occurred through the (1) Laves phases/ δ phase in the deposit, (2) Metal Carbides (in the HAZ), repaired/deposited region or substrate, (3) at substrate grain boundary; and (4) inside grain body. Representative figures of cracks/microcracks at various preferential locations are shown in Figure 5.9 (a – d). Interestingly, it has been observed that although there were some remaining porosities after repair, no fatigue cracks were found to initiate at pores. Ardi et al. [30] reported similar observations who performed HCF tests on SLM manufactured IN718. Ardi et al. [127] observed a porosity volume ratio of 0.39 % with pores $> 100 \mu\text{m}$ in diameter in SLM processed IN718, which were reduced to 0.08 % after HIP-ing. The remaining porosities were in the size range of 40–100 μm , however, the fatigue performance was not improved with reduced porosity.

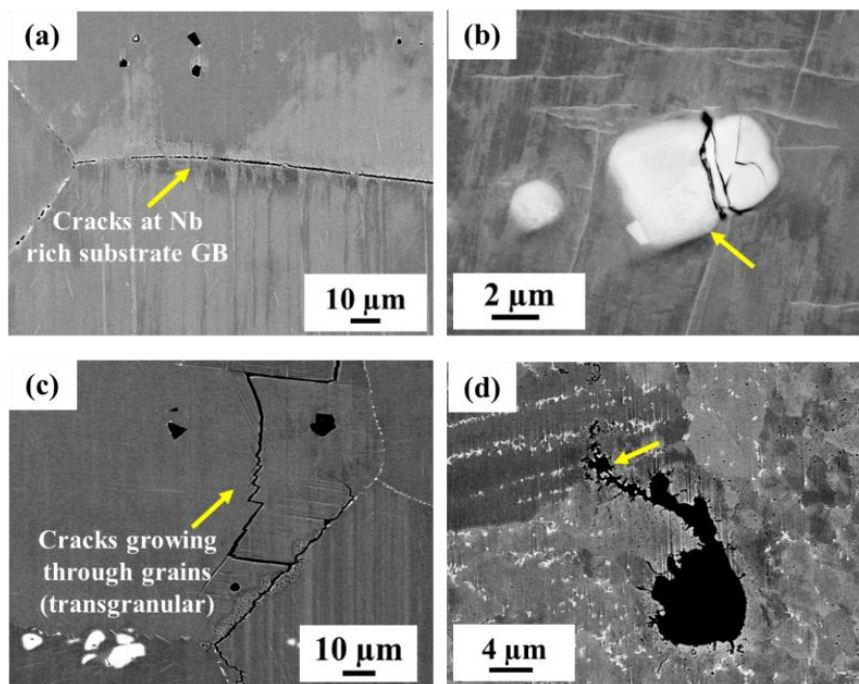


Figure 5.9: Fatigue microcracks initiating at various preferential sources on the sample surface (a) Substrate grain boundary near the repair interface (b) Broken metal carbides; (c) Transgranular cracks (d) Broken Laves phases/ δ phases.

The progression of fatigue damage was investigated on the surfaces of the specimens subjected to interrupted fatigue tests using an SEM. The fatigue damage in the repaired components is characterised in terms of the increase in the number density and the average size of fatigue cracks at various microstructural locations. This approach is similar to that used by Majumdar et al. [217] in their examination of crack initiation and propagation on IF steel sheets. The total crack length and the number density of fatigue cracks at $\sigma_{\max} = 70\text{pct}$ of YS in DA and STA conditions, shown in Figure 5.9 (a) and (b) and Figure 5.12 (a) and (b), respectively, depicts that the extent of fatigue damage increases with the number of loading cycles at different rates depending on the microstructural origin or location. The proposed damage mechanism is illustrated using a set of representative figures in Figure 5.11 (a – d) and Figure 5.13 (a – c) that show the development of the crack with an increasing number of cycles for specimens tested at 70% of YS in DA and STA conditions respectively. At the higher maximum cyclic stress interrupted tests (70% of YS), the fatigue cracks initiated from the substrate grain boundaries near the deposit zone – substrate interface in both HT conditions. In the DA condition, cracks were observed at the first interruption ($0.4 N_f$) and both the total crack length and number of cracks increased continuously until reaching a plateau at $0.6 N_f$ cycles. The fatigue cracks initially underwent intergranular growth before extending to nearby grains and a transgranular crack growth mode after $0.6 N_f$ (Figure 5.9 (a) and (b)). With increasing number of cycles, many small cracks were formed ahead of the major dominant crack that subsequently coalesced with the major crack, resulting in a final fracture through the substrate. Some broken Laves phase and Metal Carbides were also seen in the deposit zone; however, they did not appear to grow or contribute towards the failure of the material. In STA condition, under identical loading conditions, cracks appeared simultaneously in the substrate grain boundaries and the deposit zone through the Laves phase and δ phase. In the initial stages, upto $0.4 N_f$, high crack density and growth rate were observed in the substrate, as shown in Figure 5.12 (a) and (b). However, after $0.4 N_f$, the Laves phase and δ phase along the dendritic arm in the deposit zone provided an easy crack path (Figure 5.13 (c)) and the cracks developed at a very fast rate in the deposit zone, leading to the failure of the repaired composite. This resulted in premature failure of

the composite, at ~ 65 % of average N_f relative to the non-interrupted test. It is to be noted that this interrupted test (at 70% of N_f in STA condition) was repeated, and a similar result was obtained. The total number of cycles to failure at this stress level (~ 50,000 cycles) for the STA condition is relatively low compared to HCF test cycles, and the crack initiation and propagation is quite sensitive to the microstructure. Hence, it is not surprising that a higher degree of variability was present in the test results. It is also possible that the sensitivity of the microstructure to cracking was accentuated during the loading and unloading of the specimen.

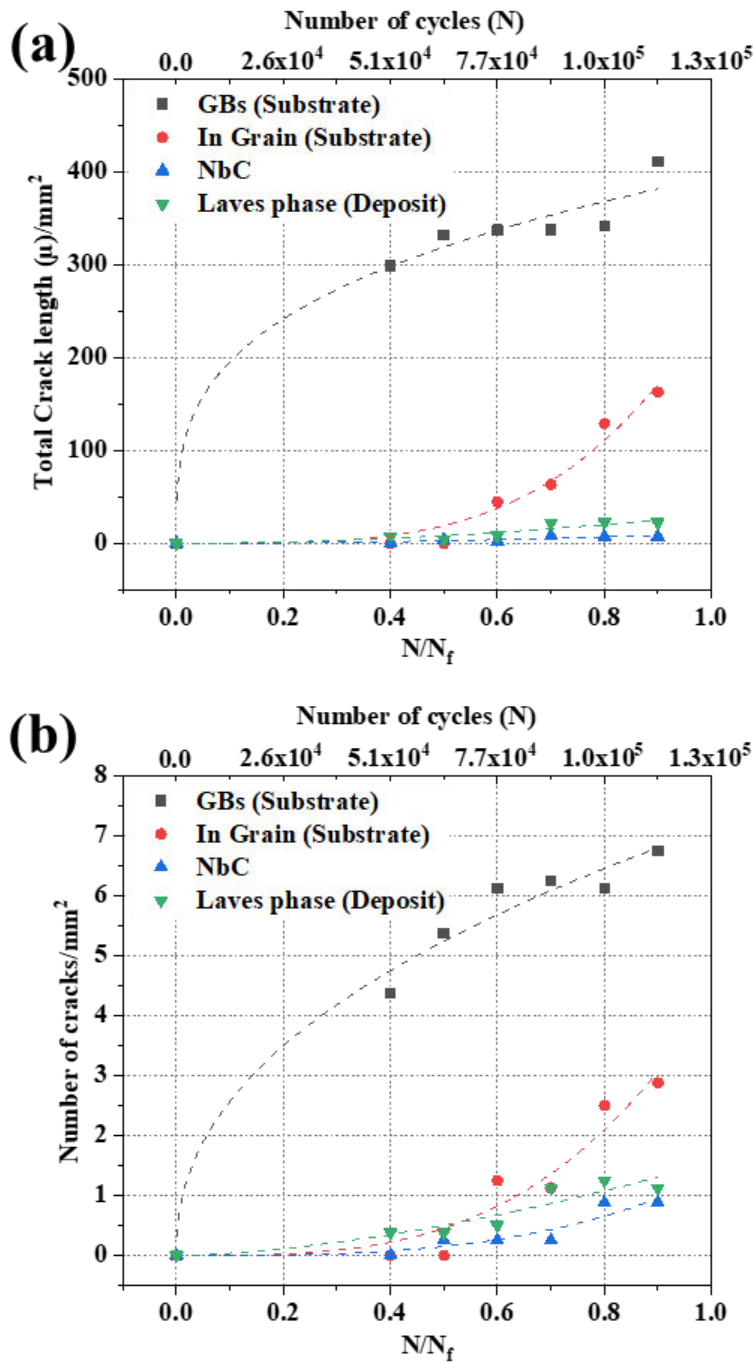


Figure 5.10: (a) Total crack length and (b) number density of fatigue cracks growing on different sources on the specimen surface at various stages of fatigue life at $\sigma_{max} = 70\text{pct}$ of YS in DA condition.

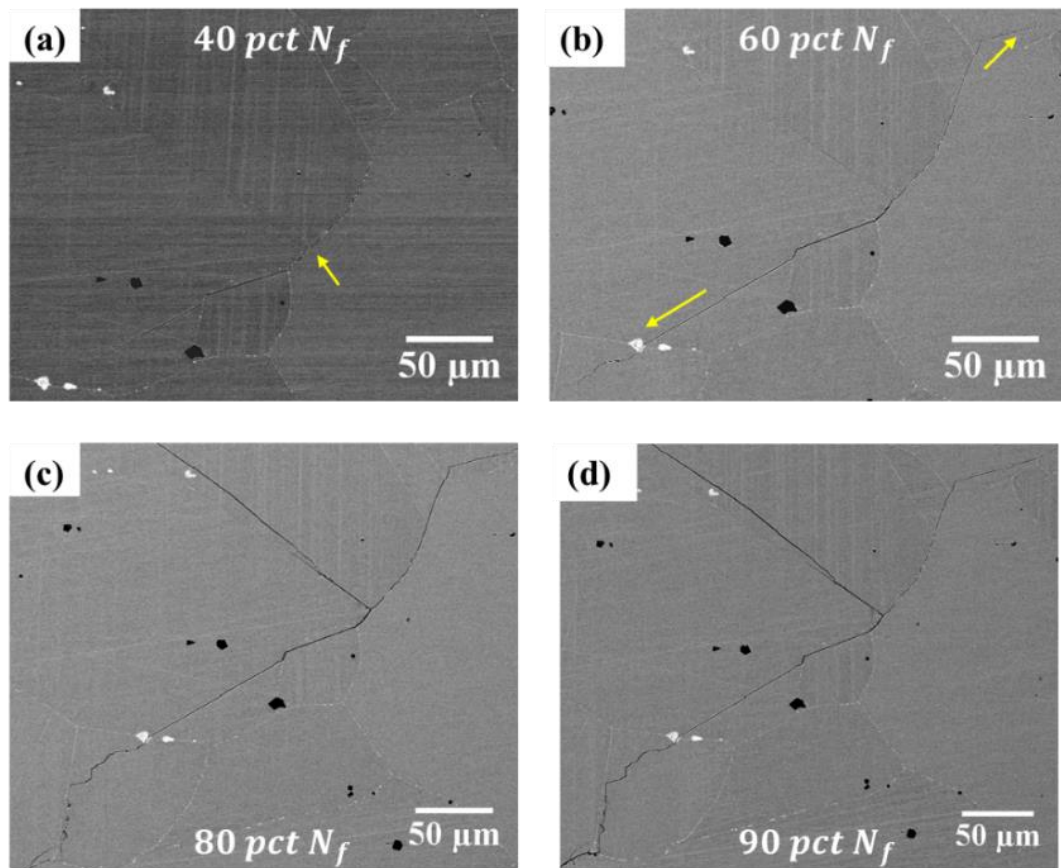


Figure 5.11: Representative figures showing the development of crack in DA specimen at 70% of YS in various stages of fatigue life: (a) 40 % N_f ; (b) 60 % N_f ; (c) 80 % N_f ; (d) 90 % N_f .

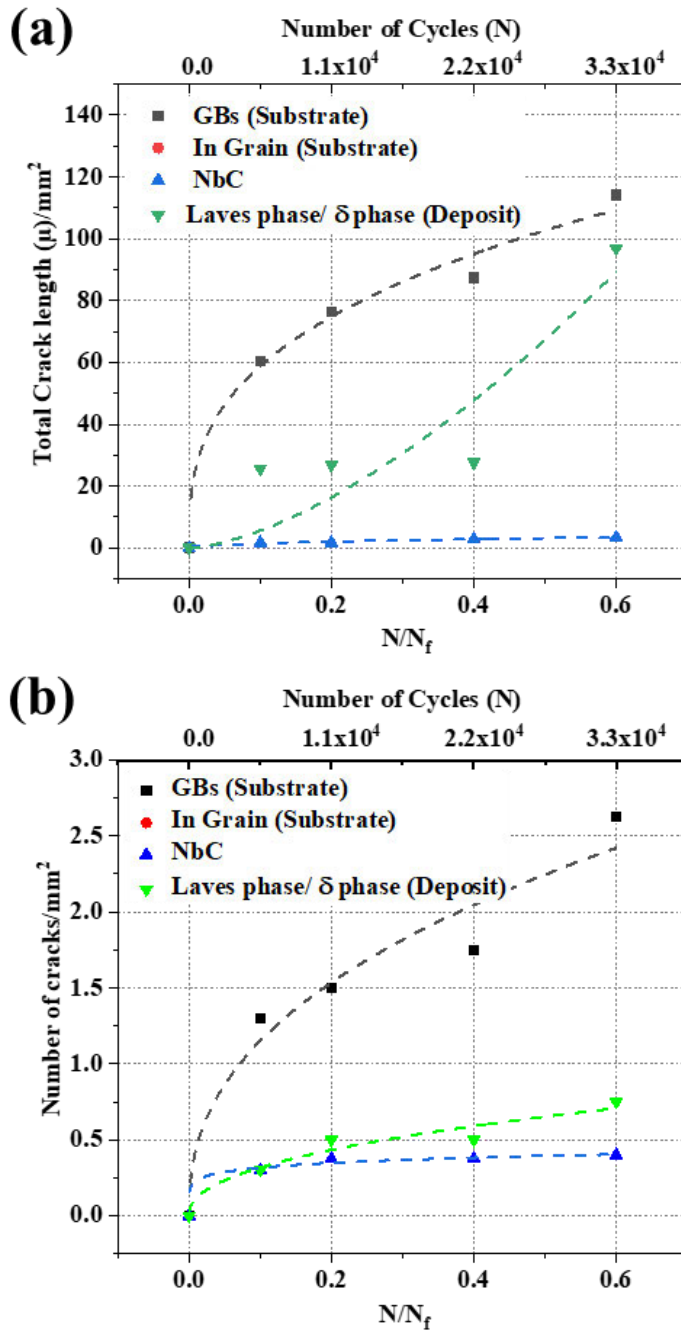


Figure 5.12: (a) Total crack length and (b) number density of fatigue cracks growing on different sources on the specimen surface at various stages of fatigue life at $\sigma_{max} = 70\text{pct}$ of YS in STA condition.

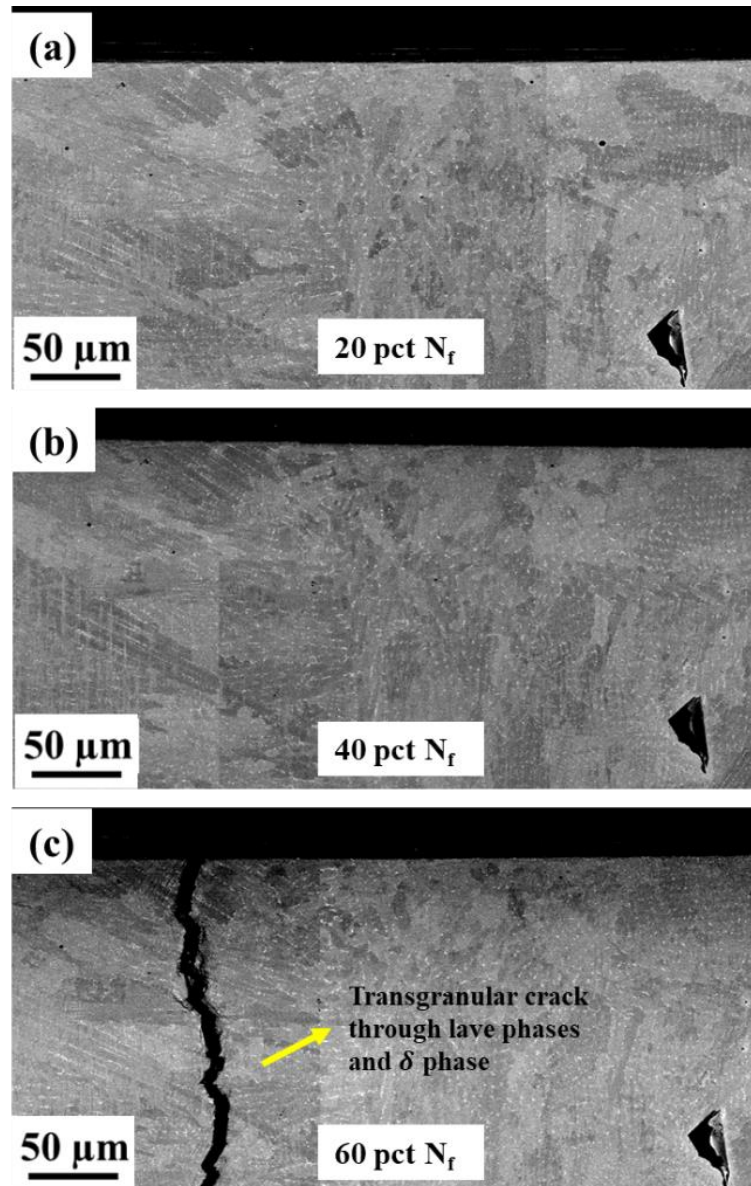


Figure 5.13: Representative figures showing the development of crack in STA specimen at 70% of YS in various stages of fatigue life: (a) 20 % N_f ; (b) 40 % N_f ; (c) 60 % N_f .

The measured crack length and the number density of cracks for interrupted tests performed at $\sigma_{\max} = 45\text{pct}$ of YS in DA condition is shown in Figure 5.14 (a) and (b), respectively, and Figure 5.16 shows the total crack length in STA condition. At 45% of YS, the STA repaired specimen exhibited better fatigue life compared to the DA repaired specimens, and in fact, the STA repaired specimen did not fail at this load level. Similar to tests performed 70% of YS, cracks first appeared in the substrate grain boundaries near the deposit zone - substrate interface for both DA and STA conditions. Representative figures are shown in Figure 5.15 (a) and Figure 5.17 (a). In DA condition, after 0.4 N_f cycles elapsed, transgranular cracks appeared in the substate as

shown in Figure 5.15 (b). The transgranular cracks originating at the substrate GB act as the major dominant crack and propagated at a high rate (Figure 5.14 (a)). As a result, the number density of transgranular cracks does not increase, as shown in Figure 5.14 (b). The cracks grow into the deposit zone only after significant growth through the substrate at $0.6 - 0.7 N_f$. In the deposit zone, the cracks grew primarily through the Laves phase as shown in Figure 5.15 (c) and Figure 5.15 (d). Interestingly, the growth of the intergranular cracks that formed at the substrate grain boundaries was restricted at the TiC particles, as indicated in Figure 5.15 (a – b). The TiC particles are identified as the round dark phases on the substrate, as shown earlier in Figure 4.21 (d) in Chapter 4.

Similar to the repaired DA specimen, the substrate grain boundaries provided preferential sites for crack initiation and growth for cyclic testing at 45% of YS in the STA condition as well. It is observed that cracks initiated in the substrate grain boundary near the repaired joint early in the fatigue life; however, the cracks never propagated, as shown in Figure 5.17 (a – b). It can be inferred that in the STA condition, the cyclic stress required to propagate these cracks is higher than achieved at maximum cyclic stress 45% of the YS. No cracks were observed at any other microstructural features for this condition. The failure mechanisms for both heat treatments and maximum cyclic stress levels are discussed in further detail in Section 5.4.2.

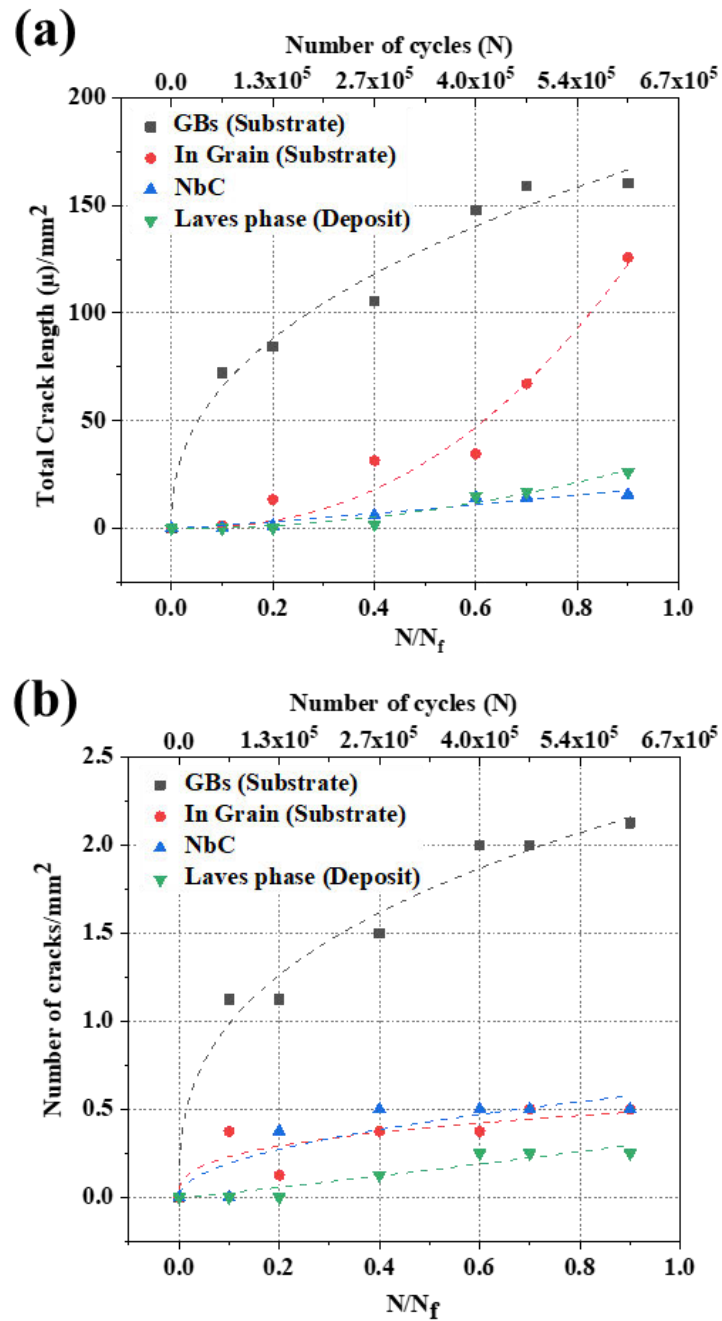


Figure 5.14: (a) Total crack length and (b) number density of fatigue cracks growing on different sources on the specimen surface at various stages of fatigue life at $\sigma_{max} = 45\text{pct}$ of YS in DA condition.

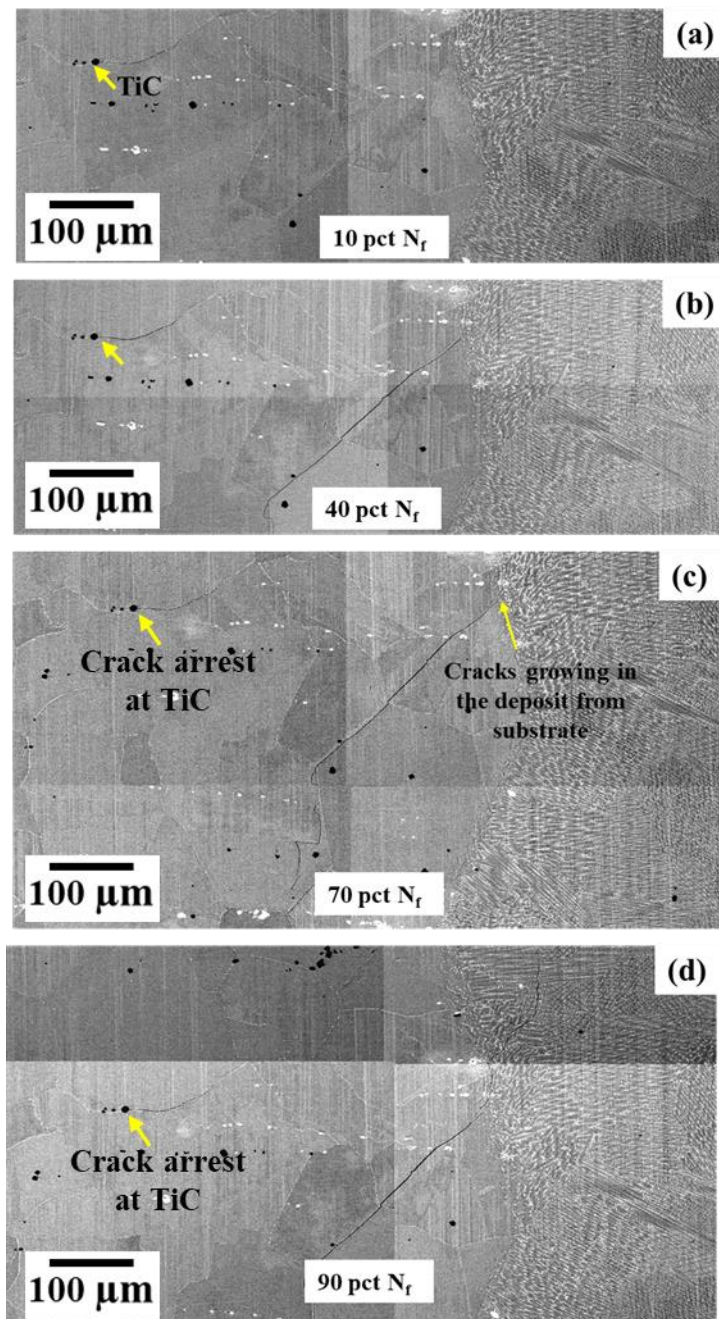


Figure 5.15: Representative figures showing the development of crack in DA specimen at 45% of YS in various stages of fatigue life: (a) 10 % N_f ; (b) 40 % N_f ; (c) 70 % N_f ; (d) 90% N_f .

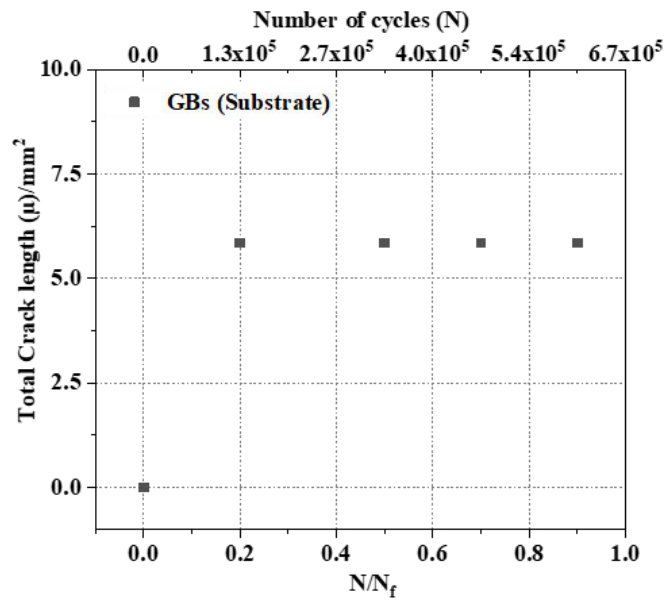


Figure 5.16: Total crack length of fatigue cracks growing on different sources on the specimen surface at various stages of fatigue life at $\sigma_{max} = 45\text{pct}$ of YS in STA condition.

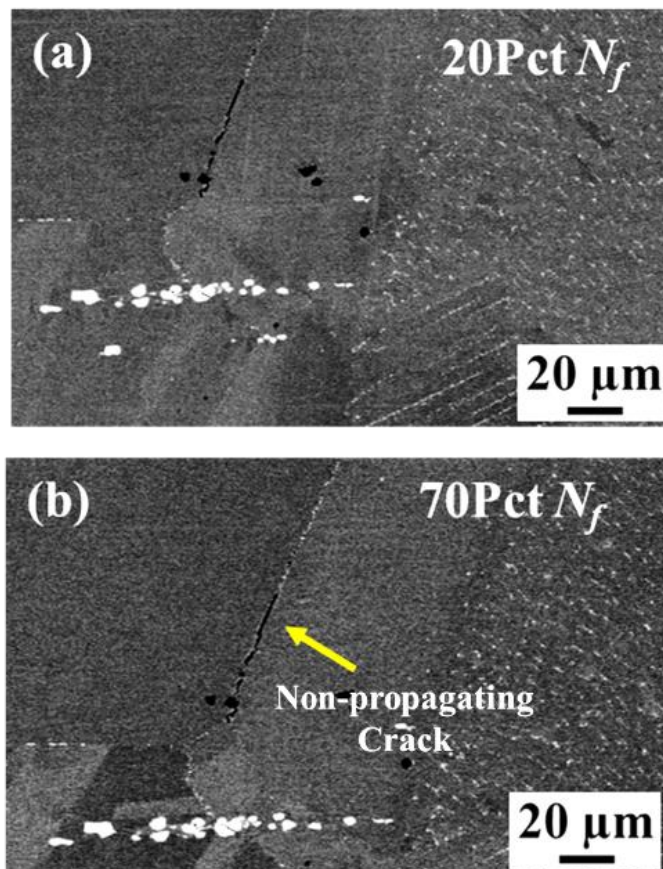


Figure 5.17: Representative figures showing the development of crack in STA specimen at 45% of YS in various stages of fatigue life: (a) 20 % N_f ; (b) 70 % N_f .

5.3.5 Final failure in uninterrupted test specimens

The surfaces of the uninterrupted failed specimens were inspected under SEM to identify the region of fatigue failure and the phases around the fatigue crack. The longitudinal surfaces were studied for samples tested to failure at 70 % of YS and 50 % of YS in both heat-treated conditions, as shown in Figure 5.18 (a – b) and Figure 5.19 (a – b), respectively. Unlike the interrupted tests that were performed at 45% of YS, for examination of final failure, specimens tested at 50 % of YS were chosen as in some cases the 45 % of YS STA specimens were run-outs.

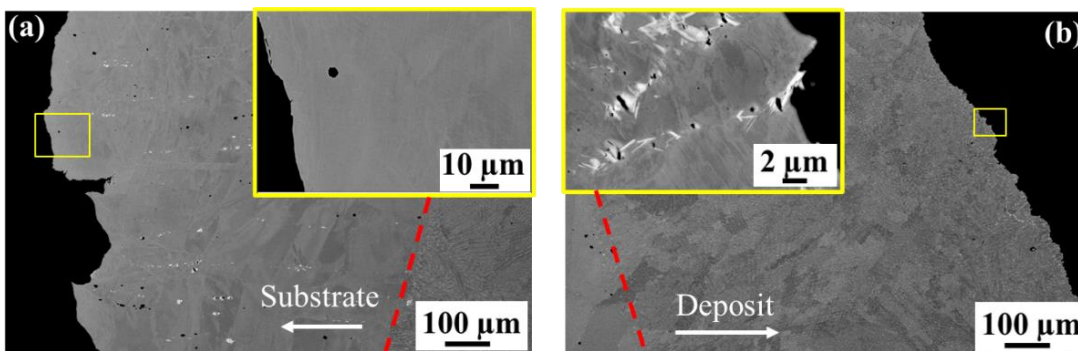


Figure 5.18: The surface of the uninterrupted test samples showing the region of final fracture, tested at 70 % of YS in (a) DA: failure in the substrate and (b) STA condition: failure in the deposit zone.

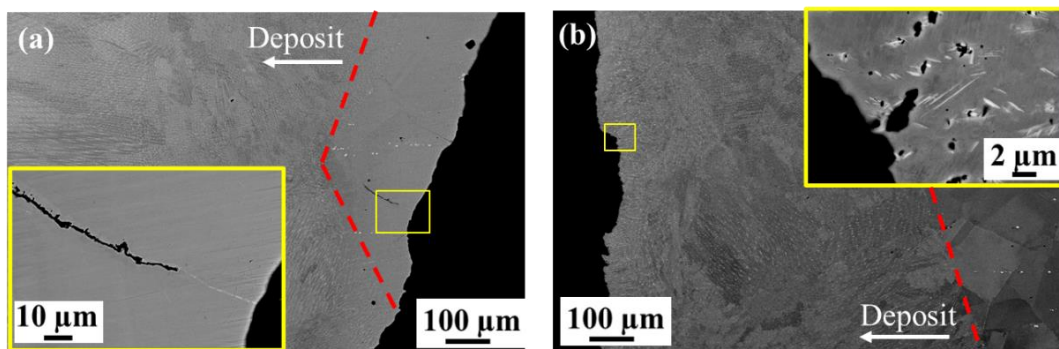


Figure 5.19: The surface of the uninterrupted test samples showing the region of final fracture, tested at 50 % of YS in (a) DA: failure in the substrate and (b) STA condition: failure in the deposit zone.

The longitudinal surface near the fatigue crack region shows that the final fracture took place ~500 – 600 μm from the interface; however, this final fracture was in the deposit for the STA condition and the substrate for the DA condition. This observation agrees well with the mechanism of failure demonstrated using the interrupted tests, as shown in the previous section (Section 5.3.4). At both maximum cyclic stress levels (70 %

and 50 % YS) for the DA specimens, as shown in Figure 5.18 (a) and Figure 5.19 (a), respectively, exhibited cracks propagating through substrate grain boundaries and twin boundaries. Some secondary grain boundary cracks near the repaired joint were observed, as shown in Figure 5.19 (a). On the contrary, the specimens tested in STA condition exhibited break-up of the Laves phase and δ phases from the matrix in the deposit was observed as shown in Figure 5.18 (b) and Figure 5.19 (b) for 70 % and 50 % YS respectively. With an increasing number of cycles, the break-up of the Laves phase and δ phases, along with the deformation of the austenitic matrix, led to the formation of microscopic voids, which provided an easy crack path and ultimately failure of the repaired composite. Moreover, the results obtained from the uninterrupted test specimens also confirm the consistency of the failure mechanism established using the interrupted tests.

The fracture surface of specimens tested under DA condition at 70 % of YS and 50 % of YS is shown in Figure 5.20 (a – d) and Figure 5.21 (a – d), respectively. The corresponding SEM micrographs for specimens tested under STA condition are represented in Figure 5.22 (a – d) and Figure 5.23 (a – d). The failure occurred in the substrate for the DA-repaired specimen and the deposit zone for the STA-repaired specimens. Therefore, the fracture surface is representative of the features of the wrought IN718 substrate in DA condition and the deposit zone in STA condition. The fracture surfaces exhibited features such as facets, secondary cracks, striation marks, and manufacturing defects, including porosities and dimpled areas that are typical of microvoid coalescence. The dimples appear to be finer, and the overall fracture surface is smoother in the STA-repaired specimen that failed in the deposit zone compared to the DA-repaired specimen that failed in the substrate region. In DA condition (Figure 5.20 (b) and Figure 5.21 (b)), after crack initiation on the specimen surface, crystallographic facets are observed. Such facets are commonly observed in high-cycle fatigue of wrought IN718, and AM IN718 tested at room temperature [126,136,218–220]. Ratchet marks and ridges are observed as seen on the fracture surface, which formed due to multiple cracks propagating on parallel planes that are interconnected via secondary perpendicular cracks [126].

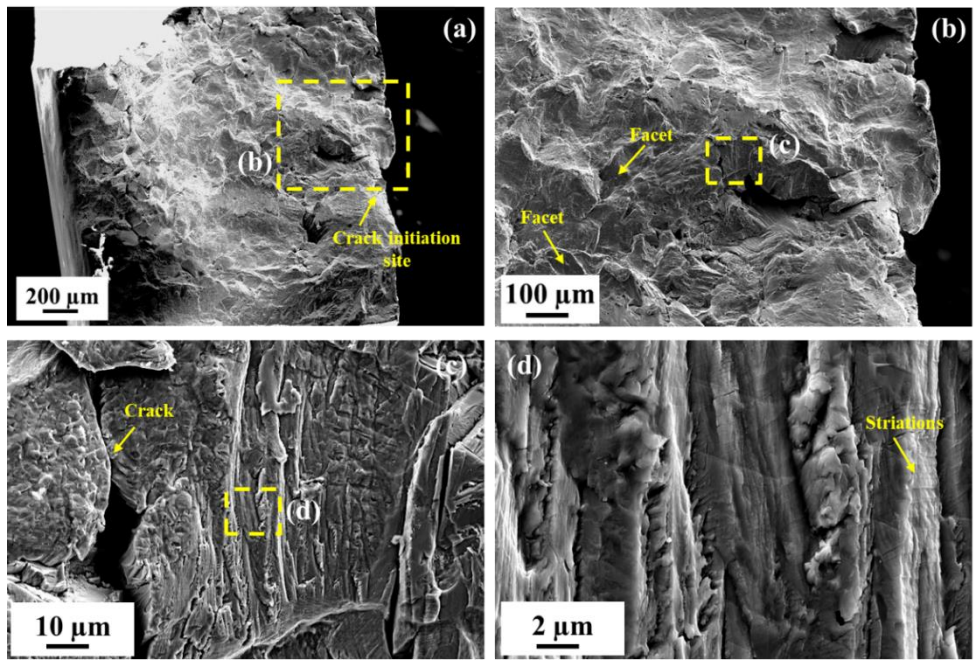


Figure 5.20: Appearances of the fracture surface of DA-repaired specimen tested at 70% of YS: (a) crack initiation sites, (b) facets and (c) cracks on the fractured surface, (d) striation marks on the fracture surface.

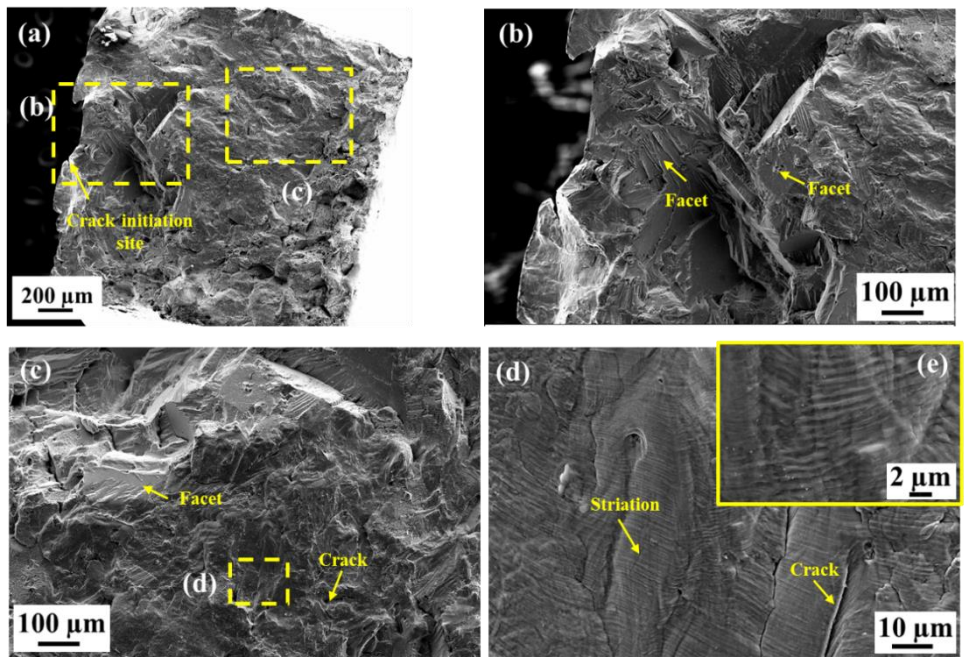


Figure 5.21: Appearances of the fracture surface of DA-repaired specimen tested at 50% of YS: (a) crack initiation sites, (b) facets and (c) cracks on the fractured surface, (d) striation marks.

In addition to dimples, the fracture topology exhibited fatigue striations are seen on the fracture surface, as shown in Figure 5.20 (d), Figure 5.21 (d), Figure 5.22 (d) and Figure 5.23 (d). Striation marks are formed due to crack blunting and reshaping during

fatigue failure or crystallographic slip lines intersecting fractured surfaces [130,217]. The STA-repaired specimen exhibited crack initiation sites associated with defects (porosities, brittle phases, or inclusions) located near the free surface (Figure 5.22 (b – c)) and Figure 5.23 (b – c)). The surface exhibited a combination of ductile and brittle micro-mechanisms, i.e., dimples and facets (intergranular and transgranular). It is known that the typical fatigue crack growth curve consists of 3 stages: (1) where cracks are first initiated, followed by (2) steady-state crack propagation stage, and (3) final rupture [85]. The fatigue striations are generally created during the crack propagation stage. Scarce fatigue striations observed on the STA specimens that failed in the deposit zone compared to the DA specimens that failed in the substrate can be attributed to rapid crack growth through the deposit zone in the specimens tested in STA condition.

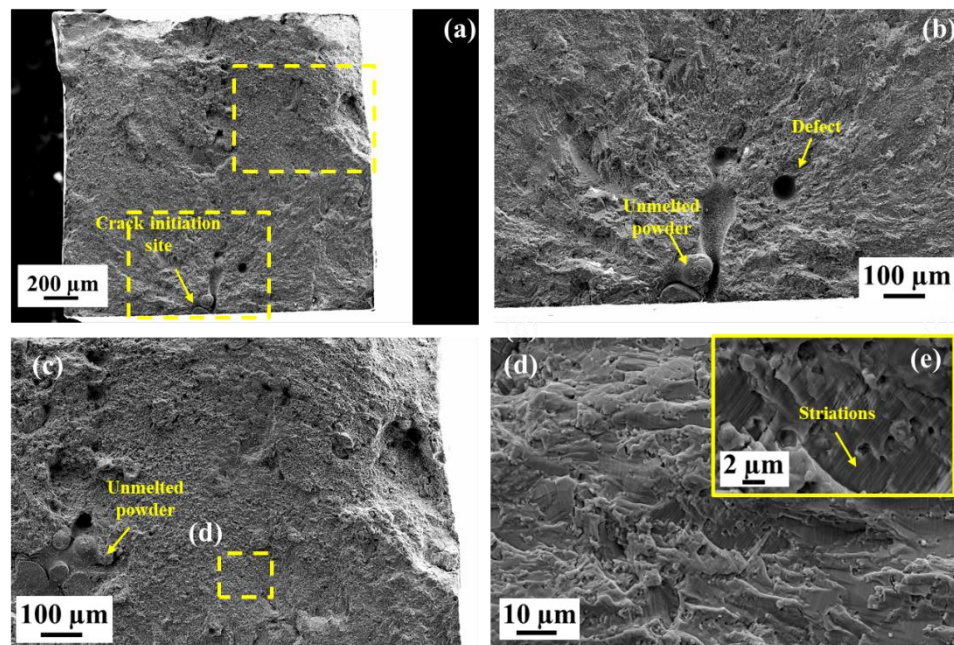


Figure 5.22: Appearances of fracture surface of STA-repaired specimen tested at 70% of YS: (a) crack initiation sites, (b) defects and (c) unmelted powder particles on the fractured surface, (d) striation marks on the fracture surface.

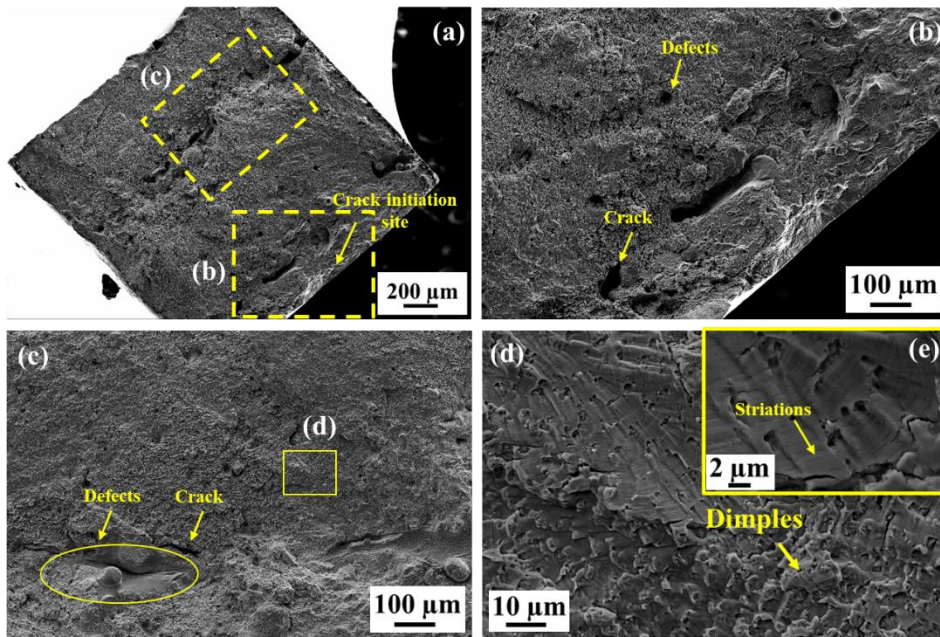


Figure 5.23: Appearances of fracture surface of STA-repaired specimen tested at 50% of YS: (a) crack initiation sites, (b) defects and (c) unmelted powder particles on the fractured surface, (d) striation marks on the fracture surface.

5.4 Discussion

5.4.1 Rationalisation of room temperature fatigue performance with the microstructure of the repaired composite under the heat-treated condition

This section discusses the major fatigue behaviour findings in Sections 5.3.3 – 5.3.5 in relation to the underlying microstructure. Discussions on the following observations are included: (1) explanation for the difference in failure location for the two post HT conditions (in the substrate region in DA condition and the deposit zone for STA-repaired specimens); (2) proposed explanation for STA-repaired composites performing comparatively better at low cyclic stress regimes and DA-repaired specimens performing better at higher cyclic stresses.

The experimental results presented in Sections 5.3.4 and 5.3.5 reveal that the substrate grain boundaries, in both heat-treated conditions, experience a significant amount of fatigue damage. It is apparent that in both the heat-treated conditions, the grain boundaries offer a favourable site for crack initiation and play a major role in the fatigue damage initiation. However, the cyclic failure mechanism is different when the maximum applied cyclic stress is above or below the inflection point (Figure 5.8).

Below the inflection point, it is observed that the STA-repaired specimens exhibit a higher fatigue limit compared to DA. It is established that, below the fatigue limit, the accumulation of fatigue damage through cyclic loading is balanced by the progressive strengthening due to strain ageing through which, during deformation, the dislocations are locked by the solute atoms and hinder their movement. Therefore, higher loads are required to move the dislocations and hence, plastic deformation that results in strengthening of the material [221]. Fatigue failure occurs when the fatigue damage predominates over strengthening. Therefore, a set of conditions above which the already initiated microcracks can propagate determines the fatigue strength. In interrupted tests performed on repaired-STA composites with maximum cyclic stress at 45% of the yield stress, which is just below the endurance limit, non-propagating microcracks at the substrate grain boundaries were observed, as shown in Figure 5.17 (a – b). At a similar maximum cyclic stress level for the DA condition, the microcracks initiating on the substrate grain boundary were able to propagate, ultimately leading to a failure (Figure 5.15 (a – c)). The role of the δ phase and Laves phase on this difference in fatigue limit in the STA and DA conditions is discussed in the following paragraphs.

The wrought material outperforms the repaired material in room temperature tests, especially at high-stress levels. The deposit zone has a significantly smaller grain size of heterogeneous distribution and no annealing twins compared to the wrought material with coarse equiaxed grains. Since the crystallographic texture is weak (in both deposit zone and substrate), various microstructural features in the repaired zone, substrate and the repaired interface/joint are likely the main competing factors influencing the fatigue performances. The microstructural features include grain size, defects and porosity, presence and fraction of Laves phase and δ precipitates. In the repaired composite various secondary phases present on either side of the repaired joint would dictate the final failure mechanism of the repaired composite. As shown in Section 5.3.1 (Figure 5.5 (a – c)), in the DA condition, the substrate grain boundaries in the HAZ region are devoid of any δ phase, with Laves phase present on the substrate grain boundaries and along the interdendritic region in the deposit zone. Mechanical properties of IN718 from uniaxial tensile tests have shown that Laves phases have poor plastic deformation capability [13,14]. The γ matrix possesses higher deformability and often leads to the formation of stress concentration sites at the γ – Laves phase interface. As the cracks predominantly initiate and grow through the

substrate grain boundaries (Section 5.3.4), at higher loads, the failure mechanism in the DA-repair specimens mimics the failure mechanism of wrought IN718. However, the absence of δ phase post DA heat treatment might have resulted in lower fatigue properties. Also, the HCF behaviour of the repaired composite in DA suggests that coarse microstructure in the substrate coupled with a high content of annealing twins has a larger effect on shortening the life of the samples than porosity and Laves phase in the deposit zone because cracks can easily form along twin boundaries [130]

From uniaxial tensile tests reported in Figure 5.7, the repaired STA condition exhibited improved ductility compared to the DA specimen. While it has been observed that δ phase improves fatigue properties in Ni-base alloys by arresting crack propagation [137,222], this only occurs at low-stress levels. Raymond [223] reported that δ phase degrades the fracture toughness and low-cycle fatigue life in wrought IN718. Similar observations are also reported by J. An et al. [224], who attributed the fatigue resistance of δ phase to its morphology. The Laves phase and δ precipitates are Nb rich, while the surrounding matrix is depleted of Nb, resulting in a lack of γ'' strengthening phase [134,138]. Therefore, near the δ phase, a region depleted in γ'' is formed that may act as micro-void initiation site. Moreover, a higher volume fraction of δ phase in the microstructure depletes the available Nb for γ'' formation during ageing treatment. During cyclic loading, dislocations are easily piled up around the long needle-like δ phase, which leads to high-stress concentration, and subsequent δ phase debonding from the matrix and helps easy crack propagation along long needle-like δ phase surrounded by precipitates free zone. Therefore, the heterogeneous distribution of the needle-like δ phase and higher volume fraction in the deposit zone made it easier to induce stress concentration sites at high-stress levels, and the STA-repaired composite at high stresses failed in the deposit zone. At low-stress levels, the debonding of the δ phase/Laves phase – γ matrix did not happen.

5.4.2 Comparison to wrought material and published additive manufactured IN718

The fatigue limit of wrought IN718 as reported in the Aerospace Structural Metals Handbook is ~500 MPa. That value is 75 MPa higher than found for the wrought IN718 used in the present study. The grain size and hence, distribution of the δ phases might be the reason for the difference in fatigue limit. However, the HCF results of the wrought IN718 agree well with the test results reported by Kashev et al. [225] on wrought IN718 at room temperature. HCF tests on wrought IN718 with different grain

sizes by Ono et al. [226] and Kevinsanny et al. [227] revealed higher fatigue life corresponded to the high strength and hardness in the fine-grained samples compared to the coarse-grained samples. It is well known that grain boundaries hinder the slip transfer between grains, leading to the formation of pileups and hardening as the grain size decreases [85]. Therefore a fine-grained material with higher hardness and strength would provide higher resistance to plastic deformation, and hence improved fatigue strength is observed [228].

The fatigue test results from the current study have been compared in Figure 5.24 with literature fatigue data for IN718 manufactured by various AM technologies [132,213,220], and weld repaired IN718 [138,139]. For a valid comparison, only literature data from room temperature HCF tests performed at $R = 0.1$ and hourglass specimen geometry was included. The fatigue limit estimated by Witkin et al. [220] on SLM manufactured IN718 tested at $R = 0.1$ was 450 MPa (see Table 2 [220]), which matches well with the specimens tested in STA condition while being ~ 100 MPa higher than the repaired composites tested under DA condition. Amsterdam et al. [8] also reported similar fatigue limit values for DED manufactured IN718. Compared to the results reported in the current investigation, Sivaprasad et al. [138] reported a significantly higher fatigue limit (~ 750 MPa) in wrought IN718. Similarly, the fatigue properties of the TIG welded IN718 composites in DA and STA conditions were consistently higher [138]. Thus, the difference in the fatigue properties compared to the present study can be attributed to the innate material properties of the IN718 substrate.

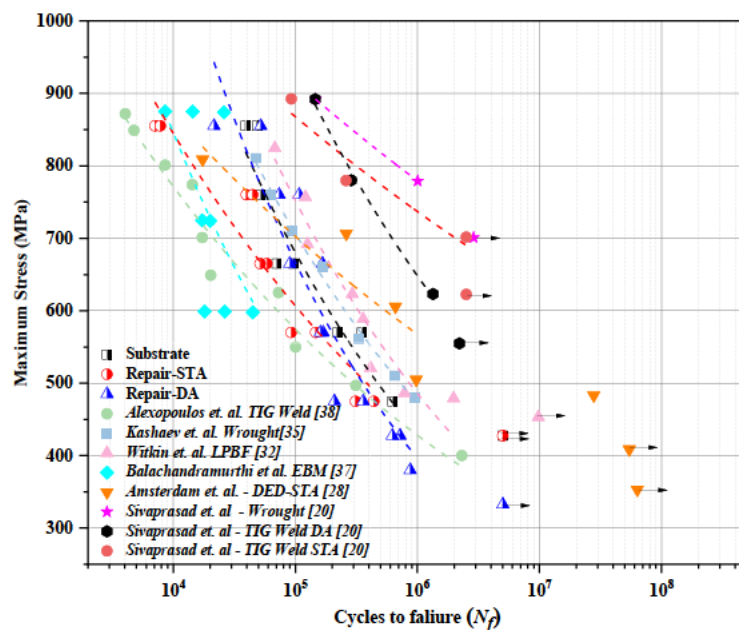


Figure 5.24: Comparison of S-N curve with existing data for IN718. For comparison, data from wrought, weld and AM IN718 were tested at room temperature, and $R = 0.1$ is used. (TIG: Tungsten Inert Gas welding, LPBF: Laser Powder Bed Fusion; EBM: Electron Beam Melting; DED: Direct Energy Deposition).

EBM fabricated IN718 tested by Balachandramurthi et al. [133] exhibited inferior fatigue performance. The fatigue performance of DED manufactured IN718 by Amsterdam et al. [132] exhibited similar fatigue performance compared to the repaired specimens tested in STA conditions. The specimens tested by Amsterdam et al. [132] were post-heat-treated at 1093°C and aged. The repaired specimens, under both heat-treated conditions, performed better than the TIG welded IN718 reported by Alexopoulos et al. [139]. Fatigue performance of TIG-welded specimens reported by Sivaprasad et al. [138] tested in DA and STA conditions shows a similar trend as reported in the present study. At higher maximum stress levels, the DA fatigue performance is better whereas, at low-stress levels, better fatigue performance and higher fatigue limit were reported for the STA specimens,

It can be summarised from the present investigation and other reports available in the literature that wrought IN718 generally outperforms IN718 processed via various additive manufacturing techniques or welding. The primary reason for the difference in the fatigue performance can be related to the difference in the microstructure due to various processing methods. Laser AM techniques can be broadly classified as direct energy deposit (DED) or laser powder bed fusion (LPBF) processes. High cooling rates of $10^3 - 10^5$ K/s are achieved during DED and $10^5 - 10^7$ K/s in LPBF processing [68]. Similarly, high cooling rates $>10^2$ K/s are achieved during welding processes [229]. The non-equilibrium phases formed during AM processes and welding results in the deterioration of fatigue properties. Post-deposit heat treatments are often employed to improve fatigue properties. In repair processes (welding/AM), to prevent coarsening of base material grains, the solution treatment temperatures are generally restricted to 980°C. The solution treatment at 980°C results in the formation of δ precipitates along with retained Laves phases. The formation of δ precipitates results in slight softening of the material, thereby deteriorating high-stress HCF properties; however, at stresses below 50% of yield strength, δ precipitates are found to be beneficial for fatigue properties.

5.5 Conclusion

The experimental work exhibits a spatial gradient of microstructure in the repaired composites. In the repaired joint, the microstructure evolves from the uniform large equiaxed grains of the substrate to a heterogeneous mix of fine columnar and equiaxed grains in the deposit zone. Since crystallographic texture was characterised as weak, the main competing features governing the fatigue performances are grain size, defects such as porosity, δ /Laves precipitates, and grain boundaries. The major conclusions derived are as follows:

1. The repaired composites exhibit inferior fatigue properties compared to the wrought substrate. However, the performance of the repaired samples is comparable to AM IN718 reported in the literature and, in some cases, better than welded IN718, tested under similar conditions ($R = 0.1$)
2. At high load levels, the DA samples performed better than the STA samples, whereas, at low loads, the STA samples performed better. Final failure has been reported in the substrate region for DA specimens and in the deposit zone for STA specimens.
3. The Nb-rich film formed in the wrought grain boundary during the deposition process act as the crack initiation sites in all the conditions tested in the current chapter.
4. In STA condition, needle-shaped δ phases coupled with Laves phases are efficient in arresting crack formation at low loads; however, at high loads provides preferential sites for stress concentration and microcrack initiation.
5. In DA conditions, the Laves phase along the HAZ grain boundaries are the first crack initiation sites, and failure happens through the coarse substrate grain boundaries.
6. It is found that grain boundary cracks can generate below the endurance limit in IN718; however, the cracks do not propagate.

CHAPTER 6**Effect of TiB₂ addition on microstructure and mechanical properties in Inconel 718 processed via Direct Energy Deposition****6.1 Introduction**

A typical Laser Direct Energy Deposition (DED) produced Inconel 718 (IN718) microstructure is characterised by columnar dendrites growing epitaxially from the substrate. IN718 is widely studied for laser Additive Manufacturing (AM) processes, with detailed microstructure and properties of AM IN718 reported in the literature [10,11,14,34,53,93,95,108,198,230]. During AM processing, the substrate acts as the primary heat sink; therefore, the heat flux is towards the substrate, and the dendrites grow opposite to the substrate [10,106]. The columnar nature of the microstructure, as observed in AM IN718, often leads to anisotropy in the deposited part [12,13,113]. An equiaxed microstructure is expected to reduce the anisotropy in the mechanical properties of the fabricated component. The effect of pre-existing nuclei on the G/R maps was shown by Gaumann et al. [186] and Babu et al. [107]. A greater number of pre-nucleation sites favours the formation of equiaxed grains. Therefore, a high number of nucleation sites can facilitate grain nucleation while restricting grain growth to achieve an equiaxed microstructure. A higher number of nucleation sites can be achieved by: (a) mechanically by agitating the melt pool during solidification; or (b) chemically by adding inoculants acting as nuclei [145]. Inoculation is considered as a successful solidification altering approach to effectively achieve grain refinement. This refers to adding grain refiners or a small number of secondary particles to promote heterogeneous nucleation and restrict grain growth.

The use of inoculant/secondary particles to alter the properties in standard alloy systems is reported in the literature. Composites and nano-composites manufactured using AM techniques are reported for alloy systems such as steels [156–158], Aluminium alloys [159,160], Titanium alloys [161], and Ni-based superalloys [162–167]. The general motivation for using inoculants is to realise tailored mechanical properties, and in some studies, microstructure modification was achieved. The common reinforcing materials used for nano-composite in AM process, especially for IN718, are listed in [165–168,231,232]. The effect of WC-W₂C addition on SLM fabricated IN718 microstructure was studied by Ho et al. [154] and presence of fine grains on the inoculant surface after heat treatment was observed. Jia et al. [162] and Gu et al. [232] used TiC as reinforcements to improve strength and wear performance

in SLM IN718. The IN718/TiC composites exhibited improved mechanical properties with improved nano-hardness and low wear rate, compared to IN718 deposits. The addition of inoculants generally enhances the strength of the composite material, despite there being evidence to suggest the reduced ductility [168]. Generally, the selection criterion of these inoculants has yet to be explored in detail. For example, an open question remains as to whether the inoculant can still act as an effective heterogeneous nucleation site if a certain crystallographic match exists between the inoculant and matrix. Ho et al. [169] observed that CoAl₂O₄ particles formed a dispersion of Al-rich nano-oxide particles in the matrix, which seemed responsible for the formation of refined equiaxed grains, reducing crystallographic texture and improved creep properties.

This chapter explores the potential of TiB₂ as an efficient grain refiner to aid the transformation of the columnar-to-equiaxed microstructure for IN718 during DED processes. The motivation for selecting TiB₂ is explained with reference to a crystallographic model. Moreover, the effect of the addition of TiB₂ on the mechanical properties of IN718/TiB₂ is elaborated.

6.2 Experimental details

6.2.1 Powder preparation and DED deposition process

Plasma atomised, spherical IN718 powders in the size range of 50 µm – 150 µm supplied by GE Additive have been used as the feedstock material. Irregular-shaped TiB₂ powders were premixed with the feedstock IN718 powders using ball milling. A customised vertical ball mill with a powder-to-ball ratio of 1:1; 200 RPM was used, and the ball milling process was performed in argon atmosphere for 6 hours. Ball milling was followed by drying the milled powders in a vacuum furnace at 120°C for 1.5 hours. TiB₂ particles with three characteristic sizes were considered: < 1 µm, < 10 µm and < 40 µm; the respective SEM images are shown in Figure 6.1 (a), Figure 6.1 (b) and Figure 6.1 (c). After the ball milling process, the corresponding composite powder decorated with the TiB₂ particles is shown in Figure 6.1 (d) - Figure 6.1 (f). Figure 6.1 (d) shows that the TiB₂ powders of size < 1 µm agglomerated during the ball milling and was not evenly distributed over the feedstock IN718 powders, and TiB₂ powders of size <40µm did not attach to the IN718 powders as shown in Figure 6.1 (f). Figure 6.1 (e) shows that the TiB₂ powders of < 10 µm seem to attach to the feedstock powders more efficiently compared to the < 1 µm and < 40 µm powders,

resulting in a uniform distribution of TiB_2 particles over the feedstock powder. Therefore, the following study was performed on the TiB_2 powders with the characteristic size of $< 10 \mu\text{m}$.

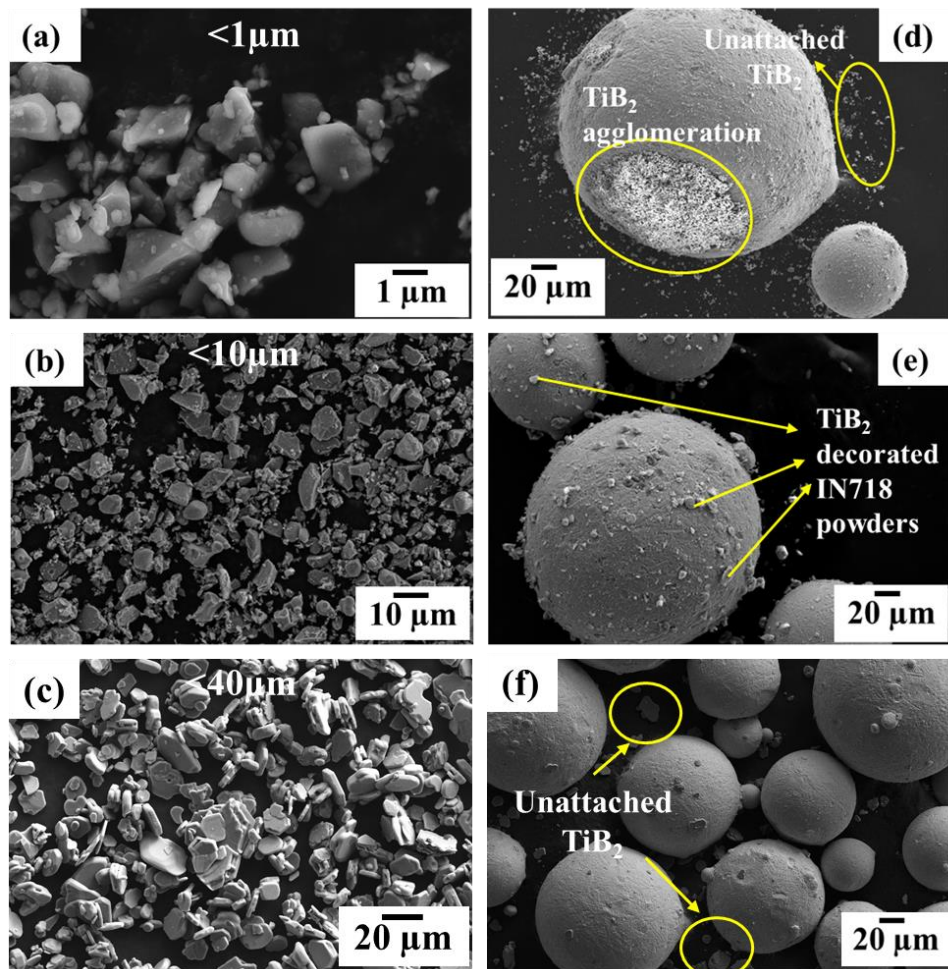


Figure 6.1: IN718 powders mixed with 1.5 wt% TiB_2 powders: (a), (b), (c) are TiB_2 powders with size of $< 1 \mu\text{m}$, $< 10 \mu\text{m}$ and $< 40 \mu\text{m}$, respectively; The corresponding TiB_2 decorated feedstock powders with TiB_2 particle size: (d) $< 1 \mu\text{m}$ (e) $< 10 \mu\text{m}$ (f) $< 40 \mu\text{m}$.

An Optomec LENS MR-7 apparatus equipped with a 1kW IPG fibre laser with a coaxial powder delivery system was used for the repair work. The process parameters used for the deposits are shown in Table 6.1. One parameter set is referred to as high energy while the other as low energy. Identification of the above-mentioned two process parameter sets can be found in Chapter 4. An alternate scanning pattern was used for all the deposition processes, as schematically shown in Figure 6.2 (a). The corresponding characterisations, including SEM investigation, EBSD and XRD, were done along the building direction on the z-x plane, as illustrated in Figure 6.2 (b).

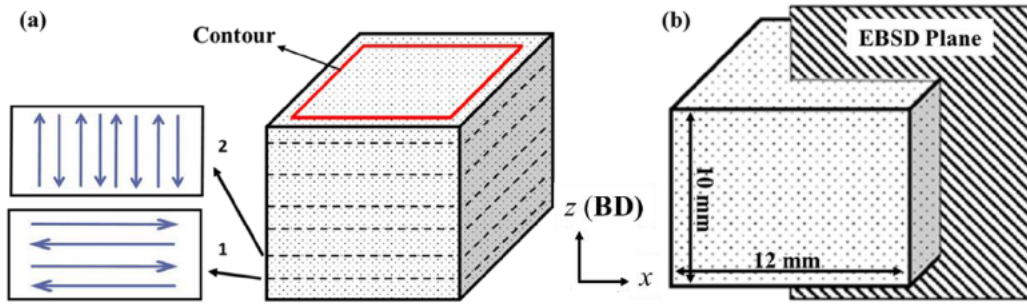


Figure 6.2: Schematics showing (a) build process; and (b) the observation plane for EBSD analysis.

Table 6.1: Printing parameters

Power	Scan speed	Hatch spacing	Layer thickness	Line energy density
W	(mm/s)	(mm)	(mm)	(J/mm)
500	6.3	0.95	0.48	78.74 (High Energy)
350	10.6	0.60	0.28	33.08 (Low Energy)

6.2.2 Fabrication of tensile test pieces and tensile testing details

Rectangular-shaped IN718 and IN718/TiB₂ specimens of dimensions (12 × 12 × 50 mm³) were fabricated vertically using DED process with the process parameters indicated in Table 6.1. Vertical and horizontal rectangular blocks were deposited. The blocks were machined off the substrate, and then tensile specimens with dimensions of 12.5 mm gauge length and 3 mm width were made using wire electro-discharge machining (EDM), as shown in Figure 6.3. This also applies to the IN718/TiB₂ specimens.

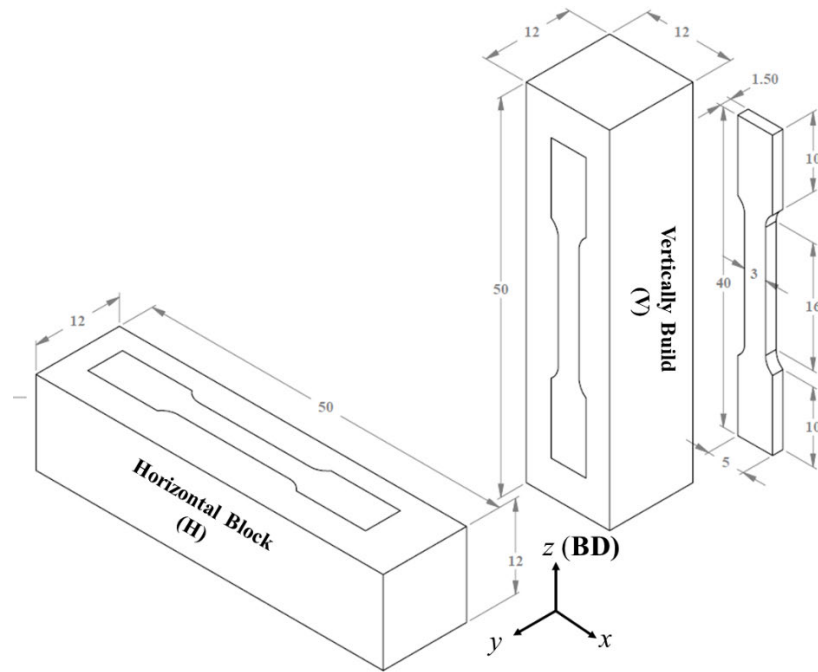


Figure 6.3: Schematic diagrams showing the specimen extraction locations with respect to the DED deposit sample blocks; dimensions of tensile specimen are noted.

All the uniaxial tensile tests were carried out using a 100 kN Instron servohydraulic universal testing unit equipped with Bluehill 3 software in Instron Wave Console. A video extensometer with a 100 mm axial field of view was used to measure strain during the tests. Displacement-controlled tensile tests were conducted at room temperature with a nominal strain rate of $1 \times 10^{-3} \text{ s}^{-1}$. The time, load, actuator displacement, and gauge extension from the extensometer were digitally recorded for all the tests. 3–4 samples were tested for each condition and then used to calculate the average values and standard error of tensile properties. Vickers microhardness was measured on both as-manufactured IN718 and IN718/TiB₂ samples with a microhardness testing machine using a 500 g and 15 s dwell-time load. For each condition, 8 – 12 indentations were performed.

6.2.3 Microstructure characterisation

Samples for microstructural characterisation were mounted, mechanically ground successively from 240 Grit to 1200 Grit, and polished with diamond suspensions from 9 μm to 1 μm and finally with OPS colloidal silica suspension. A Supra 55-VP scanning electron microscope (SEM), equipped with energy dispersive X-ray spectroscopy (EDS) and electron backscatter diffraction (EBSD) system from Oxford Instrument, was employed to characterise the microstructural features, operating at 20

kV accelerating voltage. The data obtained were analysed with HKL Channel 5 software. EBSD scans were made at low magnification for grain size analysis to cover an area greater than $1.5 \times 1.5 \text{ mm}^2$ using a step size of $2.5 \text{ }\mu\text{m}$. Grains greater than 10 pixels in the area were filtered and used for subsequent analysis according to ISO 13067 recommendation. Pole figure contouring was done with a half-width of 10° and data clustering of 5° . For a like-for-like comparison, the max MUD values for the pole figures were fixed to 8. EBSD maps for Taylor factor determination and local area misorientation were performed at higher magnification using a step size of $1.5 \text{ }\mu\text{m}$ and $0.15 \text{ }\mu\text{m}$, respectively. Note that all the EBSD mappings for Schmid factor and Taylor factor determination were done on the z-x planes for vertically built samples. In contrast, the x-y planes were investigated for horizontally built samples since these planes are the interesting areas relating to mechanical properties with regard to the loading directions.

6.3 Results

6.3.1 IN718/TiB₂ microstructure

6.3.1.1 Grain size and texture analysis

The EBSD maps, grain size distribution and pole figures of high energy as-deposit IN718 are shown in Figure 6.4 (a – c). The EBSD IPF map of as-deposit IN718 in Figure 6.4 (a) shows that the material exhibits a mix of elongated and fine-equiaxed grains in the microstructure growing along the build direction. A zig-zag type grain morphology is seen in the as-deposited material, with dendrites oriented towards the building direction intersecting at the region between the layers. The reason for such grain morphology is discussed later. Figure 6.4 (c) shows the $\{100\}$, $\{101\}$, $\{111\}$ pole figures of as-deposit IN718. The $\{100\}$ pole figure exhibits the highest pole figure intensity with MUD values of 7.9, indicating a preferred orientation in as-deposit IN718 whereby the grains grew epitaxially parallel to the $\{001\}$ direction. A $\{001\}$ texture along the building direction (\parallel BD) is often reported in AM Ni-based alloys [10,11,13,120]. For the FCC γ phase, the $\langle 100 \rangle$ crystallographic direction is the easy growth direction, and the grains having one of their $\langle 100 \rangle$ crystallographic directions aligned with the heat flow direction will exhibit the preferential growth [113]. Therefore, in the present chapter, the $\{100\}$ pole figures are reported for all subsequent deposits. Moreover, the pole figures presented here are based on >3000 grains; hence, the texture interpretation is statistically significant.

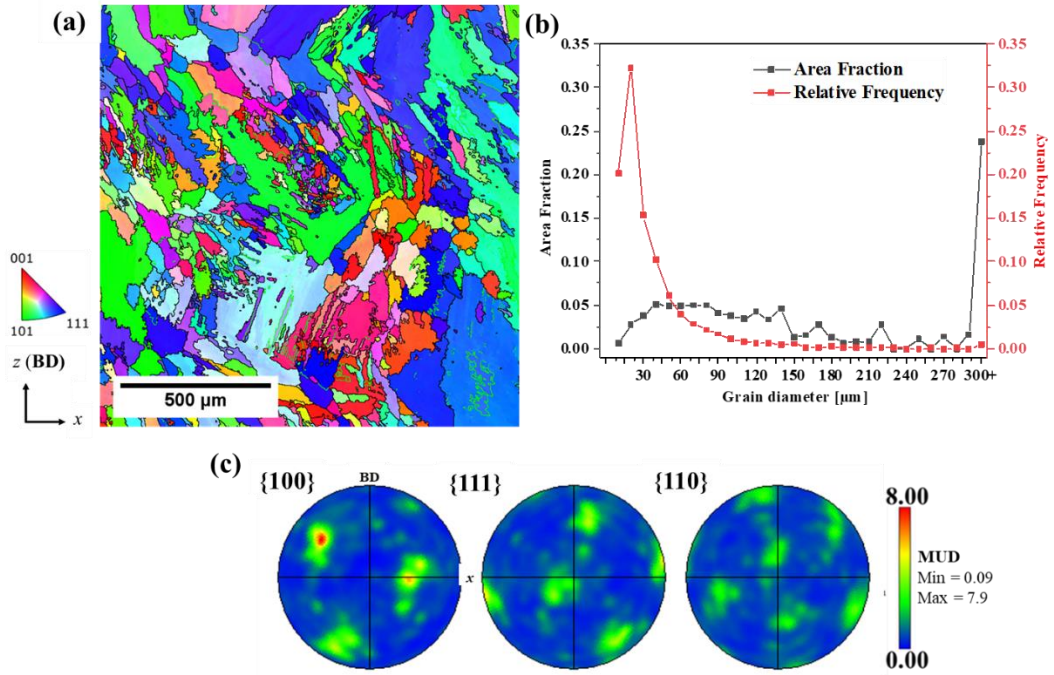


Figure 6.4: (a) EBSD IPF map for as-deposit IN718; (b) The grain size distribution as relative fraction of grain count and area fraction are compared; (d) the {100}, {111}, and {110} pole figures for as-deposit IN718.

The grain size distribution for as-deposit IN718 for high energy deposits is analysed and compared in terms of the relative fraction of the grain count and area weighted fraction, shown in Figure 6.4 (b). Relative distribution of the number of grains is often used to represent the grain size distribution from EBSD data [89,160]. The relative fraction for grains in the range 0 μm – 10 μm can be mathematically represented as

$$N_{f(0-10)} = \frac{\Sigma(\text{Number of grains with size } 0 \mu\text{m} - 10 \mu\text{m})}{\text{total number of grains}} \quad [6.1]$$

Due to the non-homogenous distribution of the grains, the count of large grains $\sim 300 \mu\text{m}$ is very low; however, these grains occupy a high percentage of area in the microstructure. As a result, it fails to represent the true nature of the microstructure. Therefore, area weighted fraction (A_f) is used as the parameter for representing the grain size distribution. A_f represents the relative fraction of the area occupied by a specific grain size range. In the present analysis, 10 μm range is used to separate the grain groups.

$$A_{f(0-10)} = \frac{\Sigma(\text{Area of grains with size } 0 \mu\text{m} - 10 \mu\text{m})}{\text{total area}} \quad [6.2]$$

The EBSD maps depicting the orientation and distribution of the grains in as-deposit IN718 deposited with high energy and low energy deposits are shown in Figure 6.5(a)

and Figure 6.5(c), respectively. The corresponding $\{100\}$ ||BD pole figures are shown in Figure 6.5(b) and Figure 6.5(d). The area fraction (A_f) distribution for as-deposit IN718 in high and low-energy deposits is compared in Figure 6.5(e). The as-deposit IN718 microstructure exhibits a high fraction of the area occupied by large grains of $>300\mu\text{m}$. In the high-energy deposit, grains of $>300\mu\text{m}$ occupied $\sim 22\%$ of the total grain area and $\sim 10\%$ in the low-energy deposits.

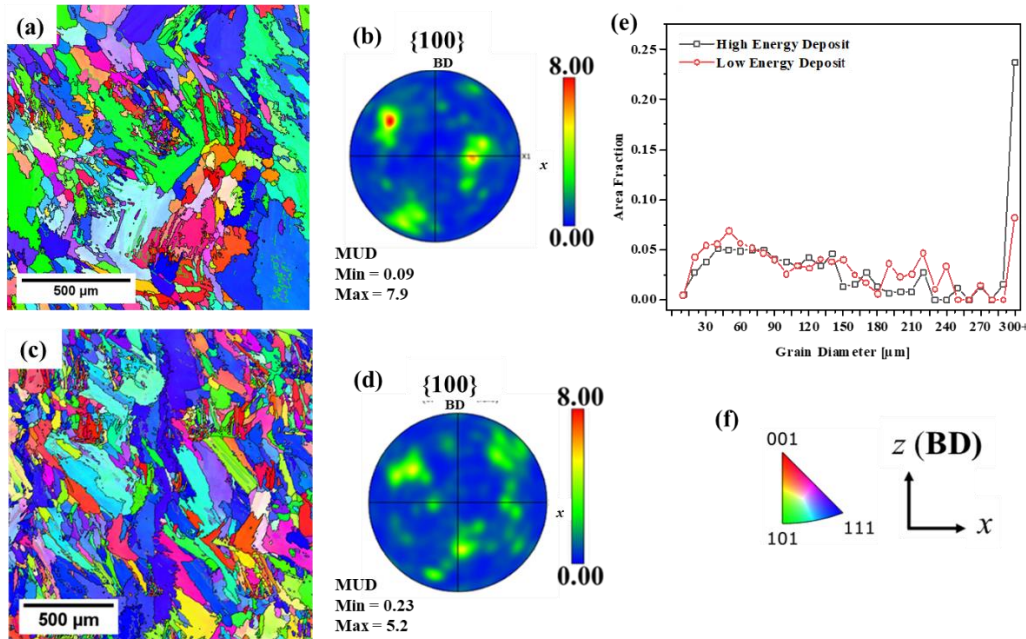


Figure 6.5: As-deposit IN718 microstructure showing (a) grain orientation, and (b) $\{100\}$ pole figures of high energy deposit; (c) grain orientation, (d) pole figures of low energy deposit; (e) grain size distribution and (f) legends showing the IPF colour and building direction.

During the solidification of an alloy, the solidification parameters: the thermal gradient G (K/mm) and solidification rate velocity R (mm/s), determines the morphology of the solidified grains. Depending upon the G/R ratio, the morphology of the resulting solid-liquid interface can be cellular dendritic, columnar dendritic, or equiaxed dendritic; a low G/R ratio favouring equiaxed dendrites. During the DED process, a large thermal gradient G at the solid/liquid interface generates large columnar grains parallel to the build direction [141,187]. Additionally, depending upon solidification conditions, either nucleation or growth rate may be predominant. It is understood that, during the solidification process, a preferential growth of the grains is expected parallel to the $\{100\}$ which is the crystallographically favoured orientation for FCC alloys. Only the grains (in the substrate) that have $\langle 100 \rangle$ direction parallel to the local heat flow

direction can grow in a polycrystalline substrate. This results in epitaxially growing grains from the substrate and results in the appearance of elongated grains when viewed on a section perpendicular to the building direction. Additionally, some new grains would form at the solid-liquid interface where the {100} crystallographic orientation parallel to the heat flow direction is not met. However, only the grains that meet the preferred crystallographic orientation grow, restricting the growth of the other grains. However, from the second layer onwards, there is a different competition between nucleation and growth because of the change in the laser scan direction. A zig-zag grain morphology occurs when the direction of primary dendrites changes by 90°. It was reported by Parimi et al. [11] and Dinda et al. [10], who studied DED IN718 and observed that the orientation of the primary dendrites might change by 60° or 90° during the deposition process, depending on the scanning patterns adopted during the deposition process. Both studies [10,11] indicated that a unidirectional scanning pattern resulted in a change of 60° and a bidirectional scanning pattern led to a 90° change in the growth direction of the primary dendrites, resulting in a zig-zag type morphology. During solidification of FCC metals and alloys, secondary dendrites grow perpendicular to the primary dendrites as the {100} planes are perpendicular to each other. A 90° change happens when there is no nucleation occurring at the layer interface and primary dendrites grow from the secondary dendrites of the previous layer. When nucleation occurs at the layer boundaries, a 60° change of the primary dendrite is observed.

In the present study, in as-deposit IN718, a mix of fine grain and elongated columnar grains is noted, as shown in Figure 6.5(a) for high energy and Figure 6.5(c) for low energy deposits. Elongated grains >300 µm are reported in the as-deposit IN718 microstructure, which is generally zig-zag shaped. The direction of laser movement was rotated by 90° after each layer. This resulted in the development of elongated zig-zag grains with no nucleation between the layers, and these large grains comprise a high fraction ~ 10 – 25 % of the total grain area. In other regions of the microstructure, the growth of the dendrites ceased due to the solidification conditions. It resulted in the formation of a fine-grained region in the as-deposit microstructure. The effect of TiB₂ addition to IN718 was investigated for both high and low energy deposits. The grain size distribution and the pole figures are studied from the EBSD maps for both energy densities. The effect of varying amounts of inoculant additions was systematically studied by increasing the amount of TiB₂ from 0.5 wt% - 2.5 wt%,

with an increment of 1 wt%. The EBSD map and corresponding $\{100\}$ pole figure for as-deposit IN718 is shown in Figure 6.6 (a) and Figure 6.6 (e), respectively. Figure 6.6 (b), Figure 6.6 (c) and Figure 6.6 (d) show the respective EBSD IPF maps for IN718/ TiB_2 deposits with 0.5 wt%, 1.5 wt% and 2.5 wt% TiB_2 ; the corresponding $\{100\}$ pole figure for IN718/ TiB_2 high energy deposits are shown in Figure 6.6 (f), Figure 6.6 (g) and Figure 6.6 (h). The area fraction distribution of as-deposit IN718 and the IN718/ TiB_2 deposits are compared in Figure 6.6 (i). Similarly, for the low energy deposits, Figure 6.7 (a) and Figure 6.7 (e) show the respective EBSD map and corresponding $\{100\}$ pole figure for as-deposit IN718. The EBSD IPF maps and the corresponding $\{100\}$ pole figure for IN718/ TiB_2 for IN718/ TiB_2 deposits with 0.5 wt%, 1.5 wt% and 2.5 wt% TiB_2 are shown in Figure 6.7 (b) and Figure 6.7 (f); Figure 6.7 (c) and Figure 6.7 (g); Figure 6.7 (d) and Figure 6.7 (h) respectively.

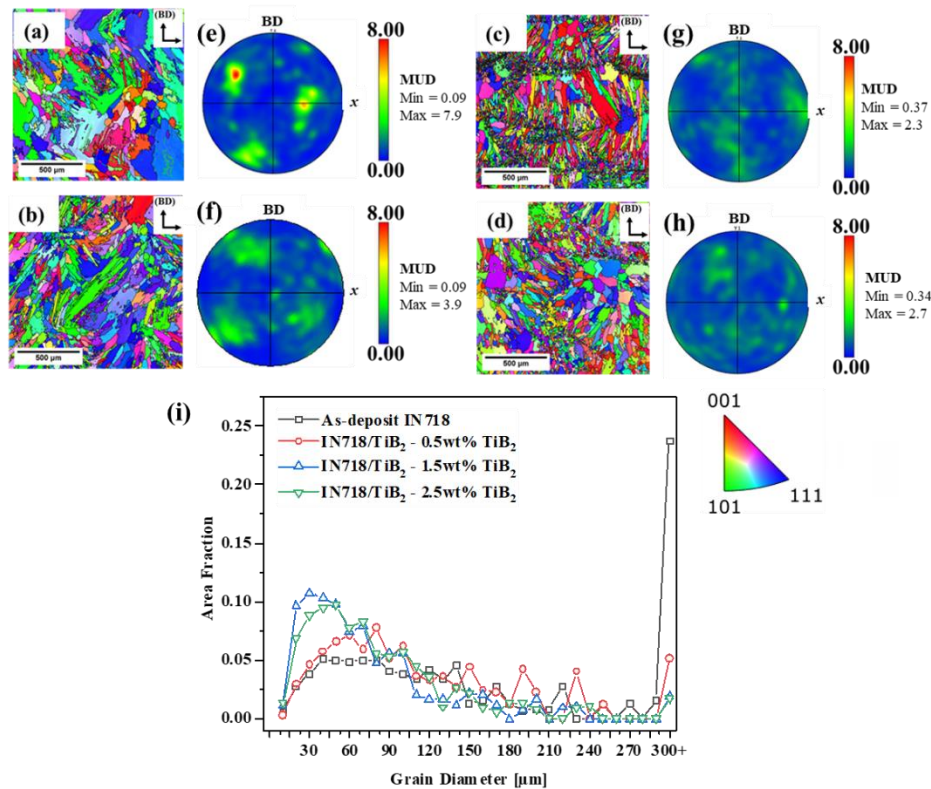


Figure 6.6: The EBSD maps and the respective $\{100\}$ pole figures of high energy density deposits in the following conditions: (a) and (e) as-deposit IN718; IN718/ TiB_2 deposited with : (b) and (f) 0.5 wt%; (c) and (g) 1.5 wt%; (d) and (h) 2.5 wt% TiB_2 ; (i) grain size distribution in IN718 and IN718/ TiB_2 deposits.

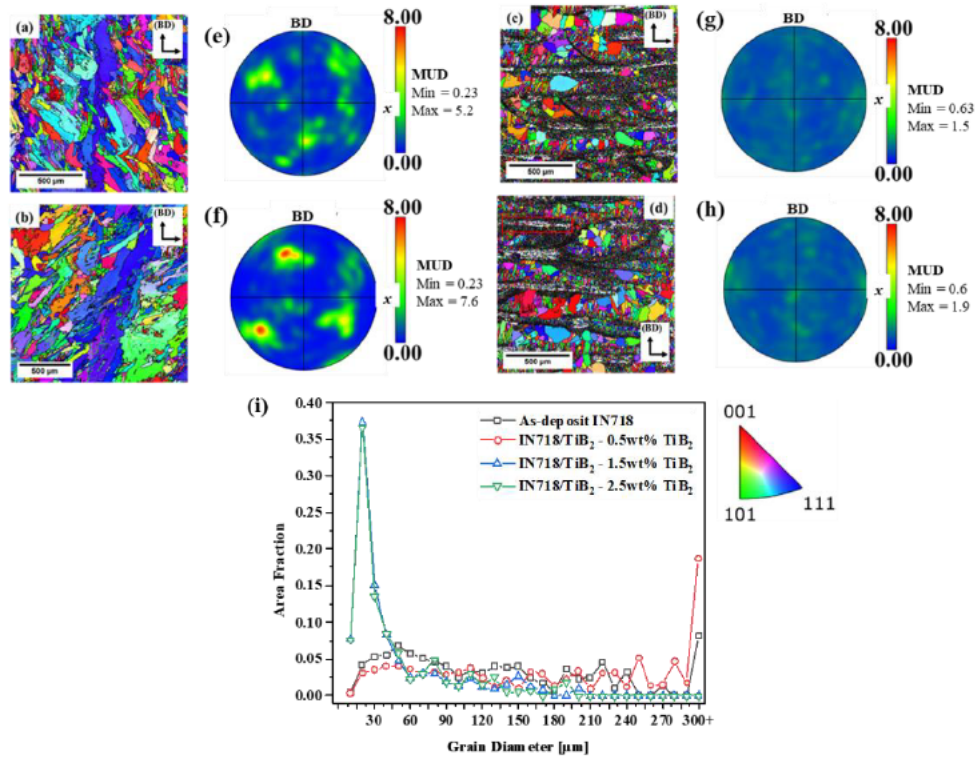


Figure 6.7: The EBSD maps and the respective $\{100\}$ pole figures of low energy density deposits in the following conditions: (a) and (e) as-deposit IN718; IN718/TiB₂ deposited with : (b) and (f) 0.5 wt%; (c) and (g) 1.5 wt%; (d) and (h) 2.5 wt% TiB₂; (i) grain size distribution in IN718 and IN718/TiB₂ deposits.

Table 6.2: Percentage of total grain area occupied by small grains ($<20 \mu\text{m}$) and large grains ($>300 \mu\text{m}$) in as-deposit IN718 and IN718/TiB₂ deposits

		Area percentage (%)			
		As-deposit	0.5 wt%	1.5 wt%	2.5 wt%
High Energy Deposit	Small Grain ($<20 \mu\text{m}$)	3.3	3.3	11	8.2
	large Grain ($>300 \mu\text{m}$)	23.7	5.1	1.8	1.7
Low Energy Deposit	Small Grain ($<20 \mu\text{m}$)	4.6	3.4	45	44
	Large Grain ($>300 \mu\text{m}$)	8.2	18.6	0	0

For both high energy (Figure 6.6 (i)) and low energy (Figure 6.7 (i)) deposits, it is observed that the area fraction of small grains ($< 20 \mu\text{m}$) increases and large grains ($> 300 \mu\text{m}$) decreases with TiB₂ addition. The percentage of area occupied by the small

grains ($< 20 \mu\text{m}$) and large grains ($> 300 \mu\text{m}$) in the deposits is summarised in Table 6.2. The percentage of the area occupied by small grains increased from 3.3 % to 11 % in high energy deposits and from 4.6 % to 5 % in low energy deposits upon TiB_2 addition. The area occupied by the large grains decreased from 24 % to 2 % in high energy deposits and was eliminated in low energy deposits. Additionally, the $\{100\}$ pole figures (Figure 6.6 (c) – (h)) and (Figure 6.7 (c) – (h)) indicates that the texture in the IN718/ TiB_2 deposits becomes weak and random with TiB_2 addition. The scale of the pole figures is kept constant for comparison. For both energy densities, significant grain refinement was observed only after $>1.5 \text{ wt} \% \text{ TiB}_2$ loading, as shown in Figure 6.6 (b), Figure 6.6 (f) for high energy deposits and Figure 6.7 (b) and Figure 6.7 (f) for low energy deposits. It can be inferred from the results that $<0.5 \text{ wt} \%$ inoculants did not create enough heterogeneous nucleation sites, and $>1.5 \text{ wt} \%$ inoculants were able to promote heterogeneous nucleation, and the columnar microstructure was broken down to a large extent. Therefore, the rest of the investigation has been conducted on $<10 \mu\text{m}$ size inoculants with 1.5 wt% TiB_2 .

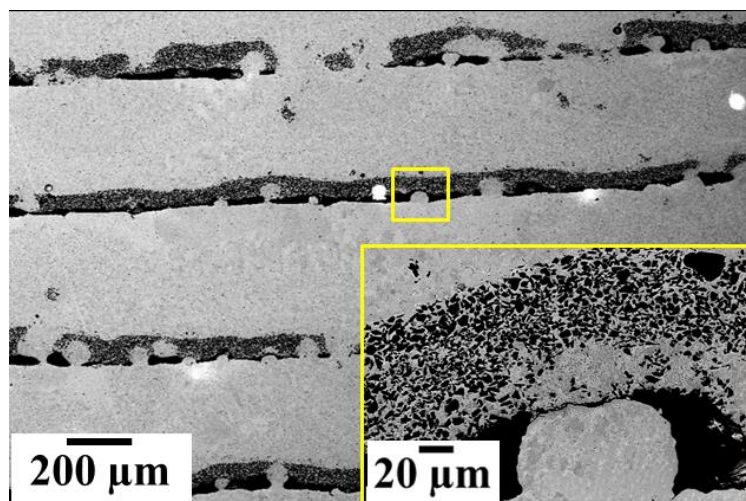


Figure 6.8: Low energy deposits having interlayer defects. Unmelted particles are observed within the interlayer defects.

Although significant grain refinement has been observed with low energy deposits with the addition of $\text{TiB}_2 >1.5 \text{ wt} \%$ (Figure 6.7 (c) and (d)), the deposits were not dense with interlayer defects observed. Figure 6.8 shows a representative SEM micrograph of IN718/ TiB_2 low energy deposit with 1.5 wt% TiB_2 with interlayer defects. The point EDS analysis presented in Figure 6.9 shows peaks of Ti from the unmelted powders near the interlayer defects, confirming that for low energy deposits with TiB_2 loading $<1.5 \text{ wt} \%$, the TiB_2 particles remain unmelted and result in

interlayer defects in the built. The reason for such a phenomenon is explained as follows.

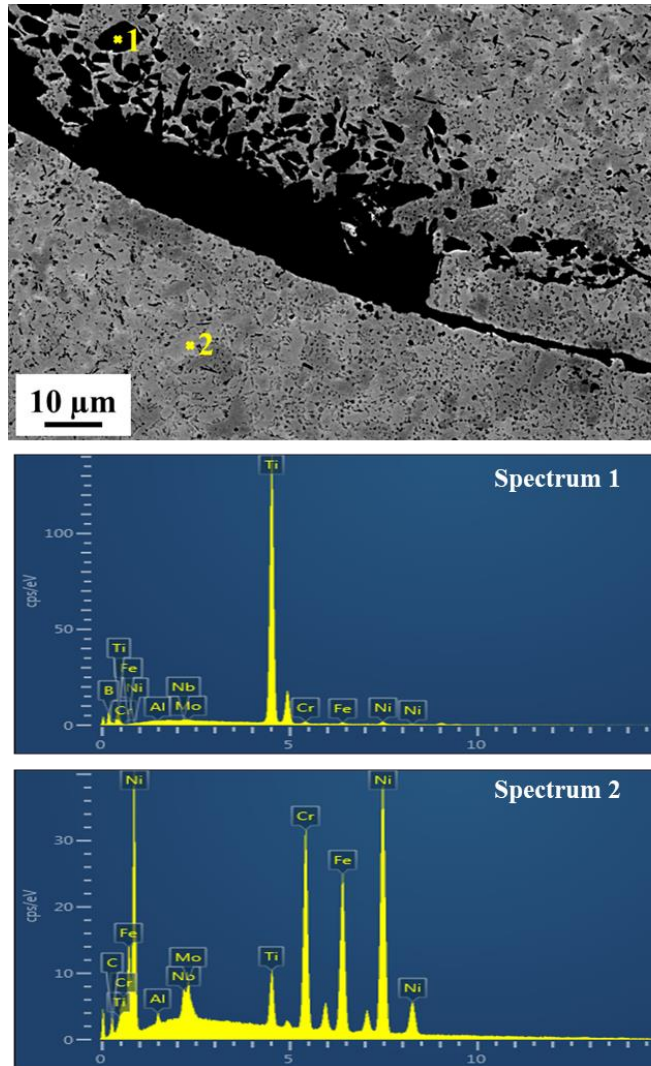


Figure 6.9: EDS of unmelted particles shows presence of TiB₂.

During the deposition process, a steep thermal gradient is developed between the centre and the edge of the pool across the surface. The surface tension on the top of the molten pool induces a thermocapillary flow on the pool surface due to the temperature gradient [157]. Dynamic viscosity (μ) is expressed according to the equation 6.3:

$$\mu = \frac{16}{15} \left(\sqrt{\left(\frac{m}{kT} \right) \gamma} \right) \quad [6.3]$$

where m is the atomic mass, k is the Boltzmann constant, γ is the melt's surface tension, and T is the melt pool temperature [233]. Based on the above equation, when the energy density (i.e. the temperature of the melt pool) is insufficient, the viscosity of the melt increases. Addition of TiB₂ results in increased viscosity of the melt pool. A

highly viscous melt pool reduces wettability and causes the melt to spheroidize rather than flow across the underlying surface. This results in inter-layer pores and is generally referred to as the ‘balling effect’ [165]. Balling effect results in the formation of discontinuous scan tracks and large inter-track pores as a current layer is being deposited. Furthermore, during the layer-by-layer AM building process, balling effect provides a severe impediment to a uniform deposition of the fresh powder on the previously processed layer and tends to produce porosity induced by poor inter-layer bonding. Therefore, it can be inferred that the ‘effective’ energy density was not sufficiently high enough to prevent the balling effect, which led to inter-layer defects during the deposition process. A low viscous melt pool is essential to allow spreading of the molten fluid outward, surrounding the reinforcing particles on the underlying surface to prevent the balling effect and achieve a higher degree of densification.

To eliminate the interlayer defects and thus achieve a dense deposit, the flow rate of the powders during the deposit was reduced whilst keeping all other parameters the same. The variation of flow rate was adopted to reduce the viscosity in the melt pool and thereby modify the ‘effective’ energy density of the deposition process. The ‘effective’ energy density was increased by systematically reducing the powder flow rate from 12 g/min – 6 g/min, without changing other process parameters. The low energy IN718/TiB₂ deposits were done with 1.5 wt% TiB₂. The process parameters used for the IN718/TiB₂ deposits with varying flow rate is represented in Table 6.3.

Table 6.3: Low energy density deposition parameters

Power	Scan speed	Hatch spacing	layer thickness	Flow rate	linear Energy Density
W	(mm/s)	(mm)	(mm)	(g/min)	(J/mm)
350	10.6	0.60	0.28	12	33.08
350	10.6	0.60	0.28	8	33.08
350	10.6	0.60	0.28	7	33.08
350	10.6	0.60	0.28	6	33.08

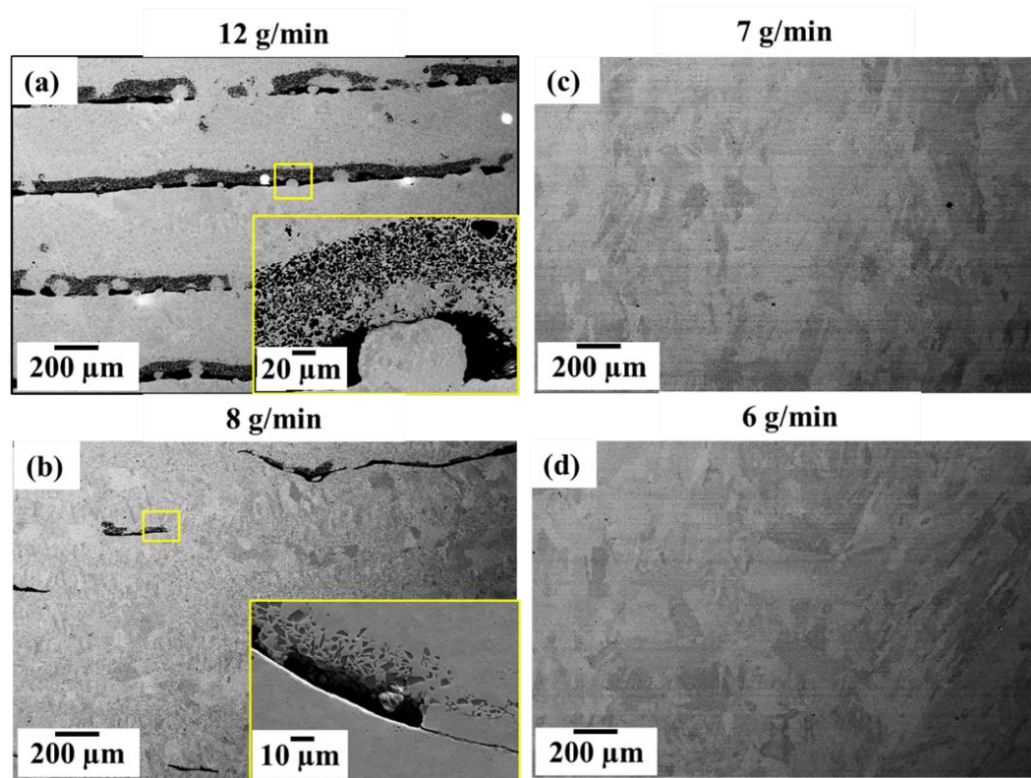


Figure 6.10: Effect of powder flow rate on the densification of IN718/ TiB_2 deposits:
 (a) 12g/min; (b) 8 g/min; (c) 7g/min; (d) 6g/min.

The resulting microstructure of IN718/ TiB_2 deposited with changing powder flow rate is shown in Figure 6.10 (a – d). The deposits with a flow rate of 12 g/min shown in Figure 6.10 (a) exhibit a high amount of defect $\sim 3\%$ in area fraction as measured from the optical micrographs. With a reduced flow rate, the number of powders fed in the melt-pool is low, thereby increasing the effective energy experienced by individual powders. The interlayer defects decreased with decreasing flow rate from 12g/min to 8gm/min, as shown in Figure 6.10 (b). Furthermore, a fully dense deposit without interlayer defects was achieved with a flow rate of $<7\text{g/min}$, as shown in Figure 6.10 (c) and Figure 6.10 (d). The effect of powder flow rate on the orientation and distribution of grains of low energy deposits can be seen from the EBSD maps shown in Figure 6.11 (a – d). The EBSD maps show that the grain morphology becomes coarser as the flow rate is reduced below 8 g/min. Figure 6.11 (e) shows the grain size distribution in the deposits with varying flow rates. The fraction of area occupied by the small grains (grain diameter $< 20 \mu\text{m}$) decreases, and a higher fraction of grains $> 100 \mu\text{m}$ is observed with decreasing flow rates.

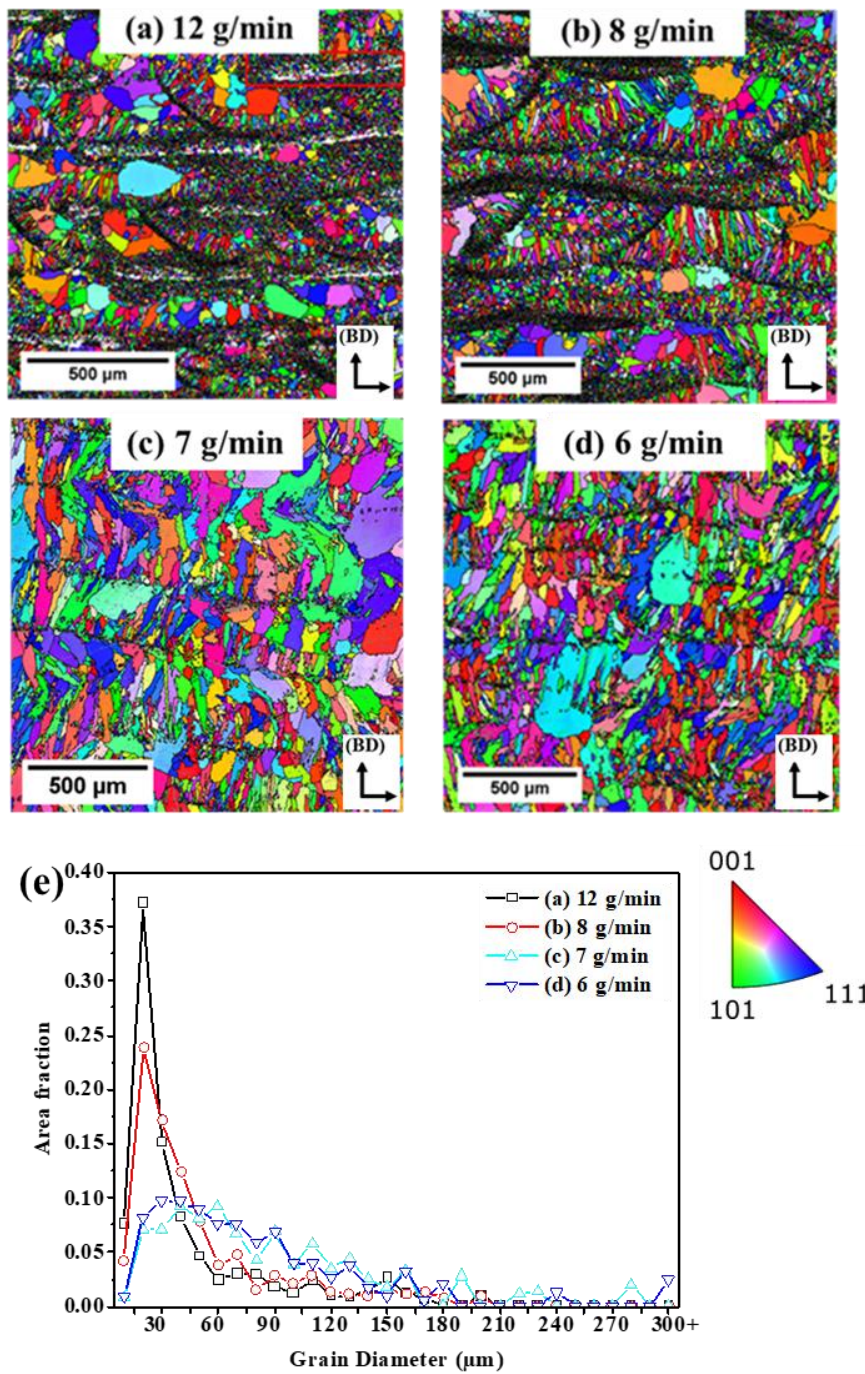


Figure 6.11: EBSD IPF maps showing effect of powder flow rate on the grain size of low energy deposits: (a) 12g/min; (b) 8g/min; (c) 7g/min; (d) 6g/min; the grain size distribution is shown.

Therefore, to achieve the full densification, the flow rate of 7g/min was combined with the low energy density in the following research, unless otherwise stated. A detailed comparison of as-deposit IN718 and IN718/ TiB_2 deposits with low energy density will be made in the following section. Note that the energy density equations (linear, area, or volumetric (see Table 1 [120])) often used in DED (or laser-based AM deposits) do not incorporate the flow rate as a variable. However, the current investigation shows

flow rate is an important variable, especially for the densification during DED prints that deserves detailed investigation.

The microstructure of IN718/TiB₂ deposits with high energy and low energy deposits are detailed and compared with the corresponding as-deposit IN718 as follows. Figure 6.12 (a – e) and Figure 6.13 (a – e) compare the microstructure and grain morphology for both IN718 and IN718/TiB₂ for high and low energy deposits, respectively. The microstructure of as-deposited IN718 and IN718/TiB₂ deposited with high energy density is shown in Figure 6.12 (a) and Figure 6.12 (b), respectively. The corresponding grain boundary maps of as-deposited IN718 and IN718/TiB₂ are shown in Figure 6.12 (c) and Figure 6.12 (d), respectively. The presence of large columnar grains with size (circle equivalent diameter) >300μm can be observed in the as-deposit IN718, Figure 6.12 (c). These large grains, indicated in red and yellow in the grain size maps, occupies a major portion of the total area in as-deposit IN718. The grain size distribution reported in Figure 6.12 (e) shows a consistently higher area fraction of grains <100μm in IN718/TiB₂ than as-deposit IN718. The grain size distribution of IN718/TiB₂ shows the area occupied by smaller grains (<20μm) increased, and the area occupied by the large grains >300μm is reduced to ~ 3 % from ~ 25 % in as-deposit IN718 (Figure 6.12 (d, e)). Similarly, in low energy deposits, the large columnar grains (> 300μm) in as-deposit IN718 shown in Figure 6.13 (a, c) were eliminated in IN718/TiB₂ deposits (Figure 6.13 (b, c)). The area fraction of smaller grains (<20μm) increased from ~ 2.5 % to 10 % upon TiB₂ addition, as indicated in Figure 6.13 (e).

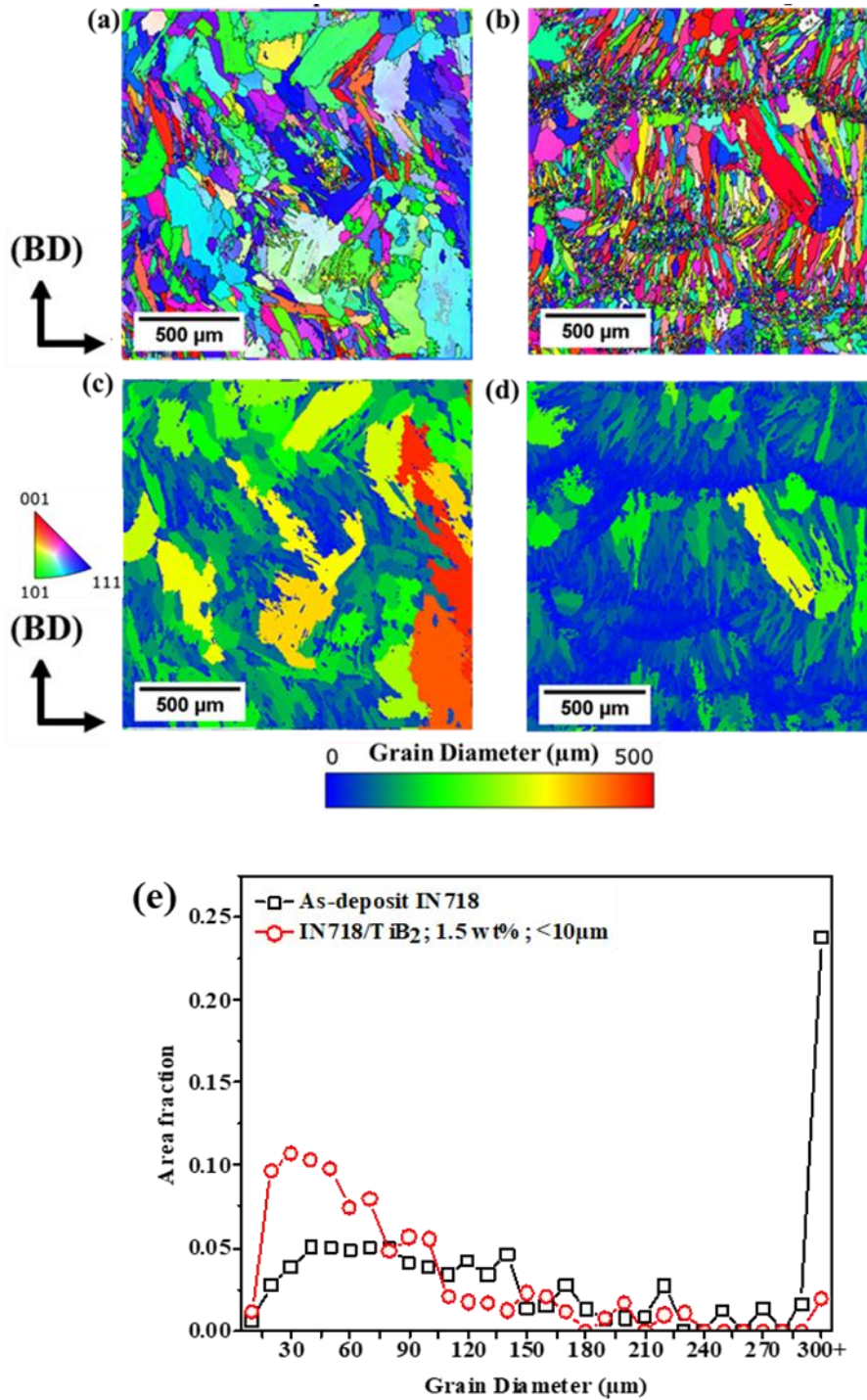


Figure 6.12: IPF EBSD maps and grain size distribution maps for high energy deposits: (a), (b) EBSD map; (c), (d) grain size map of as-deposit IN718 IN718/ TiB_2 with 1.5wt%, $<10\mu\text{m}$ TiB_2 ; and (e) grain size distribution.

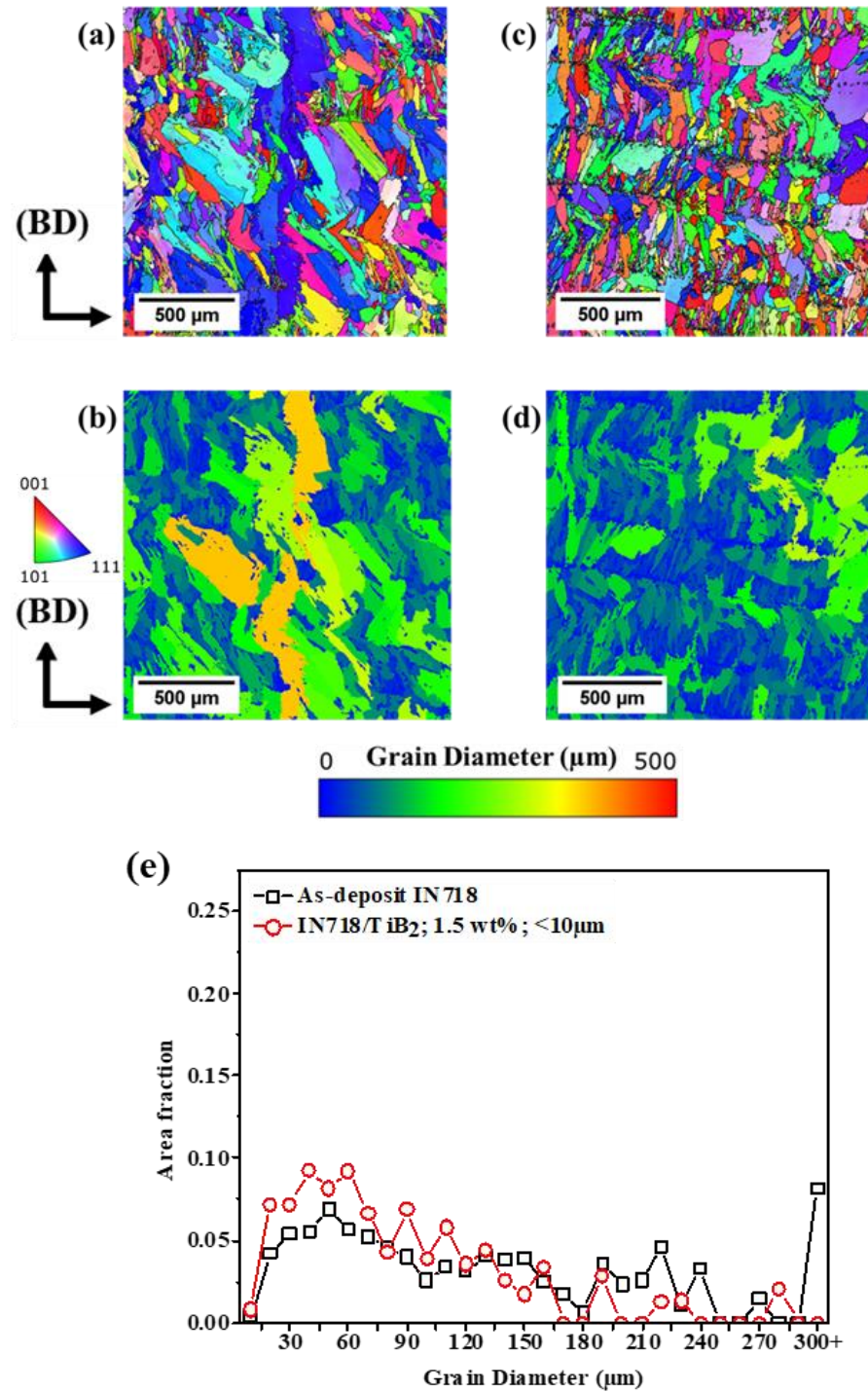


Figure 6.13: IPF EBSD maps and grain size distribution maps for low energy deposits: (a), (b) EBSD map; (c), (d) grain size map of as-deposit IN718 IN718/TiB₂ with 1.5wt%, <10μm TiB₂; and (e) grain size distribution.

6.3.1.2 Identification of the secondary phases

BSE-SEM images of as-deposit IN718 and IN718/TiB₂ are shown in Figure 6.14 (a – d). Figure 6.14 (a) and Figure 6.14 (b) show the respective micrograph of IN718 and IN718/TiB₂ deposits processed using high energy density. The corresponding

micrographs for the low energy density as-deposit IN718 and IN718/ TiB_2 are shown in Figure 6.14 (c) and Figure 6.14 (d), respectively. In as-deposited IN718 microstructure, inter-dendritic laves phases formed identified as the bright phases in Figure 6.14 (a) and Figure 6.14 (c). It is well established in the literature that Laves phase is formed due to inter-dendritic Nb and Mo segregation with a typical composition of $(\text{Ni, Fe, Cr})_2(\text{Mo, Nb, Ti})$ resulting from rapid solidification during the DED process. Its formation requires more than 10 wt% Nb, as observed by Qi et al. [93] and Zhai et al. [95] for IN718 manufactured using DED techniques. Laves phase was found to be detrimental to tensile ductility properties in IN718 welds [192] and DED (and other AM processes) fabricated IN718 [22,93] as it was believed to aid the crack initiation and propagation.

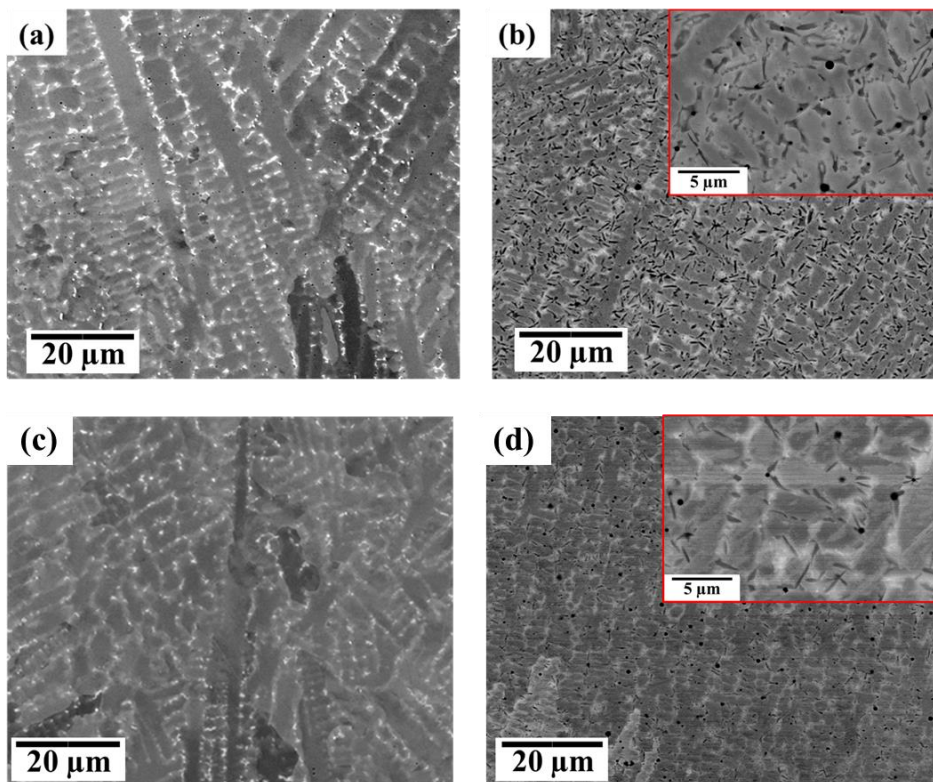


Figure 6.14: SEM images showing typical microstructures of IN718 with and without inoculants: (a), (c) As-deposit IN718; (b), (d) IN718/ TiB_2 ; (a), (b) are high energy deposits and (c), (d) are low energy deposits respectively.

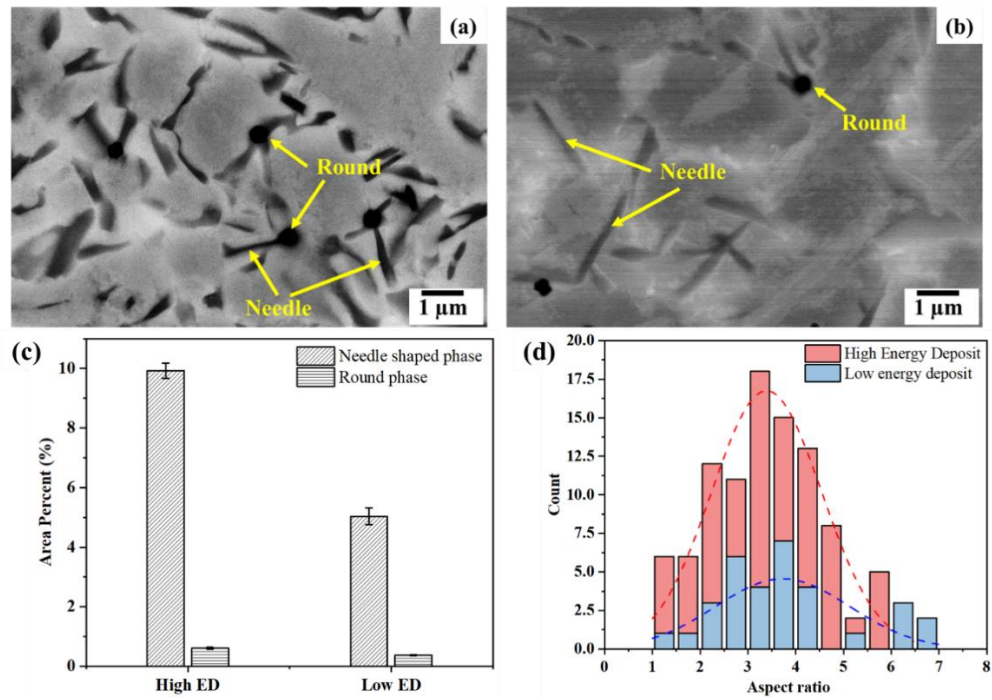


Figure 6.15: High Magnification SEM micrographs of IN718/ TiB_2 showing the needle-shaped phases and spherical phases in IN718/ TiB_2 (a) High Energy deposits, (b) low energy deposits; (c) the area fraction of these round and needle-shaped phases; (d) aspect ratio frequency distribution of the needle-shaped phases in high and low energy deposits.

The inter-dendritic Laves phases are replaced with needle/irregular shaped and round shaped precipitate phases in the IN718/ TiB_2 deposits distributed evenly throughout the deposit (Figure 6.14 (b) and Figure 6.14 (d)). High magnification micrographs of IN718/ TiB_2 for the high energy and low energy deposits are presented in Figure 6.15 (a) and Figure 6.15 (b). For both conditions, the needle and spherical-shaped phases are present in the microstructure; however, the amount of the needles reduced from $\sim 10\%$ in high energy deposits to $\sim 5\%$ in low energy deposits (Figure 6.15 (c)). The aspect ratio distribution of these needle-shaped phases is shown in Figure 6.15 (d). An identical area has been considered for analysing both high and low energy deposits. Figure 6.15 (d) shows that the mean of the aspect ratio was ~ 3.5 for both the high and low energy deposits. It can be inferred from the microstructural characterisation that upon the addition of TiB_2 to IN718, the solidification path changed and suppressed the formation of Laves phases in the as-deposit microstructure.

XRD and EDS analyses were adopted to study the new precipitate phases (needle-shaped and round) formed in IN718/ TiB_2 . The EDS elemental maps of IN718/ TiB_2 for high and low energy deposits are shown in Figure 6.16 and Figure 6.17,

respectively. The EDS elemental maps indicate that the needle-shaped phases were Cr, Mo, and B-rich phases. The EDS line scan done on the IN718/ TiB_2 is shown in Figure 6.18 (a – b). EDS line scans of the needle-shaped phase shown in Figure 6.18 (a) indicate that the needle-shaped phase is rich with Cr, Nb and Mo, and high Ti concentration is reported in the round phases as shown in Figure 6.18 (b). Therefore, it can be inferred that the round phases in IN718/ TiB_2 are possibly TiB_2 particles. Segregation of Nb in the inter-dendritic regions is also observed in the EDS elemental maps (Figure 6.16 and Figure 6.17), indicating the possible presence of Laves phases; however, the volume of Laves phase in the IN718/ TiB_2 has been greatly reduced as compared to the as-deposit IN718.

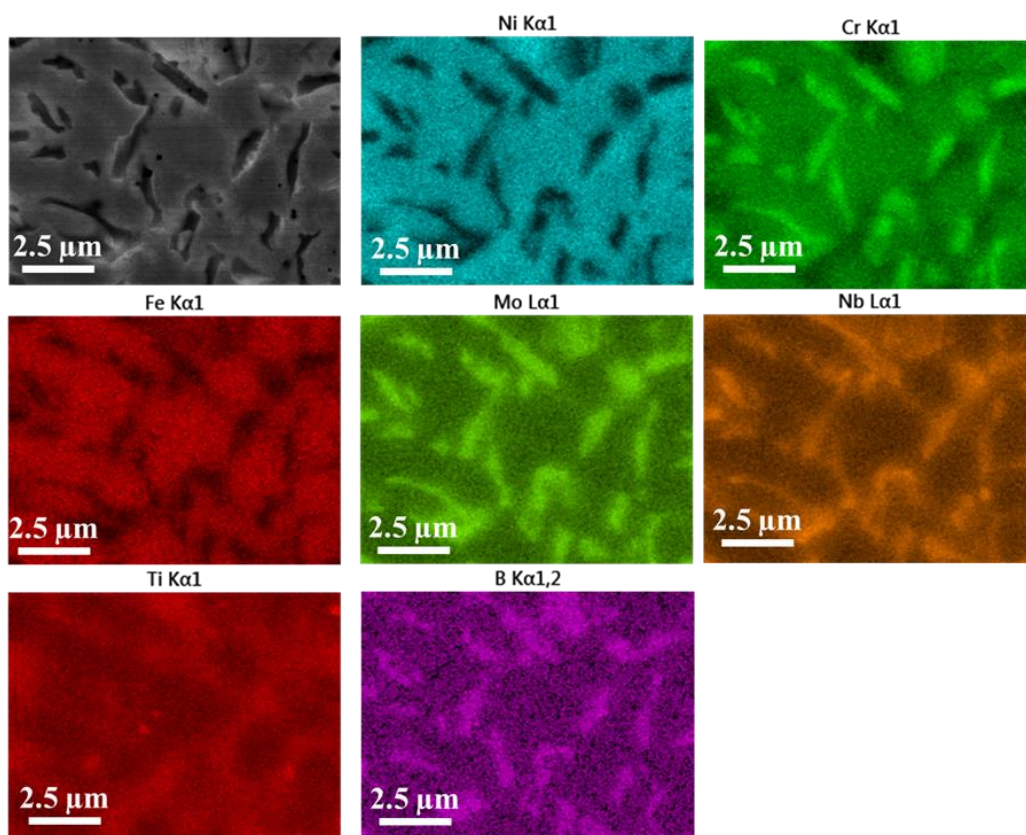


Figure 6.16: EDS elemental map for IN718/ TiB_2 deposits with high energy density.

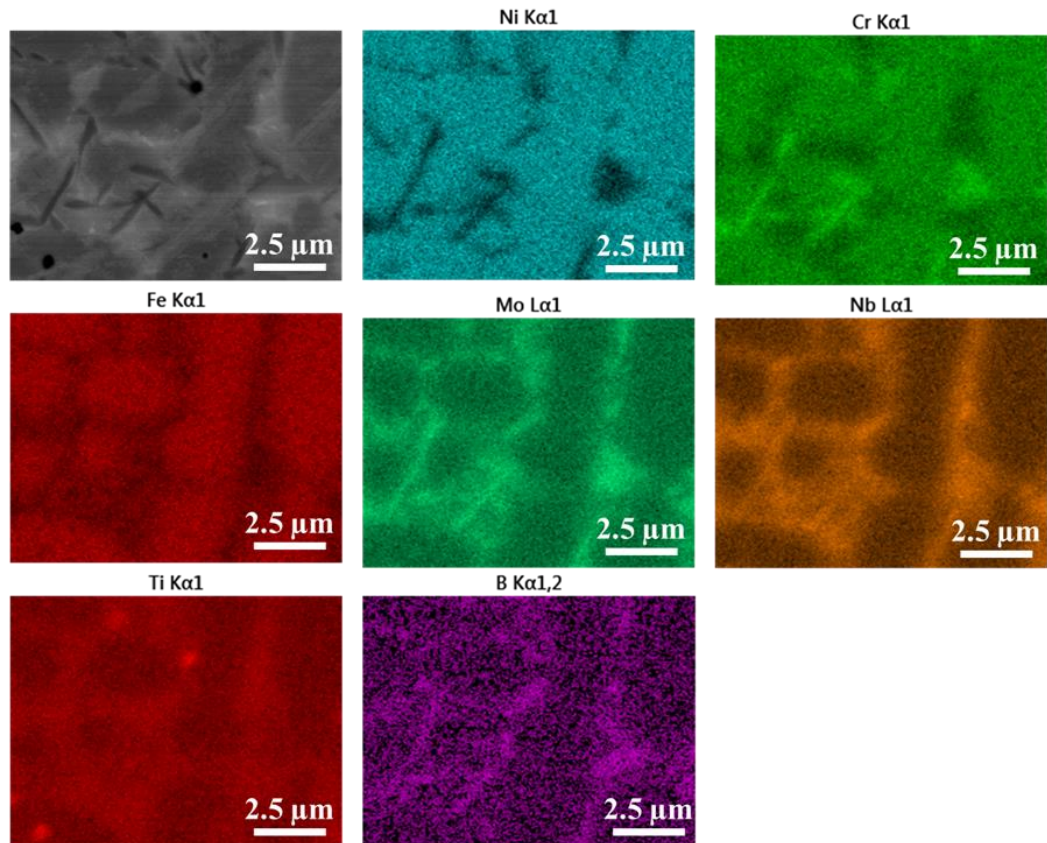


Figure 6.17: EDS elemental map for IN718/ TiB_2 deposits with low energy density.

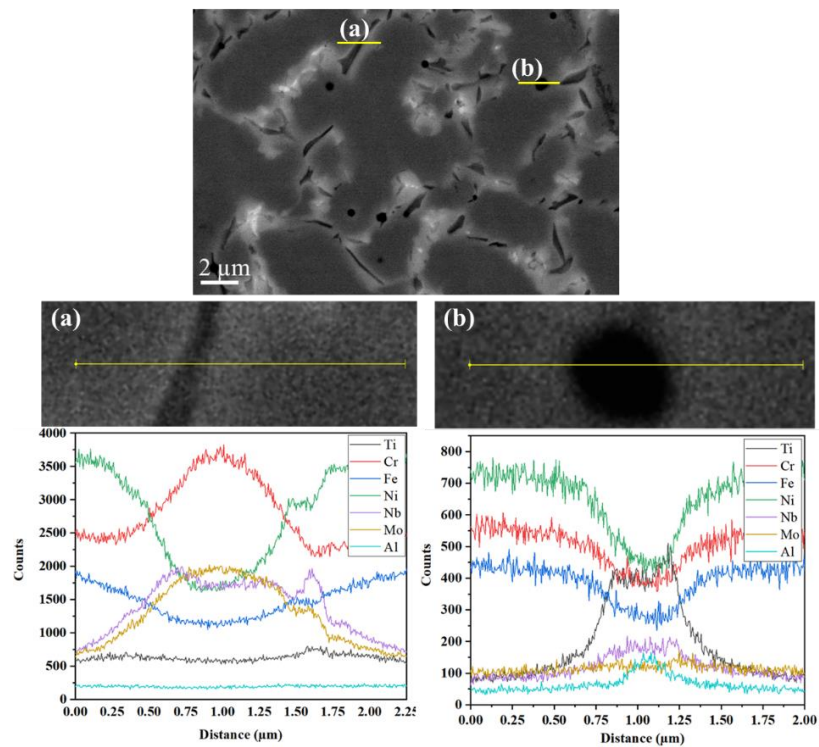


Figure 6.18: EDS line scan of IN718/ TiB_2 low energy deposit showing (a) segregation of Cr, Mo, and Nb at the needle-shaped phases and (b) Ti segregation at the round phase.

Figure 6.19 shows the XRD peaks of IN718/TiB₂ deposited at high energy and low energy densities and is compared with as-deposit IN718. The peaks corresponding to the FCC γ phase are easily indexed, however, the other peaks are indexed based on EDS results and correlating with the JCPDS database. The Laves phase peaks observed in the as-deposit IN718 are indexed using data from literature [234,235]. The inset in Figure 6.19 shows an enlarged view of the XRD peak with diffraction angles ranging from 25° - 65°. The corresponding Laves phase peaks observed in as-deposit IN718 are absent in IN718/TiB₂. Moreover, the XRD patterns do not show peaks of TiB₂, indicating partial/full dissolution of TiB₂ in the γ matrix. The peaks in IN718/TiB₂ are indexed as Cr₃B₄, and TiB₂ peaks, based on EDS results.

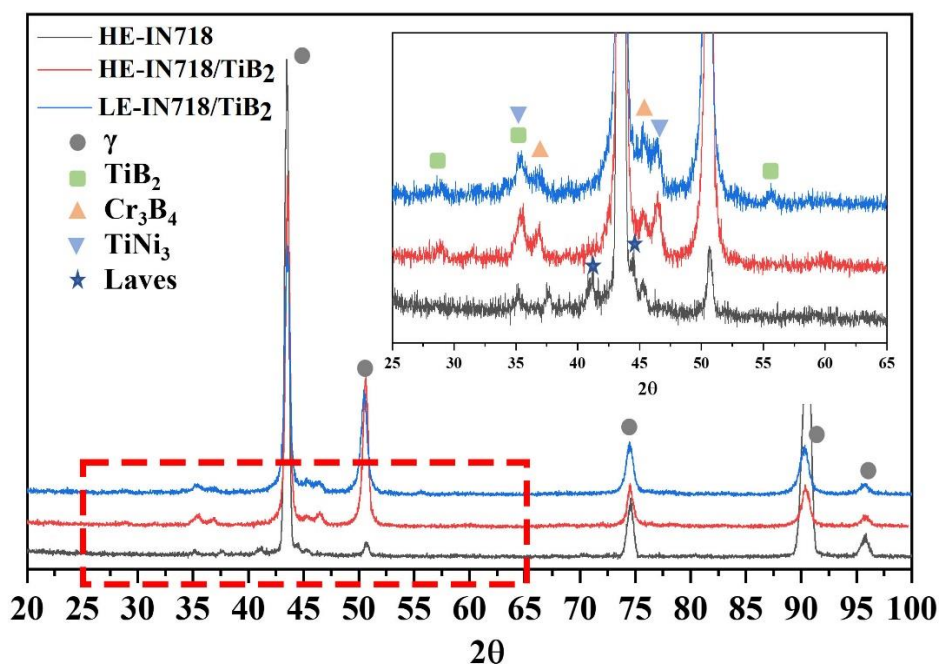


Figure 6.19: XRD patterns for as-deposit IN718 and IN718/TiB₂.

6.3.2 Mechanical properties

6.3.2.1 Hardness

Mechanical properties of the as-deposit IN718 and IN718/TiB₂ have been characterised for the deposits done at high energy and low energy densities using Vickers micro-hardness and tensile tests. Tensile tests were performed on specimens with a loading direction parallel to and perpendicular to the build direction (Figure 6.3). Generally, the hardness values in as-deposit IN718 do not show a significant dependence on energy densities, as shown in Figure 6.20. The hardness values reported in as-deposit IN718 in high and low energy deposits are ~ 250 Hv and do not satisfy the minimum hardness (350 Hv) requirement per AMS 5662 standard. The low

hardness value in as-deposit IN718 was attributed to the absence of strengthening phases γ' and γ'' that are not able to form due to the rapid cooling rates during DED processing [93,95]. TiB₂ addition leads to a significant increase in the hardness values. The hardness values in the as-deposit condition have nearly doubled and are comparable to the aged IN718 that exhibit hardness values of ~ 450 Hv. The average hardness value of the IN718/TiB₂ high energy density deposits is ~ 500 Hv, which is ~ 100 Hv higher than the low energy deposits.

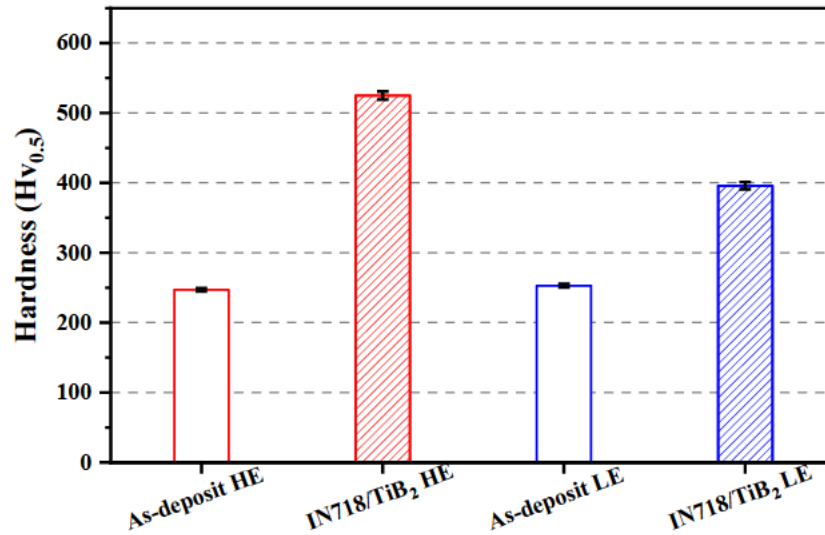


Figure 6.20: Hardness of as-deposit IN718 and IN718/TiB₂. (HE- high energy deposit; LE- low energy deposit).

6.3.2.2 Tensile test result

Room temperature tensile tests were performed on samples fabricated using high energy density parameters. Figure 6.21 (a) shows the representative room temperature tensile test engineering stress–engineering strain curves of the IN718 and IN718/TiB₂ samples. Both the vertical and horizontal DED samples were included for this comparison. Overall, the IN718/TiB₂ samples exhibited a much higher strength but reduced ductility. For example, in the vertical samples, the yield and tensile strength of the IN718/TiB₂ sample increased by ~ 400 MPa and ~ 300 MPa, respectively, when compared to the IN718 sample, while the elongation to failure reduced by $\sim 15\%$. In addition, an orientation dependence is observed from the tensile properties in both IN718 and IN718/TiB₂ samples. 3 – 4 specimens were tested in all conditions, and the average tensile test results are tabulated in Table 6.4. The tensile properties of IN718/TiB₂ deposits are comparable to post-heat-treated IN718, as shown in Table 5.2. It is observed that the yield strength and tensile strength of IN718/TiB₂ exceed post-heat treated IN718 tested in DA and STA conditions. However, the elongation in

IN718/ TiB_2 is significantly reduced compared to post HT IN718. It is noted that the results shown in Table 5.2 are from the vertical specimen, i.e., the loading direction was parallel to the build direction. The relatively low tensile strength in as-deposit IN718 can be attributed to the absence of strengthening phases γ' and γ'' that do not form during DED processing owing to the rapid cooling rates.

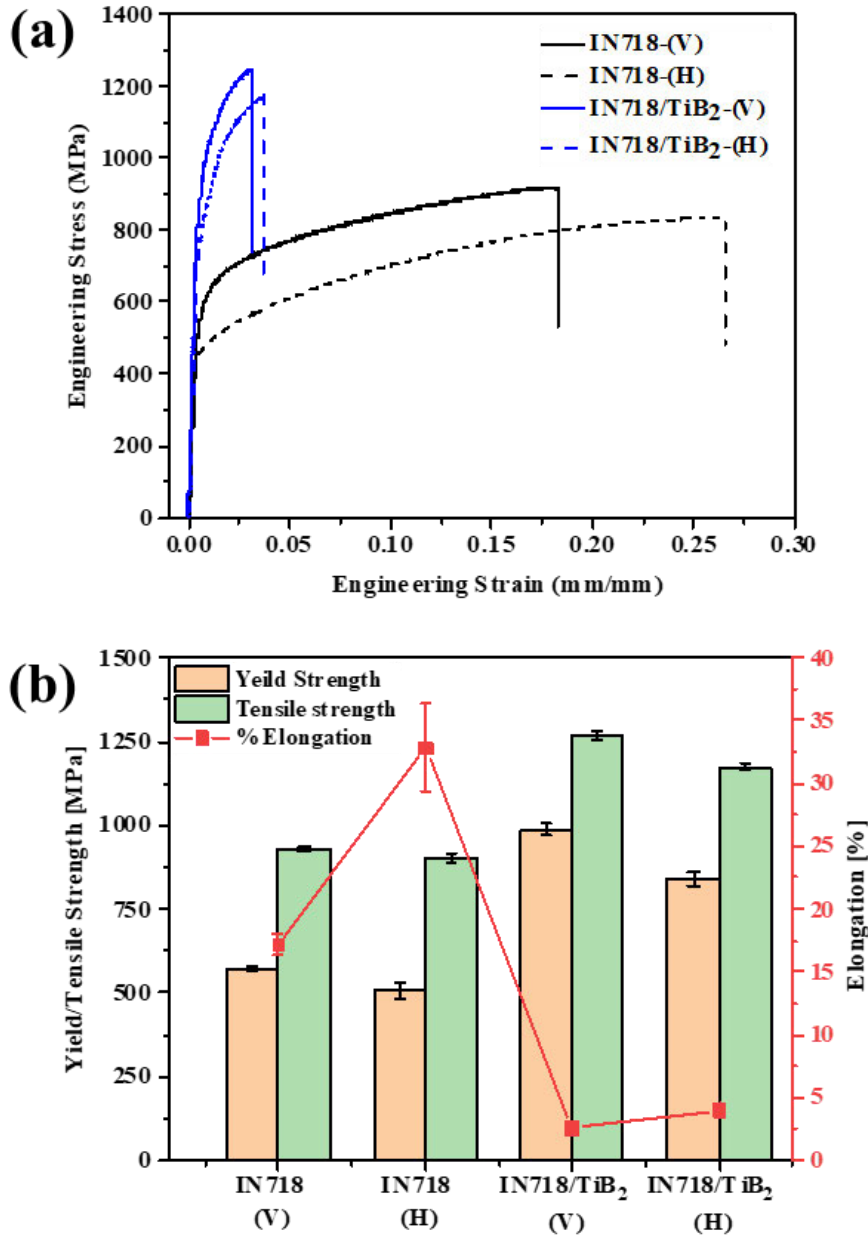


Figure 6.21: (a) Engineering stress- engineering strain curves for high energy density deposits IN718 and IN718/ TiB_2 tested in vertical (V) and horizontal (H) direction; (b) quantified yield stress, tensile stress, and percentage elongation to fracture for each condition.

Table 6.4: Tensile properties of high energy density deposits IN718 and IN718/TiB₂ tested in the vertical and horizontal direction.

Sample condition	Sample orientation	Vertical (V)	Horizontal (H)	% Δ
As-deposit IN718	$\sigma_{YS(0.2)}$ [MPa]	569 \pm 8	475 \pm 24	20
	σ_{UTS} [MPa]	930 \pm 7	871 \pm 18	6.7
	Elongation [%]	17.2 \pm 0.8	28.4 \pm 2.2	65
As-deposit IN718/TiB ₂	$\sigma_{YS(0.2)}$ [MPa]	988 \pm 18	841 \pm 19	17
	σ_{UTS} [MPa]	1267 \pm 13	1174 \pm 12	7.9
	Elongation [%]	2.6 \pm 0.2	4.0 \pm 0.4	54

Table 6.5: Tensile properties of as-deposit IN718 in different post-heat-treated conditions. All samples are manufactured using high energy density and tested in vertical specimen orientation.

Properties IN718 (Vertical Specimen)	HT condition			
	As-deposit	IN718 - DA	IN718 - STA	Wrought
Elastic Modulus [GPa]	171 \pm 7	194 \pm 17	173 \pm 10	176 \pm 10
$\sigma_{YS(0.2)}$ [MPa]	570 \pm 8	948 \pm 19	959 \pm 10	924 \pm 12
σ_{UTS} [MPa]	930 \pm 7	1134 \pm 16	1134 \pm 18	1226 \pm 10
Elongation [%]	17.20 \pm 0.8	8.50 \pm 0.2	17.20 \pm 3.5	22.4 \pm 0.6

DA: Direct aged; STA: Solution treated at 980°C and Aged

The average values of tensile properties of the as-deposit IN718 in both horizontal and vertical directions match well with the results reported by Qi et al. [93] and Zhai et al. [95] in DED manufactured IN718, tested in as-deposited condition. Figure 6.21 (b) compares the yield strength, ultimate tensile strength, and percentage elongation of the IN718 and IN718/TiB₂ samples tested in vertical and horizontal directions. The tensile test results in Figure 6.21 (b) exhibit variation in yield strength, ultimate tensile strength, and elongation with respect to build orientation relative to tensile loading axis. The ultimate tensile strength and yield strength of the vertical samples, tested parallel to the building direction, are in general higher than that tested perpendicular

to building direction, while elongation show the opposite tendency in both IN718 and IN718/TiB₂ samples. The percentage difference of tensile properties in horizontal and vertical samples is indicated as ‘%Δ’ in Table 6.4. The percentage difference in the strength properties between the vertically and horizontally built IN718 is 20% and 17% for IN718/TiB₂. This indicates that, although the addition of TiB₂ is able to reduce the intensity of the texture in deposits, however, the anisotropic tensile properties still persist.

Anisotropic mechanical behaviour is often observed in AM IN718 [See for e.g. [12,13,113,116,118,120,236]]. However, unlike in the present study, the majority of the existing literature reports specimens tested perpendicular to the build direction (horizontal) exhibiting higher strength values and lower ductility than the ones tested parallel to the build direction (vertical) [12,13,113,120]. As an exception, Deng et al. [116] observed different anisotropic behaviour in IN718 EBM deposits where the vertical samples exhibited higher strength properties compared to the horizontally built samples and the anisotropic behaviour was attributed to the presence of defects along the grain boundaries in the loading direction. It is shown that the IN718/TiB₂ builds exhibited a weaker/random texture compared to IN718 builds (Figure 6.6 (a – h) and Figure 6.7(a – h)). Moreover, the defects in all samples are relatively low. Therefore, the consistent difference in tensile properties is less likely due to texture or defects.

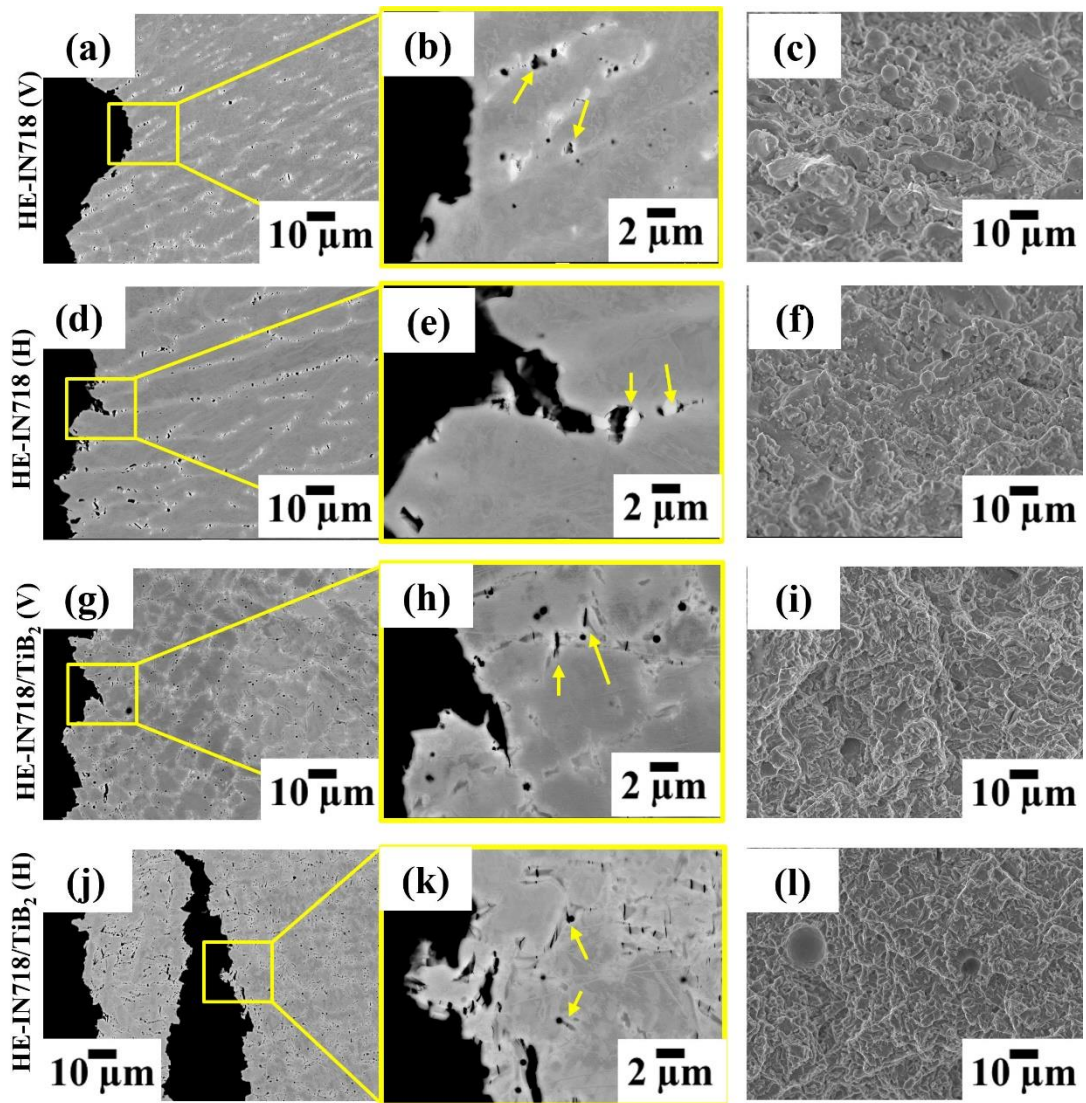


Figure 6.22: SEM cross-sectional view of the fracture surface and SEM fractography: (a), (b) and (c) HE-IN718-(V); (d), (e) and (f) HE-IN718-(H); (g), (h) and (i) HE-IN718/ TiB_2 -(V); (j), (k) and (l) HE-IN718/ TiB_2 -(H). The broken Laves phase in IN718 and the broken needle-shaped and spherical phases in IN718/ TiB_2 are indicated by arrows.

Figure 6.22 summarises the key observations of the SEM cross-sectional view of the tensile fractured surface and the corresponding SEM fractography. In terms of the IN718 deposit, micro-cracks were frequently observed in the interface between the inter-dendritic Laves phases and the IN718 matrix (Figure 6.22 a, b and Figure 6.22d, e). By contrast, for the IN718/ TiB_2 , high density of micro-cracks appeared near the interface of the matrix and the needle-shaped phases (Figure 6.22 g, h and Figure 6.22 j, k). The high loads generated due to the strengthening effect of these secondary phases were too high to be accommodated by the IN718 matrix and led to micro-crack initiation in the interface region as indicated by arrows Figure 6.22 h and Figure 6.22

k. As a result, high density of micro-cracks led to onset of early failure in IN718/TiB₂. For both the IN718 and IN718/TiB₂ samples, their fractography reveal typical ductile dimples. Occasionally, unmelted particles (possibly TiB₂) were observed on the fracture surface.

6.4 Discussion

6.4.1 TiB₂ as the inoculant for DED IN718

The present investigation demonstrates significant grain refinement, and strengthening in the IN718/TiB₂ deposits (both HE and LE) compared to the corresponding IN718 deposits. However, the microstructure in terms of the secondary phases in IN718/TiB₂ was significantly different from IN718, Figure 6.14 (a -d) and Figure 6.15 (a, b), which indicates a changed solidification sequence. The general solidification sequence of IN718 is $L \rightarrow L + \gamma \rightarrow L + NbC/\gamma \rightarrow L + \gamma \rightarrow Laves/\gamma$ [189,190]. During solidification, elements such as Nb, Mo and C have a high tendency to segregate, especially Nb with the lowest elemental partitioning coefficient of $k < 0.5$, and thus the formation of Laves phases in the last solidified region [191]. The Laves phases are detrimental to tensile ductility in DED and SLM IN718 [93,237] as they aid micro-crack initiation and propagation. Moreover, due to high cooling rates, the precipitation of γ' and γ'' is suppressed in the as-built DED IN718. TiB₂ addition seems to alter the solidification path, causing the formation of the Cr, Mo and Nb enriched needle-shaped phases, Figure 6.15a – d. The refined γ -grain microstructure in the IN718/TiB₂ also helps preventing the network formation of inter-dendritic Nb-rich Laves phases as observed in the IN718 counterpart (Figure 6.15 (a, b)).

The microstructural evolution from the premixed powder to the bulk sample of the IN718/TiB₂ is illustrated by schematic diagrams in Figure 6.23 (a – c). The TiB₂ particles are distributed evenly on the surface of feedstock IN718 powders, after the ball milling stage as shown in Figure 6.23a. During the DED processing, the high temperature of the melt pool leads to the full or partial dissolution of the TiB₂ particles, Figure 6.23b and Figure 6.23c. This agrees well with the SEM observation as shown in Figure 6.16, Figure 6.17 and Figure 6.18, revealing the presence of Ti-rich spherical precipitates in the IN718/TiB₂, as well as the XRD-based phase identification as shown in Figure 6.19. For low TiB₂ addition (0.5 wt%), the TiB₂ particles were almost melted during the DED deposition process, and the microstructure of the IN718/TiB₂ bulk sample resembles that of the IN718 (Figure 6.23d). For the higher TiB₂ content (Figure 6.23e and f), where the TiB₂ particles were able to survive in the melt, the needle-

shaped and spherical precipitates are significantly higher.

The TiB_2 addition results in the formation of needle-shaped phases rich in Cr, Nb, Mo and B in the majority, while the Ti and B enriched spherical phases in the minority. These precipitates act as the heterogeneous nucleation site resulting in the refined microstructure and strengthening the γ matrix. To generate the effective grain refinement, there is a need to ensure the minimum TiB_2 addition, which is found to be 1.5 wt.% for the DED IN718/ TiB_2 deposits (both HE and LE). The strengthening mechanisms contributing towards the increased strength of IN718/ TiB_2 deposits are discussed in Section 6.4.4.

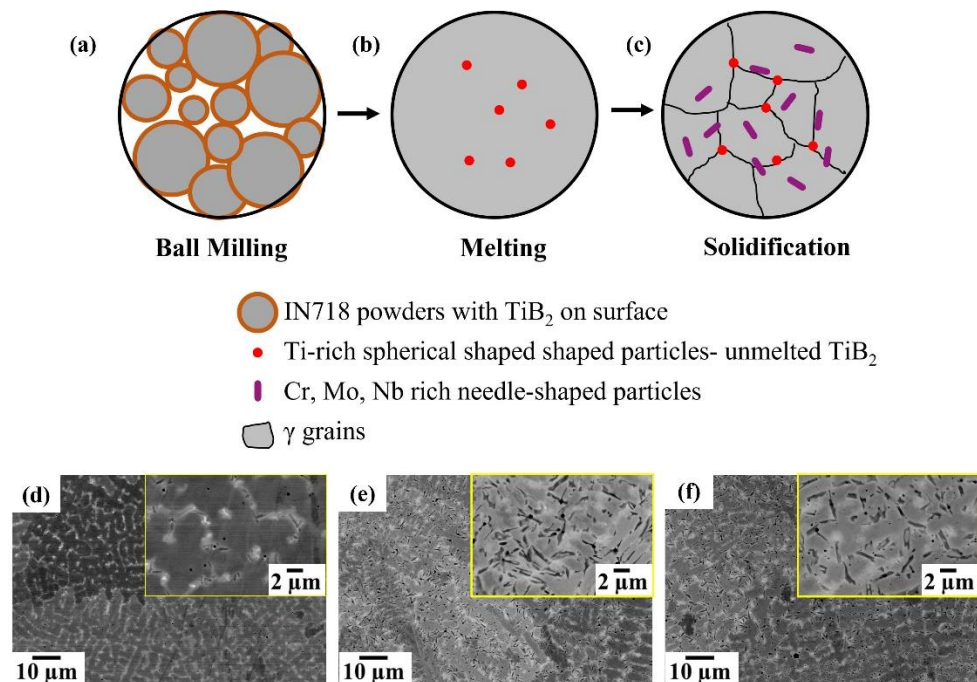


Figure 6.23: Schematic diagrams showing the effect of TiB_2 on the solidification path: (a) ball milling, (b) melting and (c) solidification; SEM micrographs for HE-IN718/ TiB_2 with TiB_2 content (d) 0.5 wt%, (e) 1.5 wt% and (f) 2.5 wt%.

6.4.2 Selecting TiB_2 as an inoculant for grain refinement in AM IN718

In the existing literature, CrFeNb has been identified as an efficient inoculant for a refining grain size of cast IN718 [148,173,174]. From crystallographic models, it has been identified that CrFeNb has three distinct matching crystal planes that have a very low degree of disregistry with the matrix lattice. However, the low melting point of CrFeNb makes it unsuitable for DED type AM processes, where temperatures $>3000^\circ\text{C}$ can be reached. The E2EM model developed by Zhang et al. [149] was used to calculate the mismatch to identify a suitable inoculant for IN718. The details of the calculations are reported in Chapter 3.

Table 6.6: Atomic mismatch between IN718 and TiB₂.

Direction Ni	Direction TiB ₂	% Mismatch	Plane Ni	Plane TiB ₂	% Mismatch
Ni [110]	$\langle 11\bar{2}0 \rangle$	-19.80	Ni (111)	$(10\bar{1}1)$	1.36
	$\langle 0001 \rangle$	-27.74		$(10\bar{1}0)$	-27.07
	** $\langle \bar{1}\bar{1}23 \rangle$	12.43		** (0001)	21.77
	** $\langle 10\bar{1}0 \rangle$	-3.76		$(11\bar{2}0)$	26.63
Ni [100]	$\langle 11\bar{2}0 \rangle$	15.28	Ni (200)	$(10\bar{1}1)$	-13.89
	$\langle 0001 \rangle$	9.67		$(10\bar{1}0)$	-46.73
	$\langle \bar{1}\bar{1}23 \rangle$	-23.84		(0001)	9.67
	$\langle 10\bar{1}0 \rangle$	-46.73		$(11\bar{2}0)$	15.28
Ni [112]	$\langle 11\bar{2}0 \rangle$	30.82	Ni (220)	** $(10\bar{1}1)$	19.46
	$\langle 0001 \rangle$	26.24		$(10\bar{1}0)$	-3.76
	$\langle \bar{1}\bar{1}23 \rangle$	-1.11		** (0001)	-27.74
	$\langle 10\bar{1}0 \rangle$	-19.80		$(11\bar{2}0)$	-19.80

**Indicates that two interatomic spacings in TiB₂ match one spacing in IN718

**Indicates that two interplanar spacings in IN718 match one interplanar spacing in TiB₂

Although pure Ni has a face-centred cubic structure with a lattice parameter of $a = 0.3524$ nm, the lattice parameter of Ni matrix in IN718 superalloy is changed to $a = 0.3586$ nm because of the addition of the alloying elements, such as Fe, Cr, Mo [173]. The closest packed directions in Inconel718 (Ni) are [110], [100], [112], among which [110] is the closest packed Ni directions. Similarly, the close-packed planes are {111}, {200} and {220}. The {111} plane can contain the directions [110] and [112]; {200} plane contains [100] and [112] directions and {220} plane contains [110] and [112] directions. TiB₂ has an HCP crystal structure: a hexagonal unit cell with 3 Ti and 6 B atoms. The lattice parameters for TiB₂ are $a = 0.3038$ nm and $c = 0.32392$ nm, from the JCPDS database. TiB₂ has four possible close or close-packed directions and four possible close or nearly close-packed planes [149]. The closed packed planes are $(10\bar{1}1)$, $(10\bar{1}0)$, (0001) , $(11\bar{2}0)$ and the four possible close or nearly close-packed directions are $\langle 0001 \rangle$, $\langle \bar{1}\bar{1}23 \rangle$, $\langle 10\bar{1}0 \rangle$ and $\langle 11\bar{2}0 \rangle$. The position of the atoms in the lattice and the corresponding close-packed and near close-packed direction for the IN718 matrix and TiB₂ is shown in Figure 6.24 (a) and Figure 6.24 (b), respectively. Also, the atom configurations on $(10\bar{1}1)$ and $(11\bar{2}0)$ planes of TiB₂ are shown in Figure 6.24 (c) and Figure 6.24 (d), respectively.

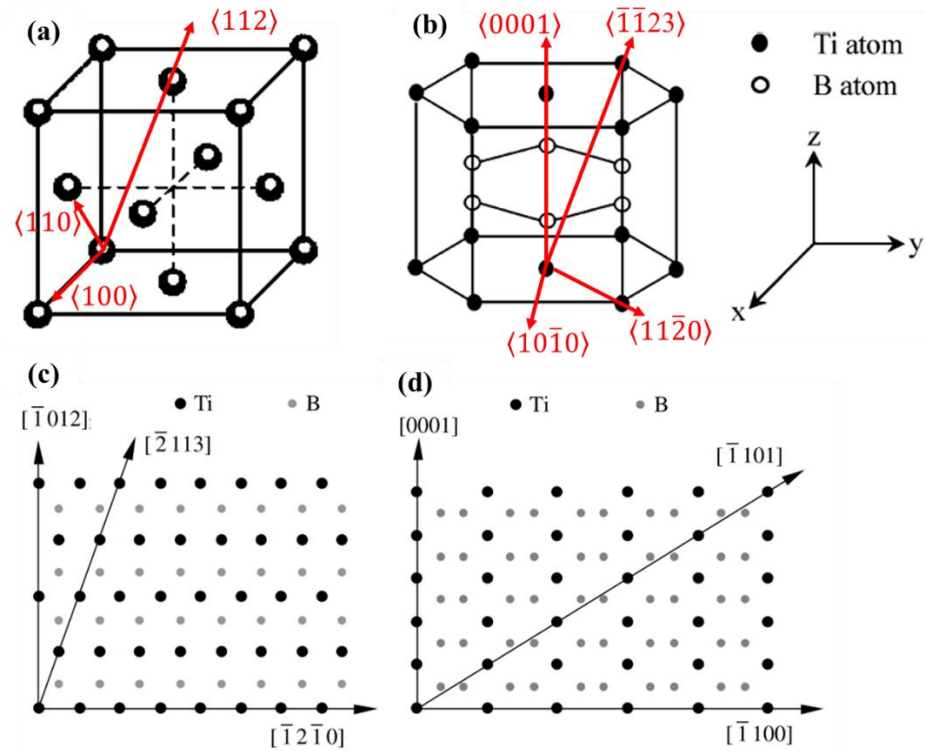


Figure 6.24: Position of atoms in the lattice and corresponding closed-packed direction indicated in (a) IN718 matrix; (b) TiB₂ [238]; Atom configurations on (c) $(10\bar{1}1)$ and (c) $(11\bar{2}0)$ planes of TiB₂ [149].

The closed packed (or nearly closed packed) plane – direction combination can form 12 direction pairs and 12 plane pairs between TiB₂ and Ni (IN718) matrix. Table 6.6 reports the mismatch of the d-value of these plane pairs and the mismatch between the closed-packed directions. From Table 6.6, three possible direction pairs with mismatch <10% are observed: $\langle 110 \rangle_{\text{Ni}} / \langle 10\bar{1}0 \rangle_{\text{TiB}_2}$; $\langle 100 \rangle_{\text{Ni}} / \langle 0001 \rangle_{\text{TiB}_2}$; $\langle 112 \rangle_{\text{Ni}} / \langle \bar{1}\bar{1}23 \rangle_{\text{TiB}_2}$. The subsequent matching plane pairs identified in Table 6.6 are: $(111)_{\text{Ni}} / (10\bar{1}1)_{\text{TiB}_2}$; $(200)_{\text{Ni}} / (0001)_{\text{TiB}_2}$; $(220)_{\text{Ni}} / (10\bar{1}1)_{\text{TiB}_2}$. The possible ORs between TiB₂ and Ni (IN718) are shown below:

$$(111)_{\text{Ni}} / (10\bar{1}1)_{\text{TiB}_2} \parallel \langle 1\bar{1}0 \rangle_{\text{Ni}} / \langle \bar{1}010 \rangle_{\text{TiB}_2}$$

$$(111)_{\text{Ni}} / (10\bar{1}1)_{\text{TiB}_2} \parallel \langle 11\bar{2} \rangle_{\text{Ni}} / \langle \bar{1}\bar{1}23 \rangle_{\text{TiB}_2}$$

$$(200)_{\text{Ni}} / (0001)_{\text{TiB}_2} \parallel \langle 011 \rangle_{\text{Ni}} / \langle \bar{1}010 \rangle_{\text{TiB}_2}$$

$$(220)_{\text{Ni}} / (10\bar{1}1)_{\text{TiB}_2} \parallel \langle 11\bar{2} \rangle_{\text{Ni}} / \langle \bar{1}2\bar{1}3 \rangle_{\text{TiB}_2}$$

$$(220)_{\text{Ni}} / (10\bar{1}1)_{\text{TiB}_2} \parallel \langle 100 \rangle_{\text{Ni}} / \langle 0001 \rangle_{\text{TiB}_2}$$

It is recommended to refine these ORs using Δg theory by Zhang et al. [149,152]; however, the refinement of OR was not performed in the current study. In addition to exhibiting low crystallographic mismatch, TiB₂ has a melting temperature (T_m) > 3000°C, which is necessary to be stable during the DED process, thereby offering a potential to create heterogeneous nucleation sites and thereby breaking down the columnar microstructure and promoting grain refinement. Therefore, considering melting temperature (T_m) and crystallographic matching, TiB₂ was chosen as an inoculant for the present study.

6.4.3 Mechanical properties and anisotropy

The possible reasons for anisotropic mechanical properties as observed in the present investigation are discussed. A non-homogeneous microstructure with elongated columnar grains results in different strengthening when the loading is done in parallel and transverse directions. The average value of the Taylor factor of the specimens tested in vertical and horizontal directions for $\{111\} \langle 110 \rangle$ slip system is reported in Table 6.7. In polycrystalline metals, the Taylor factor is a measure of the flow stress, where a higher Taylor factor indicates higher resistance to deformation. The grains requiring large amounts of slip systems to consume large plastic deformations show large Taylor factors. Therefore, to investigate the anisotropy in strength, Taylor factor maps are done based on the preferential FCC slip system of $\{111\} \langle 110 \rangle$.

Table 6.7: Measured Taylor factors of the specimens for the $\{111\} \langle 110 \rangle$ slip system

Deposition Condition	Taylor Factor
IN718-vertical	2.93
IN718-horizontal	2.85
IN718/TiB ₂ -vertical	3.05
IN718/TiB ₂ -horizontal	3.00

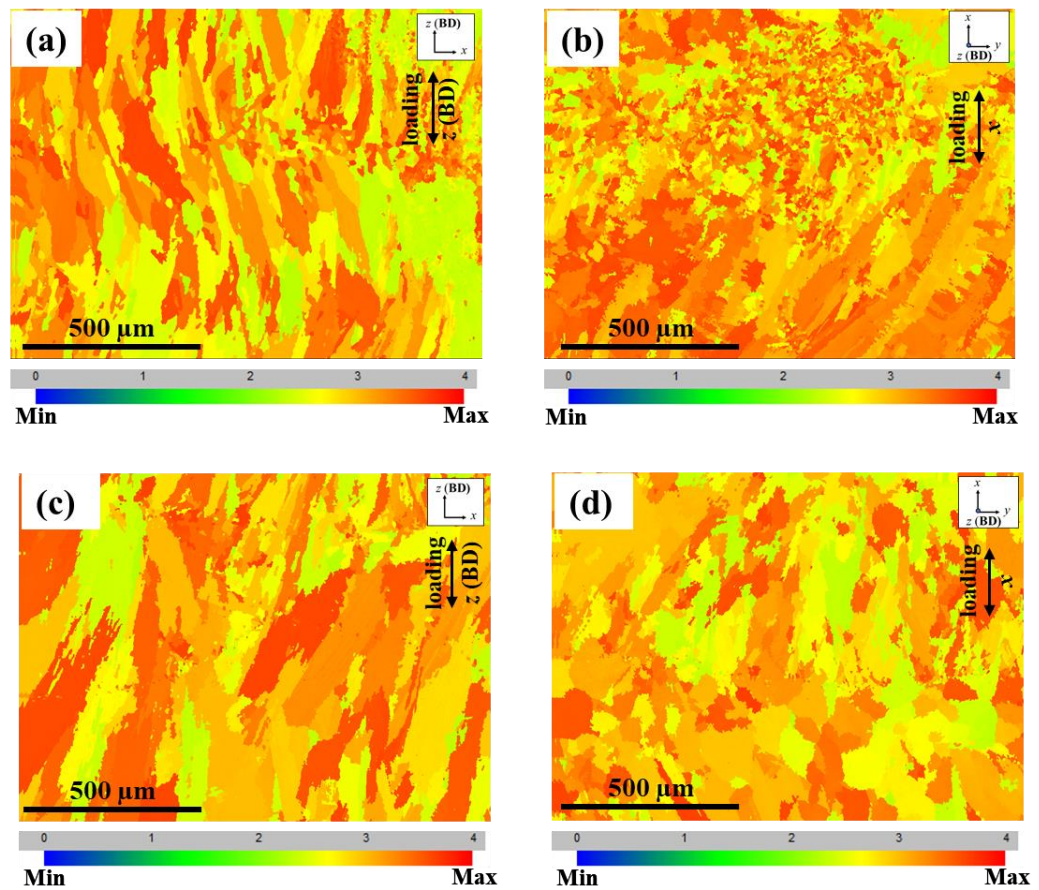


Figure 6.25: Taylor factor maps for as-deposit IN718 for High Energy deposits (a) Vertical specimen; and (b) horizontal specimen Taylor factor maps for IN718/TiB₂ for High Energy deposits: (a) Vertical specimen; and (b) horizontal specimen, Taylor factor colouring legend and average Taylor factor is indicated.

Figure 6.25 (a) and Figure 6.25 (b) compare the Taylor factor maps for as-deposit IN718 vertical and horizontal samples, respectively. The corresponding Taylor factor maps for IN718/TiB₂ vertical and horizontal samples are shown in Figure 6.25 (c) and Figure 6.25 (d). A slightly higher average Taylor Factor value of 2.93 is observed in the vertical specimens compared to 2.85 in the horizontal samples. Similarly, in the IN718/TiB₂ samples, the higher average Taylor factor value of 3.05 in the vertical samples matches with higher corresponding strength. However, the differences in the average values of Taylor factors are not significant enough to provide a possible explanation for the anisotropic properties from a crystallographic point of view. Moreover, it should be noted that for the IN718/TiB₂ builds, the ratio of the Taylor factor is $\frac{3.0}{3.05} = 0.98$, and the ratio of yield strength for horizontal to the vertical specimen is $\frac{841.0}{988.0} = 0.85$. A Higher Taylor factor ratio than the yield strength ratio

indicates that in addition to crystallographic orientation, other mechanisms are also responsible for the anisotropic mechanical behaviour [113].

Other possible factors potentially contributing to anisotropy in the deposited parts is the thermal history of the parts during the manufacturing process. In the present study, the gauge of the vertical samples is much higher up the build direction compared to the horizontal samples that are closer to the substrate. Kirka et al. [117], in EBM, manufactured IN718, observed increasing tensile strength and the elongation with the increase in the distance from the bottom of the build. The lower strength and elongation properties of the specimens machined from the lower part of the build were attributed to increasing the Laves and δ phases due to tempering and over-aging at the bottom of the build. Also, coarsening of the strengthening γ'' phase at the bottom of the build was also found to be responsible for deteriorating mechanical properties. In the current investigation, the thermal cycles experienced by the vertical samples would significantly differ from the horizontally built samples, which results in orientation dependence of mechanical properties. Furthermore, the residual stress induced by the cyclic heating during the DED process is expected to increase dislocation pile-up in the samples. Deng et al. [113] attributed residual stress accumulation during the SLM deposition process as the dominant factor contributing to anisotropic mechanical properties. They reasoned that, although machining post-deposition relieves residual stresses, the dislocation pile-up introduced by the residual stresses remains and affects the mechanical properties [113]. It is understood that the largest planar residual stress component is generated parallel to the scan vector and increases with the scan vector [239]. Therefore, the residual stresses developed in the deposited samples would vary due to the geometry of the part being built, resulting in anisotropic mechanical properties. Therefore, residual stress analysis requires detailed investigation; however, it is outside the scope of the present work.

6.4.4 Strengthening in IN718/TiB₂

TiB₂ addition to IN718 resulted in substantial improvement of hardness and strength properties. This section discusses the effect of various strengthening mechanisms and their significance to the current results. The strengthening mechanisms of metal matrix composites (MMCs) can be classified as follows [156,170,240,241]:

1. Grain boundary strengthening ($\sigma_{Hall-Petch}$);
2. Strengthening due to dislocation structure formation (σ_{CTE});

3. Orowan strengthening (σ_{Orowan}); and
4. Load transfer effect (σ_{load}).

The root mean square of these effects can predict the room-temperature yield strength. The increment of total yield strength can be expressed as the following equation [156,240–242]:

$$\Delta\sigma = \sqrt{(\Delta\sigma_{Hall-Petch})^2 + (\Delta\sigma_{Orowan})^2 + (\Delta\sigma_{CTE})^2 + (\Delta\sigma_{load})^2} \quad [6.4]$$

The individual contribution of these strengthening mechanisms is discussed as follows. Grain boundaries in a polycrystalline metal hinder dislocation movement and affect strength. Hall–Petch effect [85] is a well-known strengthening mechanism that relates grain size to the strength of the material, as shown in Eq. (3).

$$\sigma_{Hall-Petch} = \sigma_0 + k_y d^{-1/2} \quad [6.5]$$

where, σ_0 is the original strength of the material friction stress in the absence of grain boundaries, k_y is the strength coefficient, and d is the grain size of the material. In the present study, a reduction in grain size from 31.4 μm in as-deposit IN718 to 23.8 μm is observed upon TiB₂ addition, as shown in Figure 6.12 (a – b). A decrease in grain size would increase the yield strength of the IN718/TiB₂. The increase in yield strength due to grain size reduction is estimated using the following equation [240]:

$$\Delta\sigma_{Hall-Petch} = k_y d^{-1/2} \quad [6.6]$$

The contribution of grain-size strengthening is estimated using $k_y = 750 \text{ MPa}\sqrt{\mu\text{m}}$ [242] for IN718. Using the value of k_y in Eq (4) gives an increment of ~ 154 MPa. Additionally, the presence of secondary phases as reported in Figure 6.14 (b) and Figure 6.14 (d) produces a pinning effect on the grain boundaries and prevents grain growth, thus, strengthening the material.

One of the most important strengthening mechanisms in MMCs, and in the present study, is Orowan strengthening, given by the following equation [156,170,243]:

$$\sigma_{Orowan} = \frac{0.84GbM}{2\pi(1-\nu)^{3/2}\lambda} \ln \frac{d_p}{2b} \quad [6.7]$$

where G is the shear modulus of the matrix, b is Burger's vector of the matrix. The shear modulus is 76 GPa, and the Burgers vector is 0.26 nm for the IN718 matrix [196,242]. $M = 3.05$ is the Taylor factor for FCC material [243], $\nu = 0.28$ is Poisson's

ratio, and λ is the interparticle spacing between the precipitates. The interparticle spacing (λ) of 595 nm is calculated using the following Eq (6.8) [156]

$$\lambda = \sqrt{\frac{2}{3}} d_p \left(\sqrt{\frac{\pi}{4V_p} - 1} \right) \quad [6.8]$$

To determine the values of d_p and V_p , measurements were performed on 4 – 6 SEM images like the one shown in Figure 6.15 (a). For simplicity, the precipitates were treated as spheres with average particle diameter (d_p) of 289 nm. The average particle diameter (d_p) is measured considering the average width of the needle-shaped precipitates. The strengthening induced by these precipitates due to Orowan strengthening was calculated to be ~ 100 MPa. Therefore, it can be inferred from the results in the previous section that the secondary phases significantly contribute to the increase in strength properties. The volume and distribution of these phases are of particular significance. It was shown by Nguyen and Gupta [170] that both reductions in the size of the secondary particles and their distribution affect Orowan strengthening and hence the strength of the nano-composite. Also, AlMangour et al. [156] found that Orowan strengthening had the highest contribution (with a strengthening contribution of ~ 40 – 50 %) to the strengthening of 316SS/TiB₂ composites processed via SLM.

Another important strengthening mechanism in MMCs is due to an increase in geometrically necessary dislocations (GNDs) in the vicinity of the matrix- secondary phases interface due to the mismatch of elastic modulus (EM) and the coefficient of thermal expansion (CTE) between them [244]. A higher dislocation density in the composite yields higher internal stress [241]. The improvement in yield strength due to the generation of geometrically necessary dislocations to accommodate the CTE mismatch between the particle and matrix is given by the Taylor relation as indicated below [156,240,242]

$$\Delta\sigma_{GND} = \sqrt{3}\beta Gb(\sqrt{\rho_{GND}}) \quad [6.9]$$

where β is a geometric constant and ρ_{GND} denotes the GND density. For SLM deposit IN718, β value of 0.3 was used. Similarly, in this study, where the heterogeneous distribution of dislocations accumulation along the cellular wall is expected, $\beta = 0.3$ was used. The Taylor equation is used to predict the increase in flow stress due to the influence of dislocations, and in this case, the flow stress in the matrix is improved due to the presence of geometrically necessary dislocations [240]. The effect of the

addition of TiB_2 on GND density is investigated using local area misorientation maps. The local misorientation maps for the high energy deposits are shown in Figure 6.26 (a – g). Figure 6.26 (a), (d); Figure 6.26 (b), (e), and Figure 6.26 (c), (f) represent the respective band contrast map, IPF maps, and local area misorientation maps for IN718 and IN718/ TiB_2 , Figure 6.26 (g) compares the distribution of the local misorientation in IN718 and IN718/ TiB_2 . For constructing the local area misorientation maps, EBSD scans are done using a step size of $0.15 \mu\text{m}$.

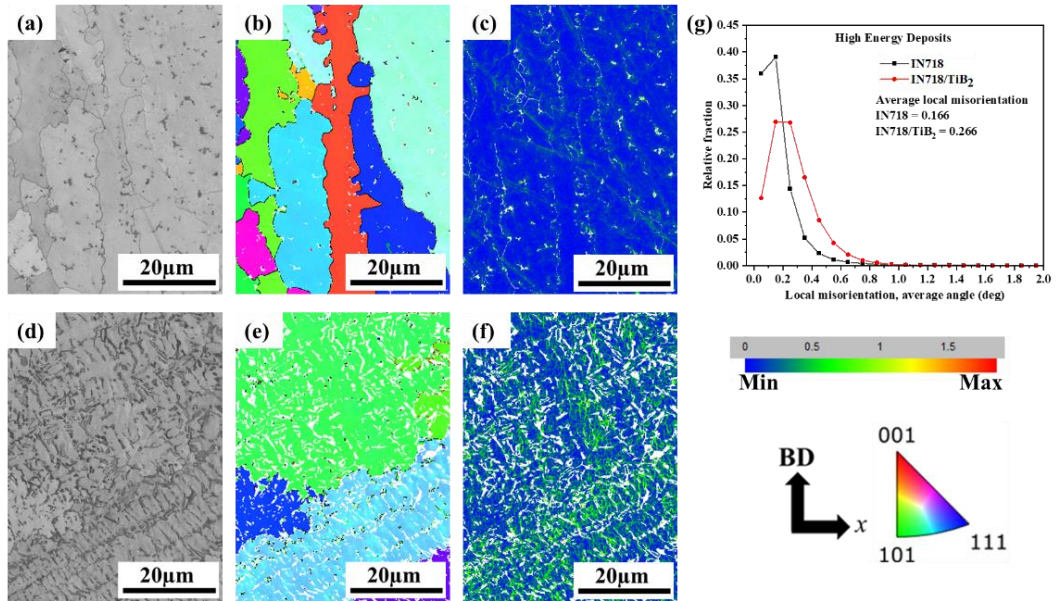


Figure 6.26: EBSD maps for high energy density deposits showing (a), (d) Band contrast maps, (b), (e) IPF maps, (c), (f) local area misorientation maps for As-deposit IN718 and IN718/ TiB_2 respectively, (g) compares the distribution of the local misorientation for IN718 and IN718/ TiB_2 .

Comparing Figure 6.26 (c) and Figure 6.26 (f), higher values of the local area misorientation are evident in the IN718/ TiB_2 deposits. The average value of local area misorientation increased from 0.164 to 0.266. An increase in the value of local misorientation values is a consequence of increased GND densities by TiB_2 addition. The local misorientation maps show the average misorientation between each step and its five nearest neighbours, which is calculated excluding any high-misorientation-angle boundaries (considered $> 10^\circ$ in this study). These local misorientation maps indicate local lattice distortion in the vicinity of the secondary phases in the IN718/ TiB_2 deposits. Therefore, it can be inferred that the micro-segregation due to TiB_2 addition led to increased GNDs in the IN718/ TiB_2 deposits. Under these conditions, most of the grains are formed with low-angle grain boundaries ($< 2^\circ$) or

sub-grains which are generally assumed to be formed by dislocation rearrangement. Thus, they are generally not considered true grain boundaries; however, they significantly influence the strengthening of the material. The relationship between average misorientation angle and dislocation density is calculated using the following Eq (6.10) [196]:

$$\rho_{GND} = \frac{\alpha\theta}{bu} \quad [6.10]$$

Where, ρ_{GND} is the dislocation density, and θ is the average value of local area misorientation, b is the Burgers vector α is a constant and was set to 3 considering the boundaries for mixed characters [196,245]. u is the distance between the misoriented points which is the “step size” of the EBSD map. Using Eq (6.9) the value of ρ_{GND} is estimated $\sim 3.54 \times 10^{14} \text{ m}^{-2}$ for IN718/TiB₂ high energy deposits, increasing from $\sim 2.23 \times 10^{14} \text{ m}^{-2}$ calculated for as-deposit IN718. The contribution of increased GND to the strength of IN718/TiB₂ ($\Delta\sigma_{GND}$) can be calculated by using the values of ρ_{GND} in and is estimated to be $\sim 340\text{MPa}$.

Furthermore, the strong bonding between the dispersed particles or the secondary phases in the present study and the matrix contributes to the transfer of the load applied to the material [241]

$$\Delta\sigma_{load} = V_p\sigma_m \left[\frac{(l+t)A}{4l} \right] \quad [6.11]$$

where V_p is the volume fraction of particles in the matrix, σ_m is the yield strength of the matrix, l is the size of the particulate parallel to the load direction, t is the thickness of the particulate, and $A = l/t$ is the particulate aspect ratio. The contribution of $\Delta\sigma_{load}$ to the strengthening of IN718/TiB₂ estimated considering spherical shaped precipitates is $\sim 30\text{MPa}$. As the volume fraction (V_p) of the reinforcing particles was low $\sim 15 \text{ vol}\%$; thus, the contribution of $\Delta\sigma_{load}$ to the strengthening of IN718/TiB₂ is less compared to the other strengthening mechanisms.

The total contribution of these strengthening mechanisms is estimated from Eq 6.4. The value of $\Delta\sigma$ calculated is $\sim 380 \text{ MPa}$ which agrees well with the difference of the YS of IN718 and IN718/TiB₂ of $\sim 400\text{MPa}$, measured experimentally as reported in Table 6.4. Note that the calculations assume identical properties of the IN718 and IN718/TiB₂ matrix. Additionally, the study is conducted on IN718 and IN718/TiB₂ in as-deposit conditions. The cooling rates during the deposition process are usually too high for the formation of the strengthening precipitates γ' , γ'' [93]; therefore, the

precipitation-related strengthening mechanisms such as dislocation-pinning and coherency strain hardening is not explored in the present chapter.

6.5 Conclusion

The present study investigates the incorporation of TiB₂ to induce columnar to equiaxed transition in DED IN718. The effect of TiB₂ addition on the microstructure and the mechanical properties is explored. The major findings are as follows:

- 7 Using a crystallographic model, TiB₂ is selected as a potent grain refiner in DED IN718. TiB₂ has a high melting temperature (T_m) and low crystallographic mismatch, making it a potent grain refiner.
- 8 The microstructures of the fabricated IN718/TiB₂ composites were different from that of as-deposit IN718. The addition of TiB₂ to IN718 resulted in significant grain refinement in the as-built microstructure. In the high-energy deposit, grains of size $>300\mu\text{m}$ occupied $\sim 22\%$ of the total grain area and $\sim 10\%$ in the low-energy deposits, which were reduced to $\sim 5\%$ upon TiB₂ addition. Moreover, a preferential $\{100\}$ texture observed along the building direction in the as-deposit IN718 became weak and random in the IN718/TiB₂ deposits. The resulting IN718/TiB₂ microstructure was found to be sensitive to the wt% of TiB₂ particle content, and TiB₂ content >1.5 wt% was optimal for inducing grain refinement.
- 9 The powder flow rate during the deposition process profoundly affected the densification of the low energy density deposits. Interlayer defects were reduced, and densification increased upon lowering the flow rate from 12 g/min to 7 g/min. Reducing the flow rate during the deposition process reduced the viscosity of the melt pool and helped reduce the balling effect.
- 10 The Laves phase often observed in the as-deposit IN718 is greatly reduced upon TiB₂ addition and replaced by Cr, Mo, B rich needle-shaped phases. Round-shaped TiB₂ is also seen in the microstructure.
- 11 The reduced crystallographic texture and refined microstructure due to TiB₂ resulted in a slight decrease in the anisotropic mechanical properties; however, anisotropy in tensile properties persists. The vertically built as-manufactured IN718 shows lower strength but higher ductility when loaded along the z (BD) direction than the horizontally built sample loaded perpendicular to the z (BD) direction. This sample orientation dependence of mechanical properties of the as-deposit IN718 requires further study.

- 12 IN718/TiB₂ exhibit significantly high hardness and strength properties from uniaxial tensile tests. The tensile strength increased from 570 MPa in IN718 to 988 MPa in IN718/TiB₂ tested parallel to the building direction. When tested perpendicular to the build direction, an increased yield strength of 840 MPa was observed in IN718/TiB₂ compared to 475 MPa in IN718 deposits.
- 13 The conventional strengthening mechanisms were presented to explain the effect of TiB₂ on the refined microstructure. The major contributing strengthening mechanisms included grain refinement, Orowan strengthening and increased GND density due to TiB₂ addition.

CHAPTER 7**Conclusions and Suggestions for Future Work****7.1 Summary and conclusions**

The work presented in this thesis has examined the use of direct energy deposition (DED) process for repair of Ni-base superalloy, Inconel 718 (IN718). Laser engineered net shaping (LENS), a common DED process, was used in the current investigation. IN718 has found widespread application in fabricating aviation and aerospace components that would operate in extremely harsh conditions, such as hot sections of gas turbine engines. The severe operating conditions often make these components susceptible to damage.

The current study commenced by studying DED IN718 processed using various process parameters combination. Based on microstructural characterisation and porosity measurements, a suitable process parameter set, with minimum porosity and mixed equiaxed and columnar microstructure, was selected for groove repairs reported in Chapter 4 and fabricating repaired composites for fatigue tests reported in Chapter 5. Chapter 4 investigates the effects of post-heat treatment (direct aged (DA) and Solution treated at 980⁰C and aged (STA) condition) on the microstructure of the repair deposit and surrounding substrate. The mechanical properties, deformation behaviour and failure mechanisms of the resulting repaired composite were investigated using 4-point bend testing coupled with digital image correlation (DIC) and cross-sectional microscopy. The fatigue properties of the repaired composites were explored and compared to wrought IN718 in chapter 5. Moreover, the failure mechanism in the repaired composite, especially near the deposit-substrate interface, was studied by intermittently stopping the fatigue tests and investigating under SEM.

IN718 deposit using DED methods exhibits columnar microstructure with elongated grains growing parallel to the heat flow direction as indicated in the literature and also observed in the current investigation. The columnar nature of the microstructure results in anisotropic mechanical properties often reported in the literature. Chapter 6 explores the potential of using grain refiners/inoculants to transform the columnar microstructure into a homogenous and equiaxed microstructure. Subsequently, the effect of addition of inoculant during DED processing of IN718 on the resulting mechanical properties is explored. Using crystallographic model, TiB₂ was selected as a potent grain refiner in DED IN718. TiB₂ has a high melting temperature (T_m) and low crystallographic mismatch, making

it a potent grain refiner. The key findings and conclusions drawn from the current investigation are summarised as follows.

- i. Same linear energy density – obtained using different power and scan speed combinations – can produce very different microstructures varying from columnar to mixed columnar-equiaxed microstructure. In the deposits with columnar – equiaxed grain morphology, elongated-shaped grains with a preferential (100) texture are generally seen.
- ii. The resultant ‘repaired composite’ exhibited a non-uniform microstructure: big equiaxed grains $\sim 90\mu\text{m}$ in the substrate with a high fraction of ($\sim 40\%$) $\Sigma 3$ twin boundaries and fine mixed columnar and equiaxed grains $\sim 25 - 30\mu\text{m}$ in the deposit zone. A high fraction ($\sim 45\%$) of LAGB is observed in the deposit zone.
- iii. For DED IN718 – repairs, low-strength heat-affected zone, which can extend up to $\sim 1\text{ mm}$ in the substrate near the deposit-substrate interface.
- iv. An effect of the angle of groovewall was evident from the 4-point bend tests with low/shallow angle – 30° in the present study was able to withstand higher deformation compared to steeper grooves with higher groove wall angles (60°).
- v. The fatigue performance of DED – repaired IN718 is found to vary with heat treatment and the stress level during cyclic loading: at high-stress ($90\% - 70\%$ YS), DA outperforms STA and at low-stress ($<50\%$ YS), STA performs better.
- vi. The substrate grain boundaries near the deposit zone-substrate interface act as preferential crack initiation sites under 4-point bend loading and cyclic loading – liquation of NbC weakens the substrate grain boundary.
- vii. In DA conditions, the Nb-rich films along the HAZ grain boundaries were the first crack initiation sites, and failure generally occurred through the coarse substrate grain boundaries. However, in the STA condition, the final failure occurred through the deposit zone. The presence of needle-shaped δ phases in the deposit zone resulted in preferential crack initiation sites at stress levels close to the yield stress of the material.
- viii. TiB_2 addition to IN718 results in significant grain refinement and much-reduced texture along with significant improvement in strength- highest among other IN718-based composites. The optimised TiB_2 powder size is found to be $<10\mu\text{m}$ with a content of $\geq 1.5\text{ wt}\%$. The tensile strength increased from 570 MPa in IN718 to 988 MPa in IN718/ TiB_2 tested parallel to the building

direction. When tested perpendicular to the build direction, an increased yield strength of 840 MPa was observed in IN718/TiB₂ compared to 475 MPa in IN718 deposits. The increase in geometrically necessary dislocations due to formation of the secondary phases, Orvan strengthening and grain size refinement were found to be the main contributors to the strengthening of IN718/TiB₂.

- ix. Although reduced crystallographic texture and refined microstructure was observed due to TiB₂, the anisotropy in tensile properties persists in the IN718/TiB₂ deposits. The vertically built as-manufactured IN718 exhibited lower strength but higher ductility when loaded along the z (BD) direction than the horizontally built sample loaded perpendicular to the z (BD) direction. This sample orientation dependence of mechanical properties of the as-deposit IN718 requires further investigation.
- x. The powder flow rate during the deposition process affects the densification of deposits – higher density can be achieved by reducing the powder flow rate from 12 g/min to 7 g/min.

7.2 Suggestions for further work

7.2.1 Repair AM substrate

In the current study, repairs are conducted on wrought IN718 substrates. With the ever-growing AM industry, more AM superalloy components are replacing conventionally manufactured components. As indicated in the literature and established in the current study, the metallurgy of AM IN718 would vary significantly from the conventionally manufactured components in terms of grain morphology and size and distribution of secondary phases. The constitutional liquation of Nb-rich carbides in the base material is an important phenomenon that dictates the ‘quality’ of the repair in terms of mechanical properties. It is observed that the failure initiates from these Nb-rich liquid films on the base material grain boundaries. Moreover, it has been well established that the constitutional liquation temperature of Laves phase is much lower than that of Nb-rich carbides, resulting in a larger heating liquation temperature range and extensive liquation in cast materials. AM fabricated IN718 contains a high amount of Laves content compared to wrought counterparts. Therefore, investigation of the effect of Laves phase on repairability/weldability of repair of AM fabricated substrates requires detailed investigation.

7.2.2 Investigation of repair weldability of IN718 after multiple repair cycles.

An IN718 superalloy component often requires multiple repairs during its service life. It is established in welding literature that the microstructures and mechanical properties of IN718 are affected by the welding process, resulting in cumulative damage due to multiple repair cycles and post-repair heat treatment. This results in reduced weldability with an increasing number of repair cycles due to a greater susceptibility to HAZ liquation cracking [1]. Therefore, it is important to evaluate the microstructural changes and performance of the repaired composites after multiple repair cycles using additive manufacturing techniques. It would be interesting to compare the repairability of IN718, repaired using traditional welding techniques and AM techniques after multiple repair cycles.

7.2.3 Investigation of fatigue damage mechanism at elevated temperature

The Inconel 718 components are generally used in turbine components, such as disks, where operating temperature reaches $\sim 500^{\circ}\text{C} - 600^{\circ}\text{C}$. Kawagoishi et al. [135] studied the fatigue properties of wrought IN718 at room and elevated temperatures and observed greater fatigue strength at low-stress regimes when tested at elevated temperatures than at room temperature. It was found that the oxide film on the material surface resisted crack growth, especially at low stresses, which outweighed the material softening due to thermally activated slip and as a result, the fatigue life of the material was improved. Gribbin et al. [130] investigated the high cycle fatigue performance of AM deposited IN718 at room temperature and 500°C tested in various sample orientations. Similar to wrought IN718, the AM deposited materials exhibited longer lives at 500°C for lower stress amplitudes than the materials at room temperature. At higher stresses, the material performed better at room temperature.

In the present study, the cyclic failure mechanism is studied at room temperature. The effect of Laves phases and δ phases on the high-temperature fatigue properties and the subsequent failure mechanism can be studied using interrupted tests similar to ones performed in Chapter 5 at elevated temperature and deserves further exploration.

7.2.4 Modification of energy density equation to include powder input flow rate

The heat input during the AM process can be correlated with key process parameters. The energy density equation commonly used in AM processing generally includes the

linear energy density and volumetric energy density. The linear energy density includes the parameters power and scan speed. In contrast, the volumetric energy density equation considers hatch spacing and layer thickness, in addition to the laser power and scan speed. It was observed in Chapter 4 of the current investigation that a similar set of linear energy density yield significantly different microstructural morphology in the deposit. The difference in grain morphology is attributed to the thermal history in the respective deposits. Moreover, the energy density equation does not consider important process parameters in the DED process, such as powder flow rate. It is observed in Chapter 6 that changing powder flow rate and keeping all other parameters constant results in a change in microstructure. Therefore, the energy density equation modification is necessary and requires further investigation.

7.2.5 Explore the parameter combination and other inoculants for columnar to equiaxed transition (CET)

From the observations in Chapter 6, it is seen that TiB₂ was able to provide CET in IN718; however, the parameter combination(s) used in the DED process led to the dissolution (partial) of the TiB₂ particles. Moreover, when low energy deposition parameters were used, desirable densification was not achieved. Therefore, exploring other process parameters that can induce grain refinement while preventing the dissolution of TiB₂ and maintaining the desired densification needs further investigation. Possible deposition strategy would include lowering the heat input during deposition process by using a lower power. To compensate for the low power and produce dense deposits other parameters especially, the powder flow rate and the layer thickness would be modified accordingly. Additionally, other ceramic refiners that can stay stable at the high temperatures associated with the DED processing, can be explored in the future.

Appendix 1

**A1. HCF test results for Investigated repaired IN718 composites (Chapter 5)
under various heat-treated conditions**

	$\Delta\sigma_{max}$ (%YS*)	Test 1	Test 2	Average (N_f)	%er	CEV
Substrate	90	48480	38881	43681	7.8	11.0
	80	46351	51919	49135	4.0	5.7
	70	70430	95902	83166	10.8	15.3
	60	220333	348578	284456	15.9	22.5
	50	624227		624227	0.0	0
	45	No failure				
DA	90	51925	21537	36731	29.2	41.4
	80	73594	107303	90448	13.2	18.6
	70	166582	89993	128288	21.1	29.9
	60	168527	160503	164515	1.7	2.4
	50	359567	208741	284154	18.8	26.5
	45	718969	621507	670238	5.1	7.3
	40	872927				
	35	No failure				
STA	90	7077	7830	7454	3.6	5.1
	80	39629	44674	42152	4.2	6.0
	70	58364	51465	54915	4.4	6.3
	60	92271	146573	119422	16.1	22.7
	50	439307		439307	0.0	0.0
	45	No failure				

YS* = 950MPa

$$\% \text{ er}^{**} = \frac{\text{Standard error}}{\text{Average } (N_f)} \times 100$$

$$\% \text{ CEV}^{***} = \frac{\text{Average } (N_f)}{\text{Standard Deviation}} \times 100$$

Appendix 2

A2. Percentage mismatch calculation using Edge-to Edge Matching model

The closest packed direction in Inconel718 (Ni) are [110], [100], [112], among which [110] is the closest packed Ni directions. Similarly, the close-packed planes are {111}, {200} and {220}. The {111} plane can contain the directions [110] and [112]; {200} plane contains [100] and [112] directions and {220} plane contains [110] and [112] directions. TiC and ZrC have FCC crystal structure with respective melting temperature $> 3000^{\circ}\text{C}$ [246–248]. The closed-packed planes in TiC and ZrC are (111), (200), and (220). The possible close or nearly close-packed directions are [110], [100], [111]. The lattice parameters for TiC and ZrC used for the calculations are $a = 0.4327$ nm and 0.4693 nm, respectively. The mismatch calculations and the OR determination are performed according to the steps described in Chapter 3 (Section 3.4). The Atomic Mismatch and the possible OR for IN718/TiC and IN718/ZrC are shown in Table A2.1 and Table A2.2, respectively.

Table A2.1: Atomic mismatch between IN718 and TiC.

Direction Ni	Direction TiC	%	Plane Ni	Plane TiC	% Mismatch
Ni [110]	[110]	-20.66	Ni (111)	(111)	-20.66
	[100]	14.68		(200)	-4.50
	[111]	-47.78		(220)	26.11
Ni [100]	[110]	14.68	Ni (200)	(111)	-39.33
	[100]	39.67		(200)	-20.66
	[111]	-4.49		(220)	14.68
Ni [112]	[110]	30.34	Ni (220)	** (111)	1.48
	*[100]	1.48		** (200)	14.68
	[111]	14.68		(220)	-20.66

*Indicates that two interatomic spacings in TiC matches one spacing in IN718

**Indicates that two interplanar spacings in IN718 matches one interplanar spacing in TiC.

Possible Orientation relation(s) of TiC with Ni:

1. $(111)_{\text{Ni}} / (200)_{\text{TiC}} \parallel \langle 112 \rangle_{\text{Ni}} / \langle 100 \rangle_{\text{TiC}}$

Table A2.2: Atomic mismatch between IN718 and ZrC.

Direction	Direction	% Mismatch	Plane Ni	Plane ZrC	% Mismatch
Ni [110]	[110]	-30.87	Ni (111)	(111)	-30.87
	[100]	7.46		(200)	-13.34
	[111]	-60.28		(220)	19.86
Ni [100]	[110]	7.46	Ni (200)	** (111)	24.44
	[100]	34.56		(200)	-30.87
	[111]	-13.33		(220)	7.46
Ni [112]	[110]	24.44	Ni (220)	** (111)	-6.85
	*[100]	-6.85		** (200)	7.46
	[111]	7.46		(220)	-30.87

*Indicates that two interatomic spacings in ZrC matches one spacing in IN718

**Indicates that two interplanar spacings in IN718 matches one interplanar spacing in ZrC.

Possible Orientation relation(s) of ZrC with IN718:

1. $(200)_{\text{Ni}} / (220)_{\text{ZrC}} \parallel \langle 011 \rangle_{\text{Ni}} / \langle 001 \rangle_{\text{ZrC}}$
2. $(200)_{\text{Ni}} / (220)_{\text{ZrC}} \parallel \langle 010 \rangle_{\text{Ni}} / \langle \bar{1}10 \rangle_{\text{ZrC}}$
3. $(220)_{\text{Ni}} / (111)_{\text{ZrC}} \parallel \langle 001 \rangle_{\text{Ni}} / \langle 1\bar{1}0 \rangle_{\text{ZrC}}$
4. $(220)_{\text{Ni}} / (200)_{\text{ZrC}} \parallel \langle 1\bar{1}0 \rangle_{\text{Ni}} / \langle 010 \rangle_{\text{ZrC}}$
5. $(220)_{\text{Ni}} / (200)_{\text{ZrC}} \parallel \langle 001 \rangle_{\text{Ni}} / \langle 011 \rangle_{\text{ZrC}}$
6. $(220)_{\text{Ni}} / (200)_{\text{ZrC}} \parallel \langle 11\bar{2} \rangle_{\text{Ni}} / \langle 010 \rangle_{\text{ZrC}}$

The lattice parameters for WC are $a = 0.29065$ nm and $c = 0.28366$ nm, from the JCPDS database. The closed packed planes are $(10\bar{1}1)$, $(10\bar{1}0)$, (0001) , $(11\bar{2}0)$ and the four possible close or nearly close-packed directions are $\langle 0001 \rangle$, $\langle \bar{1}\bar{1}23 \rangle$, $\langle 10\bar{1}0 \rangle$ and $\langle 11\bar{2}0 \rangle$. The Atomic Mismatch and the possible OR are shown in Table A2.3.

Table A2.3: Atomic mismatch between IN718 and WC.

Direction Ni	Direction	% Mismatch	Plane Ni	Plane WC	% Mismatch
Ni [110]	$\langle 11\bar{2}0 \rangle$	-14.62	Ni (111)	$(10\bar{1}1)$	9.06
	$\langle 0001 \rangle$	-11.87		$(10\bar{1}0)$	-21.58
	$*\langle \bar{1}\bar{1}23 \rangle$	19.92		** (0001)	31.50
	$*\langle 10\bar{1}0 \rangle$	0.73		$(11\bar{2}0)$	29.81
Ni [100]	$\langle 11\bar{2}0 \rangle$	18.95	Ni (200)	$(10\bar{1}1)$	-5.00
	$\langle 0001 \rangle$	20.90		$(10\bar{1}0)$	-40.38
	$\langle \bar{1}\bar{1}23 \rangle$	-13.25		** (0001)	20.90
	$\langle 10\bar{1}0 \rangle$	-40.38		$(11\bar{2}0)$	18.95
Ni [112]	$\langle 11\bar{2}0 \rangle$	33.82	Ni (220)	** $(10\bar{1}1)$	25.75
	$\langle 0001 \rangle$	35.41		$(10\bar{1}0)$	0.73
	$\langle \bar{1}\bar{1}23 \rangle$	7.53		** (0001)	-11.87
	$\langle 10\bar{1}0 \rangle$	-14.62		$(11\bar{2}0)$	-14.62

*Indicates that two interatomic spacings in WC matches one spacing in IN718

**Indicates that two interplanar spacings in IN718 matches one interplanar spacing in WC.

Possible Orientation relation(s):

1. $(111)_{\text{Ni}} / (10\bar{1}1)_{\text{WC}} \parallel \langle 1\bar{1}0 \rangle_{\text{Ni}} / \langle \bar{1}010 \rangle_{\text{WC}}$
2. $(111)_{\text{Ni}} / (10\bar{1}1)_{\text{WC}} \parallel \langle 11\bar{2} \rangle_{\text{Ni}} / \langle \bar{1}\bar{1}23 \rangle_{\text{WC}}$
3. $(200)_{\text{Ni}} / (10\bar{1}0)_{\text{WC}} \parallel \langle 011 \rangle_{\text{Ni}} / \langle \bar{1}010 \rangle_{\text{WC}}$
4. $(220)_{\text{Ni}} / (10\bar{1}0)_{\text{WC}} \parallel \langle 1\bar{1}2 \rangle_{\text{Ni}} / \langle \bar{1}2\bar{1}3 \rangle_{\text{WC}}$

Appendix 3

A3. CU Ethical Approval Documentation

18/12/2021, 11:14

P115813 | Project P115813 - CU ETHICS

(/app)

CU ETHICS

LOGOUT

PROJECTS

Project P115813

Here are all the details for your project. Click the tabs to toggle between the sections

[RETURN TO PROJECT LIST](#) (PROJECTS)

PROJECT P115813

REPAIR OF SUPERALLOY COMPONENTS USING LASER ENGINEERED NET SHAPING (LENS)

Project **Low risk**

Checklist 3

Comments 2

Approval Stages **Authorised**

Applicant Details

Full name

Riddhi Sarkar

Faculty/Subsidiary/Area

Research Institute

School/Institute/Unit

Clean Growth and Future Mobility

Supervisor

Michael Fitzpatrick

Module name

FTC-PHD - FTC PhD applications

<https://ethics.coventry.ac.uk/projects/115813>

1/7

Project Summary

Project ID

P115813

Project title

Repair of superalloy components using Laser Engineered Net Shaping (LENS)

Module code

FTC-PHD - FTC PhD applications

Brief Project Summary

The current project aims at using laser engineering net shaping (LENS) (Optomec MR-7) used to repair superalloy components. Laser additive manufacturing has been a subject of considerable attention from researchers in the past decade. Inconel 718 has been studied quite intensively for building components using various AM techniques. AM techniques as repair techniques provides many advantages over traditional techniques such as welding or brazing.

following research questions to be addressed in this project. In this projects the following research questions would be answered:

1. What is the effect of repair geometry and scan strategy on the properties of the repaired parts?
 - Study the effect of varying deposition path and repair geometry (various groove angle and sizes) on the properties of the repaired part
2. What is the effect of inoculants addition in grain refinement and reducing anisotropy of Inconel 718 repaired/deposited using laser DLD technique?
3. What is the effect of post deposit heat treatments on the cyclic deformation properties of Laser DLD the repaired/ manufactured component?

Start and end dates

14 Nov 2018 - 14 Nov 2021

Names of Co-Investigators & their organisational affiliation (place of study/employer)

-

Is this project externally funded?

Yes

Who is funding the project?

Deakin University

Has the funding been confirmed?

Yes

Use Professional Code of Ethical Practice?

No

18/12/2021, 11:14

P115813 | Project P115813 - CU ETHICS

<https://ethics.coventry.ac.uk/projects/115813>

3/7

Project Detail

What are the aims and objectives of the project?

The following research questions to be addressed in this project. Also, the underlying objectives involved in each of these research questions are discussed.

1. What is the effect of repair geometry and scan strategy on the properties of the repaired parts?

- Study the effect of various energy density on the microstructure of the deposit to find a suitable set of parameters.
- Study the effect of varying deposition path and repair geometry (various groove angle and sizes) on the properties of the repaired part

2. What is the effect of inoculants addition in grain refinement and reducing anisotropy of Inconel 718 repaired/deposited using laser DLD technique?

- Study to what extent can the anisotropy in mechanical properties be reduced using inoculant addition?

3. What is the effect of post deposit heat treatments on the Low cycle fatigue properties of Laser DLD the repaired/ manufactured component?

a. To correlate the HCF properties with the cyclic deformation mechanism and microstructure, so as to understand the HCF properties in laser additive manufacturing IN718 in room temperature and elevated temperature (650C) under the following conditions:

- i. As-built
- ii. Heat treated

b. To improve the fatigue life of the repaired component using a suitable combination of deposition strategy and post heat treatment.

Explain your research design

The current project aims at using laser engineering net shaping (LENS) (Optomec MR-7) used to repair superalloy components. Inconel 718 powders will be used for the process.

The microstructure of samples will be observed with SEM, EBSD, EDS and XRD.

Microhardness testing will be done to determine mechanical properties. For heat treatment of the samples, muffle furnace and fluidized bed will be used in the temperature range 200-1100°C. In addition, mechanical testing on the UTM will be done to evaluate mechanical properties like tensile properties and fatigue properties. Digital image correlation to be used to evaluate strain evolution during deformation.

Outline the principal methods you will use

Research will include: using literature review to develop the basic understanding. Additive printing will be done on the OPTOMECC LENS at Deakin University to optimise parameters for repairs and subsequent repairs will be done. We will later use the SEM, Optical Microscopy, EBSD, and XRD to characterise the samples. In addition, mechanical testing on the UTM will be done to evaluate mechanical properties like tensile properties and fatigue properties.

Are you proposing to use a validated scale or published research method / tool?

No

18/12/2021, 11:14

P115813 | Project P115813 - CU ETHICS

Data Analysis

1	Does the research seek to understand, identify, analyse and/or report on data/information on terrorism/terrorism policies?	No
2	Does your research seek to understand, identify, analyse and/or report on information for other activities considered illegal in the UK and/or in the country you are researching in?	No
3	Are you analysing Secondary Data?	No
4	Are you dealing with Primary Data involving people?	No
5	Personal or Sensitive data	
	Are you dealing with personal data?	No
	Are you dealing with special category data (formerly known as sensitive data)?	No
6	Is the project solely desk based secondary research?	No
7	Will the data collection, recruitment materials or any other project documents be in any language other than English?	No

<https://ethics.coventry.ac.uk/projects/115813>

5/7

Areas of Study

1

You have indicated the following are relevant to your study

Travel away from home campus

Biological samples, physical measurements/activities or substances/procedures administered to or taken from human participants

Information gathered from human participants

Biological materials including organisms, cell lines and samples (excluding humans)

Animals and their habitats, animal materials such as blood, tissue, or stool samples, primary cell cultures derived from animal tissues (excluding humans)

Hazardous substances

Machinery & equipment

Ionising Radiation

Flying unmanned aerial systems (e.g. drones)

Environmental samples

2

No

Are there any other ethical issues or risks of harm raised by the study that have not been covered by previous questions?

[RETURN TO PROJECT LIST](#) ☰ (/PROJECTS)

18/12/2021, 11:14

P115813 | Project P115813 - CU ETHICS

[HOME \(/APP\)](#) | [ABOUT \(/PAGES/ABOUT\)](#) | [ACCESSIBILITY \(/PAGES/ACCESSIBILITY\)](#)
| [PRIVACY \(/PAGES/PRIVACY\)](#) | [COPYRIGHT \(/PAGES/COPYRIGHT\)](#)

Coventry University, Priory Street, Coventry, West Midlands, CV1 5FB, United Kingdom

© Copyright Coventry University 2009 - 2021

Technical Support Request

[GET SUPPORT ⚙ \(/SUPPORT/REQUEST\)](#)

References

- [1] Q. Lu, Haz microstructural evolution in Alloy 718 after multiple repair and PWHT Cycles /, The Ohio State University, 1999.
http://rave.ohiolink.edu/etdc/view?acc_num=osu148818704954173.
- [2] Repair Welding of Ni-base Alloys, in: *Weld. Metall. Weldability Nickel-Base Alloy.*, John Wiley & Sons, Inc., Hoboken, NJ, USA, 2009: pp. 281–326.
<https://doi.org/10.1002/9780470500262.ch6>.
- [3] K. Shinozaki, H. Kuroki, X. Luo, H. Ariyoshi, M. Shirai, Effects of welding parameters on laser weldability of Inconel 718. Study of laser weldability of Ni-base, heat-resistant superalloys (1st Report), *Weld. Int.* 13 (1999) 945–951.
<https://doi.org/10.1080/09507119909452078>.
- [4] R.G. Thompson, Microfissuring of Alloy 718 in the Weld Heat-Affected Zone, *Jom.* 40 (1988) 44–48. <https://doi.org/10.1007/BF03258151>.
- [5] A. Yadollahi, N. Shamsaei, Additive manufacturing of fatigue resistant materials: Challenges and opportunities, *Int. J. Fatigue.* 98 (2017) 14–31.
<https://doi.org/10.1016/j.ijfatigue.2017.01.001>.
- [6] D. Liu, J.C. Lippold, J. Li, S.R. Rohklin, J. Vollbrecht, R. Grylls, Laser engineered net shape (LENS) technology for the repair of Ni-base superalloy turbine components, *Metall. Mater. Trans. A Phys. Metall. Mater. Sci.* 45 (2014) 4454–4469. <https://doi.org/10.1007/s11661-014-2397-8>.
- [7] Y. Ye, G. Zou, W. Long, Q. Jia, H. Bai, A. Wu, L. Liu, Diffusion brazing repair of IN738 superalloy with crack-like defect: microstructure and tensile properties at high temperatures, *Sci. Technol. Weld. Join.* 24 (2019) 52–62.
<https://doi.org/10.1080/13621718.2018.1477546>.
- [8] S. Sui, J. Chen, R. Zhang, X. Ming, F. Liu, X. Lin, The tensile deformation behavior of laser repaired Inconel 718 with a non-uniform microstructure, *Mater. Sci. Eng. A.* 688 (2017) 480–487.
<https://doi.org/10.1016/j.msea.2017.01.110>.
- [9] C. Guévenoux, S. Hallais, Y. Balit, A. Charles, E. Charkaluk, A. Constantinescu, Plastic strain localization induced by microstructural gradient in laser cladding repaired structures, *Theor. Appl. Fract. Mech.* 107 (2020)

102520. <https://doi.org/10.1016/j.tafmec.2020.102520>.
- [10] G.P. Dinda, A.K. Dasgupta, J. Mazumder, Texture control during laser deposition of nickel-based superalloy, *Scr. Mater.* 67 (2012) 503–506. <https://doi.org/https://doi.org/10.1016/j.scriptamat.2012.06.014>.
- [11] L.L. Parimi, G. Ravi, D. Clark, M.M. Attallah, Microstructural and texture development in direct laser fabricated IN718, *Mater. Charact.* 89 (2014) 102–111. <https://doi.org/10.1016/j.matchar.2013.12.012>.
- [12] E. Hosseini, V.A. Popovich, A review of mechanical properties of additively manufactured Inconel 718, *Addit. Manuf.* 30 (2019) 100877. <https://doi.org/10.1016/j.addma.2019.100877>.
- [13] M. Ni, C. Chen, X. Wang, P. Wang, R. Li, X. Zhang, K. Zhou, Anisotropic tensile behavior of in situ precipitation strengthened Inconel 718 fabricated by additive manufacturing, *Mater. Sci. Eng. A.* 701 (2017) 344–351. <https://doi.org/10.1016/j.msea.2017.06.098>.
- [14] E. Chlebus, K. Gruber, B. Kuźnicka, J. Kurzac, T. Kurzynowski, Effect of heat treatment on the microstructure and mechanical properties of Inconel 718 processed by selective laser melting, *Mater. Sci. Eng. A.* 639 (2015) 647–655. <https://doi.org/10.1016/j.msea.2015.05.035>.
- [15] D. Herzog, V. Seyda, E. Wycisk, C. Emmelmann, Additive manufacturing of metals, *Acta Mater.* 117 (2016) 371–392. <https://doi.org/https://doi.org/10.1016/j.actamat.2016.07.019>.
- [16] W.J. Sames, F.A. List, S. Pannala, R.R. Dehoff, S.S. Babu, The metallurgy and processing science of metal additive manufacturing, *Int. Mater. Rev.* 61 (2016) 315–360. <https://doi.org/10.1080/09506608.2015.1116649>.
- [17] L.N. Carter, M.M. Attallah, R.C. Reed, Laser Powder Bed Fabrication of Nickel-Base Superalloys: Influence of Parameters; Characterisation, Quantification and Mitigation of Cracking, *Superalloys 2012.* (2012). <https://doi.org/doi:10.1002/9781118516430.ch64>.
- [18] D. Deng, R.L. Peng, H. Brodin, J. Moverare, Microstructure and mechanical properties of Inconel 718 produced by selective laser melting: Sample orientation dependence and effects of post heat treatments, *Mater. Sci. Eng. A.*

-
- 713 (2018) 294–306. <https://doi.org/10.1016/j.msea.2017.12.043>.
- [19] Y. Liu, Y. Yang, D. Wang, A study on the residual stress during selective laser melting (SLM) of metallic powder, *Int. J. Adv. Manuf. Technol.* 87 (2016) 647–656. <https://doi.org/10.1007/s00170-016-8466-y>.
- [20] H.Y. Wan, Z.J. Zhou, C.P. Li, G.F. Chen, G.P. Zhang, Effect of scanning strategy on mechanical properties of selective laser melted Inconel 718, *Mater. Sci. Eng. A.* 753 (2019) 42–48.
<https://doi.org/https://doi.org/10.1016/j.msea.2019.03.007>.
- [21] X. Zhou, K. Li, D. Zhang, X. Liu, J. Ma, W. Liu, Z. Shen, Textures formed in a CoCrMo alloy by selective laser melting, *J. Alloys Compd.* 631 (2015) 153–164. <https://doi.org/https://doi.org/10.1016/j.jallcom.2015.01.096>.
- [22] T. DebRoy, H.L. Wei, J.S. Zuback, T. Mukherjee, J.W. Elmer, J.O. Milewski, A.M. Beese, A. Wilson-Heid, A. De, W. Zhang, Additive manufacturing of metallic components – Process, structure and properties, *Prog. Mater. Sci.* 92 (2018) 112–224. <https://doi.org/10.1016/j.pmatsci.2017.10.001>.
- [23] P.L. Blackwell, The mechanical and microstructural characteristics of laser-deposited IN718, *J. Mater. Process. Technol.* 170 (2005) 240–246.
<https://doi.org/https://doi.org/10.1016/j.jmatprotec.2005.05.005>.
- [24] N. Shamsaei, A. Yadollahi, L. Bian, S.M. Thompson, An overview of Direct Laser Deposition for additive manufacturing; Part II: Mechanical behavior, process parameter optimization and control, *Addit. Manuf.* 8 (2015) 12–35.
<https://doi.org/https://doi.org/10.1016/j.addma.2015.07.002>.
- [25] J. Kummailil, C. Sammarco, D. Skinner, C.A. Brown, K. Rong, Effect of Select LENS™ Processing Parameters on the Deposition of Ti-6Al-4V, *J. Manuf. Process.* 7 (2005) 42–50.
[https://doi.org/https://doi.org/10.1016/S1526-6125\(05\)70080-3](https://doi.org/https://doi.org/10.1016/S1526-6125(05)70080-3).
- [26] S.M. Kelly, S.L. Kampe, Microstructural evolution in laser-deposited multilayer Ti-6Al-4V builds: Part II. Thermal Modeling, *Metall. Mater. Trans. A Phys. Metall. Mater. Sci.* 35 A (2004) 1869–1879.
<https://doi.org/10.1007/s11661-004-0095-7>.
- [27] P.A. Kobryn, S.L. Semiatin, Microstructure and texture evolution during
-

- solidification processing of Ti–6Al–4V, *J. Mater. Process. Technol.* 135 (2003) 330–339. [https://doi.org/10.1016/S0924-0136\(02\)00865-8](https://doi.org/10.1016/S0924-0136(02)00865-8).
- [28] C. Qiu, G.A. Ravi, M.M. Attallah, Microstructural control during direct laser deposition of a β -titanium alloy, *Mater. Des.* 81 (2015) 21–30. <https://doi.org/10.1016/j.matdes.2015.05.031>.
- [29] G.A. Ravi, C. Qiu, M.M. Attallah, Microstructural control in a Ti-based alloy by changing laser processing mode and power during direct laser deposition, *Mater. Lett.* 179 (2016) 104–108. <https://doi.org/10.1016/j.matlet.2016.05.038>.
- [30] G.Q. Wu, C.L. Shi, W. Sha, A.X. Sha, H.R. Jiang, Microstructure and high cycle fatigue fracture surface of a Ti–5Al–5Mo–5V–1Cr–1Fe titanium alloy, *Mater. Sci. Eng. A.* 575 (2013) 111–118. <https://doi.org/10.1016/j.msea.2013.03.047>.
- [31] A. Bohlen, H. Freiße, M. Hunkel, F. Vollertsen, Additive manufacturing of tool steel by laser metal deposition, *Procedia CIRP.* 74 (2018) 192–195. <https://doi.org/10.1016/j.procir.2018.08.092>.
- [32] W. Huang, Y. Zhang, W. Dai, R. Long, Mechanical properties of 304 austenite stainless steel manufactured by laser metal deposition, *Mater. Sci. Eng. A.* 758 (2019) 60–70. <https://doi.org/10.1016/j.msea.2019.04.108>.
- [33] N.U. Rahman, L. Capuano, M.B. de Rooij, D.T.A. Matthews, A. Garcia-Junceda, M.A. Mekicha, L. Cordova, G. Walmag, M. Sinnaeve, G.R.B.E. Römer, Laser metal deposition of vanadium-rich high speed steel: Microstructural and high temperature wear characterization, *Surf. Coatings Technol.* 364 (2019) 115–126. <https://doi.org/10.1016/j.surfcoat.2019.02.044>.
- [34] M. Ma, Z. Wang, X. Zeng, Effect of energy input on microstructural evolution of direct laser fabricated IN718 alloy, *Mater. Charact.* 106 (2015) 420–427. <https://doi.org/10.1016/j.matchar.2015.06.027>.
- [35] T. Petrat, B. Graf, A. Gumenyuk, M. Rethmeier, Laser Metal Deposition as Repair Technology for a Gas Turbine Burner Made of Inconel 718, *Phys.*

- Procedia. 83 (2016) 761–768.
<https://doi.org/https://doi.org/10.1016/j.phpro.2016.08.078>.
- [36] X. Zhao, J. Chen, X. Lin, W. Huang, Study on microstructure and mechanical properties of laser rapid forming Inconel 718, *Mater. Sci. Eng. A.* 478 (2008) 119–124. <https://doi.org/https://doi.org/10.1016/j.msea.2007.05.079>.
- [37] L. Zhu, Z.F. Xu, P. Liu, Y.F. Gu, Effect of processing parameters on microstructure of laser solid forming Inconel 718 superalloy, *Opt. Laser Technol.* 98 (2018) 409–415.
<https://doi.org/https://doi.org/10.1016/j.optlastec.2017.08.027>.
- [38] P. Rangaswamy, M.L. Griffith, M.B. Prime, T.M. Holden, R.B. Rogge, J.M. Edwards, R.J. Sebring, Residual stresses in LENS® components using neutron diffraction and contour method, *Mater. Sci. Eng. A.* 399 (2005) 72–83.
<https://doi.org/https://doi.org/10.1016/j.msea.2005.02.019>.
- [39] J.L. Bennett, S.J. Wolff, G. Hyatt, K. Ehmann, J. Cao, Thermal effect on clad dimension for laser deposited Inconel 718, *J. Manuf. Process.* 28 (2017) 550–557. <https://doi.org/https://doi.org/10.1016/j.jmapro.2017.04.024>.
- [40] R.G. Ding, Z.W. Huang, H.Y. Li, I. Mitchell, G. Baxter, P. Bowen, Electron microscopy study of direct laser deposited IN718, *Mater. Charact.* 106 (2015) 324–337. <https://doi.org/10.1016/j.matchar.2015.06.017>.
- [41] F. Liu, X. Lin, H. Leng, J. Cao, Q. Liu, C. Huang, W. Huang, Microstructural changes in a laser solid forming Inconel 718 superalloy thin wall in the deposition direction, *Opt. Laser Technol.* 45 (2013) 330–335.
<https://doi.org/https://doi.org/10.1016/j.optlastec.2012.06.028>.
- [42] J. Kundin, L. Mushongera, H. Emmerich, Phase-field modeling of microstructure formation during rapid solidification in Inconel 718 superalloy, *Acta Mater.* 95 (2015) 343–356.
<https://doi.org/https://doi.org/10.1016/j.actamat.2015.05.052>.
- [43] F. Liu, X. Lin, G. Yang, M. Song, J. Chen, W. Huang, Microstructure and residual stress of laser rapid formed Inconel 718 nickel-base superalloy, *Opt. Laser Technol.* 43 (2011) 208–213.
<https://doi.org/https://doi.org/10.1016/j.optlastec.2010.06.015>.

- [44] F.A. España, V.K. Balla, S. Bose, A. Bandyopadhyay, Design and fabrication of CoCrMo alloy based novel structures for load bearing implants using laser engineered net shaping, *Mater. Sci. Eng. C*. 30 (2010) 50–57.
<https://doi.org/https://doi.org/10.1016/j.msec.2009.08.006>.
- [45] G.D. Ram, B.E. Stucker, A Feasibility Study of LENS® Deposition of CoCrMo Coating on a Titanium Substrate, *J. Manuf. Sci. Eng.* 130 (2008) 24503–24505. <http://dx.doi.org/10.1115/1.2898573>.
- [46] Y. Brif, M. Thomas, I. Todd, The use of high-entropy alloys in additive manufacturing, *Scr. Mater.* 99 (2015) 93–96.
<https://doi.org/https://doi.org/10.1016/j.scriptamat.2014.11.037>.
- [47] H. Dobbelstein, E.L. Gurevich, E.P. George, A. Ostendorf, G. Laplanche, Laser metal deposition of compositionally graded TiZrNbTa refractory high-entropy alloys using elemental powder blends, *Addit. Manuf.* 25 (2019) 252–262. <https://doi.org/https://doi.org/10.1016/j.addma.2018.10.042>.
- [48] H. Dobbelstein, M. Thiele, E.L. Gurevich, E.P. George, A. Ostendorf, Direct Metal Deposition of Refractory High Entropy Alloy MoNbTaW, *Phys. Procedia*. 83 (2016) 624–633.
<https://doi.org/https://doi.org/10.1016/j.phpro.2016.08.065>.
- [49] H. Dobbelstein, E.L. Gurevich, E.P. George, A. Ostendorf, G. Laplanche, Laser metal deposition of a refractory TiZrNbHfTa high-entropy alloy, *Addit. Manuf.* 24 (2018) 386–390.
<https://doi.org/https://doi.org/10.1016/j.addma.2018.10.008>.
- [50] J. Joseph, P. Hodgson, T. Jarvis, X. Wu, N. Stanford, D.M. Fabijanic, Effect of hot isostatic pressing on the microstructure and mechanical properties of additive manufactured AlxCoCrFeNi high entropy alloys, *Mater. Sci. Eng. A*. 733 (2018) 59–70. <https://doi.org/https://doi.org/10.1016/j.msea.2018.07.036>.
- [51] K.G. Prashanth, S. Scudino, T. Maity, J. Das, J. Eckert, Is the energy density a reliable parameter for materials synthesis by selective laser melting?, *Mater. Res. Lett.* 5 (2017) 386–390. <https://doi.org/10.1080/21663831.2017.1299808>.
- [52] W. Hofmeister, M. Wert, J. Smugeresky, J.A. Philliber, M. Griffith, M. Ensz, Investigation of solidification in the laser engineered net shaping (LENS) process, *JOM*. 51 (1999) 1–6.

- [53] E.L. Stevens, J. Toman, A.C. To, M. Chmielus, Variation of hardness, microstructure, and Laves phase distribution in direct laser deposited alloy 718 cuboids, *Mater. Des.* 119 (2017) 188–198.
<https://doi.org/https://doi.org/10.1016/j.matdes.2017.01.031>.
- [54] A.J. Pinkerton, Laser direct metal deposition: Theory and applications in manufacturing and maintenance, in: *Adv. Laser Mater. Process. Technol. Res. Appl.*, 2010. <https://doi.org/10.1533/9781845699819.6.461>.
- [55] T. DebRoy, H.L. Wei, J.S. Zuback, T. Mukherjee, J.W. Elmer, J.O. Milewski, A.M. Beese, A. Wilson-Heid, A. De, W. Zhang, Additive manufacturing of metallic components – Process, structure and properties, *Prog. Mater. Sci.* 92 (2018) 112–224. <https://doi.org/https://doi.org/10.1016/j.pmatsci.2017.10.001>.
- [56] J. Cao, F. Liu, X. Lin, C. Huang, J. Chen, W. Huang, Effect of overlap rate on recrystallization behaviors of Laser Solid Formed Inconel 718 superalloy, *Opt. Laser Technol.* 45 (2013) 228–235.
<https://doi.org/10.1016/j.optlastec.2012.06.043>.
- [57] Z.Y. Liu, C. Li, X.Y. Fang, Y.B. Guo, Energy Consumption in Additive Manufacturing of Metal Parts, in: *Procedia Manuf.*, 2018.
<https://doi.org/10.1016/j.promfg.2018.07.104>.
- [58] X. Gong, T. Anderson, K. Chou, Review on powder-based electron beam additive manufacturing Technology, *Manuf. Rev.* 1 (2014).
<https://doi.org/10.1051/mfreview/2014001>.
- [59] U. Scipioni Bertoli, A.J. Wolfer, M.J. Matthews, J.P.R. Delplanque, J.M. Schoenung, On the limitations of Volumetric Energy Density as a design parameter for Selective Laser Melting, *Mater. Des.* 113 (2017) 331–340.
<https://doi.org/10.1016/j.matdes.2016.10.037>.
- [60] G.D. Janaki Ram, A. Venugopal Reddy, K. Prasad Rao, G. Madhusudhan Reddy, Control of Laves phase in Inconel 718 GTA welds with current pulsing, *Sci. Technol. Weld. Join.* 9 (2004) 390–398.
<https://doi.org/10.1179/136217104225021788>.
- [61] J.T. Tharappel, J. Babu, Welding processes for Inconel 718- A brief review, *IOP Conf. Ser. Mater. Sci. Eng.* 330 (2018) 12082.
<https://doi.org/10.1088/1757-899x/330/1/012082>.

- [62] C.A. Huang, T.H. Wang, C.H. Lee, W.C. Han, A study of the heat-affected zone (HAZ) of an Inconel 718 sheet welded with electron-beam welding (EBW), *Mater. Sci. Eng. A*. 398 (2005) 275–281.
<https://doi.org/10.1016/j.msea.2005.03.029>.
- [63] J.K. Hong, J.H. Park, N.K. Park, I.S. Eom, M.B. Kim, C.Y. Kang, Microstructures and mechanical properties of Inconel 718 welds by CO₂ laser welding, *J. Mater. Process. Technol.* 201 (2008) 515–520.
<https://doi.org/10.1016/j.jmatprotec.2007.11.224>.
- [64] J. Cao, Y.F. Wang, X.G. Song, C. Li, J.C. Feng, Effects of post-weld heat treatment on microstructure and mechanical properties of TLP bonded Inconel718 superalloy, *Mater. Sci. Eng. A*. 590 (2014) 1–6.
<https://doi.org/10.1016/j.msea.2013.10.013>.
- [65] H. Qi, M. Azer, P. Singh, Adaptive toolpath deposition method for laser net shape manufacturing and repair of turbine compressor airfoils, *Int. J. Adv. Manuf. Technol.* 48 (2010) 121–131. <https://doi.org/10.1007/s00170-009-2265-7>.
- [66] L. Sexton, S. Lavin, G. Byrne, A. Kennedy, Laser cladding of aerospace materials, *J. Mater. Process. Technol.* 122 (2002) 63–68.
[https://doi.org/https://doi.org/10.1016/S0924-0136\(01\)01121-9](https://doi.org/https://doi.org/10.1016/S0924-0136(01)01121-9).
- [67] J. Song, Q. Deng, C. Chen, D. Hu, Y. Li, Rebuilding of metal components with laser cladding forming, *Appl. Surf. Sci.* 252 (2006) 7934–7940.
<https://doi.org/https://doi.org/10.1016/j.apsusc.2005.10.025>.
- [68] S. Sui, J. Chen, L. Ma, W. Fan, H. Tan, F. Liu, X. Lin, Microstructures and stress rupture properties of pulse laser repaired Inconel 718 superalloy after different heat treatments, *J. Alloys Compd.* 770 (2019) 125–135.
<https://doi.org/10.1016/j.jallcom.2018.08.063>.
- [69] L. Xue, J.-Y. Chen, M.U. Islam, J. Pritchard, D. Manente, S. Rush, Laser consolidation of Ni-base IN-738 superalloy for repairing gas turbine blades, *Int. Congr. Appl. Lasers Electro-Optics*. 2000 (2000) D30–D39.
<https://doi.org/10.2351/1.5059473>.
- [70] X. Zhang, T. Pan, W. Li, F. Liou, Experimental Characterization of a Direct Metal Deposited Cobalt-Based Alloy on Tool Steel for Component Repair,

- JOM. 71 (2019) 946–955. <https://doi.org/10.1007/s11837-018-3221-5>.
- [71] B. Rottwinkel, C. Nölke, S. Kaieler, V. Wesling, Crack Repair of Single Crystal Turbine Blades Using Laser Cladding Technology, *Procedia CIRP*. 22 (2014) 263–267. <https://doi.org/https://doi.org/10.1016/j.procir.2014.06.151>.
- [72] J. Bennett, D. Garcia, M. Kendrick, T. Hartman, G. Hyatt, K. Ehmann, F. You, J. Cao, Repairing Automotive Dies With Directed Energy Deposition: Industrial Application and Life Cycle Analysis, *J. Manuf. Sci. Eng.* 141 (2018) 21019. <http://dx.doi.org/10.1115/1.4042078>.
- [73] B. Graf, A. Gumenyuk, M. Rethmeier, Laser Metal Deposition as Repair Technology for Stainless Steel and Titanium Alloys, *Phys. Procedia*. 39 (2012) 376–381. <https://doi.org/https://doi.org/10.1016/j.phpro.2012.10.051>.
- [74] C.-M. Lin, Parameter Optimization of Laser Cladding Process and Resulting Microstructure for the Repair of Tenon on Steam Turbine Blade, 2015. <https://doi.org/10.1016/j.vacuum.2015.02.021>.
- [75] Q. Liu, Y. Wang, H. Zheng, K. Tang, H. Li, S. Gong, TC17 titanium alloy laser melting deposition repair process and properties, *Opt. Laser Technol.* 82 (2016) 1–9. <https://doi.org/https://doi.org/10.1016/j.optlastec.2016.02.013>.
- [76] R. Liu, Z. Wang, T. Sparks, F. Liou, C. Nedic, Stereo vision-based repair of metallic components, *Rapid Prototyp. J.* 23 (2017) 65–73. <https://doi.org/10.1108/RPJ-09-2015-0118>.
- [77] H. Paydas, A. Mertens, R. Carrus, J. Lecomte-Beckers, J. Tchoufang Tchoundjang, Laser cladding as repair technology for Ti–6Al–4V alloy: Influence of building strategy on microstructure and hardness, *Mater. Des.* 85 (2015) 497–510. <https://doi.org/https://doi.org/10.1016/j.matdes.2015.07.035>.
- [78] A.J. Pinkerton, W. Wang, L. Li, Component repair using laser direct metal deposition, *Proc. Inst. Mech. Eng. Part B J. Eng. Manuf.* 222 (2008) 827–836. <https://doi.org/10.1243/09544054JEM1008>.
- [79] M. Zenou, L. Grainger, Additive manufacturing of metallic materials, in: *Addit. Manuf. Mater. Process. Quantif. Appl.*, 2018. <https://doi.org/10.1016/B978-0-12-812155-9.00003-7>.
- [80] Q. Zhang, J. Zhang, Y. Zhuang, J. Lu, J. Yao, Hot Corrosion and Mechanical

- Performance of Repaired Inconel 718 Components via Laser Additive Manufacturing, *Materials* (Basel). 13 (2020) 2128.
<https://doi.org/10.3390/ma13092128>.
- [81] X. Zhang, W. Cui, W. Li, F. Liou, Effects of tool path in remanufacturing cylindrical components by laser metal deposition, *Int. J. Adv. Manuf. Technol.* (2019). <https://doi.org/10.1007/s00170-018-2786-z>.
- [82] A Review of: "SUPERALLOYS II" edited by CT. Sims, N.S. Stoloff, and W.C. Hagel A Wiley-Interscience Publication John Wiley & Sons, New York, NY 615 pages, hardcover, 1987 AU - WhITTENBERGER, J.D., *Mater. Manuf. Process.* 7 (1992) 463–468.
<https://doi.org/10.1080/10426919208947432>.
- [83] R.E. Smallman, R.J. Bishop, Chapter 8 - Strengthening and toughening, in: R.E. Smallman, R.J.B.T.-M.P.M. and M.E. (Sixth E. Bishop (Eds.)), Butterworth-Heinemann, Oxford, 1999: pp. 259–296.
<https://doi.org/https://doi.org/10.1016/B978-075064564-5/50008-2>.
- [84] E.O. Ezugwu, Z.M. Wang, A.R. Machado, The machinability of nickel-based alloys: A review, *J. Mater. Process. Technol.* (1998).
[https://doi.org/10.1016/S0924-0136\(98\)00314-8](https://doi.org/10.1016/S0924-0136(98)00314-8).
- [85] G.E. Dieter, *Mechanical metallurgy.*, McGraw-Hill, New York, 2011.
<https://doi.org/10.5962/bhl.title.35895>.
- [86] Repair Welding of Ni-base Alloys, in: *Weld. Metall. Weldability Nickel-Base Alloy.*, John Wiley & Sons, Inc., Hoboken, NJ, USA, 2009: pp. 281–326.
<https://doi.org/10.1002/9780470500262.ch6>.
- [87] G.W. Meetham, M.H. van de Voorde, *Materials for high temperature engineering applications.*, Berlin ; New York : Springer, c2000., 2000.
<http://ezproxy.deakin.edu.au/login?url=http://search.ebscohost.com/login.aspx?direct=true&db=cat00097a&AN=deakin.b1921134&authtype=sso&custid=deakin&site=eds-live&scope=site>.
- [88] K.N. Amato, S.M. Gaytan, L.E. Murr, E. Martinez, P.W. Shindo, J. Hernandez, S. Collins, F. Medina, Microstructures and mechanical behavior of Inconel 718 fabricated by selective laser melting, *Acta Mater.* 60 (2012) 2229–2239. <https://doi.org/https://doi.org/10.1016/j.actamat.2011.12.032>.

- [89] M. Ni, S. Liu, C. Chen, R. Li, X. Zhang, K. Zhou, Effect of heat treatment on the microstructural evolution of a precipitation-hardened superalloy produced by selective laser melting, *Mater. Sci. Eng. A*. 748 (2019) 275–285. <https://doi.org/https://doi.org/10.1016/j.msea.2019.01.109>.
- [90] C. Slama, C. Servant, G. Cizeron, Aging of the Inconel 718 alloy between 500 and 750 °C, *J. Mater. Res.* 12 (1997) 2298–2316. <https://doi.org/DOI:10.1557/JMR.1997.0306>.
- [91] M.L. Griffith, M.T. Ensz, J.D. Puskar, C. V Robino, J.A. Brooks, J.A. Philliber, J.E. Smugeresky, W.H. Hofmeister, Understanding the Microstructure and Properties of Components Fabricated by Laser Engineered Net Shaping (LENS), *MRS Proc.* 625 (2000) 9. <https://doi.org/DOI:10.1557/PROC-625-9>.
- [92] N.L. Richards, X. Huang, M.C. Chaturvedi, Heat affected zone cracking in cast inconel 718, *Mater. Charact.* 28 (1992) 179–187. [https://doi.org/https://doi.org/10.1016/1044-5803\(92\)90080-2](https://doi.org/https://doi.org/10.1016/1044-5803(92)90080-2).
- [93] H. Qi, M. Azer, A. Ritter, Studies of standard heat treatment effects on microstructure and mechanical properties of laser net shape manufactured INCONEL 718, *Metall. Mater. Trans. A Phys. Metall. Mater. Sci.* 40 (2009) 2410–2422. <https://doi.org/10.1007/s11661-009-9949-3>.
- [94] G.H. Cao, T.Y. Sun, C.H. Wang, X. Li, M. Liu, Z.X. Zhang, P.F. Hu, A.M. Russell, R. Schneider, D. Gerthsen, Z.J. Zhou, C.P. Li, G.F. Chen, Investigations of γ' , γ'' and δ precipitates in heat-treated Inconel 718 alloy fabricated by selective laser melting, *Mater. Charact.* 136 (2018) 398–406. <https://doi.org/https://doi.org/10.1016/j.matchar.2018.01.006>.
- [95] Y. Zhai, D.A. Lados, E.J. Brown, G.N. Vigilante, Understanding the microstructure and mechanical properties of Ti-6Al-4V and Inconel 718 alloys manufactured by Laser Engineered Net Shaping, *Addit. Manuf.* 27 (2019) 334–344. <https://doi.org/https://doi.org/10.1016/j.addma.2019.02.017>.
- [96] X. Gong, X. Wang, V. Cole, Z. Jones, K. Cooper, K. Chou, Characterization of Microstructure and Mechanical Property of Inconel 718 From Selective Laser Melting, (2015) V001T02A061. <http://dx.doi.org/10.1115/MSEC2015-9317>.

- [97] V.A. Popovich, E.V. Borisov, A.A. Popovich, V.S. Sufiiarov, D.V. Masaylo, L. Alzina, Functionally graded Inconel 718 processed by additive manufacturing: Crystallographic texture, anisotropy of microstructure and mechanical properties, *Mater. Des.* 114 (2017) 441–449.
<https://doi.org/10.1016/j.matdes.2016.10.075>.
- [98] D.H. Smith, J. Bicknell, L. Jorgensen, B.M. Patterson, N.L. Cordes, I. Tsukrov, M. Knezevic, Microstructure and mechanical behavior of direct metal laser sintered Inconel alloy 718, *Mater. Charact.* 113 (2016) 1–9.
<https://doi.org/https://doi.org/10.1016/j.matchar.2016.01.003>.
- [99] J. Strößner, M. Terock, U. Glatzel, Mechanical and Microstructural Investigation of Nickel-Based Superalloy IN718 Manufactured by Selective Laser Melting (SLM), *Adv. Eng. Mater.* 17 (2015) 1099–1105.
<https://doi.org/10.1002/adem.201500158>.
- [100] I. Taberero, A. Lamikiz, S. Martínez, E. Ukar, J. Figueras, Evaluation of the mechanical properties of Inconel 718 components built by laser cladding, *Int. J. Mach. Tools Manuf.* 51 (2011) 465–470.
<https://doi.org/https://doi.org/10.1016/j.ijmactools.2011.02.003>.
- [101] H. Xiao, S. Li, X. Han, J. Mazumder, L. Song, Laves phase control of Inconel 718 alloy using quasi-continuous-wave laser additive manufacturing, *Mater. Des.* 122 (2017) 330–339.
<https://doi.org/https://doi.org/10.1016/j.matdes.2017.03.004>.
- [102] D. Zhang, W. Niu, X. Cao, Z. Liu, Effect of standard heat treatment on the microstructure and mechanical properties of selective laser melting manufactured Inconel 718 superalloy, *Mater. Sci. Eng. A.* 644 (2015) 32–40.
<https://doi.org/10.1016/j.msea.2015.06.021>.
- [103] Y. Zhang, L. Yang, T. Chen, W. Zhang, X. Huang, J. Dai, Investigation on the optimized heat treatment procedure for laser fabricated IN718 alloy, *Opt. Laser Technol.* 97 (2017) 172–179.
<https://doi.org/https://doi.org/10.1016/j.optlastec.2017.06.027>.
- [104] L. Zhu, Z. Xu, Y. Gu, Effect of laser power on the microstructure and mechanical properties of heat treated Inconel 718 superalloy by laser solid forming, *J. Alloys Compd.* 746 (2018) 159–167.

- <https://doi.org/10.1016/j.jallcom.2018.02.268>.
- [105] K. Zhang, W. Liu, X. Shang, Research on the processing experiments of laser metal deposition shaping, *Opt. Laser Technol.* 39 (2007) 549–557.
<https://doi.org/https://doi.org/10.1016/j.optlastec.2005.10.009>.
- [106] D.D. Gu, W. Meiners, K. Wissenbach, R. Poprawe, Laser additive manufacturing of metallic components: materials, processes and mechanisms, *Int. Mater. Rev.* 57 (2012) 133–164.
<https://doi.org/10.1179/1743280411Y.0000000014>.
- [107] S.S. Babu, N. Raghavan, J. Raplee, S.J. Foster, C. Frederick, M. Haines, R. Dinwiddie, M.K. Kirka, A. Plotkowski, Y. Lee, R.R. Dehoff, Additive Manufacturing of Nickel Superalloys: Opportunities for Innovation and Challenges Related to Qualification, *Metall. Mater. Trans. A Phys. Metall. Mater. Sci.* 49 (2018) 3764–3780. <https://doi.org/10.1007/s11661-018-4702-4>.
- [108] M. Ni, S. Liu, C. Chen, R. Li, X. Zhang, K. Zhou, Effect of heat treatment on the microstructural evolution of a precipitation-hardened superalloy produced by selective laser melting, *Mater. Sci. Eng. A.* 748 (2019) 275–285.
<https://doi.org/10.1016/j.msea.2019.01.109>.
- [109] S. Sui, H. Tan, J. Chen, C. Zhong, Z. Li, W. Fan, A. Gasser, W. Huang, The influence of Laves phases on the room temperature tensile properties of Inconel 718 fabricated by powder feeding laser additive manufacturing, *Acta Mater.* 164 (2019) 413–427.
<https://doi.org/https://doi.org/10.1016/j.actamat.2018.10.032>.
- [110] S.S. Babu, N. Raghavan, J. Raplee, S.J. Foster, C. Frederick, M. Haines, R. Dinwiddie, M.K. Kirka, A. Plotkowski, Y. Lee, R.R. Dehoff, Additive Manufacturing of Nickel Superalloys : Opportunities for Innovation and Challenges Related to Qualification, *Metall. Mater. Trans. A.* 49 (2018) 3764–3780. <https://doi.org/10.1007/s11661-018-4702-4>.
- [111] O. Gokcekaya, T. Ishimoto, S. Hibino, J. Yasutomi, T. Narushima, T. Nakano, Unique crystallographic texture formation in Inconel 718 by laser powder bed fusion and its effect on mechanical anisotropy, *Acta Mater.* 212 (2021) 116876. <https://doi.org/10.1016/j.actamat.2021.116876>.
- [112] L. Zhu, Z. Xu, Y. Gu, Effect of laser power on the microstructure and

- mechanical properties of heat treated Inconel 718 superalloy by laser solid forming, *J. Alloys Compd.* 746 (2018) 159–167.
<https://doi.org/https://doi.org/10.1016/j.jallcom.2018.02.268>.
- [113] D. Deng, R.L. Peng, H. Brodin, J. Moverare, Microstructure and mechanical properties of Inconel 718 produced by selective laser melting: Sample orientation dependence and effects of post heat treatments, *Mater. Sci. Eng. A.* 713 (2018) 294–306. <https://doi.org/10.1016/j.msea.2017.12.043>.
- [114] F. Liu, X. Lin, G. Yang, M. Song, J. Chen, W. Huang, Recrystallization and its influence on microstructures and mechanical properties of laser solid formed nickel base superalloy Inconel 718, *Rare Met.* 30 (2011) 433–438.
<https://doi.org/10.1007/s12598-011-0319-0>.
- [115] T. Trosch, J. Strößner, R. Völkl, U. Glatzel, Microstructure and mechanical properties of selective laser melted Inconel 718 compared to forging and casting, *Mater. Lett.* 164 (2016) 428–431.
<https://doi.org/10.1016/j.matlet.2015.10.136>.
- [116] D. Deng, J. Moverare, R.L. Peng, H. Söderberg, Microstructure and anisotropic mechanical properties of EBM manufactured Inconel 718 and effects of post heat treatments, *Mater. Sci. Eng. A.* 693 (2017) 151–163.
<https://doi.org/10.1016/j.msea.2017.03.085>.
- [117] M.M. Kirka, K.A. Unocic, N. Raghavan, F. Medina, R.R. Dehoff, S.S. Babu, Microstructure Development in Electron Beam-Melted Inconel 718 and Associated Tensile Properties, *Jom.* 68 (2016) 1012–1020.
<https://doi.org/10.1007/s11837-016-1812-6>.
- [118] E.W. Hovig, A.S. Azar, F. Grytten, K. Sørby, E. Andreassen, Determination of anisotropic mechanical properties for materials processed by laser powder bed fusion, *Adv. Mater. Sci. Eng.* 2018 (2018).
<https://doi.org/10.1155/2018/7650303>.
- [119] M.M. Kirka, F. Medina, R. Dehoff, A. Okello, Mechanical behavior of post-processed Inconel 718 manufactured through the electron beam melting process, *Mater. Sci. Eng. A.* 680 (2017) 338–346.
<https://doi.org/10.1016/j.msea.2016.10.069>.
- [120] S.Y. Liu, H.Q. Li, C.X. Qin, R. Zong, X.Y. Fang, The effect of energy density

- on texture and mechanical anisotropy in selective laser melted Inconel 718, *Mater. Des.* 191 (2020). <https://doi.org/10.1016/j.matdes.2020.108642>.
- [121] P.S. De, *Monotonic and Cyclic Deformation Behaviour of Two Different Automotive Grade Sheet Steels*, Jadavpur University, 2016.
- [122] S. Sui, J. Chen, E. Fan, H. Yang, X. Lin, W. Huang, The influence of Laves phases on the high-cycle fatigue behavior of laser additive manufactured Inconel 718, *Mater. Sci. Eng. A.* 695 (2017) 6–13. <https://doi.org/10.1016/j.msea.2017.03.098>.
- [123] L. Xiao, D.L. Chen, M.C. Chaturvedi, Effect of boron on the low-cycle fatigue behavior and deformation structure of INCONEL 718 at 650 °C, *Metall. Mater. Trans. A Phys. Metall. Mater. Sci.* 35 A (2004) 3477–3487. <https://doi.org/10.1007/s11661-004-0185-6>.
- [124] R.M. Karimbaev, Y.S. Pyun, A. Amanov, Fatigue life extension of additively manufactured Nickel-base 718 alloy by nanostructured surface, *Mater. Sci. Eng. A.* 831 (2022) 142041. <https://doi.org/10.1016/j.msea.2021.142041>.
- [125] R. Konečná, G. Nicoletto, L. Kunz, A. Bača, Microstructure and directional fatigue behavior of Inconel 718 produced by selective laser melting, *Procedia Struct. Integr.* 2 (2016) 2381–2388. <https://doi.org/10.1016/j.prostr.2016.06.298>.
- [126] E. Salvati, A.J.G. Lunt, C.P. Heason, G.J. Baxter, A.M. Korsunsky, An analysis of fatigue failure mechanisms in an additively manufactured and shot peened IN 718 nickel superalloy, *Mater. Des.* 191 (2020) 108605. <https://doi.org/10.1016/j.matdes.2020.108605>.
- [127] D.T. Ardi, L. Guowei, N. Maharjan, B. Mutiargo, S.H. Leng, R. Srinivasan, Effects of post-processing route on fatigue performance of laser powder bed fusion Inconel 718, *Addit. Manuf.* 36 (2020) 101442. <https://doi.org/10.1016/j.addma.2020.101442>.
- [128] A.J. Sterling, B. Torries, N. Shamsaei, S.M. Thompson, D.W. Seely, Fatigue behavior and failure mechanisms of direct laser deposited Ti-6Al-4V, *Mater. Sci. Eng. A.* (2016). <https://doi.org/10.1016/j.msea.2015.12.026>.
- [129] A. Yadollahi, N. Shamsaei, S.M. Thompson, A. Elwany, L. Bian, Effects of

- building orientation and heat treatment on fatigue behavior of selective laser melted 17-4 PH stainless steel, *Int. J. Fatigue*. (2017).
<https://doi.org/10.1016/j.ijfatigue.2016.03.014>.
- [130] S. Gribbin, S. Ghorbanpour, N.C. Ferreri, J. Bicknell, I. Tsukrov, M. Knezevic, Role of grain structure, grain boundaries, crystallographic texture, precipitates, and porosity on fatigue behavior of Inconel 718 at room and elevated temperatures, *Mater. Charact.* 149 (2019) 184–197.
<https://doi.org/10.1016/j.matchar.2019.01.028>.
- [131] A.S. Johnson, S. Shao, N. Shamsaei, S.M. Thompson, L. Bian, Microstructure, Fatigue Behavior, and Failure Mechanisms of Direct Laser-Deposited Inconel 718, *JOM*. 69 (2017) 597–603. <https://doi.org/10.1007/s11837-016-2225-2>.
- [132] E. Amsterdam, Evaluation of the microstructure and mechanical properties of laser additive manufactured gas turbine alloys Ti-6Al-4V and, RTO AVT-163 Spec. Meet. (2009) 1–25.
- [133] A.R. Balachandramurthi, J. Moverare, N. Dixit, R. Pederson, Influence of defects and as-built surface roughness on fatigue properties of additively manufactured Alloy 718, *Mater. Sci. Eng. A*. 735 (2018) 463–474.
<https://doi.org/10.1016/j.msea.2018.08.072>.
- [134] V.A. Popovich, E. V Borisov, V. Heurtebise, T. Riemslog, A.A. Popovich, V.S. Sufiiarov, Creep and Thermomechanical Fatigue of Functionally Graded Inconel 718 Produced by Additive Manufacturing BT - TMS 2018 147th Annual Meeting & Exhibition Supplemental Proceedings, in: T.M. & Materials Society Metals (Ed.), Springer International Publishing, Cham, 2018: pp. 85–97.
- [135] N. Kawagoishi, Q. Chen, H. Nisitani, Fatigue strength of Inconel 718 at elevated temperatures, *Fatigue Fract. Eng. Mater. Struct.* 23 (2000) 209–216.
<https://doi.org/10.1046/j.1460-2695.2000.00263.x>.
- [136] Y. Ono, T. Yuri, N. Nagashima, H. Sumiyoshi, T. Ogata, N. Nagao, High-cycle fatigue properties of Alloy718 base metal and electron beam welded joint, *Phys. Procedia*. 67 (2015) 1028–1035.
<https://doi.org/10.1016/j.phpro.2015.06.196>.
- [137] K. Sivaprasad, S. Ganesh Sundara Raman, Influence of weld cooling rate on

- microstructure and mechanical properties of alloy 718 weldments, *Metall. Mater. Trans. A Phys. Metall. Mater. Sci.* 39 (2008) 2115–2127. <https://doi.org/10.1007/s11661-008-9553-y>.
- [138] K. Sivaprasad, S.G.S. Raman, Influence of magnetic arc oscillation and current pulsing on fatigue behavior of alloy 718 TIG weldments, *Mater. Sci. Eng. A.* 448 (2007) 120–127. <https://doi.org/10.1016/j.msea.2006.10.048>.
- [139] N.D. Alexopoulos, N. Argyriou, V. Stergiou, S.K. Kourkoulis, Fatigue behavior of Inconel 718 TIG welds, *J. Mater. Eng. Perform.* 23 (2014) 2973–2983. <https://doi.org/10.1007/s11665-014-1028-2>.
- [140] M. Gäumann, C. Bezençon, P. Canalis, W. Kurz, Single-crystal laser deposition of superalloys: processing–microstructure maps, *Acta Mater.* 49 (2001) 1051–1062. [https://doi.org/https://doi.org/10.1016/S1359-6454\(00\)00367-0](https://doi.org/https://doi.org/10.1016/S1359-6454(00)00367-0).
- [141] Y. Lee, M. Nordin, S.S. Babu, D.F. Farson, Effect of fluid convection on dendrite arm spacing in laser deposition, *Metall. Mater. Trans. B Process Metall. Mater. Process. Sci.* 45 (2014) 1520–1529. <https://doi.org/10.1007/s11663-014-0054-7>.
- [142] K. V Yang, Y. Shi, F. Palm, X. Wu, P. Rometsch, Columnar to equiaxed transition in Al-Mg(-Sc)-Zr alloys produced by selective laser melting, *Scr. Mater.* 145 (2018) 113–117. <https://doi.org/https://doi.org/10.1016/j.scriptamat.2017.10.021>.
- [143] A. De, T. DebRoy, A perspective on residual stresses in welding, *Sci. Technol. Weld. Join.* 16 (2011) 204–208. <https://doi.org/10.1179/136217111X12978476537783>.
- [144] K. V Yang, Y. Shi, F. Palm, X. Wu, P. Rometsch, Columnar to equiaxed transition in Al-Mg(-Sc)-Zr alloys produced by selective laser melting, *Scr. Mater.* 145 (2018) 113–117. <https://doi.org/10.1016/j.scriptamat.2017.10.021>.
- [145] M. Gäumann, R. Trivedi, W. Kurz, Nucleation ahead of the advancing interface in directional solidification, *Mater. Sci. Eng. A.* 226–228 (1997) 763–769. [https://doi.org/10.1016/s0921-5093\(97\)80081-0](https://doi.org/10.1016/s0921-5093(97)80081-0).
- [146] B.S. Murty, S.A. Kori, M. Chakraborty, Grain refinement of aluminium and

-
- its alloys by heterogeneous nucleation and alloying, *Int. Mater. Rev.* 47 (2002) 3–29. <https://doi.org/10.1179/095066001225001049>.
- [147] J.P. Dennison, GRAIN REFINEMENT BY THE INTRODUCTION TO THE MELT OF OXIDE PARTICLES PRE-DISPERSED IN METAL STRIP., in: 1983: pp. 139–150. <https://www.scopus.com/inward/record.uri?eid=2-s2.0-0020869599&partnerID=40&md5=20d23e75a9562587d6de81ed95a8a8f4>.
- [148] F. Wang, J. Zhang, T. Huang, L. Liu, H. Fu, Preparation of Inoculants Used in Superalloy and Analysis of the Atomic Matching Models, *J. Mater. Sci. Technol.* 29 (2013) 387–392. <https://doi.org/https://doi.org/10.1016/j.jmst.2013.02.007>.
- [149] M. Zhang, P. Kelly, M. Easton, J. Taylor, Crystallographic study of grain refinement in aluminum alloys using the edge-to-edge matching model, *Acta Mater.* 53 (2005) 1427–1438. <https://doi.org/10.1016/j.actamat.2004.11.037>.
- [150] L. Liu, T. Huang, Y. Xiong, A. Yang, Z. Zhao, R. Zhang, J. Li, Grain refinement of superalloy K4169 by addition of refiners: cast structure and refinement mechanisms, *Mater. Sci. Eng. A.* 394 (2005) 1–8. <https://doi.org/https://doi.org/10.1016/j.msea.2004.10.005>.
- [151] BRUCE L. BRAMFITT, The Effect of Carbide and Nitride Additions on the Heterogeneous Nucleation Behavior of Liquid Iron, *Metall. Trans.* 1 (1970) 1987–1995.
- [152] M.-X. Zhang, P.M. Kelly, Edge-to-edge matching model for predicting orientation relationships and habit planes—the improvements, *Scr. Mater.* 52 (2005) 963–968. <https://doi.org/10.1016/j.scriptamat.2005.01.040>.
- [153] M.X. Zhang, P.M. Kelly, Edge-to-edge matching and its applications: Part II. Application to Mg-Al, Mg-Y and Mg-Mn alloys, *Acta Mater.* 53 (2005) 1085–1096. <https://doi.org/10.1016/j.actamat.2004.11.005>.
- [154] I.-T. Ho, Y.-T. Chen, A.-C. Yeh, C.-P. Chen, K.-K. Jen, Microstructure evolution induced by inoculants during the selective laser melting of IN718, *Addit. Manuf.* 21 (2018) 465–471. <https://doi.org/https://doi.org/10.1016/j.addma.2018.02.018>.
- [155] J.H. Martin, B.D. Yahata, J.M. Hundley, J.A. Mayer, T.A. Schaedler, T.M.
-

-
- Pollock, 3D printing of high-strength aluminium alloys, *Nature*. 549 (2017) 365–369. <https://doi.org/10.1038/nature23894>.
- [156] B. AlMangour, Y.K. Kim, D. Grzesiak, K.A. Lee, Novel TiB₂-reinforced 316L stainless steel nanocomposites with excellent room- and high-temperature yield strength developed by additive manufacturing, *Compos. Part B Eng.* 156 (2019) 51–63. <https://doi.org/10.1016/j.compositesb.2018.07.050>.
- [157] B. AlMangour, D. Grzesiak, J.M. Yang, Rapid fabrication of bulk-form TiB₂/316L stainless steel nanocomposites with novel reinforcement architecture and improved performance by selective laser melting, *J. Alloys Compd.* 680 (2016) 480–493. <https://doi.org/10.1016/j.jallcom.2016.04.156>.
- [158] B. AlMangour, D. Grzesiak, J.M. Yang, Selective laser melting of TiB₂/316L stainless steel composites: The roles of powder preparation and hot isostatic pressing post-treatment, *Powder Technol.* 309 (2017) 37–48. <https://doi.org/10.1016/j.powtec.2016.12.073>.
- [159] X.P. Li, G. Ji, Z. Chen, A. Addad, Y. Wu, H.W. Wang, J. Vleugels, J. Van Humbeeck, J.P. Kruth, Selective laser melting of nano-TiB₂decorated AlSi10Mg alloy with high fracture strength and ductility, *Acta Mater.* 129 (2017) 183–193. <https://doi.org/10.1016/j.actamat.2017.02.062>.
- [160] L. Xi, P. Wang, K.G. Prashanth, H. Li, H. V. Prykhodko, S. Scudino, I. Kaban, Effect of TiB₂ particles on microstructure and crystallographic texture of Al-12Si fabricated by selective laser melting, *J. Alloys Compd.* 786 (2019) 551–556. <https://doi.org/10.1016/j.jallcom.2019.01.327>.
- [161] D. Gu, Y.-C. Hagedorn, W. Meiners, K. Wissenbach, R. Poprawe, Nanocrystalline TiC reinforced Ti matrix bulk-form nanocomposites by Selective Laser Melting (SLM): Densification, growth mechanism and wear behavior, *Compos. Sci. Technol.* 71 (2011) 1612–1620. <https://doi.org/https://doi.org/10.1016/j.compscitech.2011.07.010>.
- [162] Q. Jia, D. Gu, Selective laser melting additive manufacturing of TiC/Inconel 718 bulk-form nanocomposites: Densification, microstructure, and performance, *J. Mater. Res.* 29 (2014) 1960–1969. <https://doi.org/10.1557/jmr.2014.130>.
-

- [163] X. Yao, S.K. Moon, B.Y. Lee, G. Bi, Effects of heat treatment on microstructures and tensile properties of IN718/TiC nanocomposite fabricated by selective laser melting, *Int. J. Precis. Eng. Manuf.* 18 (2017) 1693–1701. <https://doi.org/10.1007/s12541-017-0197-y>.
- [164] L. Chen, Y. Sun, L. Li, Y. Ren, X. Ren, In situ TiC/Inconel 625 nanocomposites fabricated by selective laser melting: Densification behavior, microstructure evolution, and wear properties, *Appl. Surf. Sci.* 518 (2020) 145981. <https://doi.org/10.1016/j.apsusc.2020.145981>.
- [165] D. Gu, H. Zhang, D. Dai, M. Xia, C. Hong, R. Poprawe, Laser additive manufacturing of nano-TiC reinforced Ni-based nanocomposites with tailored microstructure and performance, *Compos. Part B Eng.* 163 (2019) 585–597. <https://doi.org/10.1016/j.compositesb.2018.12.146>.
- [166] J.M. Wilson, Y.C. Shin, Microstructure and wear properties of laser-deposited functionally graded Inconel 690 reinforced with TiC, *Surf. Coatings Technol.* 207 (2012) 517–522. <https://doi.org/10.1016/j.surfcoat.2012.07.058>.
- [167] B. Zhang, G. Bi, P. Wang, J. Bai, Y. Chew, M.S. Nai, Microstructure and mechanical properties of Inconel 625/nano-TiB₂ composite fabricated by LAAM, *Mater. Des.* 111 (2016) 70–79. <https://doi.org/10.1016/j.matdes.2016.08.078>.
- [168] B. Li, B. Qian, Y. Xu, Z. Liu, F. Xuan, Fine-structured CoCrFeNiMn high-entropy alloy matrix composite with 12 wt% TiN particle reinforcements via selective laser melting assisted additive manufacturing, *Mater. Lett.* 252 (2019) 88–91. <https://doi.org/10.1016/j.matlet.2019.05.108>.
- [169] I.T. Ho, T.H. Hsu, Y.J. Chang, C.W. Li, K.C. Chang, S. Tin, K. Kakehi, A.C. Yeh, Effects of CoAl₂O₄ inoculants on microstructure and mechanical properties of IN718 processed by selective laser melting, *Addit. Manuf.* 35 (2020) 101328. <https://doi.org/10.1016/j.addma.2020.101328>.
- [170] Q.B. Nguyen, M. Gupta, Increasing significantly the failure strain and work of fracture of solidification processed AZ31B using nano-Al₂O₃ particulates, *J. Alloys Compd.* 459 (2008) 244–250. <https://doi.org/10.1016/j.jallcom.2007.05.038>.
- [171] J.R. Kennedy, A.E. Davis, A.E. Caballero, S. Williams, E.J. Pickering, P.B.

- Prangnell, The potential for grain refinement of Wire-Arc Additive Manufactured (WAAM) Ti-6Al-4V by ZrN and TiN inoculation, *Addit. Manuf.* 40 (2021) 101928. <https://doi.org/10.1016/j.addma.2021.101928>.
- [172] S. Holland, X. Wang, J. Chen, W. Cai, F. Yan, L. Li, Multiscale characterization of microstructures and mechanical properties of Inconel 718 fabricated by selective laser melting, *J. Alloys Compd.* 784 (2019) 182–194. <https://doi.org/10.1016/j.jallcom.2018.12.380>.
- [173] W. Yang, P. Qu, L. Liu, Z. Jie, T. Huang, F. Wang, J. Zhang, Nucleation Crystallography of Ni Grains on CrFeNb Inoculants Investigated by Edge-to-Edge Matching Model in an IN718 Superalloy, *Adv. Eng. Mater.* 20 (2018) 1700568. <https://doi.org/10.1002/adem.201700568>.
- [174] Y. Xiong, J. Du, X. Wei, A. Yang, L. Liu, D. Zeng, Grain refinement of superalloy IN718C by the addition of inoculants, *Metall. Mater. Trans. A Phys. Metall. Mater. Sci.* 35 A (2004) 2111–2114. <https://doi.org/10.1007/s11661-004-0159-8>.
- [175] T. Zhai, Y.G. Xu, J.W. Martin, A.J. Wilkinson, G.A.D. Briggs, Self-aligning four-point bend testing rig and sample geometry effect in four-point bend fatigue, *Int. J. Fatigue.* 21 (1999) 889–894. [https://doi.org/10.1016/S0142-1123\(99\)00084-5](https://doi.org/10.1016/S0142-1123(99)00084-5).
- [176] ASTM, Standard Practice for Conducting Force Controlled Constant Amplitude Axial Fatigue Tests of Metallic Materials, *Test.* 03 (2002) 4–8. <https://doi.org/10.1520/E0466-15.2>.
- [177] M.M. Attallah, R. Jennings, X. Wang, L.N. Carter, Additive manufacturing of Ni-based superalloys: The outstanding issues, *MRS Bull.* 41 (2016) 758–764. <https://doi.org/DOI:10.1557/mrs.2016.211>.
- [178] S. Bose, S.F. Robertson, A. Bandyopadhyay, Surface modification of biomaterials and biomedical devices using additive manufacturing, *Acta Biomater.* 66 (2018) 6–22. <https://doi.org/10.1016/j.actbio.2017.11.003>.
- [179] K. Feng, Y. Chen, P. Deng, Y. Li, H. Zhao, F. Lu, R. Li, J. Huang, Z. Li, Improved high-temperature hardness and wear resistance of Inconel 625 coatings fabricated by laser cladding, *J. Mater. Process. Technol.* 243 (2017) 82–91. <https://doi.org/10.1016/j.jmatprotec.2016.12.001>.

- [180] C.J. Liang, C.L. Wang, K.X. Zhang, M.L. Liang, Y.G. Xie, W.J. Liu, J.J. Yang, S.F. Zhou, Nucleation and strengthening mechanism of laser cladding aluminum alloy by Ni-Cr-B-Si alloy powder based on rare earth control, *J. Mater. Process. Technol.* 294 (2021) 117145. <https://doi.org/10.1016/j.jmatprotec.2021.117145>.
- [181] M.M. Alam, Z. Barsoum, P. Jonsén, H.Å. Häggblad, A. Kaplan, The effects of surface topography and lack of fusion on the fatigue strength of laser hybrid welds, *ICALEO 2009 - 28th Int. Congr. Appl. Lasers Electro-Optics, Congr. Proc.* 102 (2009) 38–46. <https://doi.org/10.2351/1.5061586>.
- [182] F.G. Al-Abtah, E. Mahdi, S. Gowid, The use of composite to eliminate the effect of welding on the bending behavior of metallic pipes, *Compos. Struct.* 235 (2020) 111793. <https://doi.org/10.1016/j.compstruct.2019.111793>.
- [183] G. Ziółkowski, K. Gruber, E. Tokarczyk, R. Roszak, M. Ziegenhorn, X-ray Computed Tomography for the ex-situ mechanical testing and simulation of additively manufactured IN718 samples, *Addit. Manuf.* 45 (2021) 102070. <https://doi.org/10.1016/j.addma.2021.102070>.
- [184] W. Tillmann, C. Schaak, J. Nellesen, M. Schaper, M.E. Aydinöz, K.P. Hoyer, Hot isostatic pressing of IN718 components manufactured by selective laser melting, *Addit. Manuf.* 13 (2017) 93–102. <https://doi.org/10.1016/j.addma.2016.11.006>.
- [185] D.H. Smith, J. Bicknell, L. Jorgensen, B.M. Patterson, N.L. Cordes, I. Tsukrov, M. Knezevic, Microstructure and mechanical behavior of direct metal laser sintered Inconel alloy 718, *Mater. Charact.* 113 (2016) 1–9. <https://doi.org/10.1016/j.matchar.2016.01.003>.
- [186] C. Bezençon, M. Gäumann, Columnar to equiaxed transition in solidification processing AU - Kurz, W., *Sci. Technol. Adv. Mater.* 2 (2001) 185–191. [https://doi.org/10.1016/S1468-6996\(01\)00047-X](https://doi.org/10.1016/S1468-6996(01)00047-X).
- [187] P. Nie, O.A. Ojo, Z. Li, Numerical modeling of microstructure evolution during laser additive manufacturing of a nickel-based superalloy, *Acta Mater.* 77 (2014) 85–95. <https://doi.org/10.1016/j.actamat.2014.05.039>.
- [188] Y. Li, K. Chen, R.L. Narayan, U. Ramamurty, Y. Wang, J. Long, N. Tamura, X. Zhou, Multi-scale microstructural investigation of a laser 3D printed Ni-

- based superalloy, *Addit. Manuf.* 34 (2020) 101220.
<https://doi.org/10.1016/j.addma.2020.101220>.
- [189] Y. Chen, K. Zhang, J. Huang, S.R.E. Hosseini, Z. Li, Characterization of heat affected zone liquation cracking in laser additive manufacturing of Inconel 718, *Mater. Des.* 90 (2016) 586–594.
<https://doi.org/10.1016/j.matdes.2015.10.155>.
- [190] K.R. Vishwakarma, N.L. Richards, M.C. Chaturvedi, Microstructural analysis of fusion and heat affected zones in electron beam welded ALLVAC® 718PLUS™ superalloy, *Mater. Sci. Eng. A.* 480 (2008) 517–528.
<https://doi.org/10.1016/j.msea.2007.08.002>.
- [191] C. Radhakrishna, K. Prasad Rao, The formation and control of Laves phase in superalloy 718 welds, *J. Mater. Sci.* 32 (1997) 1977–1984.
<https://doi.org/10.1023/A:1018541915113>.
- [192] G.D. Janaki Ram, A. Venugopal Reddy, K. Prasad Rao, G.M. Reddy, J.K. Sarin Sundar, Microstructure and tensile properties of Inconel 718 pulsed Nd-YAG laser welds, *J. Mater. Process. Technol.* 167 (2005) 73–82.
<https://doi.org/10.1016/j.jmatprotec.2004.09.081>.
- [193] M. Ma, Z. Wang, X. Zeng, Effect of energy input on microstructural evolution of direct laser fabricated IN718 alloy, *Mater. Charact.* 106 (2015) 420–427.
<https://doi.org/https://doi.org/10.1016/j.matchar.2015.06.027>.
- [194] A. Segerstark, J. Andersson, L.-E. Svensson, O. Ojo, Microstructural characterization of laser metal powder deposited Alloy 718, *Mater. Charact.* 142 (2018) 550–559.
<https://doi.org/https://doi.org/10.1016/j.matchar.2018.06.020>.
- [195] C. Zhong, A. Gasser, J. Kittel, K. Wissenbach, R. Poprawe, Improvement of material performance of Inconel 718 formed by high deposition-rate laser metal deposition, *Mater. Des.* 98 (2016) 128–134.
<https://doi.org/https://doi.org/10.1016/j.matdes.2016.03.006>.
- [196] J.H. Park, G.B. Bang, K.A. Lee, Y. Son, Y.H. Song, B.S. Lee, W.R. Kim, H.G. Kim, Effect of Preheating Temperature on Microstructural and Mechanical Properties of Inconel 718 Fabricated by Selective Laser Melting, *Met. Mater. Int.* (2022). <https://doi.org/10.1007/s12540-022-01169-w>.

- [197] E.M. Fayed, M. Saadati, D. Shahriari, V. Brailovski, M. Jahazi, M. Medraj, Effect of homogenization and solution treatments time on the elevated-temperature mechanical behavior of Inconel 718 fabricated by laser powder bed fusion, *Sci. Rep.* 11 (2021) 1–17. <https://doi.org/10.1038/s41598-021-81618-5>.
- [198] A. Segerstark, J. Andersson, L.E. Svensson, O. Ojo, Microstructural characterization of laser metal powder deposited Alloy 718, *Mater. Charact.* 142 (2018) 550–559. <https://doi.org/10.1016/j.matchar.2018.06.020>.
- [199] R.G. Ding, Z.W. Huang, H.Y. Li, I. Mitchell, G. Baxter, P. Bowen, Electron microscopy study of direct laser deposited IN718, *Mater. Charact.* 106 (2015) 324–337. <https://doi.org/10.1016/j.matchar.2015.06.017>.
- [200] S. Baskutis, J. Baskutiene, R. Bendikiene, A. Ciuplys, Effect of weld parameters on mechanical properties and tensile behavior of tungsten inert gas welded AW6082-T6 aluminium alloy, *J. Mech. Sci. Technol.* 33 (2019) 765–772. <https://doi.org/10.1007/s12206-019-0131-6>.
- [201] N.E. Ipek, F. Elaldi, Analysis of welding groove angle and geometry on strength of armor steel, *Mater. Manuf. Process.* 27 (2012) 1437–1441. <https://doi.org/10.1080/10426914.2012.709343>.
- [202] K. Devendranath Ramkumar, R. Jagat Sai, V. Santhosh Reddy, S. Gundla, T. Harsha Mohan, V. Saxena, N. Arivazhagan, Effect of filler wires and direct ageing on the microstructure and mechanical properties in the multi-pass welding of Inconel 718, *J. Manuf. Process.* 18 (2015) 23–45. <https://doi.org/10.1016/j.jmapro.2015.01.001>.
- [203] R. Cortés, E.R. Barragán, V.H. López, R.R. Ambriz, D. Jaramillo, Mechanical properties of Inconel 718 welds performed by gas tungsten arc welding, *Int. J. Adv. Manuf. Technol.* 94 (2018) 3949–3961. <https://doi.org/10.1007/s00170-017-1128-x>.
- [204] C. Jiang, Z.-K. Liu, Computational investigation of constitutional liquation in Al–Cu alloys, *Acta Mater.* 51 (2003) 4447–4459. [https://doi.org/10.1016/S1359-6454\(03\)00280-5](https://doi.org/10.1016/S1359-6454(03)00280-5).
- [205] B. Radhakrishnan, R.G. Thompson, A phase diagram approach to study liquation cracking in alloy 718, *Metall. Trans. A.* 22 (1991) 887–902.

<https://doi.org/10.1007/BF02658999>.

- [206] R. Nakkalil, N.L. Richards, M.C. Chaturvedi, The influence of solidification mode on heat affected zone microfissuring in a nickel-iron base superalloy, *Acta Metall. Mater.* 41 (1993) 3381–3392. [https://doi.org/10.1016/0956-7151\(93\)90218-H](https://doi.org/10.1016/0956-7151(93)90218-H).
- [207] R. Vincent, Precipitation around welds in the nickel-base superalloy, Inconel 718, *Acta Metall.* 33 (1985) 1205–1216. [https://doi.org/10.1016/0001-6160\(85\)90231-7](https://doi.org/10.1016/0001-6160(85)90231-7).
- [208] S. Benhadad, N.L. Richards, M.C. Chaturvedi, The influence of minor elements on the weldability of an INCONEL 718-type superalloy, *Metall. Mater. Trans. A Phys. Metall. Mater. Sci.* 33 (2002) 2005–2017. <https://doi.org/10.1007/s11661-002-0033-5>.
- [209] L.O. Osoba, O.A. Ojo, Influence of laser welding heat input on HAZ cracking in newly developed Haynes 282 superalloy, *Mater. Sci. Technol.* 28 (2012) 431–436. <https://doi.org/10.1179/1743284711Y.0000000078>.
- [210] A.R. Balachandramurthi, J. Moverare, N. Dixit, D. Deng, R. Pederson, Microstructural influence on fatigue crack propagation during high cycle fatigue testing of additively manufactured Alloy 718, *Mater. Charact.* 149 (2019) 82–94. <https://doi.org/10.1016/j.matchar.2019.01.018>.
- [211] V.A. Popovich, E. V Borisov, A.A. Popovich, V.S. Sufiiarov, D. V Masaylo, L. Alzina, Impact of heat treatment on mechanical behaviour of Inconel 718 processed with tailored microstructure by selective laser melting, *Mater. Des.* 131 (2017) 12–22. <https://doi.org/https://doi.org/10.1016/j.matdes.2017.05.065>.
- [212] D.T. Ardi, L. Guowei, N. Maharjan, B. Mutiaro, S.H. Leng, R. Srinivasan, Effects of post-processing route on fatigue performance of laser powder bed fusion Inconel 718, *Addit. Manuf.* 36 (2020) 101442. <https://doi.org/10.1016/j.addma.2020.101442>.
- [213] A.R. Balachandramurthi, J. Moverare, N. Dixit, D. Deng, R. Pederson, Microstructural influence on fatigue crack propagation during high cycle fatigue testing of additively manufactured Alloy 718, *Mater. Charact.* 149 (2019) 82–94. <https://doi.org/10.1016/j.matchar.2019.01.018>.

- [214] H.L. Wei, J. Mazumder, T. DebRoy, Evolution of solidification texture during additive manufacturing, *Sci. Rep.* 5 (2015) 16446.
<https://doi.org/10.1038/srep16446>.
- [215] D.D. Krueger, S.D. Antolovich, R.H. Van Stone, Effects of grain size and precipitate size on the fatigue crack growth behavior of alloy 718 at 427 °C, *Metall. Trans. A.* 18 (1987) 1431–1449. <https://doi.org/10.1007/BF02646657>.
- [216] E. Hosseini, V.A. Popovich, A review of mechanical properties of additively manufactured Inconel 718, *Addit. Manuf.* 30 (2019) 100877.
<https://doi.org/10.1016/j.addma.2019.100877>.
- [217] S. Majumdar, D. Bhattacharjee, K.K. Ray, On the Micromechanism of Fatigue Damage in an Interstitial-Free Steel Sheet, *Metall. Mater. Trans. A.* 39 (2008) 1676–1690. <https://doi.org/10.1007/s11661-008-9537-y>.
- [218] Z. Song, W. Gao, D. Wang, Z. Wu, M. Yan, L. Huang, X. Zhang, Very-high-cycle fatigue behavior of inconel 718 alloy fabricated by selective laser melting at elevated temperature, *Materials (Basel)*. 14 (2021) 1–16.
<https://doi.org/10.3390/ma14041001>.
- [219] L. Zhong, H. Hu, Y. Liang, C. Huang, High cycle fatigue performance of inconel 718 alloys with different strengths at room temperature, *Metals (Basel)*. 9 (2019) 1–14. <https://doi.org/10.3390/met9010013>.
- [220] D.B. Witkin, D. Patel, T. V. Albright, G.E. Bean, T. McLouth, Influence of surface conditions and specimen orientation on high cycle fatigue properties of Inconel 718 prepared by laser powder bed fusion, *Int. J. Fatigue*. 132 (2020) 105392. <https://doi.org/10.1016/j.ijfatigue.2019.105392>.
- [221] G.E. Dieter, D.J. Bacon, D. Bacon, *Mechanical Metallurgy*, McGraw-Hill, 1988. <https://books.google.com.au/books?id=hlabmB3e8XwC>.
- [222] S. Li, J. Yang, J. Zhuang, Q. Deng, J. Du, X. Xie, B. Li, Z. Xu, Z. Cao, Z. Su, C. Jiang, The Effect of Delta-Phase on Crack Propagation Under Creep and Fatigue Conditions in Alloy 718, in: *Superalloys 718, 625, 706 Var. Deriv.*, TMS, 1994: pp. 545–555.
https://doi.org/10.7449/1994/Superalloys_1994_545_555.
- [223] E.L. Raymond, EFFECT OF GRAIN BOUNDARY DENUDDATION OF

GAMMA PRIME ON NOTCH-RUPTURE DUCTILITY OF INCONEL NICKEL- CHROMIUM ALLOYS X-750 AND 718, AIME MET SOC TRANS. 239 (1967) 1415–1422.

- [224] J. An, L. Wang, Y. Liu, W. Cai, X. Song, The role of δ phase for fatigue crack propagation behavior in a Ni base superalloy at room temperature, *Mater. Sci. Eng. A.* 684 (2017) 312–317. <https://doi.org/10.1016/j.msea.2016.12.029>.
- [225] N. Kashaev, M. Horstmann, V. Ventzke, S. Riekehr, N. Huber, Comparative study of mechanical properties using standard and micro-specimens of base materials Inconel 625, Inconel 718 and Ti-6Al-4 v, *J. Mater. Res. Technol.* 2 (2013) 43–47. <https://doi.org/10.1016/j.jmrt.2013.03.003>.
- [226] Y. Ono, T. Yuri, N. Nagashima, T. Ogata, N. Nagao, Effect of microstructure on high-cycle fatigue properties of Alloy 718 plates, *IOP Conf. Ser. Mater. Sci. Eng.* 102 (2015). <https://doi.org/10.1088/1757-899X/102/1/012001>.
- [227] Kevinsanny, S. Okazaki, O. Takakuwa, Y. Ogawa, K. Okita, Y. Funakoshi, J. Yamabe, S. Matsuoka, H. Matsunaga, Effect of defects on the fatigue limit of Ni-based superalloy 718 with different grain sizes, *Fatigue Fract. Eng. Mater. Struct.* 42 (2019) 1203–1213. <https://doi.org/10.1111/ffe.12989>.
- [228] Y. Murakami, *Metal fatigue: effects of small defects and nonmetallic inclusions*, Academic Press, 2002.
- [229] S.G.K. Manikandan, D. Sivakumar, K.P. Rao, M. Kamaraj, Effect of weld cooling rate on Laves phase formation in Inconel 718 fusion zone, *J. Mater. Process. Technol.* 214 (2014) 358–364. <https://doi.org/10.1016/j.jmatprotec.2013.09.006>.
- [230] J. Jones, M. Whittaker, R. Buckingham, R. Johnston, M. Bache, D. Clark, Microstructural characterisation of a nickel alloy processed via blown powder direct laser deposition (DLD), *Mater. Des.* 117 (2017) 47–57. <https://doi.org/10.1016/j.matdes.2016.12.062>.
- [231] B. Li, B. Qian, Y. Xu, Z. Liu, J. Zhang, F. Xuan, Additive manufacturing of ultrafine-grained austenitic stainless steel matrix composite via vanadium carbide reinforcement addition and selective laser melting: Formation mechanism and strengthening effect, *Mater. Sci. Eng. A.* 745 (2019) 495–508. <https://doi.org/10.1016/j.msea.2019.01.008>.

- [232] D. Gu, G. Meng, C. Li, W. Meiners, R. Poprawe, Selective laser melting of TiC/Ti bulk nanocomposites: Influence of nanoscale reinforcement, *Scr. Mater.* 67 (2012) 185–188. <https://doi.org/10.1016/j.scriptamat.2012.04.013>.
- [233] T. Rong, D. Gu, Formation of novel graded interface and its function on mechanical properties of WC_{1-x} reinforced Inconel 718 composites processed by selective laser melting, *J. Alloys Compd.* 680 (2016) 333–342. <https://doi.org/10.1016/j.jallcom.2016.04.107>.
- [234] Y. Chen, Y. Guo, M. Xu, C. Ma, Q. Zhang, L. Wang, J. Yao, Z. Li, Study on the element segregation and Laves phase formation in the laser metal deposited IN718 superalloy by flat top laser and gaussian distribution laser, *Mater. Sci. Eng. A.* 754 (2019) 339–347. <https://doi.org/10.1016/j.msea.2019.03.096>.
- [235] J. Schneider, L. Farris, G. Nolze, S. Reinsch, G. Cios, T. Tokarski, S. Thompson, Microstructure Evolution in Inconel 718 Produced by Powder Bed Fusion Additive Manufacturing, *J. Manuf. Mater. Process.* 6 (2022). <https://doi.org/10.3390/jmmp6010020>.
- [236] G.E. Bean, T.D. McLouth, D.B. Witkin, S.D. Sitzman, P.M. Adams, R.J. Zaldivar, Build Orientation Effects on Texture and Mechanical Properties of Selective Laser Melting Inconel 718, *J. Mater. Eng. Perform.* 28 (2019) 1942–1949. <https://doi.org/10.1007/s11665-019-03980-w>.
- [237] E. Chlebus, K. Gruber, B. Kuźnicka, J. Kurzac, T. Kurzynowski, Effect of heat treatment on the microstructure and mechanical properties of Inconel 718 processed by selective laser melting, *Mater. Sci. Eng. A.* 639 (2015) 647–655. <https://doi.org/https://doi.org/10.1016/j.msea.2015.05.035>.
- [238] L. Yu, X. Liu, H. Ding, X. Bian, A new nucleation mechanism of primary Si by peritectic-like coupling of AlP and TiB₂ in near eutectic Al-Si alloy, *J. Alloys Compd.* 432 (2007) 156–162. <https://doi.org/10.1016/j.jallcom.2006.06.005>.
- [239] L. Parry, I.A. Ashcroft, R.D. Wildman, Understanding the effect of laser scan strategy on residual stress in selective laser melting through thermo-mechanical simulation, *Addit. Manuf.* 12 (2016) 1–15. <https://doi.org/10.1016/j.addma.2016.05.014>.

- [240] C.S. Goh, J. Wei, L.C. Lee, M. Gupta, Properties and deformation behaviour of Mg-Y₂O₃ nanocomposites, *Acta Mater.* 55 (2007) 5115–5121.
<https://doi.org/10.1016/j.actamat.2007.05.032>.
- [241] A. Sanaty-Zadeh, Comparison between current models for the strength of particulate-reinforced metal matrix nanocomposites with emphasis on consideration of Hall-Petch effect, *Mater. Sci. Eng. A.* 531 (2012) 112–118.
<https://doi.org/10.1016/j.msea.2011.10.043>.
- [242] K.C. Chang, M.Y. Lee, T.H. Hsu, Y.J. Chang, K.C. Lo, H.S. Kim, K.K. Jen, A.C. Yeh, An effective strengthening strategy of nano carbide precipitation and cellular microstructure refinement in a superalloy fabricated by selective laser melting process, *Metals (Basel)*. 11 (2021).
<https://doi.org/10.3390/met11111691>.
- [243] Y. Li, D. Parfitt, P.E.J. Flewitt, X. Hou, J. Quinta de Fonseca, B. Chen, Microstructural considerations of enhanced tensile strength and mechanical constraint in a copper/stainless steel brazed joint, *Mater. Sci. Eng. A.* 796 (2020). <https://doi.org/10.1016/j.msea.2020.139992>.
- [244] Q.B. Nguyen, M. Gupta, Enhancing compressive response of AZ31B magnesium alloy using alumina nanoparticulates, *Compos. Sci. Technol.* 68 (2008) 2185–2192. <https://doi.org/10.1016/j.compscitech.2008.04.020>.
- [245] R.K. Dutta, R.H. Petrov, R. Delhez, M.J.M. Hermans, I.M. Richardson, A.J. Böttger, The effect of tensile deformation by in situ ultrasonic treatment on the microstructure of low-carbon steel, *Acta Mater.* 61 (2013) 1592–1602.
<https://doi.org/10.1016/j.actamat.2012.11.036>.
- [246] R.W. Harrison, W.E. Lee, Processing and properties of ZrC, ZrN and ZrCN ceramics: a review, *Adv. Appl. Ceram.* 115 (2016) 294–307.
<https://doi.org/10.1179/1743676115Y.0000000061>.
- [247] R. Mahmoodian, M. Hamdi, M.A. Hassan, A. Akbari, Mechanical and Chemical Characterization of a TiC/C System Synthesized Using a Focus Plasma Arc, *PLoS One*. 10 (2015) e0130836–e0130836.
<https://doi.org/10.1371/journal.pone.0130836>.
- [248] Y. Miyamoto, M. Niino, M. Koizumi, FGM research programs in japan — from structural to functional uses, Woodhead Publishing Limited, 1997.

<https://doi.org/10.1016/b978-044482548-3/50002-0>.